University of Sheffield

Development of Refractory High Entropy Alloys for Additive Manufacturing

L. A. U. Farquhar

A thesis submitted in partial fulfilment of the requirements for the degree of Doctor of Philosophy

in the

Department of Materials Science and Engineering

2024

Development of Refractory High Entropy Alloys for Additive Manufacturing

Lucy Anna Ursula Farquhar

A thesis submitted in partial fulfilment of the requirements for the degree of Doctor of Philosophy

in the

Department of Materials Science and Engineering

March, 2024

Abstract

High Entropy Alloys (HEAs) are a class of alloys consisting of multiple primary elements with similar content, exhibiting many promising properties, therefore garnering interest in many sectors such as nuclear and aerospace. HEAs are frequently reported as having good mechanical properties, particularly when manufactured by additive manufacturing (AM). In AM, components are built up layer-by-layer using a moving heat source to sequentially melt feedstock to build up a geometrically optimised 3D part with a controlled microstructure. AM is especially useful in manufacturing refractory HEAs (RHEAs), due to the high melting temperatures involved and the difficulties associated with their manufacture via conventional methods such as casting and machining. AM enables the manufacture of these types of high temperature alloys with complex part geometries, suitable for highly specialised applications in the pursuit of increasing efficiency and reducing material waste.

This thesis concerns development of new HEAs suitable for AM, more specifically for the AM process *laser powder bed fusion* (PBF-LB/M). *In-situ alloying* (ISA), a technique where powders are blended prior to the AM process and alloyed using the motion of the laser and the melt pool, is explored. The impact of different elemental additions on alloying is assessed, including the benefit of minimising melting point differences and the tendency of that elemental addition to segregate, impacting the miscibility of the addition in the base alloy. The impact of elemental powder size, shape and contamination on the ISA process is also explored, showing that although defects can form due to low powder flowability, representative homogeneous microstructures can be obtained, comparable to equivalent samples manufactured using pre-alloyed powder.

An alloy design procedure is also proposed, using empirical parameters to design solid solution HEAs suitable for high temperatures. The top ranked HEAs are then manufactured via arc-melting, resulting in 4 solid solution RHEAs. The AM processability of these alloys is then assessed using melt tracks, providing information on their crack susceptibility. Consequently, a new solid-state cracking indicator is proposed based on considering the impact of bond energy on ductility, which is used along with a solidification cracking indicator and 12 conventional alloys from literature to map AM crack susceptibility for new HEAs. The AM processable $Mo_5Nb_{35}Ti_{30}V_{30}$ RHEA is then manufactured via ISA and pre-alloyed powder comparing the results. The pre-alloyed samples are heat-treated, initiating the formation of a secondary TiCN phase on cell and grain boundaries, which coarsens with heat treatment time due to atmospheric infiltration. The removal of the cellular microstructure, interstitial strengthening and coarsening of the TiCN results in an improvement in alloy mechanical properties compared to the as-built condition. High throughput alloy design and optimisation is important to facilitate rapidly evolving industrial requirements for high performance materials. The results of this thesis aim to streamline and accelerate the alloy screening process, while also minimising time and costs associated with alloy development.

Acknowledgements

My PhD has been quite the journey and there are many people who have helped me along the way who deserve my endless gratitude. Though there is not space to name all these amazing people, many have earned a special mention.

Firstly, to my primary supervisor Prof. Russell Goodall, who allowed space for me to explore my own ideas, while providing constant calmness, advice and input along the way. Having a brilliant supervisor is such a privilege and I am so grateful for those hours spent puzzling over metallurgy and finding solutions to seemingly endless problems. Thank you also to my secondary supervisor Prof. Iain Todd for the infinite depth of AM knowledge, the professional support and encouragement to pursue crazy ideas and to Lukas Jiranek for the industrial insight.

I am lucky to work with many incredible women, all of whom have impacted me profoundly. Thank you to Frances Livera who is one of the kindest, most selfless and proactive people I know and to Elaine Livera for her unwitting brilliance and willingness to help. Thank you to Felicity Freeman for her calm wisdom, Wunmi Olukoya for her endless enthusiasm and to Kathy Christofidou, who somewhat by lucky chance has become an invaluable mentor, role model and friend.

Thank you to my colleagues and friends who without which PhD life would have been much less interesting. To Lova Chechik for the endless tangents and silly questions which lead to many moments of inspiration, to Alex Goodall for his encouragement and practical ways of thinking, to Kavi Sharma for always being there, whether that be with a solution or with a welcome, often food-based, distraction and to Ashley Scarlett and Sam Lister for the laughs and the friendship. Thank you to George Maddison for his technical know-how, to Rob Snell for saving me from endless hours of building cubes and for bouncing around ideas, to Hugh Banes for diligently educating me about the wonders of modelling, and to Jonah Shrive for his brilliance at expertly operating microscopes. To Josh Berry for being the best conference buddy, to Henry Saunders for the constant questions and insightful conversations and to the rest of the amazing crew in H8 and H6. Thank you also to Matteo di Benedetti, Harry Day, Jonathan Wood and Michael Wright for supporting my teaching and helping me build my confidence.

I would also like to thank my other friends who have probably got fed up of how much I talk about metal, but stuck around anyway. Thank you to Harmonie and Phoebe for putting up with me for many years through thick and thin despite my lack of communication and to Emily and Libby for helping me believe that finishing my PhD was possible. Thank you all my brilliant friends at Hallamshire Harriers, for reminding me how fun running is again and those at DNC netball club, especially Beth and Rachel.

Finally, thank you to my family. To my mum who thought I was crazy for applying for engineering in the first place yet supports me wholeheartedly every step of the way and to my dad for his kindness and for building me up when imposter syndrome starts taking hold. Thank you to

my brothers; Andrew for his sincerity and enthusiasm and Nick for always being unapologetically himself and reminding me to always do the same. Lastly, thank you to my amazing Grandma Diane, who always encouraged me to do what whatever made me happy and I really hope I have made her proud in the process.

Contents

List of Figures

List of Tables

Chapter 1

Introduction

With the imminent threat of climate change and the need for increased energy efficiency, many sectors are looking towards the development of new materials and processing methods to enable the improvements required. High entropy alloys (HEAs) are a new class of alloys, which instead of one primary element, comprise of multiple elements with similar content. First proposed in 2004, HEAs have developed into a large research field with alloys showing promise for many applications, including in nuclear and aerospace sectors [1–3]. Refractory HEAs (RHEAs) in particular are an exciting group of alloys, due to their excellent mechanical properties, often retained at high temperatures, indicating their potential to surpass nickel superalloys as next generation alloys for operation at high-temperatures.

Additive manufacturing (AM) is a process which enables the production of complex components through use of a heat source, usually a laser, to sequentially melt powder layer-by-layer to build up a 3D part. AM of HEAs was first reported in 2011 by Zhang *et al.* concerning laser cladding of the CoCrCuFeNi system [4], with AM of RHEAs specifically first reported by Dobbelstein *et al.*, concerning directed energy deposition (DED) of equiatomic MoNbTiV [5]. Following after this, production of HEAs via laser powder bed fusion (PBF-LB/M) processing was first reported in 2015 by Brif *et al.* [6], with the first RHEA was produced by PBF-LB/M by Zhang *et al.* in 2018 [7]. Many HEAs are highly processable by AM, with reports stating remarkable resulting improvements in mechanical properties, compared to conventional casting methods, typically because of the microstructural refinement [8]. However, due to high costs and lead-times associated with manufacturing of HEA and particularly RHEA powders, many studies use in-situ alloying (ISA) to produce representative samples of these alloys, where elemental or partially alloyed powders are blended prior to the AM process and are then alloyed in-situ by the action of the laser.

This study sets out to evaluate the processes involved in development of novel HEA systems for use in AM. The aim is to understand the complex interactions considered in HEA alloy design

and then propose ways which assessment of alloy processability and characterisation can be accelerated to limit the time and resources needed for alloy development. Several identified objectives contribute to achieving this goal:

- Evaluate the use of ISA and the respective considerations involving alloying elements, process parameters, defects and powder characteristics, as well as the effects of these considerations of part quality. To this end, ISA will be applied to different HEA compositions and the resulting microstructures and quality will be compared to equivalent samples manufactured with pre-alloyed powder. Enabling assessment of whether ISA is a viable tool by which to produce representative AM parts with microstructures which resemble those produced with optimised powder.

- Attempt to design and evaluate new HEAs, in new compositional spaces, selecting for suitability for processing via AM. This involves steps all the way from theoretical prediction, manufacture of preliminary samples and evaluation of AM processability to the successful AM of a new RHEA composition. Where effective methods do not exist, such as in prediction of solid-state cracking, a new approach is developed and validated using the pool of HEAs designed.

- Employ post processing heat treatments in order to fully understand the stability of the RHEA manufactured and the effect of AM on the microstructure and phase formation. This includes characterisation of precipitation of secondary phases and assessment of resulting mechanical properties.

This thesis comprises a series of five results chapters, each written in paper format. One of the chapters has previously been published in a peer reviewed journal. The author of this thesis is responsible for most aspects of the work reported, including conceptualisation, methodology, experimentation and data analysis, as well as being first author on all the papers. The contributions of any other authors are outlined prior to each chapter. Rather than references being included at the end of each paper, the references have been combined to avoid duplication and have been displayed at the end of thesis. The list of figures and tables is also compiled at the beginning of the thesis, but any abbreviations are defined in each chapter, as they would be in a paper.

Chapter 2 provides a high-level review of the relevant literature surrounding the objectives of this thesis, including background for much of the work proposed in the following chapters. As a detailed introduction is included in each chapter, this information is not repeated in this review chapter and where relevant, reference is made to the chapter where more background information can be found.

Chapter 3 introduces a preliminary study into the considerations involved in successful ISA, considering the additions of elemental powders to a base HEA powder. The effect of the elemental

additions on homogeneous alloying is assessed via scanning electron microscopy (SEM), energy dispersive x-ray spectroscopy (EDS) and x-ray diffraction (XRD), based on comparison of melting points and the effect of that element on segregation in that alloy system.

Chapter 4 outlines a model, which uses empirical parameters defined in the literature, to design new HEAs for high temperature applications with solid-solution microstructures. Previously these parameters have been used to design HEAs with a single phase, however in this study, multi-phase solid-solution phases were also desired. The resulting alloys are then manufactured via arc-melting and characterised using SEM, EDS and XRD to assess the success of the alloy design model.

Chapter 5 concerns the assessment of AM processability of some of the HEAs discussed in Chapters 3 and 4, through melt tracks on the surface of cast material. The results of these melt tracks, including the cracking behaviour of each alloy, are then used to validate a proposed new solid-state cracking indicator, along with 12 conventional alloys with varying levels of AM processability reported in literature. The AM processability of each alloy is then mapped based on the susceptibility to solidification and solid-state cracking.

Building on the results from Chapter 3, Chapter 6 compares ISA of the $Mo_5Nb_{35}Ti_{30}V_{30}$ RHEA with PBF-LB/M of equivalent samples of the same alloy manufactured from pre-alloyed powder. The powder characteristics, and contamination, as well as sample defect formation, processing parameters, homogeneity and microstructures are compared through various characterisation techniques, including electron back-scattered diffraction (EBSD) and powder analysis using a powder rheometer. These results are then used to assess the effect of variable powder feedstock and determine under what conditions homogeneous microstructures can be produced via ISA compared to the pre-alloyed equivalent.

Chapter 7, investigates the effect of post-processing heat treatments on the microstructure and compressive properties of $Mo_5Nb_{35}Ti_{30}V_{30}$ after PBF-LB/M using pre-alloyed powder. This outlines specifically the effect of interstitial infiltration on the precipitation and growth of a secondary phase and the impact of the formation of this phase, as well as the recovery of the cellular microstructure produced by AM, on the compressive properties of the alloy.

Finally, Chapter 8 forms an overall conclusion of the reported studies, commenting on their corresponding impact on the HEA development process. Chapter 9 suggests future work which could be completed to add to the findings reported in this thesis, as well as the general predicted direction of the field as a whole.

Chapter 2

Research Context

2.1 High Entropy Alloys

High Entropy Alloys (HEAs) represent an exciting new research opportunity with a broad scope, offering the potential to create materials tailored exactly to their application. There are approximately 30 conventional alloy systems which consist of one principal element with the addition of small fractions of alloying elements, made to obtain desirable properties [9]. HEAs consist of combinations of multiple alloying elements with a similar proportion of each element, resulting in a high configurational entropy. In theory this high entropy is a key contributing factor to enable the stability of solid solution phases and acts in opposition to the enthalpy of formation of intermetallic phases which cause embrittlement [2]. Hence HEAs should have a very stable solid-solution microstructure, as well as high corrosion resistance and toughness. Despite the attractive simplicity of this idea, the high entropy stabilised phase hypothesis has since been disproved [10]; however there is no doubt that the broad scope of HEA research offers opportunities to discover new high performance alloys, in as-yet unexplored compositional spaces. With this shift in the theoretical framework around such alloys, and the exploration of these systems finding different behaviours, there have been developments in the nomenclature prevalent in the community. More recently HEAs have also been referred to as multi-principal element alloys (MPEAs), multi-component alloys (MCAs) and complex concentrated alloys (CCAs). However, the term is still widely recognised, and in this work HEA is used as a blanket term for all alloys which fit any of those definitions.

Different varieties of HEAs have shown exceptional material properties, when compared with their conventional alloy counterparts. This includes, but is not limited to, high strength and ductility [11,12], high hardness [13,14], retained mechanical strength and microstructural stability at high temperatures [15], fracture toughness at cryogenic temperatures [16], wear resistance [17], corrosion resistance [18] and oxidation resistance [19]. However, despite being a promising new

material area of interest for many industrial sectors, including in aerospace and nuclear, there are few, if any, confirmed widely used applications for HEAs, but no doubt this landmark is not far away.

2.1.1 Origins and Principles

The origin of the HEA research field can be traced back to two seminal papers, published by Yeh *et al.* and Cantor *et al.* in 2004 [1,2]. Where HEAs were first defined as containing 5-13 elements at between 5 at% - 35 at% composition [2]. This definition, as well as many founding principles of the HEA field, have since expanded as the field has developed. Yeh *et al.* initially defined 4 'core effects' as inherent features unique to HEAs [2], the validity of which has since been questioned. These effects are; high entropy stabilised solid solution phases, lattice distortion, sluggish diffusion and the 'cocktail effect'.

Counter to popular belief there are very few HEAs which have been shown experimentally to be stable at all temperatures up to melting. One such example is the equiatomic MoNbTaVW HEA [20], as well as Mo_xNbTiV_yZr [21] and $Al_xCoCrFeNi$ (for low x and y) [22, 23] and some other less researched alloys covered in a review by Steurer [24]. The vast majority of HEAs either contain multiple phases even at room temperature or have a stable single phase at room temperature which breaks down at higher temperatures. An example of this is the equiatomic CoCrFeMnNi HEA, the first alloy proposed by Cantor *et al.* in 2004, now consequently known as the 'Cantor' alloy [1]. Initially, the CoCrFeMnNi alloy was widely researched because of its apparent stable single phase microstructure and corresponding mechanical properties [10, 25–30]. However this belief was disproved after studies showed the formation of a Cr-rich σ phase when heat treated for prolonged exposure times at temperatures below 800°C [31–33].

Many of the other 'core effects' have been rigorously studied to assess their validity. The lattices of HEAs are said to be severely strained due to the varied sizes of atoms and therefore bonds between elements of different sizes. But even long before the popularity of HEAs, Hume-Rothery *et al.* stated that solid solutions tend to be unstable if the atomic size mismatch between solvent and solute atoms is too large. [34]. Density function theory (DFT) has been used to model lattice strain in HEAs and showed that the strain level is comparable to that reported in binary alloys, and indeed is within the error associated with atomic vibration at room temperature [35,36]. Hence a particularly distorted lattice is not necessarily the default phase, especially if another phase is thermodynamically and spatially preferable.

The atomic lattices of HEAs are also thought to hinder diffusion due to the local fluctuations in bonding environment. Although many HEAs do show sluggish diffusion, Divinski *et al.* proved this cannot be assumed, as the diffusion retardation cannot be simply related to the number of alloying elements [37]. The so-called 'cocktail effect' is a much more difficult property to

assess, as it is defined quite abstractly, as 'the overall effect from composition, structure and microstructure' by Yeh [38]. The cocktail effect, first proposed by Ranganathan as concept for any alloy, seems to encapsulate the complexity and uncertainty associated with HEA development [39]. Even with state-of-the-art modelling methods such as DFT or CALculation of PHAse Diagrams (CALPHAD), the physical metallurgy of one HEA is completely different from the next, encompassing hugely complex interactions between the alloy chemistry, processing method and post-processing methods. A complexity which also represents a huge opportunity to develop new and nuanced alloys for future high performance applications, if those compositions can be found in the vast HEA compositional space.

2.1.2 HEA design

The majority of HEA studies have focused on single phase alloys containing mainly transition elements, which primarily have their plastic behaviour determined by solid solution strengthening. Designing HEAs represents a challenge to researchers trying to find a way to predict the phases and stability of different near-equiatomic compositions of elements. For conventional alloy systems, where there is usually one principal element alloyed with small additions of other elements, predictors such as the Hume-Rothery rules have proved useful [34]. But these alloy systems are often well known, therefore when adding in different elements there is some confidence as to the effect those elements will have on phase formation, by either being a stabiliser or inhibitor of a given phase. However, developing HEAs in new compositional spaces often means not being able to anticipate the effect of changing elemental composition on the microstructure, with secondary effects often occurring when trying to promote the formation of specific phases. In theory, the high configurational entropy of HEAs stabilizes the solid solution phases over other phases like intermetallic compounds [40]. But in reality, secondary phases and intermetallic phases form readily, therefore predictive parameters and methods need to reflect these results.

There are a few approaches which can be used to try and design new HEAs with a given desired microstructure. The first and simplest approach is using empirical parameters based on fundamental HEA design principles or on other criteria such as the Hume-Rothery rules. Empirical parameters are in general based on three concepts. The first concept is the physical interaction of atoms within the lattice and trying to quantify the distortion and strain that this creates. Examples of this are the atomic size mismatch δ and residual lattice strain ε_{RMS} [41,42]. The second concept relates to thermodynamic considerations and often attempts to find compositions that result in minimised Gibb's free energy of the alloy system. Parameters could include enthalpy of mixing ΔH_{mix}, entropy of mixing ΔS_{mix} and a combination of these parameters such as Ω [43–45]. The third concept is based on electronic interactions between atoms and includes variables such as valence electron concentration VEC and electronegativity χ. Lastly, a combination of these

concepts can be combined as is seen with the Λ parameter [46]. An example of phase prediction based on a combination of δ and ΔH_{mix} is shown in Figure 2.1.

The weakness of this approach is that by definition the limits are fitted to experimental data, which has often been collected using small sample sizes, and the validation is based on as-cast microstructures. Hence these non-equilibrium microstructures do not necessarily accurately reflect the wider phase formation and phase stability of the HEAs concerned. Use of these parameters at least narrows the range of alloys that are feasible, despite a high degree of uncertainty. Many of them are often used in conjunction with other variables to further refine the possible selection of alloys that satisfy the criteria. More about these parameters and the limits for phase formation is covered in Chapter 4.

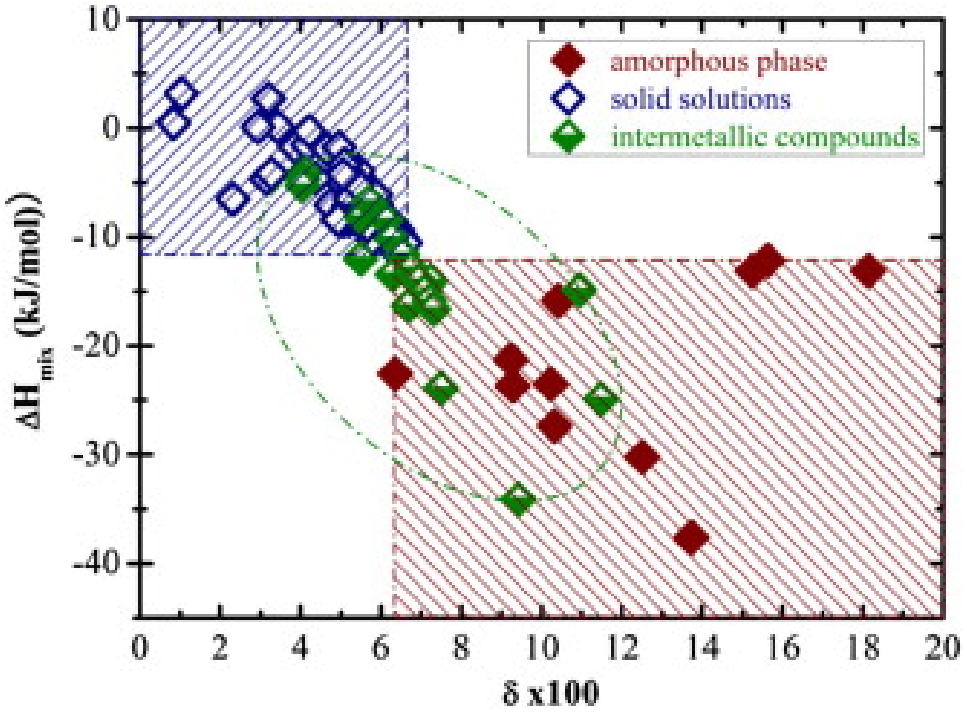

Figure 2.1: *δ vs ΔH_{mix} plot showing corresponding phases in HEAs. The dash-dotted regions highlight the individual region to form solid solutions, intermetallic compounds and the amorphous phase. [47]*

The complexity of HEA design is ever increasing and now there is much more emphasis on finding multi-phase HEAs which can mimic those microstructures which are typical for optimising performance in conventional alloy systems. There is now substantial interest in Dual-Phase HEAs (DP-HEAs) in particular, as there have been some discoveries of DP-HEAs with good tensile properties including a $Fe_{20}Co_{20}Ni_{41}Al_{19}$ eutectic HEA with a RT tensile strength of 1103 MPa and a total elongation of 18.7% [48]. The equimolar AlCoCrFeNi has body centred cubic (BCC), face-centred cubic (FCC) and σ phases with a high yield strength at temperatures up to 900

K, however phase transformations at 773 K limit the long term use of the alloy at temperatures exceeding this value [49]. As well as this, there has also been some research into transformation-induced plasticity-assisted (TRIP) DP-HEAs which has shown increased strength and ductility due to the strain hardening from metastable phases [11]. TRIP DP-HEAs under cyclic loading showed unexpected partial reversibilty which was not seen in comparable TRIP steels [50]. There has also been a recent study into High Entropy Super-Alloys (HESAs) where the methodology behind conventional super-alloys have been combined with a further broadened definition of HEAs [51]. These alloys are based on Ni and Co but also make use of high amounts of more cost effective elements not usually seen in high quantities in super-alloys, such as Fe. The alloys were found to have a FCC matrix strengthened with $L1_2$ precipitates resulting in a higher cost specific tensile strength than CM247LC.

In order to encompass these more complex design needs more novel tools can now be employed to find these more specific alloy types (these are covered comprehensively in some review papers, most notably those by Pickering *et al.*, Miracle *et al.* and George *et al.* [52–55]). CALPHAD is a tool which uses equilibrium phase diagrams based on Gibbs-Helmholtz free energies for every phase to predict the phases which will form in a particular alloy. It is now a common tool used to predict the phase formation of many different types of conventional alloy systems. It is however in its relative infancy with HEAs, with the prediction of phases of only some alloys, such as those related to the CoCrFeMnNi HEA in particular, now reliably accurate [56,57]. The main issue with use of CALPHAD for HEAs is that it is based on thermodynamic databases and ternary phase diagrams which derive from a very small experimentally validated sample set, compared to a vast space where compositions can be varied. Hence it often identifies phases wrongly or predicts too few or too many phases. Also historically it has been based purely on equilibrium phases so missed many metastable phases that are often key for strengthening, such as martensite in steels and Ti-based alloys [56]. More recently there has been the introduction of varied cooling rates, even an additive manufacturing (AM) module, but the use of these with HEAs introduces yet more uncertainty. An example of CALPHAD use in HEA design comes from the work of Senkov *et al.*, where thousands of HEA compositions were screened and 157 new potential equiatomic alloys were found [58]. Also finding that the likelihood of single phase formation reduced as the amount of components increased, converse to the initially proposed high entropy stabilised solid solution core effect for HEAs [59]. However, it was acknowledged that many of the ternary phase diagrams are either unavailable or incomplete in the thermodynamic database, therefore reducing the validity of predictions for some less common elemental combinations.

CALPHAD is often used now in conjunction with other tools such as machine learning (ML), data mining and artificial intelligence along with modelling techniques like DFT [60]. DFT is a useful tool to be able to model and understand materials at an atomic scale. However, it is

generally very computationally expensive, especially for HEAs, as due to the number of possible atomic interactions between so many components, large supercells of over 1000 atoms are needed to obtain representative results [61]. ML techniques on the other hand, can be a very efficient and quick way to predict the properties of new alloys. ML can be used in conjunction with previously described empirical parameters, utilising data which has been generated by experiments or computation [60]. But although there are algorithms such as random forest which are able to work with small datasets, HEA datasets are still limited in size and quality, with many alloys only reported in the as-cast state or using unreliable CALPHAD generated values [62]. Hence with the development and improvement of CALPHAD techniques and experimental validation of more HEAs to create high quality larger databases, ML is likely to become an even more indispensable tool for HEA development.

2.1.3 Refractory High Entropy Alloys

After the discovery of the CoCrFeMnNi alloy in 2004, research mainly focused on similar HEAs based on the same pool of 3d-transition metal elements. A key development came in 2010 when Senkov *et al.* introduced the first two refractory HEAs (RHEAs), the equiatomic MoNbTaVW and MoNbTaW alloys, outlining their exceptional microhardness [20]. Senkov *et al.* confirmed that these new RHEAs show improved mechanical properties, which are retained at elevated temperatures as shown in Figure 2.2 [63]. Since then, RHEAs have received a lot of attention, mainly for their high temperature capabilities and relatively low density in comparison to other alloys with these capabilities.

2.1.3.1 Processing

There are many review papers concentrated on RHEAs specifically, citing many exciting properties, but also many challenges involved in their manufacture, processing and oxidation resistance [3, 15, 55]. Typically HEAs more widely have been manufactured via processes such as vacuum arc melting, due to the ability to make high purity samples in a controlled inert atmosphere. This technique is often used to manufacture RHEAs, and has resulted in homogeneous samples with excellent mechanical properties [63–65]. However, to avoid segregation and incomplete melting, multiple melting of samples is required to ensure uniformity, which can be a lengthy process. Other manufacturing methods more suitable to high-throughput alloy manufacture have since been used, such as magnetron or vacuum sputtering, where electrons are fired at a target material, displacing atoms onto a substrate to form a thin film in a vacuum. Due to high cooling rates, the material often has higher hardness, a more refined microstucture or better corrosion properties than when produced by casting [66]. As shown by Alvi *et al.*, by producing a nanocrystalline, CuMoTaWV

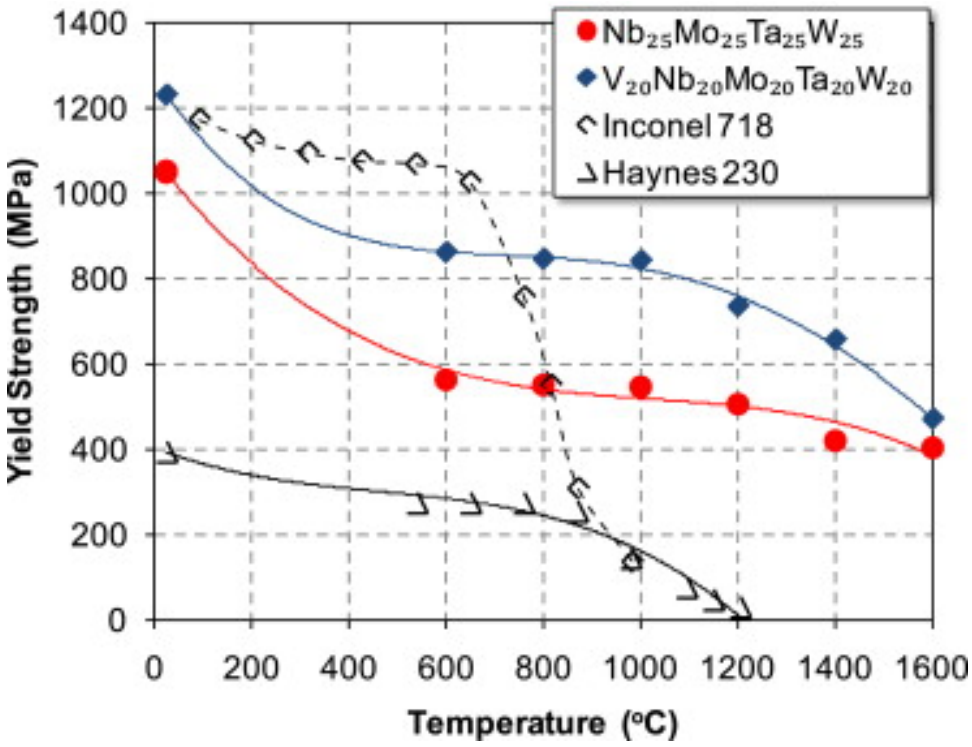

Figure 2.2: *Temperature dependence of the yield stress of VNbMoTaW and NbMoTaW and two nickel alloys: Inconel 718 and Haynes 230 [63]*

equitomic alloy with high hardness and elastic modulus [67].

The other methods under investigation for manufacturing RHEAs are powder metallurgy, such as spark-plasma sintering (SPS) and AM. SPS relies on the use of metal powders, which are consolidated in a die by the application of pressure and high current, to provide heating. It is a rapid process, which results in smaller grain sizes, higher strengths and less segregation than arc-melting. This process is often coupled with mechanical alloying so that the overall initial feedstock can be elemental powders and results in very high strength materials. An example is the use by Kang *et al.* in production of a $Al_{0.1}$CrNbVMo RHEA, with lower density than most nickel alloys and a compressive strength exceeding 1400 MPa at 1000°C [68]. The AM of RHEAs is further covered in Section 2.3.2 and Chapters 6 and 7 of this thesis.

2.1.3.2 Microstructures and mechanical properties

Referring to existing literature, most RHEAs are reported to have a single phase solid-solution BCC microstructure, as many of the refractory metal elements have a BCC structure themselves and good mutual solubility [3]. The other most common phases found in RHEAs, alongside a BCC matrix phase, are B2 and Laves phases [69–71]. There are also a few other examples of differing strengthening phases appearing in a BCC matrix including M_5Si_3 [72], MC or M_2C [73–76],

MN [77–80] and a hexagonal close packed (HCP) phase [81].

An example of engineered precipitation of a B2 phase, in effort to mimic the dual-phase microstructures seen in many superalloys, is shown in Figure 2.3 [82]. Soni *et al.* showed that the single phase BCC microstructure decomposes to form B2 channels around BCC precipitates which then invert after 120 hours at 600°C. Soni *et al.* also showed that an alloy with similar composition, but with a 2 phase nano-scale B2+BCC microstructure of differing morphology, has a high yield strength of 1075 MPa and a good compressive ductility [83]. Kube *et al.* used CALPHAD to design RHEAs containing Ru-B2 precipitates with thermal stability up to 1900°C [70]. Many of the B2 precipitates formed in the alloys manufactured also had small lattice misfits from the BCC matrix phase, showing potential for the formation of coherent phase boundaries in these types of alloys. When Cr, Ta, Nb are present, then often a C14 or C15 Laves phase can form in RHEAs, which often increases strength, but at the expense of any ductility if the percentage of Laves phase is too high. Wang *et al.* studied the microstructures and compressive properties of HfMoTiZrCr, HfMoNbZrCr, and HfMoNbTiCr equiatomic RHEAs which had 63, 70 and 31% Laves phase respectively along with a BCC phase [84]. The alloys with a high Laves phase fraction showed brittle fracture, whereas at 31% Laves phase, there was a resulting ultimate strength of 2480 MPa and a small improvement in the plastic strain to 4.3%. Guo *et al.* also utilised the Laves phase in a $MoFe_{1.5}CrTiWAlNb$ RHEA, to form a coating via laser cladding, with a hardness of 913 HV [85]. Due to the formation of an oxide film the HEA coating also showed a better oxidation resistance at 800°C compared to an M2 steel.

The addition of interstitial or non-metallic elements such as C and N to form strengthening phases in RHEAs, as might be done in a steel, for example, is a practice still in its infancy. However where it is found most is in the engineering of RHEA coatings, made by laser cladding or sputtering [80]. These elements are also used to manufacture RHEAs with very high hardness, an example of which being the equiatomic MoNbTaW. Which when milled with N promotes the formation of coherent $(Nb,Ta)_2CN$ and (Mo,W)(Nb,Ta)N phases [77], where, after subsequent annealing, a peak median hardness of 17.8 GPa was achieved. Addition of these elements can also increase strength at high temperatures whilst maintaining the ductility of an underlying BCC matrix phase. He *et al.* manufactured a $Re_{0.1}Hf_{0.25}NbTaW_{0.4}C_{0.25}$ which showed a compressive strength of 1026 MPa at 1450°C as well as a reasonable plasticity at room temperature of 10.2% [73]. Wu *et al.* manufactured and annealed $C_xHf_{0.25}NbTaW_{0.5}$ and $NbTaW_{0.5}(Mo_2C)_x$ RHEAs, to create lamellar and dendritic microstructures of MC and BCC matrix phases resulting in high room temperature strengths for the high C content alloys [75]. When higher levels of these elements are added, then the materials formed are often called high entropy ceramics, a notable examples of this is in the work by Wang *et al.* on the $(Hf_{0.25}Ta_{0.25}Zr_{0.25}Nb_{0.25})C_xN_{1-x}$ system where ($x = 1$, 0.9, 0.8, 0.7, 0.6 and 0.5) [86]. These samples mainly formed BCC single phases, the only

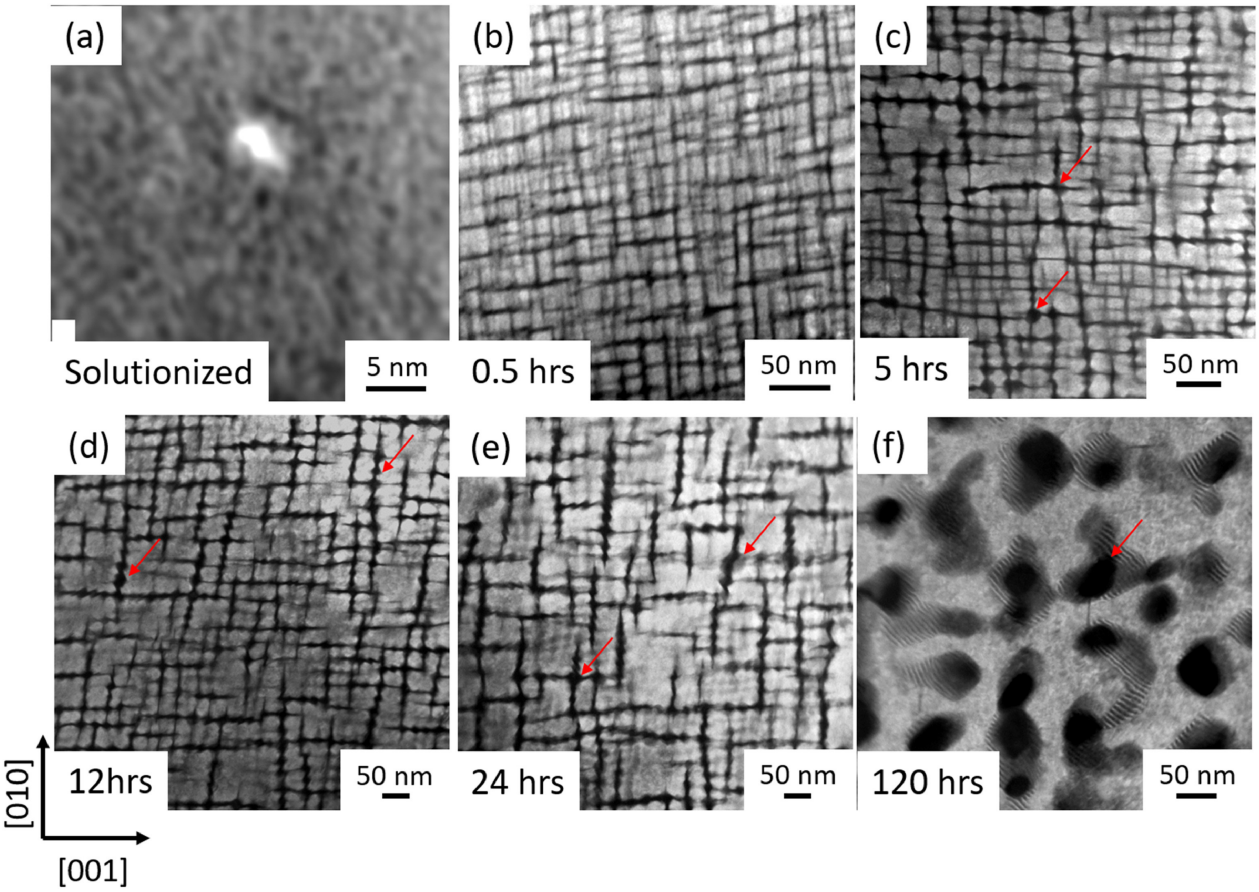

Figure 2.3: *Scanning transmission electron spectroscopy (STEM) images taken along <001> cube axis of the annealed samples of $Al_{0.5}NbTa_{0.8}Ti_{1.5}V_{0.2}Zr$ at 600 °C for x hours, where x = (a) 0, (b) 0.5, (c) 5, (d) 12, (e) 24, and (f) 120. The light phase is the Nb and Ta-rich BCC phase and the dark phase is the Al and Zr rich B2 phase [82]*

precipitation was HfO_2 in the high N samples, however hardness decreased with increasing N, inversely proportional to the alloy's calculated VEC.

Similarly, Wan *et al.* manufactured a NbMoTaWHfN alloy, which had a three phase microstructure including BCC and HfN and small amounts of HCP MN [79]. As shown in Figure 2.4, the compressive curves at showed yield strengths at ambient temperature, 1000, 1400, and 1800 °C of 1682, 1192, 792, and 288 MPa, respectively, much higher than other reported RHEAs. Tian *et al.* also showed the impact of the addition of small amounts of an increasing MN in a BCC matrix, showing a reduction in room temperature ductility with increasing N, with no benefit to strength after reaching 0.2 at% N [78]. However, compressive strength at 1000°C increased from 195 MPa with 0 at% N to 350 MPa with 0.4 at% N. Wang *et al.* showed a similar trend in room temperature properties with N doping of a NbTaTiZr alloy, this time via tensile testing [87].

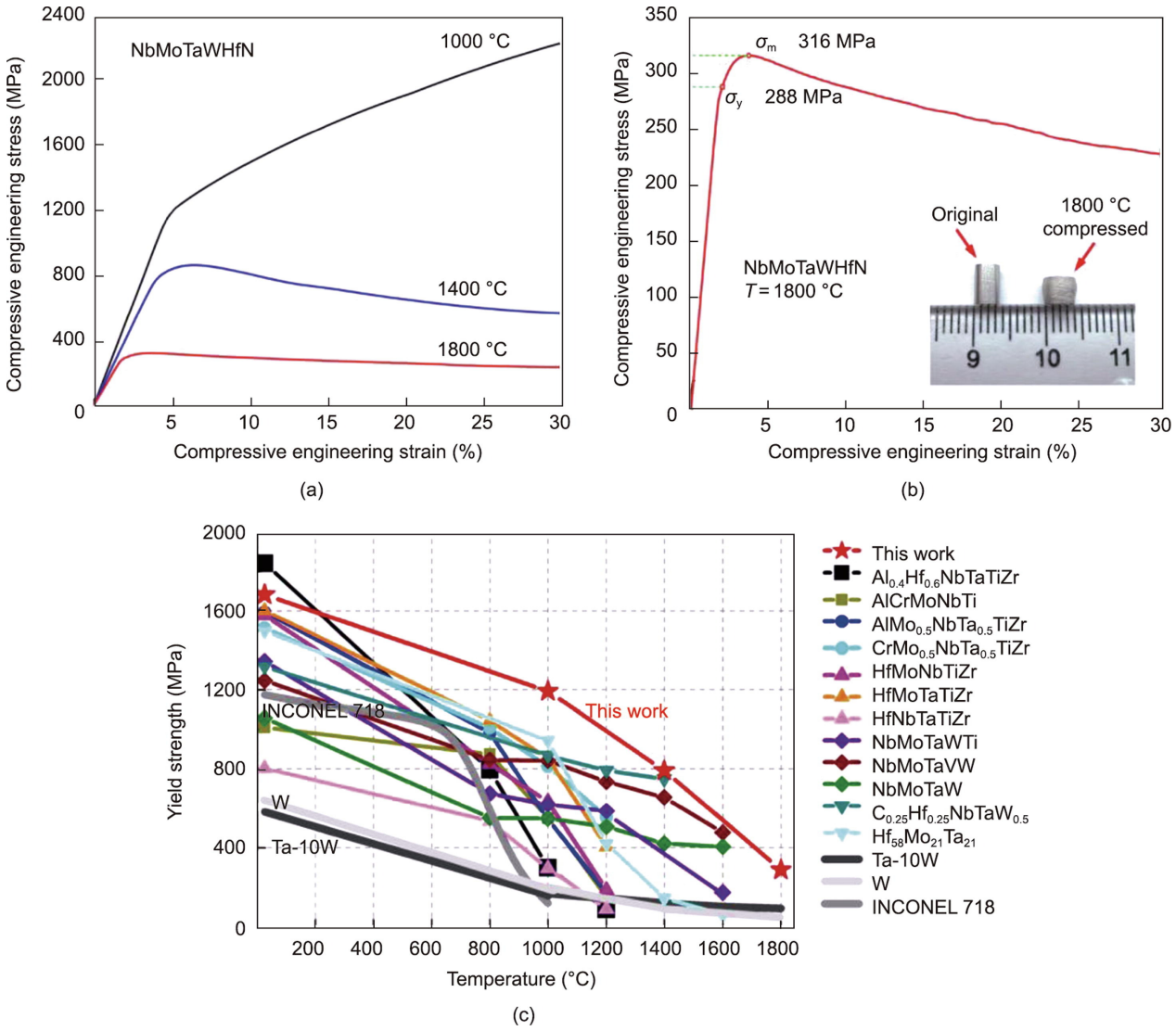

Figure 2.4: *(a) Compressive engineering stress–strain curves of NbMoTaWHfN at 1000, 1400, and 1800°C; (b) enlarged curve for 1800°C in (a); (c) yield stress of NbMoTaWHfN and other refractory alloys at different temperatures [79].*

2.2 Additive Manufacturing

Additive Manufacturing (AM) is defined as "a process of joining materials to make objects from 3D model data, usually layer upon layer" [88]. AM offers the opportunity for rapid prototyping of complex objects with minimal waste. It also often reduces the need for subsequent machining and assembly steps in the manufacturing process. AM has developed massively over recent decades from manufacture of low quality plastic components to now being used for optimised metallic or even ceramic parts for high performance and critical applications, with interest from aerospace and automotive industries in particular [89, 90]. There are many different types of AM, the main ones including material extrusion (MEX), sheet lamination (SHL), binder jetting (BJT), material jetting (MJT), vat polymerisation, directed energy deposition (DED) and powder bed fusion (PBF) [91]. Metal AM processes specifically can be split into three distinct groups:

- Binder jetting - "Additive manufacturing process in which a liquid bonding agent is selectively deposited to join powder materials" [91]. BJT alternates the deposit of layers of metal powder and liquid binder material, which acts as an adhesive to build up a part. It is regarded as one of the fastest AM processes, however parts require post-processing treatments like sintering to achieve full density and remove the binder material [92].

- Directed energy deposition - "Additive manufacturing process in which focused thermal energy is used to fuse materials by melting as they are being deposited" [91]. DED uses a high powered heat source, which is usually a laser or electron beam, to melt material as it it deposited onto a work-piece [93]. This can be done in 4 or 5 axes, either using powder feedstock with a nozzle to control powder flow rate or using wire feedstock. DED is also often used in alloy development as multiple powder feedstocks, using different hoppers, can be used at once, so the effect of varying compositions can be studied.

- Powder bed fusion - "Additive manufacturing process in which thermal energy selectively fuses regions of a powder bed" [91]. PBF also commonly uses a laser or electron beam as a heat source but the powder feedstock is supplied in a powder bed which moves down incrementally as layers are deposited, resulting in the final part being submerged in powder. Generally for metallic components, Laser PBF (PBF-LB/M) has a much higher dimensional accuracy than laser DED (DED-LB/M), as the laser spot size is smaller, however build times are much slower. Electron beam PBF (PBF-EB/M) uses faster scan rates and induces less residual stress than PBF-LB/M, however melt pools are much larger reducing it's accuracy in comparison [94].

2.2.1 Laser Powder Bed Fusion

This work is focussed on the use of PBF-LB/M as a tool for alloy development, for a few key reasons. Firstly, many AM products, and particularly some for high temperature use, such as heat exchangers, require the manufacture of thin walls and high dimensional accuracy. Hence PBF-LB/M is preferable for this reason over PBF-EB/M or any DED equivalent. Secondly, although DED can be used to quickly assess varying alloy compositions through the use of multiple powder hoppers, this requires large volumes of powder, whereas PBF-LB/M can be done with a few kg of powder reducing the costs of powder production and acquisition. Elemental powders can also be pre-blended prior to the process, in order to study the effect of so-called "in-situ alloying" (ISA), where elemental powders are alloyed during the AM process, through the melting and mixing of powders in the melt pool, similar to the effect of using multiple hoppers in DED. Lastly, PBF/LB-M is by far the most researched AM process and is well established in aerospace industries, with alloy development using this process gaining popularity, meaning there is a wealth of research to build upon and a need for further developmental work to be completed in this area [95].

The PBF-LB/M process works by creating layers of a certain thickness by lowering a base plate incrementally. When the base plate is lowered the wiper/roller will deposit a new layer of powder supplied by a powder reservoir on top on the base plate, as shown in Figure 2.5. A part is built up by a laser scanning across each layer, melting regions in a pattern according to the input computer aided design (CAD) file, to consolidate that powder into one bulk entity. To melt the specified cross sectional area, the laser completes a number of hatches, with a pre-defined hatch spacing between. The angle of these hatches compared to the previous layer can be varied to ensure homogeneity by changing the hatch rotation angle. The aim is for the melt pool created by the laser to penetrate through multiple layers at a time and for the hatches to overlap so that the whole cross-section is melted and the layers are fully bonded. The surrounding powder bed supports the part and conducts excess heat away, allowing for the manufacture of complex components with inner details, channels and overhangs. There are many process parameters to control in the PBF-LB/M process and in this work the main parameters are often combined to give an estimate of the energy input to melt a given volume of powder, which is known as the volumetric energy density (VED) [96]:

$$VED = \frac{P}{vlh} \tag{2.1}$$

where P is laser power, v is laser scanning velocity, l is layer thickness and h is hatch spacing. The input VED for high density part manufacture tends to vary for different materials, dependent on thermal properties and phase formation, as well as for different part geometries. If the VED input is too low then the part will commonly contain lack of fusion or gas porosity, whereas if

VED input is too high then keyhole porosity can occur [97].

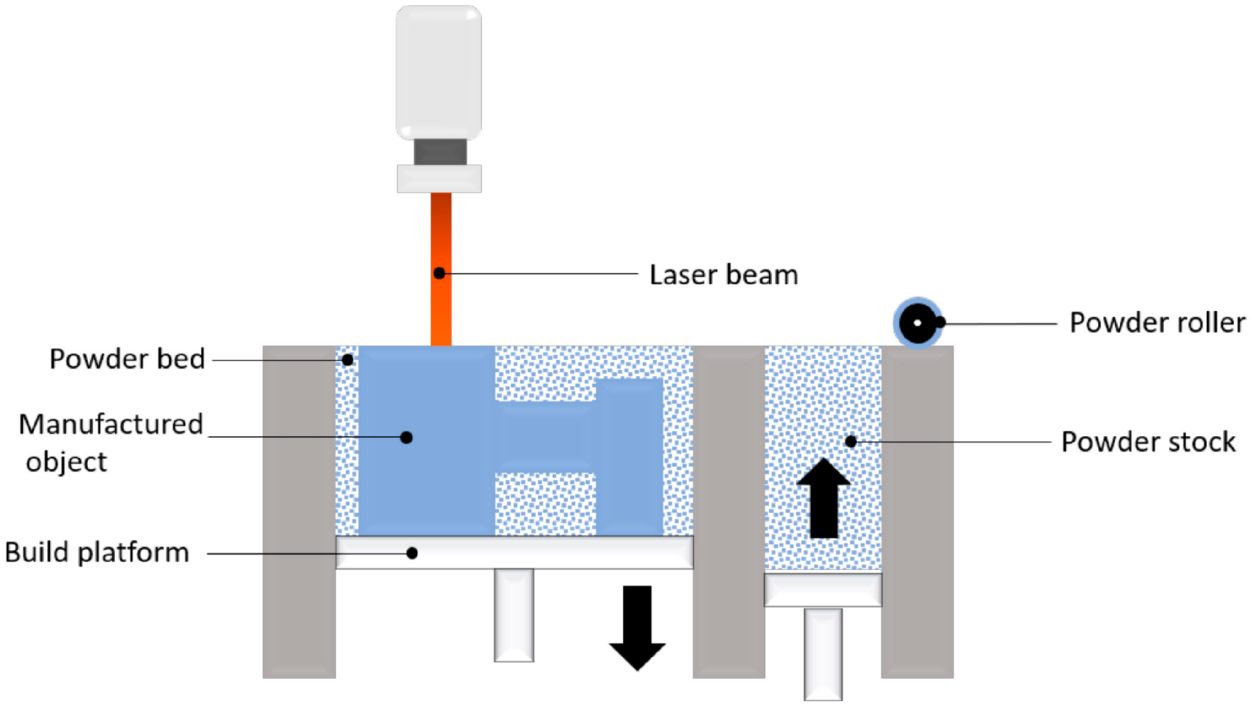

Figure 2.5: *Schematic showing the PBF-LB/M process [98]*

2.2.2 Defects in PBF-LB/M

2.2.2.1 Porosity

When VED is too low, there are a few common defect types seen in built samples. Lack of fusion occurs when there is insufficient overlap between laser passes, such that powder in the area between is partially- or un-melted, forming voids. This can also occur if the hatch spacing, in isolation, is too large such that melt pools do not overlap no matter the VED [99]. The voids are usually irregularly shaped, 50 µm or larger, are sometimes interconnected and often include un-melted satellite powder particles. Gas porosity is most commonly due to the entrapment of gases in the powder resulting from supersaturation in the melt pool. These pores are usually spherical and on the order of 5 to 20 µm. Pore formation is mitigated by increasing VED to ensure slower cooling rates and time for gas to escape while material is molten [100].

In high VED AM or welding processes, keyhole porosity is often observed. Where the transition to keyhole-mode melting is defined by when the depth of the melt pool reaches greater than the half-width of the melt pool defined at the melt pool surface [101]. This type of porosity occurs when keyhole-mode is not controlled and keyholes become unstable, repeatedly forming

and collapsing, leaving pores containing trapped vapour during solidification [99]. These pores are often spherical but larger than pores formed by gas porosity, usually between 10 - 50 µm and their frequency can be reduced by reducing the input VED. The dependence of lack of fusion and keyhole porosity on input VED is shown in Figure 2.6.

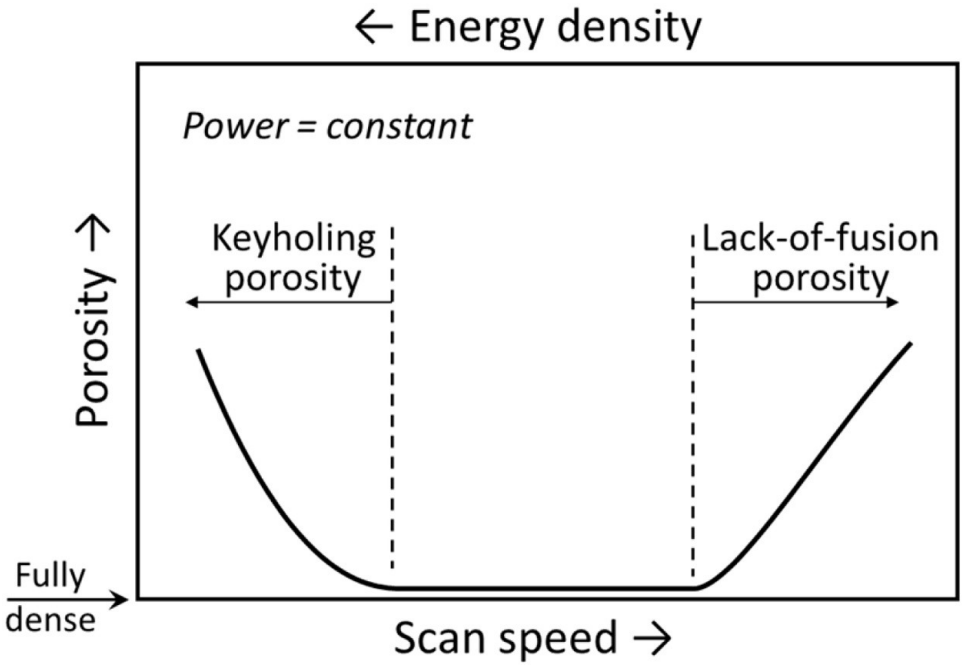

Figure 2.6: *Dependence of the type of porosity with changes in scan speed and energy density (here illustrated with constant power) [102]*

2.2.2.2 Cracking

The defects discussed above can occur with any metal subjected to the PBF-LB/M process if the laser parameters are not optimised. Cracking is also a common defect in AM, which, in some cases, can be mitigated by processing conditions. Susceptibility to cracking is often very much dependent on alloy composition, solidification behaviour and phase formation itself. There are 3 main types of cracking commonly reported in AM processes; solidification cracking, liquation cracking and solid-state cracking.

Solidification cracks form in the latter stages of solidification, due to shrinkage at grain boundaries (GBs) and interdendritic regions, where a liquid film has yet to solidify [99, 103]. The main factors influencing this type of crack formation are the solidification temperature range, the cooling rate and the final inter-facial liquid morphology and composition.

Liquation cracking occurs in the partially melted zone (PMZ) of a melt pool when reheated to below the melting point of the main phase but above the melting point of the GB precipitates, inducing localised melting of those precipitates [104]. The residual tensile stress in the AM process

can result in tearing the GB and separating the liquid films. In nickel alloys liquation can occur due to the γ/γ' eutectic [105], whereas more generally it occurs in alloys with wider freezing ranges, a higher fraction of liquid during freezing or with increasing GB segregation [104].

Solid-state cracking can be divided into several categories. Ductility-dip cracking is perhaps the most common and occurs due a sharp reduction in ductility for many materials including austenitic stainless steels, nickel alloys and titanium alloys between 0.5 to 0.9 of the solidus temperature T_s [103]. It primarily occurs along GBs, so the presence of high angle GBs and certain GB precipitates can be contributing factors; however it can occur intragranularly if brittle phases are distributed within grains. Other types of solid-state cracking such as strain-age cracking in nickel super alloys also occur due to a combination of the formation of precipitates or other brittle phases such as carbides and residual stress induced by the AM process [103].

2.2.3 Process Mapping for AM

Many studies focus on porosity-based AM defects or distortion rather than cracking, creating so-called processing maps where parameters can be optimised concurrently to result in dense parts. The first of these was proposed by Vasinonta *et al.*, mapping the optimum melting point, melt pool length and deposition height for DED processes and varying parameters to maintain this for parts of differing geometries [106]. Further processing maps of similar type replaced melt pool length with cooling rate $\dot{T}$ and thermal gradient G [107].

Subsequent work used VED to optimise for maximum relative density, while also allowing for the comparison across different materials and machines. Jägle *et al.* used VED to evaluate precipitation in an aluminium alloy, a maraging steel and Inconel-738LC, while comparing between PBF-LB/M and DED-LB/M processes [108]. Building on this work, to account for machine differences, the hatch spacing in the VED equation has also been replaced with beam diameter D_b, to get a better approximation of the beam interaction volume [109]. Scipioni Bertoli *et al.*, however, concluded that VED is only applicable for a narrow range of parameters and that it does not capture the complex melt pool dynamics accurately enough to be used as a design tool in isolation.

Thomas *et al.* took this methodology further by introducing a dimensionless mapping mechanism by which to account for more machine parameters and also material properties [110]. The resulting map is shown in Figure 2.7, where the the reciprocal of the hatch spacing (normalised by the beam radius $1/h^* = r_B/h$) is plotted against the energy parameter E^*. The lines of constant normalised equivalent energy density E_0^* allow for direct comparison of E^* resulting from processing parameters and the theoretical heat input which would result in melting, calculated using material properties. Theoretically when $A = 0.5$ then melting should occur when $E_0^* = 1$, however optimum parameters for most materials lie roughly where $E_0^* = 4$. Also included on

this diagram are the threshold of formation of many defects including porosity, void formation and even cracking, but these are largely material specific and cannot be applied globally to all materials.

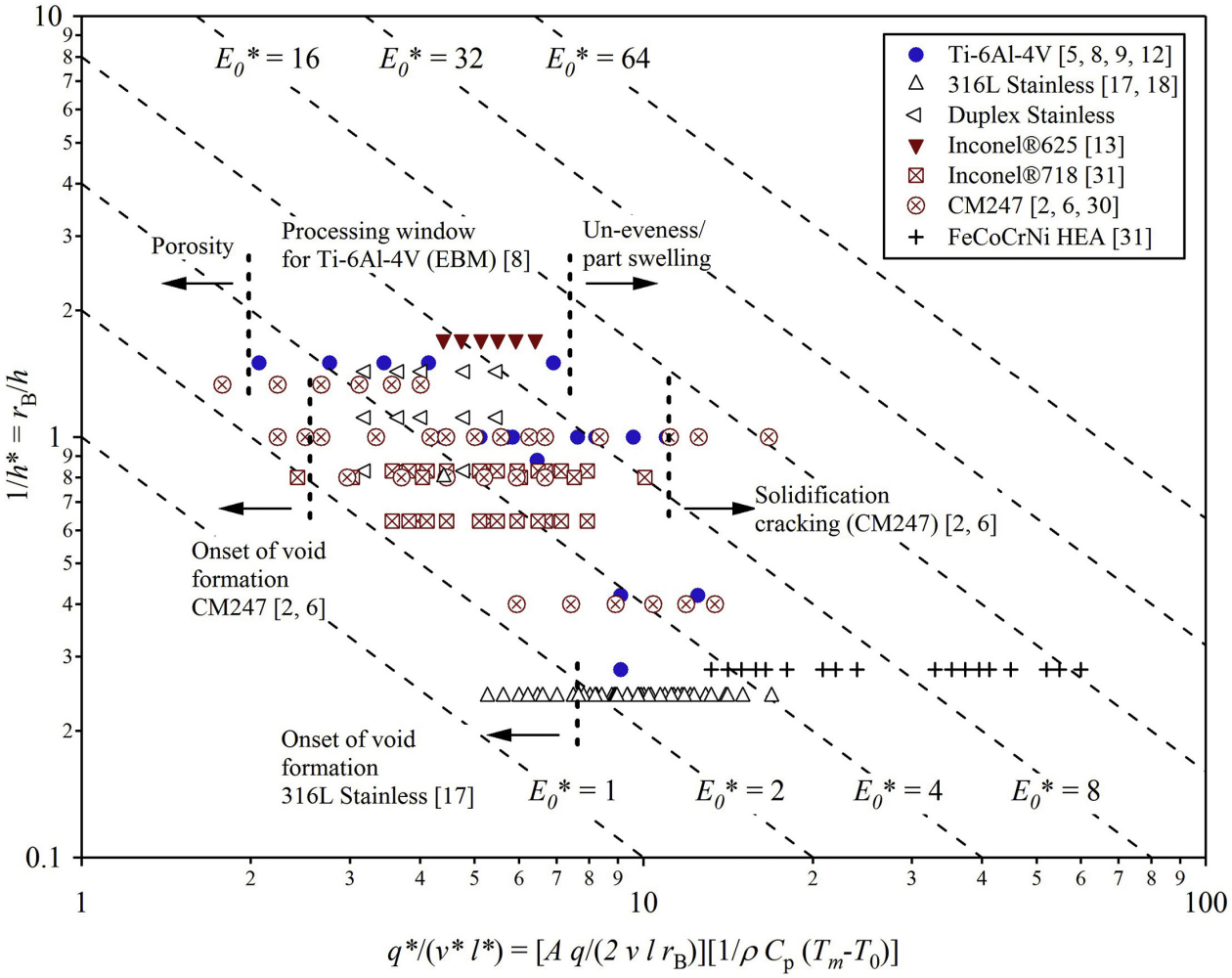

Figure 2.7: *Normalised processing diagram for PBF-LB/M for a range of alloy systems. Contours of constant normalised equivalent energy density, E_0^*, are provided by the dashed lines [110].*

Further research in this area introduced considerations of the heat transfer in the material during the AM process such as work by Hann *et al.* and subsequently King *et al.* on normalised enthalpy, defined as [111, 112]:

$$\frac{\Delta H}{h_s} = \frac{AP}{h_s\sqrt{\pi\alpha v r_b^3}} \tag{2.2}$$

where ΔH is the specific enthalpy, h_s is the enthalpy at melting, A is absorptivity, P is laser power, α is the thermal diffusivity of the molten material and r_B is the radius of the Gaussian beam at the surface. This parameter was primarily used to predict melt pool size, but breaks

down after the transition from conduction-mode melting to keyhole-mode melting. Trapp *et al.* also used the same parameter, to try to assess and predict this transition, showing that there is a drastic increase in absorptivity once a keyhole has formed, explaining the break down in the use of normalised enthalpy for keyhole-mode melting [113].

There has been some effort to find parameters which can identify other types of defects in AM and the susceptibility of different alloys to these defects. Mukerjee *et al.* introduced a thermal strain parameter by using the Buckingham Pi theorem to combine dimensionless numbers relating to thermal distortion. Parameters are also introduced for vaporisation of elements, and lack of fusion porosity formation based on a ratio of melt pool depth to layer thickness [114]. The thermal strain parameter indicating thermal distortion is shown here:

$$\varepsilon* = \frac{\beta \Delta T}{EI} \frac{t}{F\sqrt{\rho}} H^{3/2} \tag{2.3}$$

where $\varepsilon*$ is the thermal strain parameter, β is the volumetric thermal contraction coefficient, EI is the flexural rigidity of the substrate plate (where E is Young's modulus and I is the second moment of inertia), t is the deposition time, F is the Fourier number, ρ is the density and H is the heat input per unit length ($H = \frac{AP}{v}$). Mukherjee *et al.* determined that some alloys are more susceptible to certain types of defect than others e.g. Ti-6Al-4V is more susceptible to thermal distortion compared to Inconel 625 and 316 stainless steel. A similar parameter, which preceded the thermal strain parameter is named the stress performance indicator (SPI) by Deffley *et al.* [115]:

$$\sigma_{PI} = \frac{E\alpha_{CTE}}{2k(1-\upsilon)} \tag{2.4}$$

where E is elastic modulus, α_{CTE} is linear thermal expansion coefficient, k is thermal conductivity and υ is Poisson's ratio. Attempting to assess the effect that the heating and cooling cycles will have on stress accumulation in AM, however heat input is not modelled, which is also a large contributor and source of process variation. More recently, effort has been made to simulate melt pool formation through the use of techniques such finite element modelling (FEM) or computational fluid dynamics (CFD) [116–121]. However, these modelling techniques and many of those outlined above require significant prior knowledge of material, powder and absorption properties, many of which simply are not available in the case of novel alloy development.

2.2.4 Assessing Printability

A large proportion of current work is attempting to assess printability of already established alloys, where printability is defined by Wei as "the ability of an alloy feedstock, to be converted to a

component with acceptable metallurgical, mechanical and functional requirements for a specific application" [117]. Many printability issues can be resolved by adjusting process parameters. However cracking can occur by many different mechanisms and for alloys that are prone to this, there is a very small (or even non-existent) processing window where dense, un-cracked parts can be manufactured. The cracking indicators used for AM commonly come from welding literature, or even from casting, despite the large differences between cooling rates and other the conditions experienced by the material in these processes [103]. Additional information about cracking and its prediction in AM is also included in Chapter 5.

2.2.4.1 Solidification Cracking

As stated previously, solidification cracking susceptibility can depend on solidification temperature range, the cooling rate and the final inter-facial liquid morphology and composition. The simplest assessment of solidification cracking is made by examining the size of the freezing range, however this does not provide specific information on the behaviour at the end of solidification, which is thought to be the most important stage in the formation of solidification cracks [103]. Consequently, there are 2 types of predictive models: metallurgical models using solidification ranges, curves and phase diagrams and thermo-mechanical models assessing the strain associated with the shrinkage [122, 123].

Examples of metallurgical models include the crack susceptibility coefficient (CSC) from Clyne and Davies and the Kou cracking indicator which focuses on the final stages of solidification [124, 125]. Clyne and Davies defined the CSC as the ratio of time in the vulnerable temperature range where cracks can propagate to the time available for stress relaxation. This is a simple model based on many assumptions, including that the vulnerable time is between solid fraction 0.9 to 0.99 and the relaxation time is between solid fraction 0.4 to 0.9, where 0.4 was later determined to be consequential as the dendrite coherency point for many materials [126, 127]. Kou *et al.* used a parameter to assess a materials susceptibility to solidification cracking, which was named the solidification cracking indicator [104, 124]:

$$SCI = \left| \frac{dT}{d(f_s^{1/2})} \right| \tag{2.5}$$

where f_s is the solid fraction and T is the temperature describing a Scheil solidification curve. Based on analysis of Al alloys, this value was first somewhat arbitrarily calculated for the range $0.87 < f_s < 0.94$; however other work has used different ranges which better fit the alloys concerned in each case [105, 124]. The Scheil solidification model assumes there is no diffusion in the solid phases, hence for alloys where there is a high solubility of the solute in the solid phase, such as Mg in Al, the SCI does not predict accurate cracking behaviour. This error could however

be resolved through the use of a solidification model which allows solid-state diffusion.

The model proposed by Rappaz, Drezet, and Gremaud is an example of a thermo-mechanical indicator, where the critical strain rate is calculated [128]. It considers liquid feeding in the mushy zone and tension transverse to the welding direction, hence predicting crack formation if liquid feeding is insufficient to account for the deformation caused by a tensile strain perpendicular to the dendrite growth direction. However, GBs where cracks are thought to occur, are not considered as the mushy zone is considered as one semi-solid structure [124].

2.2.4.2 Liquation Cracking

Liquation cracking is often predicted based on composition and prior knowledge of low melting point phases which could form, such as eutectics. In welding or AM of nickel alloys, liquation cracking is predicted based on formation of GB phases such as low melting point carbides or the $\gamma - \gamma'$ eutectic [129, 130]. Low melting point carbide formation can be predicted based on the weight fraction of Cr and Co in the nickel alloy [122]. More broadly tendency to liquate increases with increasing grain-boundary segregation or with grain size, as well as in alloys with a larger freezing range and liquid fraction during cooling, similar to solidification cracking [104]. Cracking also increases with higher heat input, so it follows that the AM process can be somewhat optimised to reduce liquation cracking. But in depth knowledge of phase formation and morphology is essential in predicting susceptibility to liquation cracking, hence it is difficult to predict in alloys with unknown phase diagrams or microstructures.

2.2.4.3 Solid-State Cracking

Solid-state cracking in all forms can be predicted based on the solidification range and the induced strain, but it often is predicted based on the formation of brittle phases, in particular those on GBs, where cracks are most likely to initiate [130]. In nickel alloys, for example, strain age cracking (SAC) is often predicted based on γ' or carbide content [131].

Theories for the onset of ductility dip cracking (DDC) include the impact of GB embrittlement caused by impurities such as S and P. Nishimoto *et al.*, studied welds in Inconel 690, with varying S and P content, confirming that segregation to the GBs, caused by S and P, resulted in an increase in DDC [132]. There are, however, conflicting reports in the literature about the influence of carbides on nickel-alloy DDC susceptibility. Ramierez *et al.* report that the formation of medium size (1 µm) carbides can increase the resistance to DDC in nickel alloys, by increasing GB pinning and tortuosity. Grain boundary triple points are thought to be likely initiation points, however if strain accumulation can be limited by pinning from precipitates then void formation can be reduced [133, 134]. On the other hand, Ahn *et al.* report an increase in DDC as GB precipitation

of Nb-rich carbides increases in Inconel 690 [135]. However, the grain morphology in that case seems much closer to equiaxed, and the carbides much more numerous than that reported by Ramirez *et al.*. High angle GBs themselves are also more generally prime locations for initiation of DDC due to the increased strain which results from the lack of coherence [136].

Similar work on welding of austenitic stainless steels shows DDC formation in the columnar zone, where there are straight GBs, so cracks can propagate unimpeded [137]. Yu *et al.* found that DDC resistance can be increased by precipitation along the GB, either by γ austenite precipitating on the boundaries of δ ferrite grains or vice versa, depending on the alloy concerned. An illustration of this is shown in Figure 2.8.

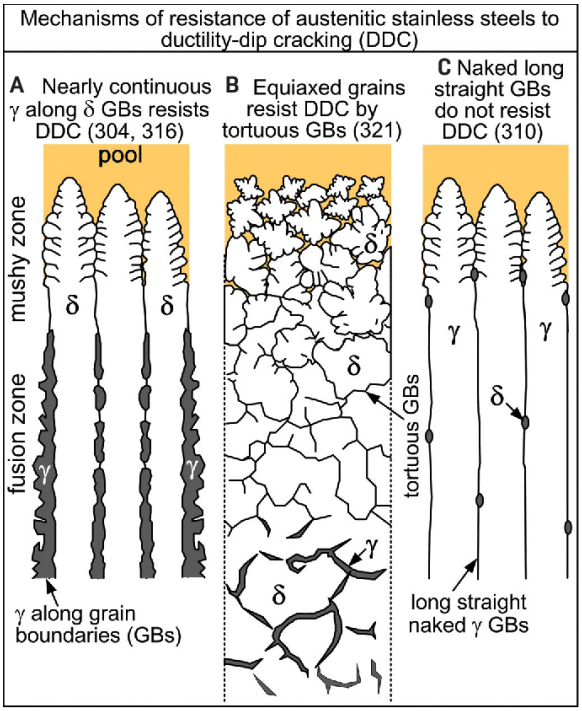

Figure 2.8: *Mechanisms of DDC resistance of austenitic stainless steels: (A) Almost continuous γ along the boundaries between columnar δ dendrites resists DDC; (B) tortuous GBs between equiaxed δ-ferrite grains resist DDC; (C) straight boundaries between columnar γ dendrites are unable to resist DDC [137].*

Overall, similar to liquation cracking, SAC and DDC are massively dependent on phase formation, grain and precipitate morphology and GB segregation. It appears that GB carbide formation can either promote DDC if the grains are equiaxed or pin GB sliding and inhibit crack initiation in columnar grains. But more conclusively the formation of deleterious phases due to high levels of contaminants segregating to GBs seems to increase DDC susceptibility. For PBF-LB/M of new alloys in new compositional spaces, where solid-state cracking is a concern, there are few tools to use aside from CALPHAD through which to predict crack susceptibility. Even CALPHAD methods (when accurate) only predict the presence of the phase, not morphology or location,

therefore it is impossible to confidently predict whether its presence could result in a positive or negative effect on DDC formation.

2.2.5 Alloy Design for AM

Many of the predictive methods described previously have been used to design alloys for AM specifically. Where alloy behaviour is known, this often involves adjustments to a known alloy composition, or even adjustments to the feedstock or process itself. Work by Pollock *et al.* is a good demonstrator of the composition adjustment approach, where two new nickel-alloy compositions were designed using CALPHAD, and then successfully manufactured using PBF-EB/M, despite being a high γ' nickel alloys [138]. A suite of predictive tools such as CALPHAD and DFT were also used to find a Co-Ni alloy which was produced by AM with limited testing required [139]. Other nickel-alloys have been designed via ML and use of neural networks, by altering the composition of the very printable Inconel 718 alloy [140]. There are also many examples of modifications of alloy composition to reduce crack susceptibility or to refine the microstructure, including the addition of oxide powders to HEAs or carbide powders to titanium alloys via ISA [138, 141–144], a practice detailed in Section 2.2.6 and in Chapters 3 and 6.

As there is large interest in AM of nickel-alloys, there are some notable examples of new alloys which have been designed with manufacture by AM in mind. Tang *et al.* designed ABD-900AM, a medium γ' fraction alloy and compared its printability with that of CM247LC and Inconel 939 [105]. The freezing range and the Kou solidification cracking indicator were used, along with using γ' content as an indicator of SAC susceptibility, producing ABD-900AM, which avoids cracking while maintaining creep resistance. Conduit *et al.* used neural networks based on material parameters such as creep and oxidation resistance, as well as processability for DED-LB/M [145]. CALPHAD was also used to predict γ' content, the γ' solvus and general phase stability. The resulting alloy, named 'AlloyDLD', showed properties matching the neural network predictions and is reported to be have better high temperature mechanical properties than similar commercially available alloys. There is also an example of a Ti-alloy designed to have a refined microstructure and not the extensive columnar grains usually seen in AM [146]. Zhang *et al.* added 8.5 wt% Cu to Ti to create a binary alloy, where Cu was added to refine β grains as well as to initiate a eutectoid reaction and eutectoid microstructure [147].

There has also been a recent notable example of using many of the previously described parameters, to assess and screen a RHEA for use in AM. Mullin *et al.* used the Clyne and Davies CSC, the Kou SCI to predict solidification cracking and proposed the Deffley SPI to predict solid-state cracking, in the C103 Nb-based AM processable alloy and the $Hf_{10}Mo_xNb_{35}Ta_{30-x}Ti_{25}$ RHEA [115, 124, 125, 148]. Using substrates manufactured from the alloy concerned, coated in a layer of the same powder (elemental powder blend for the RHEA), the AM processability of

both alloys was assessed using melt tracks. Solid-state cracking was seen in all of the RHEA compositions, except the alloy with no Mo, which showed less cracking than the C103 alloy. The SPI indicated the cracking behaviour of the C103 alloy correctly, however was incorrect for the RHEA, most likely because the material properties were calculated by rule of mixtures, which has a large error associated, especially for thermal properties. However there was more success predicting solid-state cracking with the $D = \gamma_{surf}/\gamma_{usf}$ parameter proposed by Gu *et al.* for HEAs, where γ_{surf} is surface energy of a slip plane and γ_{usf} is unstable stacking fault energy [149]. Lack of solidification cracking in the RHEA and presence of it in the C103 alloy was predicted correctly by both SCI and the CSC, showing that these parameters can be successfully used with refractory alloys.

2.2.6 In-situ alloying

ISA is a term coined to describe the simultaneous manufacture of functional parts from alloys which are produced as a result of mixed powder feedstocks [150]. For PBF-LB/M, this involves mixing powders prior to loading the powder reservoir, powders are then deposited, and the alloying process occurs due to the powders melting or dissolving in the melt pool, aided by the fluid flow. For DED processes, multiple hoppers containing different powders are often used and the powder mixing itself happens just prior to entry or on entry to the melt pool. Processing a material via ISA adds even more complexity to the AM process as imperfect process optimisation can result in un-melted elements, preferential elemental vaporisation or incomplete alloying, as well as common AM defects such as lack of fusion, keyholes, gas porosity and cracking. This strategy is useful for rapid alloy design and evaluation of new alloys, hence is particularly useful in development of new alloy systems such as HEAs [151–154].

2.2.6.1 Microstructural refinement

A frequent application of ISA is for microstructural refinement and deliberate phase distribution. The as-built microstructure of parts manufactured by PBF-LB/M often consists largely of columnar grains formed by epitaxial growth of dendrites from prior deposited layers, orientated in the build direction [146]. This creates anisotropic material properties and therefore equiaxed grain growth is often preferable. The columnar to equiaxed transition can be achieved by modification of AM parameters to change the temperature gradient, cooling rate and velocity of the solid/liquid interface. An effective way of promoting equiaxed grain growth is by providing nucleation sites for solidification ahead of the solid/liquid interface. These are often powder particles of higher melting point material to provide heterogeneous nucleation sites [146, 155, 156]. Using a similar methodology, ISA can also result in achieving the dispersion of particular secondary phases once

melted. An example of this is demonstrated by Smith *et al.* who used resonant acoustic mixing to coat CoCrNi powder with yttrium oxides, resulting in the dispersion of fine nano-scale oxides throughout a component [157].

The use of ISA for grain refinement in AM has been extensively studied for Ti-alloys in particular. The powder added for this purpose often has a substantially smaller particle size than the base powder, initiating more potential heterogeneous nuclei [156]. Bermingham *et al.* added La_2O_3 particles to a Ti-3Al-8V-6Cr-4Mo-4Zr alloy used for wire-arc DED [146]. The final structure contained 85% equiaxed grains, however the columnar microstructure could not be fully removed and nucleant particles agglomerated, reducing their effectiveness. Zhang *et al.* also showed that adding small amounts of boron to Ti-6Al-4V reduced grain size and increased α lath refinement, with similar results also shown with C and Si additions [142, 143, 158]. Simonelli *et al.* achieved substantial grain refinement in Ti-6Al-4V through addition of 2 - 4 wt% Fe with a D_{50} of 5.7 µm compared to a D_{50} of 33.5 µm in the base powder, and similar refinement was also achieved with Nb powder additions [159, 160]. Micrographs produced by Simonelli *et al.* showing grain refinement with increasing Fe content are shown in Figure 2.9. Similar approaches have been taken with Si in Al-Si alloys to reduce thermal expansion and cracking as well as refining microstructure [161].

2.2.6.2 Alloy modifications

ISA also can be used as an alloy design and optimisation tool to test particular compositions prior to manufacture of expensive pre-alloyed powders. This is why it is used so extensively in the AM of HEAs, as most new HEA compositions have to be manufactured in small bespoke batches, meaning testing many compositions soon becomes too costly in both time and money. On the other hand, elemental powders can often be bought off the shelf and blended, so ISA can offer an insight into the microstructures which will form under AM processing conditions. ISA, both of CoCrFeNi-based HEAs and of RHEAs are covered in Section 2.3 and Chapters 3 and 6, hence this section will mainly concern ISA of other alloy systems.

ISA has been used previously for compositional optimisation of Al-Cu alloys, where it was found Cu particles did not diffuse well, leaving areas of partially alloyed Cu [162]. However, the nano-scale lamellar eutectic microstructure of the Al33Cu alloy produced had a compressive strength of about 1000 MPa. ISA has also been used to add refractory β stabilisers such as Nb, Ta and Mo to β-Ti powder, to stabilise the β-phase to obtain materials with low elastic modulus (to match that of bone) but high strength for biomedical applications [150]. To this end, Wang *et al.* studied the ISA of Ti-xNb alloys where x = 0, 15, 25, 45 at%, finding unmelted Nb in all samples except the cp-Ti, but achieving the desired low modulus in the Ti-25Nb alloy [163]. Huang *et al.* did a similar study, this time for Ti-Ta binary alloys, finding a low modulus (71

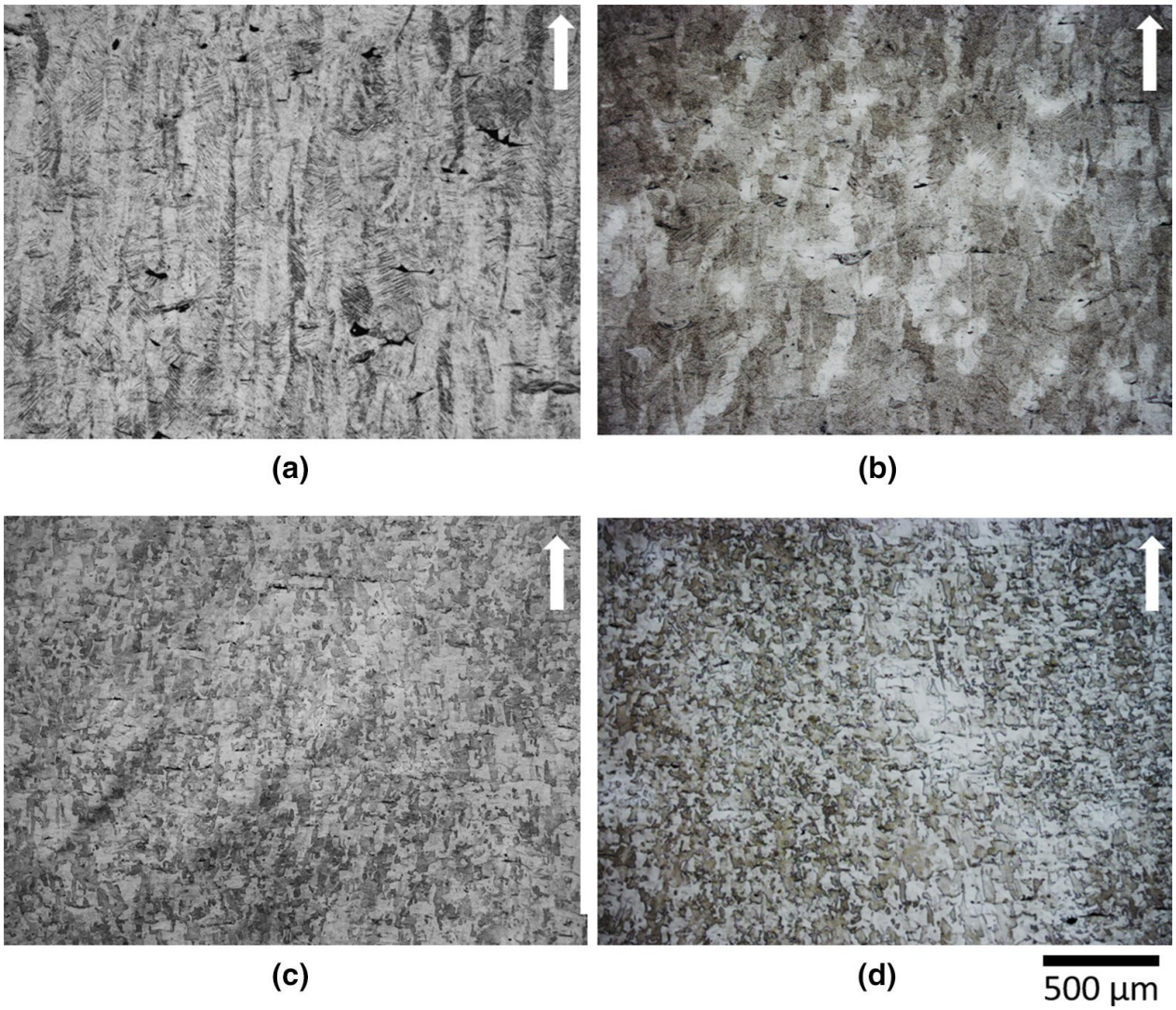

Figure 2.9: *Optical micrographs of the as-built microstructures of the (a) Ti-6Al-4V, (b) Ti-6Al-4V-2Fe, (c) Ti-6Al-4V-3Fe, and (d) Ti-6Al-4V-4Fe samples. The arrows indicate the building direction [159].*

GPa) for the Ti-30Ta alloy [164]. The VED was kept constant for all samples, hence the samples with high Ta compositions contained more unmelted Ta particles, meaning the prior β-grains were largely equiaxed due to the Ta particles acting as inoculants. The Ti-xRe (x = 0, 0.5, 1.0, 1.5 at%) binary system has been studied by Chlebus *et al.*, offering even more of a challenge as Re has a melting point almost double that of Ti, 3185°C and 1668°C respectively [165]. The addition of 1.5 at% Re more than doubled the yield strength, reduced the elastic modulus but sacrificed the ductility. An effect which was likely due to un-melted Re particles providing discontinuities for crack initiation, despite attempting to increase VED to mitigate this. The fracture surface, showing the detrimental impact of un-melted Re particles on ductility, is shown in Figure 2.10.

ISA has also been suggested as a cost-effective method by which to produce Ni-Ti based

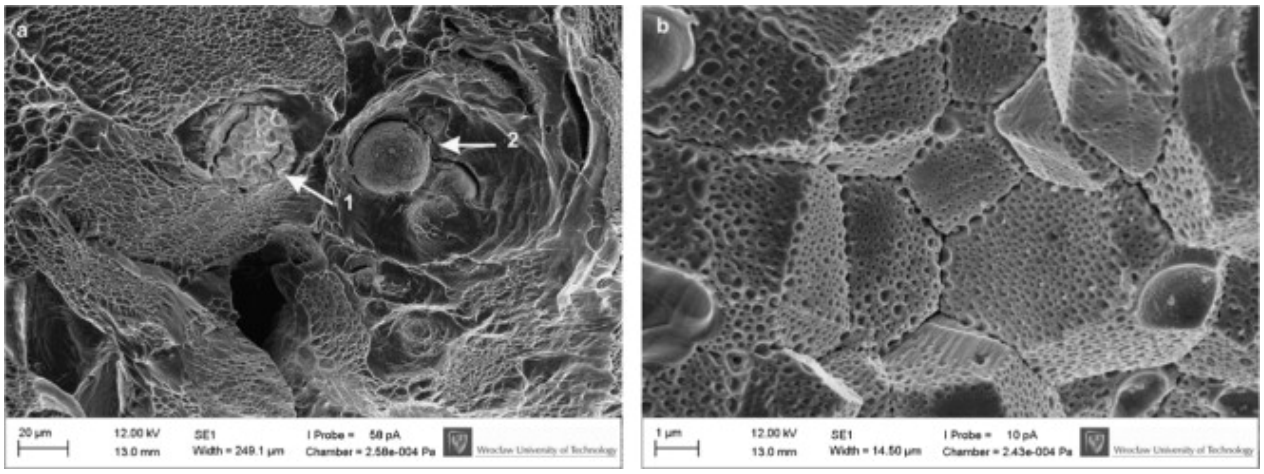

Figure 2.10: *(a) SEM image showing cracked (arrow 1) and non-cracked (arrow 2) Re particles inside large dimples and (b) higher-magnification image of brittle fracture surface with the Re particle indicated by arrow 2 [165].*

shape memory alloys. Wang *et al.* studied this via different AM techniques and showed that if solidified rapidly, NiTi would form alongside many brittle and metastable phases [166]. There were some problems from the ISA process itself, including excessive vaporisation of Ni when manufactured by DED-LB/M and creation of an unstable melt pool in PBF-LB/M due to the exothermic reaction of the mixing of the Ni and Ti powders, causing keyholes. Zhang *et al.* found that Ni-Ti can be manufactured to be at least 99.5% dense, if speeds are slow enough to not produce metastable Ni_2Ti and if a further homogenisation heat-treatment is used to precipitate the NiTi phase responsible for the shape memory effect [167].

Fe-alloys and steels are less extensively researched in the ISA field, however there are a few examples where it has been used. Pollock *et al.* looked into how to successfully process 431 steel powder by adding 20% TiC and obtained a desired refined microstructure, via the TiC acting as a nucleant to control solidification and solid-state transformations [138]. A FeNiSi soft magnetic alloy was also manufactured by PBF-LB/M by coating silicon steel powder with Ni. The composition was homogeneous and porosity could be nearly eliminated, but cracks occurred due to the brittleness of the material [168].

2.3 AM of HEAs

AM of HEAs is an area of increasing interest for a few main reasons. Conventional manufacturing methods such as casting or more commonly arc-melting require materials to be remelted numerous times to reduce in-homogeneity. This problem is exacerbated in HEAs due to the number of component elements. On top of this, some HEAs require fast cooling rates in order to suppress

the precipitation of undesired phases [169]. Lastly, after producing a billet, the machining of many HEAs, especially RHEAs is difficult without employing machining techniques like wire electrical discharge machining (Wire-EDM), which severely limits the complexity and dimensional freedom of parts [170]. AM offers the chance to solve all these problems at once, enabling manufacture of complex geometries along with high heating and cooling rates, which can suppress intermetallic phase formation due to hindering diffusion and trapping of solutes [171]. Because of this interest there are now many review papers covering AM of HEAs specifically [8, 151, 152, 154, 172–174]. AM of HEAs, especially RHEAs, is discussed throughout this thesis, so this section includes an overview of the field, mainly focusing on PBF-LB/M, but including other processes where applicable. More specific insight relevant to the work in this thesis is discussed in the relevant chapters.

2.3.1 CoCrFeNi-based HEAs

The first known attempt at AM of a HEA concerns laser cladding of CoCrCuFeNi via ISA of elemental powders [4]. As previously stated, ISA is particularly utilised in the manufacture of HEAs by AM, due to the cost associated with manufacture of suitable bespoke powder feedstocks. Zhang *et al.* added Si, Mo and Mn to the CoCrCuFeNi alloy creating a high quality coating, with a dendritic morphology once the additions had been added. Following this work, Yao *et al.* reported the first attempt at laser cladding of the CoCrFeMnNi alloy with pre-alloyed gas atomised powder, manufacturing samples with no pores or cracks and a hardness of 360 HV, which was largely retained at high temperatures [175]. To the author's knowledge, the first work to report PBF-LB/M of a HEA was that of Brif *et al.*, concerning the CoCrFeNi alloy [6]. The samples, manufactured from pre-alloyed powder, reportedly had a yield strength of 600 MPa with an elongation of 32%, compared to 188 MPa and 50% when manufactured by vacuum arc-melting. Li *et al.* were the first to manufacture the CoCrFeMnNi alloy via PBF-LB/M of pre-alloyed powder [176]. They found that as well as an FCC phase, a tetragonal σ phase formed and this, along with the AM process conditions, refined the microstructure, resulting in improved mechanical properties compared with arc-melted specimens [176]. These high strengths resulting from the microstructure induced by the AM process have been verified by other publications [177–180]. However Zhang *et al.* recently found that the CoCrFeMnNi alloy can be susceptible to solid-state cracking due to high thermal stresses if the change in scanning angle between two layers is too large [181]. As cracks tended to propagate on high angle GBs, cracking was mitigated by reducing the change in scanning angle between layers. Chen *et al.* were successful in improving the microhardness of the same alloy made by PBF-LB/M but using CoCrFeNi pre-alloyed powder with the addition of Mn elemental powder [182].

The Al_xCoCrFeNi group of alloys have also been used with PBF-LB/M, with difficulties found

in getting the expected elemental compositions and producing a two phase FCC/BCC grain structure as the proportion of Al is increased, as shown in Figure 2.11 [183, 184]. The AlCrFeNiTa alloy was also tested with hopes the Ta addition would provide high temperature stability, however the resulting component contained a large proportion of non-molten Ta particles [183]. Wu *et al.* showed similar results with C-reinforced CoCrFeNi [185]. Fujieda *et al.* have had success manufacturing the $Co_{1.5}CrFeNi_{1.5}Ti_{0.5}Mo_{0.1}$ HEA via PBF-LB/M and saw high tensile strength and pitting corrosion resistance in excess of that seen in nickel alloys used for corrosive environments [186, 187]. There also have been investigations into PBF-EB/M of HEAs including the AlCoCrFeNi system, resulting in improved ductility compared to the cast alloy [188].

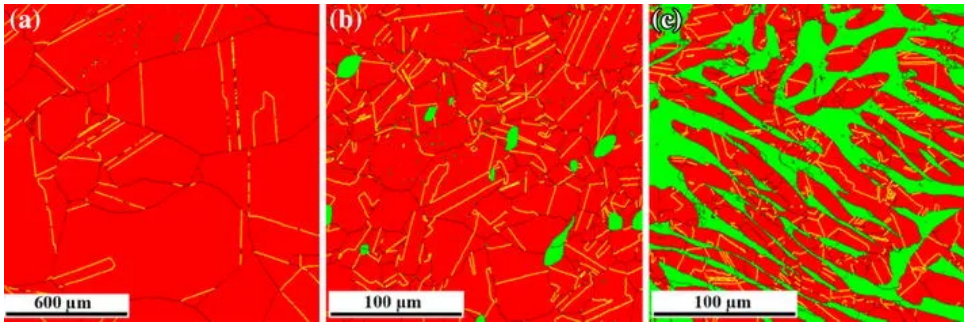

Figure 2.11: *EBSD phase map of (a) $CoCrFeNiAl_{0.4}$, (b) $CoCrFeNiAl_{0.7}$, and (c) $CoCrFeNiAl_{1.0}$ arc-melted samples showing FCC (red) and BCC (green) phases. Grain boundaries (>5°, black lines) and twin boundaries (yellow lines) in FCC phase are also shown [183]*

Perhaps the most notable recent development in the AM of CoCrFeNi-based HEAs, is the manufacture of the $AlCoCrFeNi_{2.1}$ alloy by Ren *et al.* [189]. PBF-LB/M was utilised to manufacture a non-equilibrium microstructure consisting of dual-phase BCC/FCC eutectic colonies, with lamellae on the scale of tens of nanometres compared to the 1 - 5 µm lamellar spacing reported in cast eutectic HEAs. There was also no $L1_2$ or B2 present in the AM samples, phases which were present in cast samples. The eutectic colonies formed in alignment with the maximum thermal gradient and as the melt pool shape was largely semicircular, these orientations are random, resulting in samples with isotropic material properties, an uncommon feat in AM. Due to these factors, the resulting mechanical properties for AM samples, shown in Figure 2.12, are much higher strength than the cast samples, with higher ductility. They also surpass the strength-ductility combinations of many conventional AM alloy systems [189].

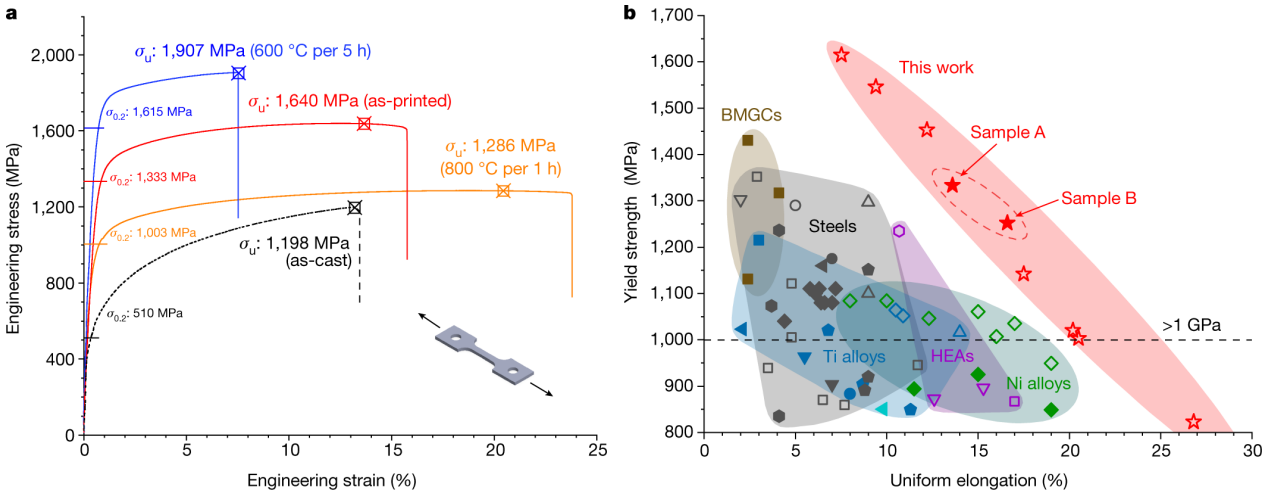

Figure 2.12: *(a) Tensile engineering stress–strain curves of the as-built and annealed AlCoCrFeNi$_{2.1}$. The yield strength ($\sigma_{0.2}$) and ultimate tensile strength (σ_u) are indicated. (b) Tensile yield strength versus uniform elongation of AM AlCoCrFeNi$_{2.1}$ compared with conventional alloys manufactured by AM in the literature, including other HEAs. The solid and hollow symbols represent the properties of as-printed and post-annealed samples, respectively [189].*

2.3.2 RHEAs

2.3.2.1 DED-LB/M

Research into AM of RHEAs has been gaining popularity due to their high temperature mechanical properties, which are in many cases superior to those of conventional alloys [63]. The first attempt at DED-LB/M of a RHEA was made by Dobbelstein *et al.* on the equiatomic MoNbTaW alloy via ISA. Samples cracked during processing and the stoichiometry deviated from equiatomic, however effective compositional grading was suggested to be possible with better controlled powder flows and process parameters [5]. After this work was published a small number of studies were completed on laser cladding of RHEAs, many showing high hardness even at high temperatures [190–192].

In more recent years, the reporting of ISA via DED-LB/M of RHEAs has accelerated in the literature [5, 153, 193–199]. Notable studies include that by Zhang *et al.*, who achieved a fully alloyed microstructure in the $Ti_{42}Hf_{21}Nb_{21}V_{16}$ RHEA with a tensile yield strength of approximately 1000 MPa and a elongation of 22% [199]. Guo *et al.* showed similar results with a TiZrHfNb equiatomic RHEA [200]. Zhang *et al.* also completed DED-LB/M using pre-alloyed powder of the $Al_{0.3}NbTi_3VZr_{1.5}$ [201]. A BCC matrix phase formed, along with ω precipitation and a metastable GB Laves phase which disappeared after solution treatment. The as-built samples showed brittle fracture, while after solution treatment the samples had a yield strength of 1032 MPa and elongation of 25%, attributed to solid-solution strengthening and the effect of the ω

nano-precipitates.

ISA by DED-LB/M of RHEAs is much more convenient than PBF-LB/M as elemental powders in the particle size range suitable for DED-LB/M are cheaper and easier to manufacture than for PBF-LB/M [202]. DED can be more tolerant of non-spherical powder particles as the process is slower, the melt pool is much larger in order to encapsulate the particles and compositional adjustments can easily be made to achieve nominal composition. In PBF-LB/M so-called spreadability of the powder (the ability to form the successive layers of unmelted powder with good repeatability and homogeneity) affects the deposition of the powder. Depending on the processing parameters, the heating and cooling rates can be too rapid to allow full diffusion and alloying of all elements, especially if there is a large discrepancy in melting points. If attempted, manufacture of pre-alloyed powders for PBF-LB/M rather than DED-LB/M is also more costly in terms of material. This is as a smaller size fraction of powder when produced, by atomisation, for example, is within the typical size range acceptable for PBF-LB/M (15 - 45 μm), than the typical particle size range required for DED-LB/M (45 - 105 μm) [202].

2.3.2.2 ISA via PBF-LB/M

PBF-LB/M of a RHEA was first attempted by Zhang *et al.* who published several papers on PBF-LB/M of the WTaMoNb alloy system via ISA. It was found it was possible to create a component with no warping with excellent microhardness and corrosion resistance compared to traditional superalloys [7, 203]. Zhu *et al.* used PBF-LB/M to manufacture the $V_{0.5}Nb_{0.5}ZrTi$ RHEA, achieving a yield strength of 1450 MPa [204]. However there were problems with un-melted elements and cracking in many samples, shown in Figure 2.13, attributed to the high thermal gradient and discrepancies in elemental thermal expansion. Wang *et al.* studied the effect of varying Mo composition for a $NbTa_{0.5}TiMo_x$ RHEA, showing the presence of un-melted Ta particles in all samples, with cracking present in many samples [205]. It was found that the samples have a refined equiaxed microstructure and that increasing Mo increases the hardness and compressive strength of the alloy, but reduces the ductility. Lastly, Cai *et al.* built $MoNbTaW(TiNi)_x$ ($x = 10$, 15, 20, 25 at%), using spherical powders, where all alloys showed no cracks or macrosegregation [206]. The compressive yield strength of the alloy where $x = 20$ at% was an impressive 2513 MPa with an elongation of 11%; reportedly this was the highest compressive strength of any HEA studied previously. The resulting stress-strain curves and hardness values are shown in Figure 2.14. The high strength is attributed to the coherent GB between the BCC matrix phase and a B2 phase, as well as the fine equiaxed grains formed by the ISA process.

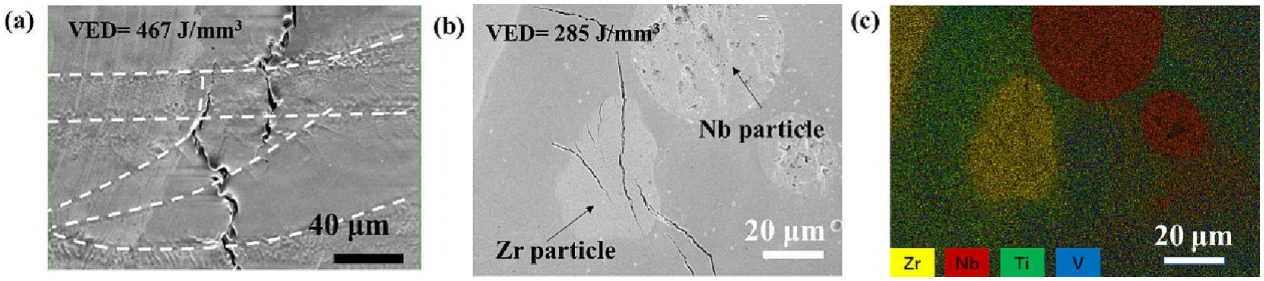

Figure 2.13: *(a) SEM image of the high VED $V_{0.5}Nb_{0.5}ZrTi$ sample, showing cracking; (b) BSE image of the lower VED $V_{0.5}Nb_{0.5}ZrTi$ sample showing un-alloyed Zr and Nb; (c) EDS elemental mapping image of the lower VED $V_{0.5}Nb_{0.5}ZrTi$ sample [204].*

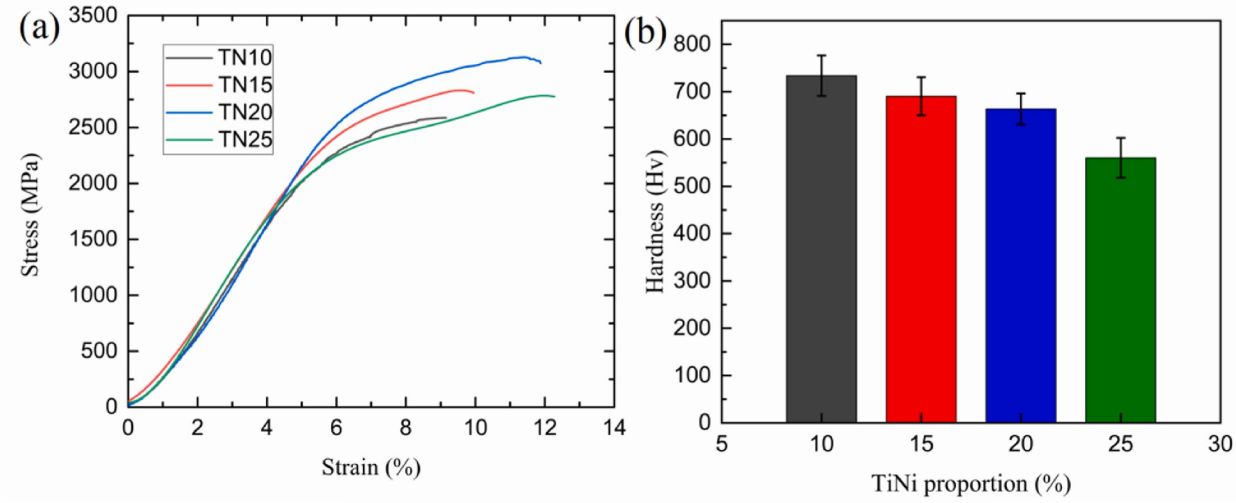

Figure 2.14: *Mechanical properties of $MoNbTaW(TiNi)_x$ (x = 10, 15 20, 25 at%) RHEAs where TN10, TN15, TN20 and TN25 denotes the increments of x: (a) Compressive properties at room temperature; (b) Vickers hardness at room temperature [206].*

2.3.2.3 PBF-LB/M with pre-alloyed powders

Due to the reasons described previously, few publications have manufactured RHEAs via PBF-LB/M with pre-alloyed powders, with only a few using optimised spherical powders [207–209]. Liu *et al.* used non-spherical fluidised powder to manufacture the equiatomic MoTaTiW RHEA with high relative density [207]. The Ti forms an interdendritic HCP phase with the other elements primarily in the dendritic BCC phase. This separation is attributed to the difference in melting points and atomic size mismatch, but crucial contaminants such as N or C were not reported so it is difficult to identify this phase confidently. Gu *et al.* manufactured the similar MoNbTaVW RHEA using spherical pre-alloyed powder [208]. Cracks were found on the top surface of all samples, and the resulting densest sample had a hardness of 664 HV, 1.3 times higher than the same alloy produced by arc-melting. Gokceka *et al.* manufactured a $Ti_{28.33}Zr_{28.33}Hf_{28.33}Nb_{6.74}Ta_{6.74}Mo_{1.55}$ 'Bio' RHEA, using near spherical powder [209]. They showed that the suppression of segregation resulted in a low modulus, good strength and ductility and good cyto-compatibility, all essential properties for effective bio-materials.

2.4 Summary

This section has reported the relevant literature surrounding high entropy alloys (HEAs), additive manufacturing (AM) and more specifically AM of HEAs themselves. HEAs were proposed in 2004, but since then many compositions have been proposed which show promise for many applications, including aerospace [15]. Refractory HEAs (RHEAs) in particular show high strength, often combined with good ductility, which is retained at high temperatures [63]. Much HEA literature has reported on the development of single phase HEAs, however the focus is now shifting to the development of multi-phase HEAs which better mimic the microstructures seen in high performance superalloys [51]. However there is still much more to be discovered about the effect of secondary phase formation in RHEAs, especially when manufactured via AM processes.

For any alloy to be successfully processed by AM, there are many variables to consider about the process and the alloy properties. Many defects found in AM processed materials can be mitigated by refining the process parameters such as porosity, caused by lack of fusion or unstable keyholes, and extensive cracking [99]. However many alloys are inherently crack susceptible, and for these alloys it is often very difficult to find a optimum AM processing window, without fundamental changes to the alloy composition itself first. For solidification cracking there are predictive parameters which can be applied for any alloy, such as the Kou solidification cracking indicator [124]. But solid-state cracking and liquation cracking are currently only predicted on the basis of in-depth microstructural knowledge of a particular alloy system, including the size,

location and morphology of precipitates. Therefore, this approach is not accurately usable with new alloy systems and compositions such as HEAs.

Once a HEA is proposed, producing powders for AM can be very difficult, costly and time-consuming. Hence, many reports (including for other alloys, not just HEAs) employ in-situ alloying (ISA) to attempt building of representative samples to quickly test compositions. Often resulting in equiaxed microstructures, while dealing with problems such as un-melted particles and unexpected phase formation due to binary elemental interactions [150]. Success when using ISA is iterative and specific to the given alloy system, there is yet to be a study which reports on the success of in-situ alloying more generally and the important associated considerations. ISA has been used in directed energy deposition (DED) of RHEAs, however it is less utilised in powder bed fusion (PBF), partially due to the availability of high quality elemental powders in a suitable particle size range. Where PBF has been used there have been results reported with varying success, including a HEA with a impressive strength of over 2500 MPa [206]. PBF of RHEAs using pre-alloyed powders is even more rare, as bespoke RHEA powder is incredibly difficult to source, but some optimistic preliminary results have been reported [209]. Though all these studies have been completed on known RHEA systems which were not developed for AM specifically, perhaps an approach such as the one taken to develop new AM nickel alloys, would result in a RHEA more optimised for AM [105].

Chapter 3

In-Situ Alloying of CoCrFeNiX High Entropy Alloys by Selective Laser Melting

3.1 Journal details and author contributions

3.1.1 Journal

Metals
Volume 12
Issue 3
2022
ISSN 20754701
https://doi.org/10.3390/met12030456

3.1.2 Author Contributions

Lucy Farquhar - Conceptualisation, methodology, operation of Aconity mini for CoCrFeNi and CoCrFeNiTi, sample design and preparation, data analysis, sample XRD characterisation, writing of original draft.
George Maddison - Operation of the Aconity mini PBF-LB/M machine for manufacture of the CoCrFeNiCu
Liam Hardwick - Operation of the Microscope for SEM and EDS images
Frances Livera - Support with operation of the Aconity mini for manufacture of CoCrFeNi, writing - review and editing
Iain Todd - Conceptualisation, support with methodology, supervision
Russell Goodall - Conceptualisation, support with methodology, supervision, writing - review and

editing

3.2 Background

As introduced in Chapter 2, in-situ alloying (ISA) is extensively used in the manufacture of high entropy alloys (HEAs) by additive manufacturing (AM). ISA is commonly used as a preliminary assessment tool or as the only option by which to produce the alloy using an AM process, instead of purchasing expensive, bespoke powder. Optimisation of the ISA and AM process is usually done on an alloy-by-alloy basis, where a statistical parameter optimisation is used to find process parameters which result in dense parts, with a fully alloyed or near fully alloyed microstructure [154]. However for many alloys, even despite optimisation and attempts at producing homogeneous parts, there is no feasible way to manufacture these alloys by ISA to give representative microstructures. A good example of this, is in the work by Wang *et al.* in manufacturing Ti-xNb alloys, where for every variation of x, except $x = 0$, there were un-melted Nb particles found in the microstructure [163]. In the case of a vast difference in the melting points of elements within the alloy nominal composition, the common resolution is to increase the input VED, to increase the temperature and decrease cooling rates. However melting or dissolving high melting point elements can often mean vaporisation of low melting point elements, leading to deviation from the nominal composition. As well as the defects associated with high VED such as keyholes.

As well as a large discrepancy in melting point of elements, as is the case with Ti and Nb, there are other factors to consider when assessing whether an alloy is a suitable candidate for ISA, in particular with HEAs. Binary reactions between elements could form phases which would not occur if proper mixing between all elements had occurred. The rapid heating and cooling in AM also means that even if melting has occurred, sufficient mixing and diffusion often has not, resulting in local in-homogeneity. The resulting phases from this complex process could be brittle, hence enabling crack propagation, especially if there are also un-melted particles where cracks could initiate. In this chapter the amenability of two CoCrFeNi-based alloys to ISA is assessed, by using pre-alloyed equiatomic CoCrFeNi base powder mixed with either elemental Cu or Ti powder, to form the equiatomic CoCrCuFeNi and CoCrFeNiTi HEAs. The aim is to assess the effects of the different elemental additions and how they influence the homogeneity, defects and density of samples produced, while comparing these results to laser powder bed fusion (PBF-LB/M) of the CoCrFeNi powder itself.

N.B. To be consistent with the published paper, here terms such as selective laser melting (SLM), directed laser deposition (DLD) and scanning electron beam melting (SEBM) have been used to describe AM processes. Everywhere else in this thesis these processes will be referred to

as PBF-LB/M, DED-LB/M and PBF-EB/M respectively.

The full set of PBF-LB/M parameters used for each of the CoCrFeNi-based alloy samples are included in Appendix A.

Paper: In-Situ Alloying of CoCrFeNiX High Entropy Alloys by Selective Laser Melting

Lucy Farquhar[1], George Maddison[1], Liam Hardwick[1], Frances Livera[1], Iain Todd[1], Russell Goodall[1]

1 – Department of Materials Science and Engineering, University of Sheffield, Sheffield S1 3JD, UK

Correspondence: laufarquhar1@sheffield.ac.uk

Abstract

High Entropy Alloys are a class of alloys which have been shown to largely exhibit stable microstructures, as well as frequently good mechanical properties, particularly when manufactured by additive manufacturing. Due to the large number of potential compositions that their multi-component nature introduces, high throughput alloy development methods are desirable to speed up the investigation of novel alloys. Here, we explore once such method, in-situ alloying during additive manufacture, where a powder of a certain pre-alloyed composition is mixed with the required composition of powder of an additional element, such that alloying takes place when powders are melted during the process. To test the effectiveness and capability of the approach, selective laser melting has been used to manufacture pre-alloyed CoCrFeNi, and also CoCrFeNiCu and CoCrFeNiTi alloys by combining pre-alloyed CoCrFeNi powder with elemental powders of Cu and Ti. Processing parameter variations are used to find the highest relative density for each alloy, and samples were then characterised for microstructure and phase composition. The CoCrFeNi alloy shows a single phase face centred cubic (FCC) microstructure, as found with other processing methods. The CoCrFeNiCu alloy has a two phase FCC microstructure with clear partitioning of the Cu, while the CoCrFeNiTi alloy has an FCC matrix phase with NiTi intermetallics and a hexagonal close packed (HCP) phase, as well as un-melted Ti particles. The microstructures therefore differ from those observed in the same alloys manufactured by other methods, mainly due to the presence of areas with higher concentrations than usually encountered of Cu and Ti respectively. Successful in-situ alloying in this process seems to be improved by the added elemental powder having a lower melting point than the base alloy, as well as a low inherent tendency to segregate. While not producing directly comparable microstructures however, the approach does seem to offer advantages for the rapid screening of alloys for AM processability, identifying, for example, extensive solid-state cracking in the CoCrFeNiTi alloy.

Keywords

High Entropy Alloys; Additive Manufacturing; Selective Laser Melting; Laser Processing; In-Situ Alloying; Microstructure

3.3 Introduction

High Entropy Alloys (HEAs) are a novel group of alloys which have attracted attention in recent years due to their microstructural stability and mechanical properties. HEAs were originally defined as alloys with 5 - 13 elements with concentrations varying between 5 - 35 at%, however that definition has since been expanded to include an even broader range of alloys, including those with 4 elements [2, 6, 210, 211]. Since HEAs contain multiple elements with similar composition the expectation is that the microstructure will be complex with multiple phases; however in reality many have a stable single phase, in part due their high entropy. An example of this is the first reported HEA, discovered by Cantor *et al.*, which contained the elements CoCrFeNiMn in equiatomic proportions, and resulted in a stable single phase microstructure [1]. This alloy has provided a basis for much of the further research into HEAs of this type, including into processing by additive manufacturing (AM).

AM is a process where parts are built up layer by layer to often create complex geometries and internal features which cannot be achieved by other manufacturing methods. Often AM parts are also exposed to high cooling rates which can result in microstructural refinement as well as inhibit segregation. One of the most widespread AM methods is selective laser melting (SLM) and therefore this method was selected for use in this work. HEAs in general have been extensively researched for use in AM, as compiled in some recent review articles [152, 154]. However, early work on CoCrFeNi alloys specifically, for AM mainly focused on laser cladding, including where CoCrFeNiCu was shown to have excellent corrosion resistance [4, 175, 212]. This contrasts with other work on the corrosion of CoCrFeNiCu in a bulk as-cast form, which indicates that the corrosion resistance is lower than typical stainless steels [213]. There are also examples of this type of HEA also being produced by Direct Laser Deposition (DLD), where Xiang *et al.* noted that there was significant solute-trapping resulting in a more homogeneous microstructure compared to cast specimens of the CoCrFeNiMn alloy [180, 214, 215].

Previously, in-situ alloying has been used to manufacture HEAs with varying success and without comparison between elements. The CoCrFeMnNi alloy was manufactured via SLM by alloying the Mn in-situ, and this resulted in the vaporisation of some of the Mn, and a reduction of Mn in some areas [182]. Cagirici *et al.* also recently added Ti to the pre-alloyed CoCrFeMnNi and used Scanning Electron Beam Melting (SEBM) for in-situ alloying, resulting in a homogeneous distri-

bution of Ti, as well as the appearance of surface cracks and brittle phases as the Ti concentration was increased [216]. In-situ alloying of elemental powders alone has also been used to manufacture refractory HEAs with some vaporisation of the lower melting point elements [7, 153, 197, 203]. As well as also being utilised to manufacture refractory HEAs using sintering, resulting in parts with high but uneven density, due to differing spreading abilities of the elements [217].

This work focuses primarily on in-situ alloying of Cu and Ti elemental additions to pre-alloyed CoCrFeNi powder using the SLM process to produce equiatomic HEAs. The reason for completing this research is to try and assess the validity of mixing additional elemental powders to a base powder to manufacture a fully alloyed sample with a homogeneous microstructure. In this work, the term in-situ refers only to the melting and alloying of multiple powders together using the SLM process. It aims to discover what considerations are necessary and to ascertain whether this technique is valid to accelerate further alloy development, as it avoids the need to manufacture each individual alloy in quantity and in powder form for experimental AM trials. The SLM of the CoCrFeNi alloy itself without any additions has been researched previously and has shown a single phase face-centred cubic (FCC) microstructure [6, 218]. Multiple different investigations into CoCrFeMnNi have been completed, also showing a single phase FCC microstructure [176, 177, 179, 182, 219–222]. The CoCrFeNiAl system made via SLM has also a proved a popular alloy due to its tendency to form a dual phase FCC and body centred cubic (BCC) structure with a high hardness and corrosion resistance [183, 223–225]. Slight variations on this type of alloy with AlCrCuFeNi [226], AlCoCrCuFeNi [227] and AlCoCuFeNi [228] were also manufactured, all with a high crack susceptibility.

Cu and Ti were selected for this research as they show markedly different behaviour and microstructural consequences when alloyed with CoCrFeNi. They also have melting points above (1688 °C for Ti) and below (1084 °C for Cu) that of the CoCrFeNi alloy which is 1414 °C [6], therefore providing insight into the importance of relative melting temperature for in-situ alloying. Focussing on the alloys concerned in this study, CoCrFeNiTi-type alloys have been manufactured via SLM by Fujieda *et al.* where $Co_{1.5}CrFeNi_{1.5}Ti_{0.5}Mo_{0.1}$ shows an impressive tensile strength of 1178.0 MPa and elongation of 25.8% [186–188]. A $CoCrFeNiTi_{0.2}$ alloy has also been made by laser cladding which showed a eutectic lamellar microstructure of an FCC and a Laves phase [229]. Shun *et al.* also previously made CoCrFeNiTi-type alloys by arc-melting, showing the appearance of a plate like structure containing a R phase and a Laves phase as the concentration of Ti was increased [230]. The CoCrFeNiCu alloy has not been reported to have been manufactured by SLM, however it has been made by laser cladding with small additions of Mo, Mn and Si, and showed a single phase FCC microstructure [4]. When manufactured by other methods (primarily arc-melting), this alloy consistently has a dual phase FCC microstructure with Cu-lean grains surrounded by a Cu-enriched FCC phase on the grain boundaries [231–235].

3.4 Materials and Methods

Each SLM build used gas atomised, pre-alloyed, nominally equimolar CoCrFeNi powder, the measured composition of which, before the process, is shown in Table 3.1. Elemental powders of Cu and Ti were obtained for combination with this, and were added such that each element had a concentration of 20 at%. All specimens were manufactured using an AconityMINI SLM machine with a maximum laser power of 200 W and a spot size of 70 µm. For the CoCrFeNi samples, 5 mm $\times$ 5 mm $\times$ 10 mm specimens were produced. For the CoCrFeNiCu 7 mm diameter $\times$ 10 mm cylinders were made and for the CoCrFeNiTi 7 mm $\times$ 7 mm $\times$ 10 mm specimens were produced. Prior to mixing, the particle size for each powder was measured using a laser diffraction particle size analyser (Mastersizer 2000, Malvern UK). The pre-alloyed CoCrFeNi powder and elemental powders were mixed by tumbling them together on multiple axes for 15 minutes.

Table 3.1: *Chemical composition of CoCrFeNi powder, analysed using XRF (AMG Superalloys UK) taken from work by Brif et al. using the same powder [6].*

Element	Fe	Co	Cr	Ni	Al	Si	Zr	Other
wt.%	23.48	26.28	21.07	27.16	0.14	0.10	0.11	$<$0.05

Processing parameters have a large effect on material microstructure and properties in SLM, as the melt penetration depth of the laser influences the fusion between layers of the deposited powder. The previous study on SLM of CoCrFeNi by Brif *et al.* was completed using the Renishaw SLM125 with a pulsed laser system [6]. The AconityMINI uses a continuous laser, meaning the parameters used by Brif *et al.* could not be directly employed. Therefore, a statistical 'Design of Experiment' (DOE) for each alloy was created using Minitab software by varying the laser power (70 - 190 W), scanning velocity (400 - 1300 mm/s) and hatch spacing (20 - 130 µm) while keeping a constant layer thickness of 30 µm. The power is limited by the maximum power of the AconityMINI which is 200 W, the layer thickness was kept the same for all parts to allow each part to be built on the same build plate in the same run of the machine. The same parameter set was used to build each of the in-situ alloyed samples and these parameters are included in full in Appendix A. Initial microstructural studies were completed using a Clemex optical microscope. The specimens were analysed as-deposited without any subsequent treatment. All specimens were sectioned perpendicular to the layer deposition direction and were prepared by standard grinding and polishing methods. This included polishing with diamond suspension down to 1 µm and finishing with colloidal silica solution with a particle size of 0.05 µm. The relative density of each specimen was calculated by quantifying the internal porosity. This was done by analysing a cross-section and then employing an automatic thresholding procedure in the image analysis software ImageJ [236].

Subsequent phase characterisation was carried out by X-ray Diffraction (XRD) using a Bruker D2 Phaser Diffractomer with a Cu K_α radiation source ($\lambda = 1.54$ Å). Further microstructural characterisation as well as imaging of the powders, was carried out using a FEI Inspect F50 Scanning Electron Microscope (SEM) and Energy Dispersive X-ray Spectroscopy (EDS). The spot size and accelerating voltage were 4 and 20 kV respectively, and the working distance was approximately 10 mm. The software used for EDS analysis was AZtec (Oxford instruments).

3.5 Results

3.5.1 Powder Analysis

The SEM of images of each of the powders are shown in Figure 3.1 along with the particle size percentile values in Table 3.2. It is seen that all of the powders have a near spherical morphology, with the CoCrFeNi showing some non-spherical satellite particles. It is also shown that the average particle size of the Cu powder is 40.0 µm which is larger than that of the CoCrFeNi and Ti powders. There has been some limited research completed into AM of powders of different particle size distributions where smaller particles were interstitial between larger particles resulting in a higher packing density and a more homogeneous part [237]. However, the particle size difference in this case is not enough for the CoCrFeNi to be interstitial in the packing of the larger Cu particles, therefore it is assumed that both powder mixes will result in comparable packing densities.

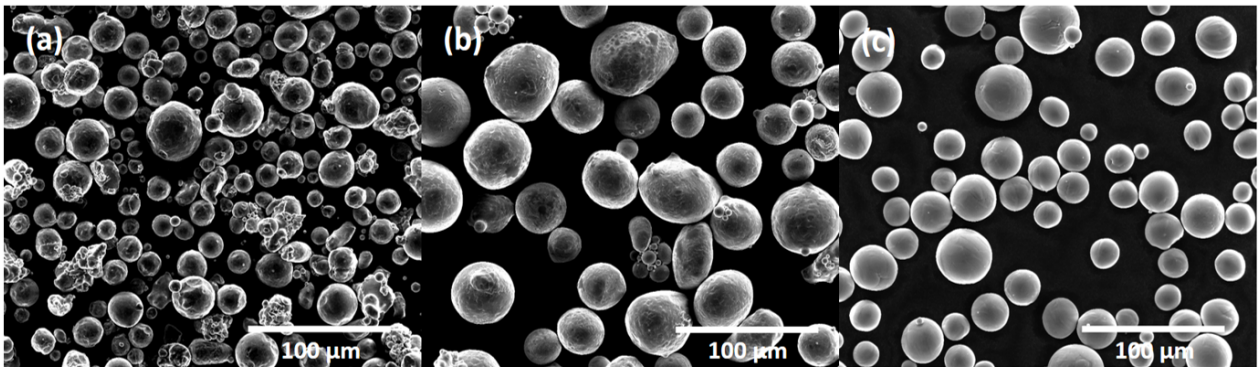

Figure 3.1: *Secondary electron images of the powders used for SLM. (***a***) CoCrFeNi, (***b***) Cu, (***c***) Ti.*

Table 3.2: *Particle diameter percentile values prior to mixing from the laser diffraction particle size distribution for each of the powders. Where D_{10}, D_{50} and D_{90} are the 10th, 50th and 90th percentile values of the particle diameter distribution for each powder.*

Powder	D_{10} (µm)	D_{50} (µm)	D_{90} (µm)
CoCrFeNi	17.9	30.1	49.0
Cu	26.5	40.0	59.8
Ti	19.9	29.2	42.8

3.5.2 Processing Parameters and Density

Representative optical micrographs for the highest relative density condition for each alloy are shown in Figure 3.2. Table 3.3 shows the corresponding parameters, relative density and volume energy density (VED) for each of the micrographs shown in Figure 3.2. VED is calculated by using the equation:

$$VED = P/vht, \tag{3.1}$$

where P is the laser power (W), v is the scanning velocity (mm/s), h is the hatch spacing (µm) and t is the layer thickness (µm).

From Figure 3.2 and Table 3.3, it can be seen that CoCrFeNi has an extremely high relative density. This is not unexpected, as this alloy in pre-alloyed powder form has been shown to be highly compatible with SLM in previous work [6]. The optimal input VED for this alloy (from those explored) was also considerably higher than that of the alloys with additions, resulting in some small keyholes, but notably no solidification cracking or hot tearing. The lack of such defects suggests that the solid solution microstructure seen previously is likely stable in SLM, as if there were high levels of micro-segregation, solidification cracks would have formed. The appearance of small keyholes indicates the the VED here is most likely at the higher end of the processing window for this alloy.

Figure 3.2 and Table 3.3 also show a high relative density of 99.13% was achieved for the CoCrFeNiCu alloy. The input VED necessary for this density was considerably lower than that required for the alloy without Cu. This could be due to the fact that copper has a lower melting point than the other constituent elements, as well as it being highly thermally conductive. Meaning that it could possibly be melting at a lower temperature and result in more effective heat transfer within the melt pool and in solidification. The porosity seen in this sample in image (b) in Figure 3.2 appears to be caused mainly by lack of fusion, where powder has not been completely

melted in some areas. There also is some solidification cracking seen, which is much more prevalent the samples with higher VED. The lack of fusion indicates that the VED used for this sample is at the lower boundary of the processing window for this alloy and further work is needed to try and narrow down which parameters would result in dense parts.

Results from the CoCrFeNiTi build with highest density are also shown in Figure 3.2 and Table 3.3. This shows a vastly reduced relative density compared to the other alloys manufactured. There is extensive cracking seen in this alloy, unlike the other alloys, as well as some larger, wider pores, suggesting that the addition of Ti has increased the crack susceptibility. The VED for this sample was also very low, but as most of the porosity is likely to be caused by cracking as well as lack of fusion, relating VED to the highest relative density is not necessarily useful in this case. If the VED were increased, the level of cracking would also probably increase, but the porosity caused by lack of fusion would decrease. The cause of the cracking seen in this alloy is further explored in Section 3.5.4.

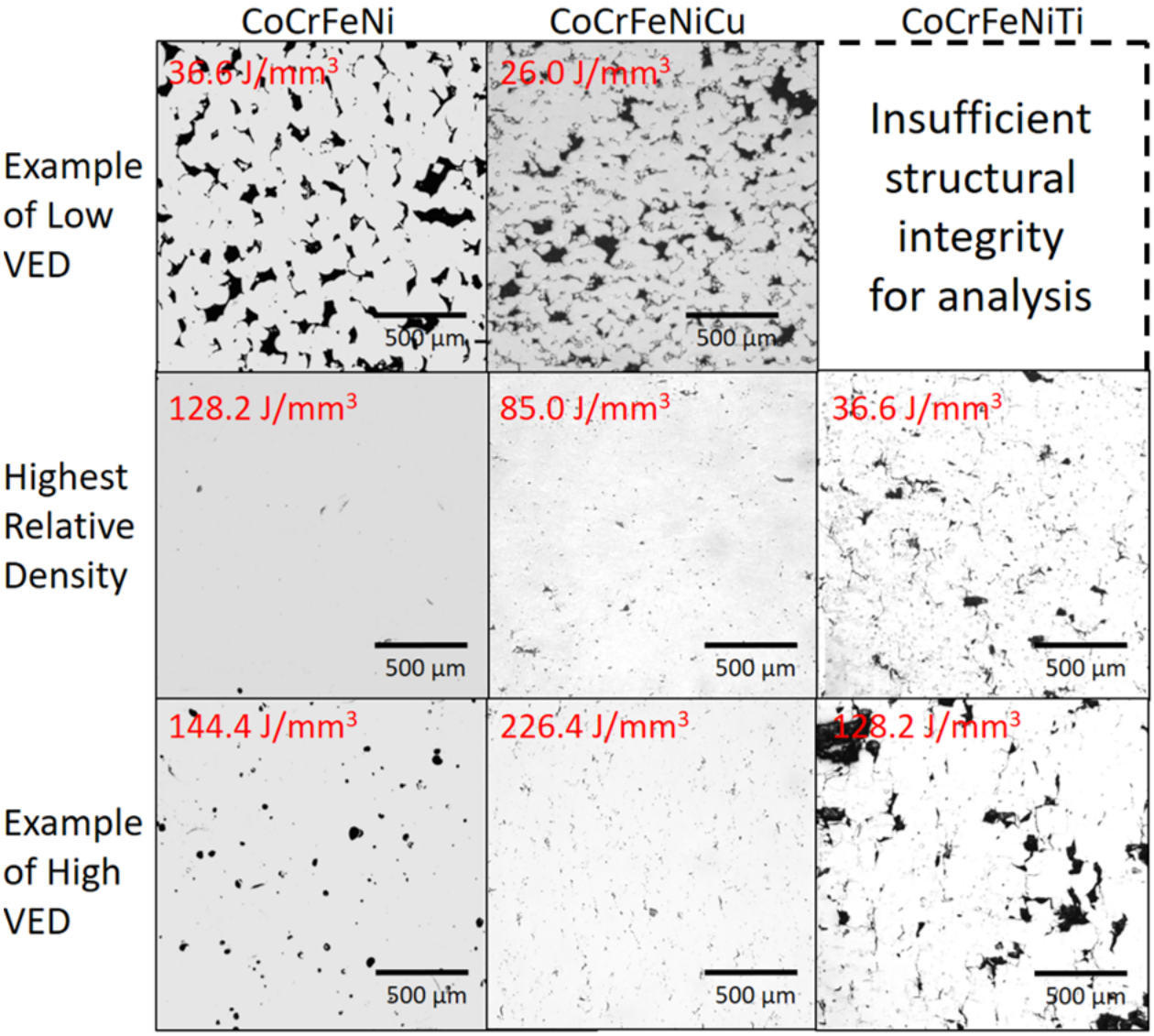

Figure 3.2: *Optical micrographs of highest relative density sample, as well as examples of samples with low and high VED, for each alloy resulting from the DOE. VED values for each sample are shown in red. All scale bars are 500 µm. The low VED sample for the CoCrFeNiTi alloy had insufficient structural integrity for sectioning and subsequent analysis.*

Table 3.3: *SLM processing parameters and the calculated VED for the sample with highest relative density for each alloy.*

Alloy	**Relative Density (%)**	**Laser Power P (W)**	**Scanning Velocity v (mm/s)**	**Hatch Spacing h (µm)**	**Layer Thickness t (µm)**	**VED (J/mm^3)**
CoCrFeNi	99.88	94	582	42	30	128.2
CoCrFeNiCu	99.13	130	850	60	30	85.0
CoCrFeNiTi	95.61	70	850	75	30	36.6

For each of the alloys manufactured by SLM, the relative density has been plotted against the input VED in Figure 3.3. CoCrFeNi shows a clear trend relating density and VED, where the highest density parts are likely to be seen where VED is between 60 - 130 J/mm^3. At a VED lower than this range, parts have reduced density due to lack of fusion. If the VED is higher than this range, parts have reduced density due to excessive keyhole formation. A similar, but less well defined, trend can be seen for CoCrFeNiCu. It is suspected that the addition of Cu could cause localised variation in thermal properties, so porosity is perhaps more variable than in the purely pre-alloyed powder. There is a definite VED range where parts with a consistently high density are made, between 75 - 125 J/mm^3. There is no trend seen in the plot for CoCrFeNiTi, due to the formation of cracks, via a mechanism not seen in the other alloys. At a lower VED there is lack of fusion and fewer cracks but at a higher VED there is the appearance of some keyholes but a vast increase in cracking. So, because of the higher crack susceptibility of this alloy, it is difficult to define a firm processing window in this case. This explains why the VED for the highest density sample of this alloy, shown in Table 3.3, is so low, as cracking is reduced. It should be noted that alternative measures such as normalised energy density could offer different insights into material process-ability, however they could not be utilised in this case, due to the unknown thermal properties of the materials [110].

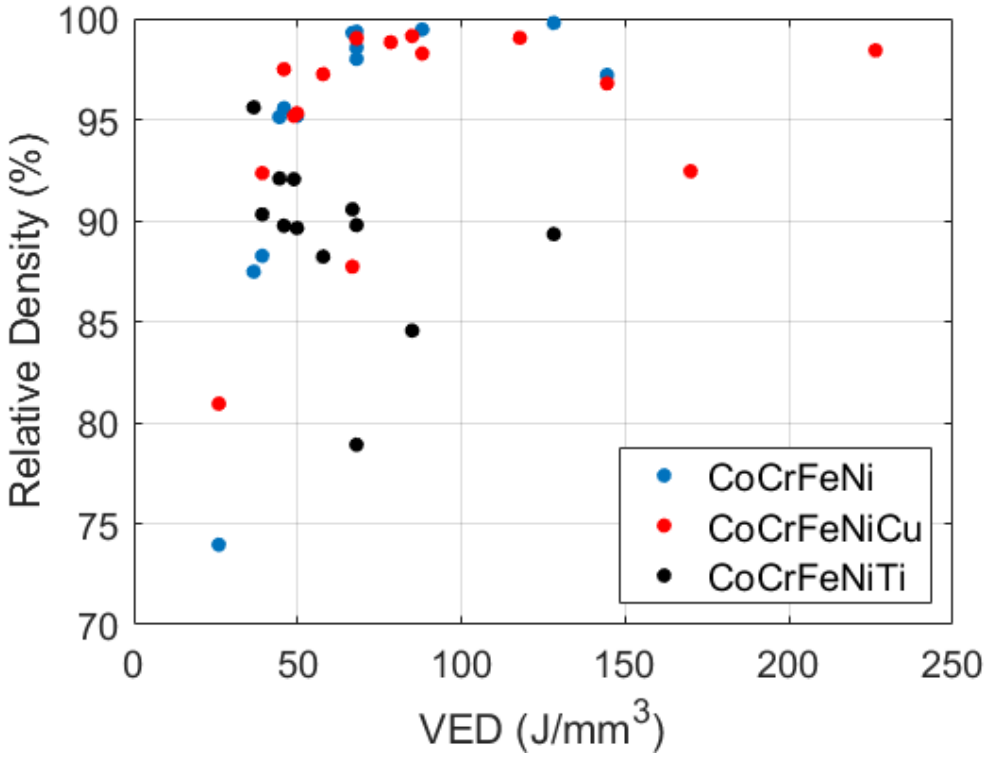

Figure 3.3: *Plots for each alloy, showing relative densities of each part for the corresponding input VED.*

3.5.3 XRD

XRD results given in Figure 3.4 show that both the CoCrFeNi and CoCrFeNiCu have a FCC microstructure with similar lattice parameters. The CoCrFeNiCu shows some peak broadening compared to the CoCrFeNi, indicative of a variation in lattice parameter. This could be caused by the uneven distribution of copper which could be causing some additional lattice distortion in some areas. The CoCrFeNiTi alloy shows an FCC phase, but also the appearance of peaks relating to the NiTi intermetallic and a Laves hexagonal close packed (HCP) phase which is most likely $TiCo_2$. The FCC peaks are also quite broad, suggesting there is some variation in the lattice parameter caused by the Ti not being homogeneously distributed throughout the FCC phase, in a similar manner to Cu in the previous alloy.

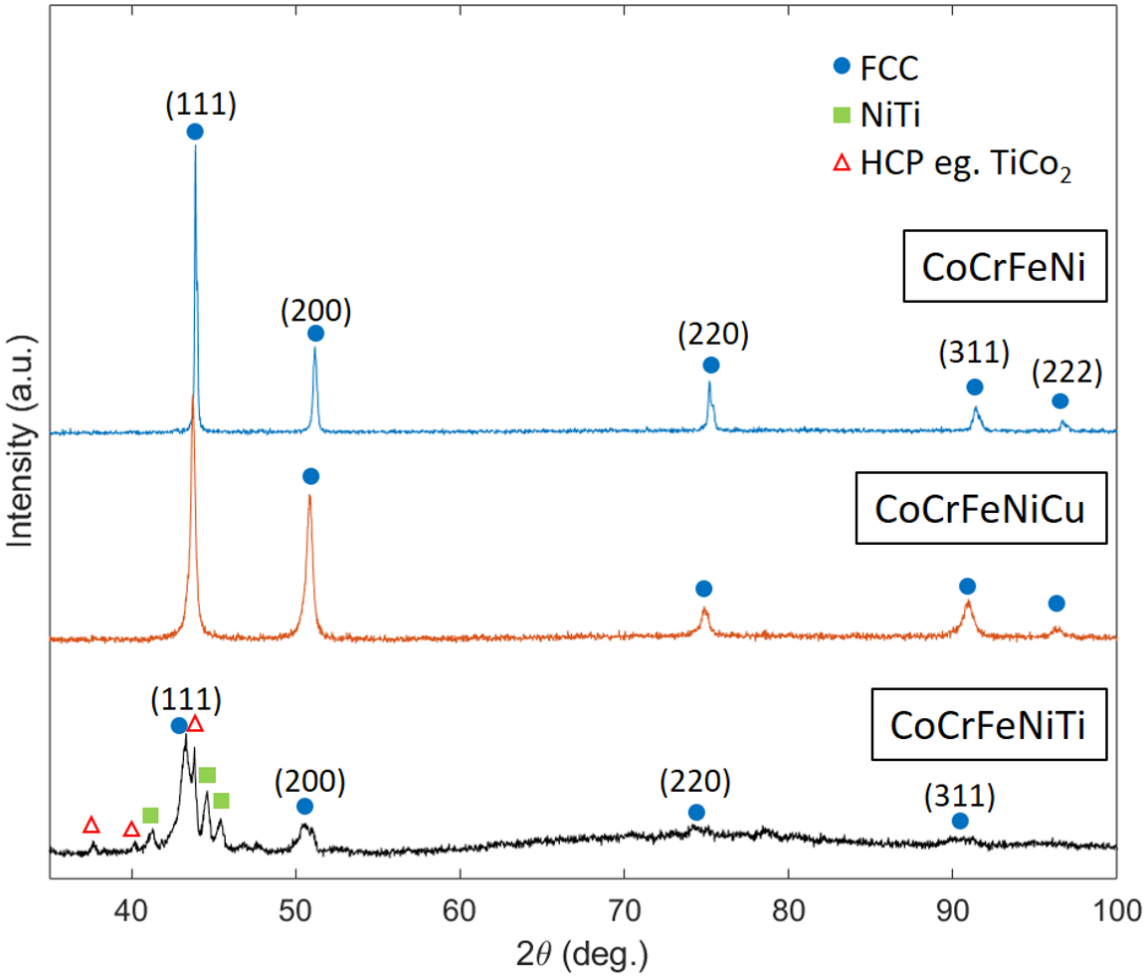

Figure 3.4: *XRD patterns using Cu K_α radiation for CoCrFeNi, CoCrFeNiCu and CoCrFeNiTi samples. For CoCrFeNi, CoCrFeNiCu and CoCrFeNiTi the lattice parameter for the FCC phase in each case is $a \approx 3.57$ Å, $a \approx 3.58$ Å and $a \approx 3.61$ Å respectively.*

3.5.4 Microstructure

SEM results for each alloy are shown in Figure 3.5. XRD showed a single phase FCC microstructure for the CoCrFeNi alloy, as seen in previous research into this composition [6]. This result is further confirmed by the EDS maps shown in Figure 3.5a, where elements are seen to be homogeneously distributed.

XRD analysis of the CoCrFeNiCu alloy in Figure 3.4 showed an apparent single phase FCC structure. It can be seen from EDS however that there is quite a substantial variation in the composition of phases within the alloy, with one phase highly enriched in Cu and the other depleted in Cu but roughly equiatomic in other elements. This is in line with the results of other work examining this alloy system produced by other manufacturing methods [235, 238]. It is likely

the second phase enriched in Cu has a lattice parameter near to that of pure Cu ($a \approx 3.6149$ Å). However, this phase was not easily resolved by XRD as it is evidently less abundant that the other phase and the peaks may have superimposed with the peaks of the other more abundant phase. It is noteworthy that the peaks on the CoCrFeNiCu case appear to be broadened, which may be evidence of this effect.

As outlined in work by Verma *et al.*, Cu has a positive enthalpy of mixing with all other elements in this alloy, so will not mix with them under equilibrium conditions [238]. The microstructure seen in that previous work showed Cu-rich second phase at the grain boundaries with a homogeneous distribution throughout. However in this work it is likely that the combination of elemental Cu powder with CoCrFeNi pre-alloyed powder, followed by the use of the SLM process for in-situ alloying, has exacerbated this phenomenon. The most Cu rich regions are of similar size to the elemental powder particles at 15 - 45 µm and EDS point scans show that these regions are between 75 - 92 at% Cu with other elements at equiatomic proportions. This is suggestive of the copper not properly mixing with the rest of the alloy in the molten state, and retaining some of the distribution it had as powder. The Cu depleted phase still contains between 3 - 17 at% Cu, showing there has been some diffusion of the Cu into the main FCC phase. Perhaps due to the high cooling rates and rapid solidification in SLM this Cu was trapped in the FCC lattice rather than being able to segregate to the full extent on the grain boundaries as in equilibrium conditions.

EDS results for the CoCrFeNiTi alloy are shown in Figure 3.5(c). Firstly, it is clear to see that there are un-melted Ti particles, where EDS point scans show that no alloying has taken place. This clearly demonstrates the input VED in this case did not cause a temperature high enough to melt or dissolve those particles, as discussed in Section 3.5.2. The un-melted particles appear to have served as crack initiation sites for some examples of the extensive cracking seen throughout this sample. These cracks generally seem to propagate through the grains and are very straight and angular, which is characteristic of solid-state cracking due to residual stress rather than the jagged edges produced by solidification cracking. A similar example of this type of solid-state cracking is seen in work by Zhang *et al.* on the CoCrFeNiMn alloy, where solid-state cracks initiated from smaller solidification cracks and propagated along high angle grain boundaries [181]. From EDS point scans it can be seen that the proportion of Ti varies between 1.3 at% to 23 at% in the vicinity of the un-melted Ti particles with all other elements remaining equiatomic throughout. It is clear that the intermetallic and brittle phases are distributed throughout an FCC matrix and not segregated at the grain boundaries as seen in the previous work mentioned, and this would explain why crack propagation is through grains themselves.

As seen in Section 3.5.2, it has not been possible to define an optimum build processing window for this alloy and this is further confirmed by microstructural analysis. For this alloy, the

in-situ alloying process was not completely successful, as there were still unalloyed Ti particles present. This could be due at least partially to its higher melting point than the other elements. A higher VED would be necessary to melt or dissolve the Ti particles; however an increase in VED will only increase the severity of the solid-state cracking.

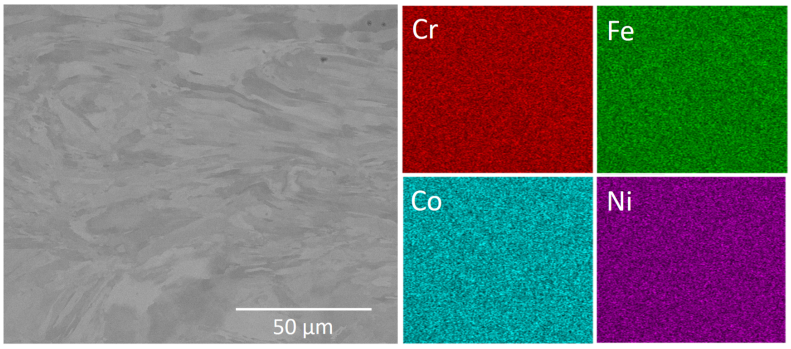

(a) *CoCrFeNi*

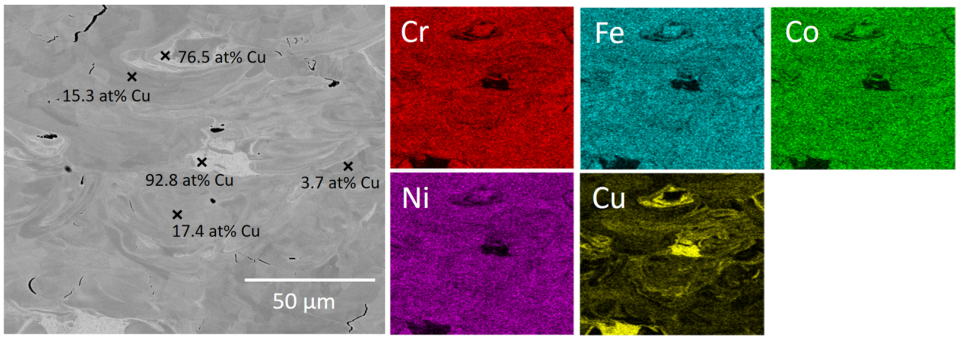

(b) *CoCrFeNiCu*

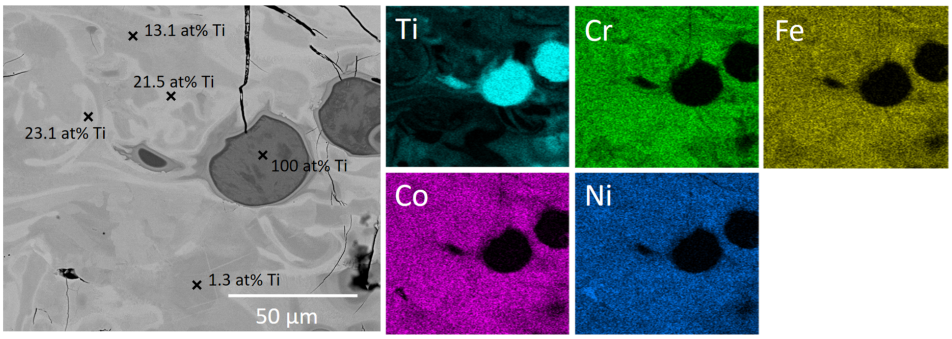

(c) *CoCrFeNiTi*

Figure 3.5: *Back Scattered Electron (BSE) images and accompanying EDS scans of the (***a***) CoCrFeNi, (***b***) CoCrFeNiCu and (***c***) CoCrFeNiTi alloys. EDS point scans show the variation in concentration of Cu and Ti, where all other elements remained equiatomic.*

3.6 Discussion

In this work, SLM builds of CoCrFeNi, CoCrFeNiCu and CoCrFeNiTi were completed where the SLM process itself was used for in-situ alloying of the additional powders (Cu and Ti) to the pre-alloyed CoCrFeNi powder. A DOE was completed for each alloy and the part determined to have the highest density by image analysis for each alloy was further analysed by XRD and SEM/EDS.

The CoCrFeNi build resulted in a part with a high relative density and a homogeneous single phase FCC microstructure with a clear processing window, as seen in Figure 3.3. The CoCrFeNiCu alloy resulted in a high relative density and showed a wider possible processing window. The microstructure showed two FCC phases—one depleted and one enriched in Cu. The Cu particles did alloy with the pre-alloyed powder, but due to the tendency for Cu to segregate in this alloy there were large areas of high concentrations of Cu. These were much larger than the grain boundary segregation seen in this alloy manufactured by other methods [238]. The CoCrFeNiTi alloy had very low relative density and showed extensive cracking due to residual stresses. There was no distinct processing window for this alloy as increased VED resulted in increased cracking and reducing the VED resulted in un-melted Ti particles and lack of fusion defects. The microstructure was shown to have an FCC matrix with the presence of NiTi and a HCP phase, as cracks propagated through the grains not along grain boundaries.

The in-situ alloying process was more successful in the case of the Cu, as Cu particles were at least partially alloyed with the pre-alloyed elements. This is likely because the melting point of Cu at 1084 °C is much lower than that of CoCrFeNi at 1414 °C and the melting point of Ti is higher at 1688 °C. Therefore, Cu will more readily dissolve into solid solution or melt at lower temperatures than Ti. This indicates that in future alloy development using this method, consideration should go into the additional elemental powder melting point relative to the base powder. There also should be some consideration of whether the additional element commonly causes grain boundary segregation in that alloy, if that alloy has been manufactured previously by AM or by other means. If that element tends to segregate then adding it as an addition to a pre-alloyed powder will result in highly segregated wider regions with a differing morphology to common grain boundary segregation. Also in this case, most likely due to rapid cooling, elements like Cu have been incorporated into the main phase in varying levels throughout the sample, which differs from the alloy when produced by methods with slower cooling rates. Therefore in order to compare alloys manufactured in this way to those by conventional methods, subsequent heat treatment steps would be necessary to homogenise the microstructure.

3.7 Conclusions

In this work, elemental Cu and Ti powders were mixed with pre-alloyed CoCrFeNi powder, in equiatomic proportions, and then alloyed in-situ via SLM. The corresponding microstructure of the sample with highest relative density for each alloy was then analysed. The main findings of this work are summarised as follows:

- The build of the CoCrFeNi alloy resulted in a sample with high relative density at a VED of 128.2 J/mm^3 and single phase FCC microstructure with a clear and wide processing window.

- The build of the CoCrFeNiCu alloy showed high relative density, a well-defined processing window and two FCC phases; one depleted and one rich in Cu. The VED which produced the highest relative density was low at 85.0 J/mm^3 compared to that of the CoCrFeNi, most likely due to the addition of Cu which has a lower melting point. The Cu did alloy with the pre-alloyed base powder but there were large areas of high Cu concentration due to its inherent tendency to segregate with the other constituent elements.

- The build of CoCrFeNiTi show a low relative density and no clear processing window. Some Ti particles remained un-melted, while some Ti had alloyed to produce brittle intermetallic NiTi and HCP phases in an FCC matrix. There was extensive solid-state cracking seen in every sample. The VED which resulted in the sample of highest density was low at 36.6 J/mm^3, as this was the sample in which the least cracking occurred even though there was some lack of fusion porosity.

- A component of the success of in-situ alloying is deemed dependent on the melting temperature of the elemental powder being less than or comparable to the melting temperature of the base alloy powder. In this case the melting temperature of Cu (1084 °C) is much lower than that of CoCrFeNi (1414 °C) and the melting point of Ti is higher (1688 °C), resulting in un-melted Ti particles.

- The tendency of the additional element to segregate at grain boundaries, in the same alloy manufactured by other methods, should also be an indicator of whether that elemental addition is suitable for in-situ alloying. If the element tends to segregate, like Cu in this study, this can result in areas of high concentration of that element, with a differing morphology to common grain boundary segregation.

Finally, It has been shown that in-situ alloying could be a useful tool with which to develop novel alloys quickly. In the future, further work involving heat treatments of in-situ alloyed

samples could possibly result in a more homogeneous microstructure, therefore expanding the range of elements which could be added and alloyed successfully.

Author Contributions

Conceptualisation, L.F., I.T. and R.G.; methodology, L.F., I.T. and R.G.; investigation, L.F., G.M., L.H. and F.L.; original draft preparation, L.F.; review and editing, F.L. and R.G.; supervision, I.T. and R.G. funding acquisition, R.G. and I.T. All authors have read and agreed to the published version of the manuscript.

Funding

This work was supported by Science Foundation Ireland 18/EPSRC-CDT/3584, the Engineering and Physical Sciences Research Council EP/S022635/1 and the Manufacture using Advanced Powder Processes (MAPP) EPSRC Future Manufacturing Hub EP/P006566/1. We wish to acknowledge the Henry Royce Institute for Advanced Materials, funded through EPSRC grants EP/R00661X/1, EP/S019367/1, EP/P02470X/1 and EP/P025285/1, for access to the Aconity3D Mini at The University of Sheffield.

Conflicts of Interest

The authors declare no conflict of interest.

Chapter 4

Design and Assessment of Novel High Entropy Alloys for High Temperature Applications

4.1 Author Contributions

Lucy Farquhar - Conceptualisation, methodology, writing of alloy design code, manufacture of samples via arc-melting, sample prep, data analysis, sample characterisation, writing of original draft.
Iain Todd - Supervision
Russell Goodall - Conceptualisation, support with methodology, supervision, writing - review and editing

4.2 Background

High entropy alloys (HEAs) have been designed using many different tools in the past including density functional theory (DFT), CAlculation of PHAse Diagrams (CALPHAD), machine learning (ML) and empirical parameters. All alloy design approaches have their pros and cons, as discussed in Chapter 2. Therefore, especially with quality and quantity of data currently lacking in HEA databases, each design methodology includes a large margin for error when it comes to predicting HEA properties and microstructures.

Previously, empirical parameters such as atomic size mismatch δ, valence electron concentration (VEC) and enthalpy of mixing ΔH_{mix} have commonly been used to design single phase solid

solution alloys. Even though multiple reports have included limits for multi-phase solid-solution formation, such as a lattice strain ε_{RMS} between 5 - 10% or $\delta > 4.6$, these parameters are not often utilised in studies to find new alloys [41,239]. Therefore, in this work new HEAs are designed by employing limits for multi-phase solid-solution formation on 10 different empirical parameters. Using a palette of 24 elements by varying the composition of each element from 5 - 35 at%, over a million quaternary alloys are filtered through the empirical parameter ranges. In order for the alloys to be suitable for aerospace applications requiring operation at high temperatures and also AM, the density, melting temperature and melting temperature range are calculated and used to remove unsuitable alloys. The resulting top ranked alloys are then manufactured via arc-melting.

Paper: Design and Assessment of Novel High Entropy Alloys for High Temperature Applications

Lucy Farquhar[1], Iain Todd[1], Russell Goodall[1]

1 – Department of Materials Science and Engineering, University of Sheffield, Sheffield S1 3JD, UK

Correspondence: laufarquhar1@sheffield.ac.uk

Abstract

Refractory High-entropy alloys (RHEAs) represent a large potential research area for high strength alloys exhibiting relative stability at elevated temperatures, especially when made by additive manufacturing (AM) due to microstructural refinement. Here, empirical parameters are used to predict the microstructure and stability of new quaternary RHEAs, from a pool of 24 possible elements varying between 5 - 35 at% composition. Empirical parameters such as atomic size mismatch δ and the enthalpy of mixing ΔH_{mix} are calculated along with estimates for relevant properties such as density, melting temperature and cost for each composition. The alloys with different compositions are filtered to remove those with empirical values and properties outside of acceptable ranges. The remaining compositions are then ranked based on their density, melting temperature and a combination of melting temperature and density with equal weighting. The resulting nine RHEAs ranked highest are then manufactured via vacuum arc-melting and categorised to evaluate the success of the alloy design model by assessing their microstructures and processability. A total of four out for the nine non-equiatomic RHEAs contained only body centred cubic (BCC) phases, therefore showing potential for further research into their suitability for high temperature applications.

Keywords

High-Entropy Alloys, Alloy Design, Additive Manufacturing, Laser Powder Bed Fusion

4.3 Introduction

Over the past few decades interest in the area of High-Entropy Alloys (HEAs) has increased following their discovery by Yeh *et al.* and the invention of the CoCrFeMnNi alloy by Cantor *et al.* in 2004 [1, 2]. HEAs represent an exciting new research opportunity with a broad scope to create materials tailored exactly to their application, consisting of combinations of five or more alloying elements in similar proportions, resulting in a high configurational entropy. Many HEAs have very stable microstructures as well as high corrosion resistance, toughness and good high temperature mechanical properties [3, 53].

Additive manufacturing (AM) is a novel manufacturing technique, where parts are built up layer-by-layer, allowing the formation of complex geometries (for example with inner channels) and minimal waste compared to subtractive manufacturing methods. The AM process can also be tuned so as to refine material microstructure, a process which can enhance or improve material properties. This has been shown to be the case with some of the researched HEAs, especially in metal laser powder bed fusion (PBF-LB/M) processes, making HEAs good candidates for high temperature applications [8, 151, 152, 154].

There has been some interest into developing HEAs specifically for high temperature applications. Refractory HEAs (RHEAs) are obvious candidates for these applications as refractory elements have high melting points and these alloys tend to have high hardness values which are largely maintained at high temperatures. Senkov *et al.* have published multiple research papers on RHEAs. The equiatomic RHEAs VNbMoTaW and NbMoTaW show impressive yield strength at high temperatures compared to conventional nickel superalloys such as Haynes 230 and Inconel 718 [20, 63].

There is now substantial interest in Dual-Phase HEAs (DP-HEAs), looking to mimic the microstructure and properties seen in two-phase nickel superalloys, suitable for high temperature applications. When designing HEAs it is a challenging to find a way to predict the phases and stability of different near-equiatomic compositions of elements. For conventional alloy systems, where there is usually one principal element alloyed with small additions of other elements, predictors such as the Hume-Rothery rules have proved useful [34]. In theory, the high configurational entropy of HEAs stabilizes the solid solution phases over other phases like intermetallic compounds [40]. But in reality, secondary phases and intermetallic phases form readily, therefore predictive parameters and methods need to reflect these results. Many studies now use techniques such as density functional theory (DFT), CALculation of PHAse Diagrams (CALPHAD) or machine learning (ML) to search for new potential HEA compositions. However DFT is very computationally expensive for HEAs, in order to simulate enough atoms to encompass the complexity [35]. Accuracy of CALPHAD and ML rely on the use of well populated, high quality and

quantity databases in different forms, which due to the vast HEA compositional space and infancy of the research field, are not always available [56, 60]. Hence, first principle empirical parameters and approximations are often a quick and simple method by which to predict HEA properties.

Empirical parameters are in general based on three concepts. The first concept is the physical interaction of atoms within the lattice and trying to quantify the distortion and strain that this creates. Examples of this are the atomic size mismatch δ and residual lattice strain ε_{RMS} [41, 44]. The second concept relates to thermodynamic considerations and often attempts to reduce the Gibb's free energy of the alloy system. Parameters could include enthalpy of mixing ΔH_{mix}, ΔS_{mix} and Ω [43]. The third concept is based on electronic interactions between atoms and includes variables such as valence electron concentration VEC and Pauling electronegativity χ [240, 241]. Lastly, these concepts can be combined as is seen with the Λ parameter [46]. The empirical parameters used for phase prediction are summarised in Table 4.1. Some predictive techniques are more successful than others, and for all of these parameters there are alloys which are an exception to the rule. Use of these parameters narrows the range of alloys that are feasible, despite the degree of uncertainty. Many of them are often used in conjunction with other variables to further refine the possible selection of alloys that satisfy the criteria.

The majority of current HEA design research is focused on finding single phase HEAs. However, with careful consideration the composition and using the multi-phase formation criteria for each parameter, it is, in theory, possible to use them to find multi-phase HEAs that could be candidates for high temperature applications, as detailed in Table 4.1.

Table 4.1: *Established parameters in the study of HEAs. If criteria is given for single and multi-phase solid solution phase formation then this is indicated by separate columns. Otherwise if criteria is purely for solid solutions only, or for the formation of body centred cubic (BCC), face centred cubic (FCC) or hexagonal close packed (HCP) phases, then this is given in one column.* c_i *is molar fraction of the* i^{th} *element,* c_j *is molar fraction of the* j^{th} *element,* ΔH_{ij}^{mix} *is the enthalpy of mixing of* i^{th} *and* j^{th} *elements calculated using the miedema model [242],* R *is the gas constant (8.314* $JK^{-1}mol$*),* $(VEC)_i$ *is the valence electron concentration of the* i^{th} *element,* T_m *is melting temperature calculated using the rule of mixtures,* $S_H = \Delta H_{mix}/T_m$*,* S_E *is excess entropy of mixing,* χ_i *is the Pauling electronegativity of the* i^{th} *element,* $\bar{\chi}$ *is the average Pauling electronegativity,* r_i *is the atomic radius of* i^{th} *element,* $\bar{r}$ *is average atomic radius,* ε_i *is intrinsic residual strain,* r_S *is atomic radius of smallest element,* r_L *is atomic radius of largest element.*

Parameter	**Formula**	**Solid Solution**		**Ref.**
		Single Phase	**Multi Phase**	
Enthalpy of Mixing ΔH_{mix} (kJ/mol)	$\Delta H_{mix} = 4\sum_{i=1,i\neq j}^{n} c_i c_j \Delta H_{ij}^{mix}$	$-22 \leq \Delta H_{mix} \leq 7$ $-12 \leq \Delta H_{mix} \leq 10$ $-16 \leq \Delta H_{mix} \leq 0$		[44, 47, 243]
Entropy of Mixing ΔS_{mix} (J/Kmol)	$\Delta S_{mix} = -R\sum_{i=1}^{n} c_i ln c_i$	$11 \leq \Delta S_{mix} \leq 19.5$		[44]
VEC	$VEC = \sum_{i=1}^{n} c_i (VEC)_i$	FCC $VEC > 8$, BCC $VEC < 6.87$ HCP $VEC \approx 3$ FCC $VEC > 7.8$, BCC $VEC < 6.7$		[239, 240, 244]
Ω	$\Omega = \frac{T_m \Delta S_{mix}}{\mid \Delta H_{mix} \mid}$	$\Omega \geq 1.1$		[45]
ϕ	$\phi = \frac{\Delta S_{mix} - S_H}{\mid S_E \mid}$	$\phi > 20$	$1 < \phi < 20$	[243, 245]
χ	$\chi = \sqrt{\sum_{i=1}^{n} c_i (\chi_i - \bar{\chi})^2}$	$\Delta\chi > 0.133$ (except for alloys containing Al)		[241]

δ	$\delta = 100\sqrt{\sum_{i=1}^{n} c_i \left(1 - \frac{r_i}{\bar{r}}\right)^2}$	$\delta < 8.5$ $\delta < 6.5$ $\delta < 6.6$ $\delta < 4.6$	$6.6\% < \delta \leq 9\%$ $\delta > 4.6\%$	[42, 44, 45, 47, 239]
ε_{RMS}	$\varepsilon_{RMS} = \sqrt{\sum_{i=1}^{n} c_i \varepsilon_i^2}$	$\varepsilon_{RMS} < 5\%$	$5\% < \varepsilon_{RMS} < 10\%$	[41]
γ	$\gamma = \frac{\left(1 - \sqrt{\frac{(r_S+\bar{r})^2 - \bar{r}^2}{(r_S+\bar{r})^2}}\right)}{\left(1 - \sqrt{\frac{(r_L+\bar{r})^2 - \bar{r}^2}{(r_L+\bar{r})^2}}\right)}$	$\gamma < 1.175$		[246]
α_2	$\alpha_2 = \sum_{i}^{n} \sum_{j \geq i}^{n} \frac{c_i c_j \mid r_i + r_j - 2\bar{r} \mid}{2\bar{r}}$	$0 \leq \alpha_2 \leq 0.06$	$0.02 \leq \alpha_2 \leq 0.07$	[247]
Λ	$\Lambda = \frac{\Delta S_{mix}}{\delta^2}$	$\Lambda > 0.96$	Two phase $0.24 < \Lambda < 0.96$ Compounds form $\Lambda < 0.24$	[46]

In this work the empirical parameters shown in Table 4.1 will be used for alloy design and phase prediction for novel HEAs suitable for high temperature applications. The resulting alloys are then ranked based on melting point and density (high melting point and low density being desirable) with the most promising alloys then being manufactured by arc melting. The resulting alloys will then be classified based on their microstructure and the accuracy of the model will be evaluated based on these findings.

4.4 Methodology

A computational tool is proposed which calculates the values of all the empirical parameters in Table 4.1 for varied compositions of alloys from a palette of elements, to find novel multi-phase

HEAs for high temperature aerospace applications. A multi-phase solid solution alloy, mimicking, if possible, the microstructures of nickel superalloys, is desirable for aerospace applications and could provide enhanced strength compared to single phase alternatives. A sequential filtering system is applied to remove alloys that have calculated values outside of the limits of the empirical parameters for multi-phase solid solution formation and for properties such as melting temperature (T_m), density (ρ) and cost in USD per cm^3, shown in Table 4.2. The resulting alloys are then ranked based on density, melting temperature and an equally weighed combination of both melting temperature and density, properties which are particularly important for high temperature aerospace applications. The range of elemental melting temperatures in the alloy is also limited to 1500 K, as a large range of element melting temperatures could mean difficulties with manufacturing the alloy by PBF-LB/M, especially via in-situ alloying [248]. If the range is too large there could be some vaporisation of the lower melting point elements causing gas porosity and compositional variation at high temperatures, or lack of fusion and un-melted elemental particles at lower temperatures, due to the higher melting point elements.

Table 4.2: *Limits on each parameter used to find multi-phase solid solution alloys. Alloys that have a calculated value outside these limits are removed.*

Parameter	**Acceptable Range**
Enthalpy of Mixing ΔH_{mix} (kJ/mol)	$-22 \leq \Delta H_{mix} \leq 7$
Entropy of Mixing ΔS_{mix} (J/Kmol)	$10 \leq \Delta S_{mix} \leq 20$
VEC	$3 \leq$ VEC ≤ 11
Ω	$\Omega > 1.1$
χ	$\chi > 0.11$
δ	$3.5 \leq \delta \leq 8$
ε_{RMS}	$4 \leq \varepsilon_{RMS} \leq 11$
γ	$\gamma < 1.2$
α_2	$0.01 \leq \alpha_2 \leq 0.08$
Λ	$0.2 \leq \Lambda \leq 1$
Material Property	**Acceptable Range**
Density ρ (g/cm^3)	$\rho < 15$
Cost C USD/cm^3	C < 1
Melting Temperature T$_m$ (^{o}C)	$T_m > 1500$
Melting temperature range of elements T_m^{range} (^{o}C)	$T_m^{range} < 1500$

The elements included in the palette for the model are Li, B, C, Mg, Al, Si, Sc, Ti, V, Cr, Mn, Fe, Co, Ni, Cu, Zn, Y, Zr, Nb, Mo, Sn, Hf, Ta and W. This excludes elements that are too high

in price and those that are difficult to handle or process eg. Mg. Some non-metals such as C and Si were also added as they often form compounds which have positive effects on strength such as grain boundary precipitation. An array is formed which creates all possible combinations of these elements, where there are 10,626 and 42,504 combinations of different elements for quarternary alloys and quinary alloys respectively.

Compositions of each element can be varied between 5 - 35 at% in 5 at.% graduations so as to stay within the defined composition limits of HEAs [2]. An array of possible composition values is then formed containing all the possible compositions that each combination of elements could have. This results in 133 and 1214 different compositions for quarternary and quinary alloys respectively. Therefore combining this with the different combinations of elements, this results in the modelling of 1,413,258 possible quarternary alloys and 51,599,856 quinary alloys. Quanternary alloys are focused on in this work to reduce processing time, alloy complexity and to allow for a simplified assessment of the methodology, despite not satisfying the initial definition of HEAs to contain at least five elements.

A sequential filtering system is then applied to remove alloys that are outside the specified limits on each empirical parameter, shown in Table 4.2. These are based on the solid solution and multi-phase criteria shown in Table 4.1 as well as some other material properties that are important for high temperature aerospace applications, especially when manufactured by AM. These properties are density, cost, melting temperature and range in melting temperatures of constituent elements. Density, cost and melting temperature are estimated by using the rule of mixtures and the cost is estimated based on the price of bulk elements at the time of writing (2020). Many of the parameters are not independent, so applying criteria for one often negates the need to apply criteria on others, but all criteria are applied here, to ensure robustness of the model. The alloys that have fulfilled this criteria are then ranked based on their density, melting temperature and an equally weighted combination of both density and melting temperature. A flow chart demonstrating the steps of the alloy design model is shown in Figure 4.1.

Following the result of the alloy design model the top three ranked alloys of different elemental composition in each of the 3 ranking configurations (9 alloys in total) are manufactured and analysed. The alloys are made via arc-melting using a Bruker MAM1 arc-melter and were flipped and remelted 5 times. The alloys were then sectioned, mounted and polished by conventional polishing methods. Subsequent phase characterisation was then carried out by X-ray diffraction (XRD) using a Bruker D2 Phaser Diffractomer with a Cu K_α radiation source ($\lambda = 1.54$ Å). Further microstructural characterisation was carried out using a FEI Inspect F50 scanning electron microscope (SEM) with energy dispersive X-ray spectroscopy (EDS) using AZtec (Oxford Instruments). The spot size and accelerating voltage were be 4 and 20 kV respectively, and the working distance was approximately 10 mm.

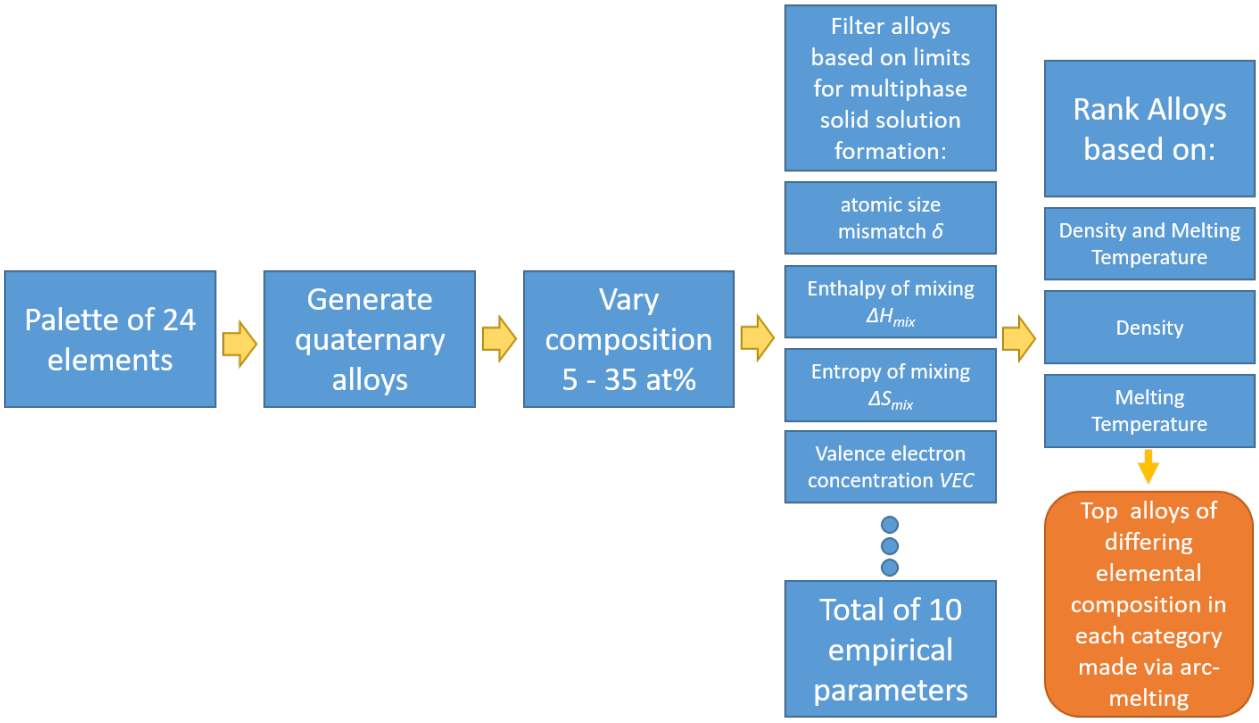

Figure 4.1: *Flow chart of the different stages of the HEA design model.*

4.5 Results & Discussion

After filtering, 2612 quaternary alloys were ranked based on density, melting temperature and a combination of both with equal weighting. Table 4.3 shows the results of the modelling process for quaternary alloys and Table 4.4 shows the corresponding empirical parameters and predicted physical properties for each alloy. To ensure a varied range of different alloy types, only the highest ranked alloy for each set of elements is included.

Alloys containing a large amount of Ti and V ranked very highly, as Ti and V having a low densities relative to their melting points. Many of the alloys also contain high levels of Mo and Nb, due to their high melting points. However, high levels of elements such as Ti in many of the highly ranked alloys presents an issue, as Ti tends to oxidise excessively when at temperatures near its melting point, meaning the alloys could also have low oxidation resistance, if exposed to high temperatures in air. An alloy containing large amounts of Si has also been ranked very highly, even though usually efforts are made to ensure the composition of Si is low enough to form small amounts of silicides to strengthen the alloy without compromising the ductility. To combat this, in future work the levels of certain elements should be constrained to be within certain limits, based on specific knowledge of the effects of those elements.

Table 4.3: *The alloys resulting from the alloy design model showing the top three in each ranking configuration. Alloys are ranked by (1-3) density, (4-6) melting temperature and (7-9) density and melting temperature.*

Alloy Number	Elements				Composition at%			
1	Ti	V	Nb	Mo	30	30	35	5
2	Si	V	Cr	Mo	30	30	5	35
3	Ti	Zr	Nb	Mo	35	30	30	5
4	Zr	Nb	Mo	Ta	20	25	35	20
5	Cr	Nb	Mo	Ta	20	25	35	20
6	V	Cr	Mo	Ta	30	15	35	20
7	Ti	V	Cr	Mo	35	35	25	5
8	Ti	V	Mn	Mo	35	35	25	5
9	Al	Ti	V	Cu	5	35	35	25

Table 4.4: *The resulting alloys from the alloy design model and their corresponding empirical parameters and predicted physical properties.*

Alloy	1	2	3	4	5	6	7	8	9
VEC	4.75	5.1	4.4	5.15	5.55	5.5	4.95	5.2	6.05
δ	4.29	6.84	5.21	5.98	4.91	4.20	6.33	4.60	5.79
ΔH_{mix} (kJ/mol)	-0.96	-4.92	1.28	-3.9	-6.02	-2.84	-4.41	-4.16	-5.65
ΔS_{mix} (J/Kmol)	10.30	10.30	10.30	11.28	11.28	11.10	10.23	10.23	10.23
Ω	25.08	4.76	18.36	8.03	5.20	10.30	4.90	4.82	3.30
α_2	0.013	0.020	0.016	0.018	0.014	0.011	0.018	0.013	0.016
γ	1.11	1.19	1.19	1.19	1.15	1.15	1.18	1.12	1.15
Λ	0.55	0.21	0.37	0.31	0.46	0.62	0.25	0.48	0.30
χ	0.12	0.22	0.18	0.33	0.27	0.27	0.13	0.13	0.14
ε_{RMS}	4.32	6.93	5.20	5.95	4.96	4.21	6.34	4.59	5.80
T_m (^{o}C)	2063.25	2002.4	2007.85	2502.55	2503.55	2364.3	1841.8	1688.55	1550.86
ρ (g/cm^3)	6.68	6.45	6.61	10.33	10.47	9.79	6.01	6.07	6.08
C (USD/cm^3)	0.18	0.10	0.16	0.96	0.94	0.89	0.08	0.07	0.07
T_m^{range} (^{o}C)	957	1207	957	1144	1139	1139	957	1373	1241.75

Table 4.5: *The resulting alloys characterised by a traffic light system to indicate their success in satisfying the model design criteria. Green: All peaks identified as BCC phases. Amber: Some peaks unidentified or due to complex phases, detrimental immiscible elements, BCC phases present. Red: Processing issues eg. brittle fracture or excessive vaporisation.*

Alloy Number	Elements				Composition at%			
1	Ti	V	Nb	Mo	30	30	35	5
2	Si	V	Cr	Mo	30	30	5	35
3	Ti	Zr	Nb	Mo	35	30	30	5
4	Zr	Nb	Mo	Ta	20	25	35	20
5	Cr	Nb	Mo	Ta	20	25	35	20
6	V	Cr	Mo	Ta	30	15	35	20
7	Ti	V	Cr	Mo	35	35	25	5
8	Ti	V	Mn	Mo	35	35	25	5
9	Al	Ti	V	Cu	5	35	35	25

4.5.1 Arc-Melting & Microstructural Analysis

Manufacturing of all alloys was attempted by arc-melting and low magnification images of the resulting samples after metallographic preparation are shown in Figure 4.2. Two of the alloys were unable to be acceptably processed - Alloy 2 and Alloy 8. Alloy 2 was extremely brittle, most likely due to the high fraction of Si, resulting in fracturing in multiple places and disintegration when sectioned. This was enough to determine that this alloy would be unsuitable for the application so it was not further analysed. During arc-melting, the Mn in Alloy 8 vaporised heavily due to its boiling point of 2061 ^{o}C being much less than the melting point of Mo at 2617 ^{o}C and near to that of V at 1902 ^{o}C. So therefore this alloy was also discounted from further investigation as this would also be problematic for an alloy manufactured by AM, however the resulting sample image can be seen in Figure 4.2. For this reason, these alloys are indicated in red in Table 4.5. All other alloys are categorised as green and amber, where green indicates that all peaks in their corresponding XRD patterns have been identified as BCC (or un-melted elements) and amber indicates some peaks were characteristic of other more complex phases, alongside BCC phases. Many of the samples contain un-melted or un-alloyed elements, indicating either the samples were not flipped and re-melted enough times, the arc-melter power was not sufficient or that the element does not dissolve readily in the surrounding material composition.

4.5.1.1 Green Alloys

Alloys are categorised as "green" if they have have all peaks identified as either BCC phases or as elements which may have been un-melted by the arc-melting process. XRD patterns for the

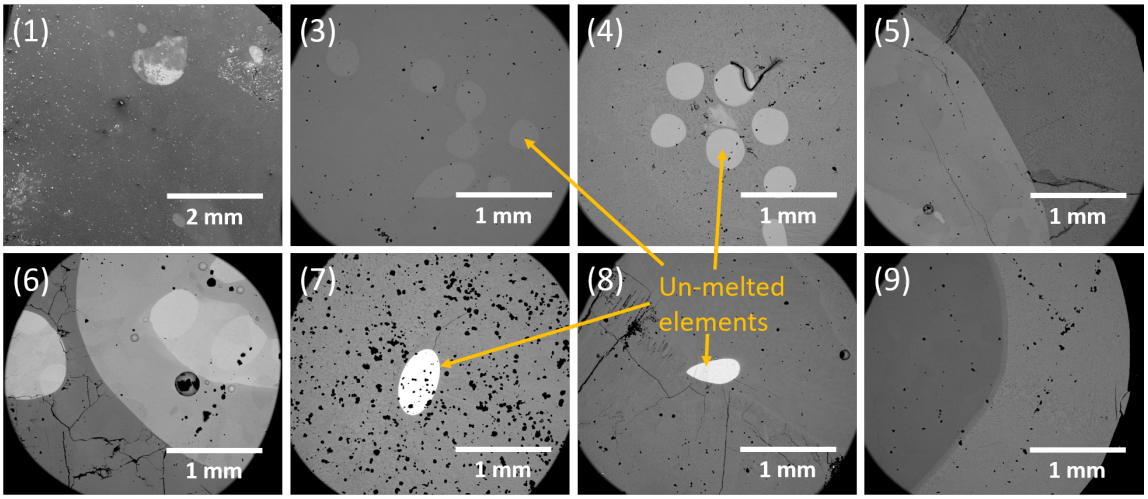

Figure 4.2: *Low magnification images of the arc-melted HEAs resulting from the alloy design model, where each alloy is labelled with their corresponding number. Alloy 2 is not included as it was too brittle for metallographic preparation. All images are Secondary Electron images (SE) except for the image of alloy 1 which is a backscattered electron (BSE) image.*

alloys categorised as green are shown in Figure 4.3 and the higher magnification SEM images are shown in Figure 4.4. In all cases the identification of such phases as un-melted elements has been confirmed by EDS point scans. However this does not mean that these peaks identified as un-melted particles could not also be superimposed on peaks of other phases with a similar lattice parameter. In some of these green alloys, it is probable that these peaks are caused by a second phase.

In Alloy 1 there is a small peak identified for Mo but otherwise there is a BCC structure, as shown in Figure 4.3. The SEM in Figure 4.4 shows 2 apparent phases, where one appears to be in large grains and the other on the grain boundaries (GBs). EDS point scans show these phases to be of similar composition of approx 30 at% Ti - 39 at% V - 27 at% Nb - 7 at% Mo and 29 at% Ti - 42 at% V - 22 at% Nb - 6 at% Mo respectively. It is likely these phases have very similar lattice parameters and that is causing the peak superposition evident at $2\theta \approx 72.5^o$ and $2\theta \approx 41^o$ on the XRD pattern. It is also worth noting the discrepancy between the nominal composition of Nb and V in this alloy and the two phases present, as there is much lower concentration of both elements than expected in both phases. It is suspected this is due to in-homogeneity caused by the arc melting process, meaning there could be other areas of the arc-melted button which will have an unexpectedly high concentration or un-alloyed zones of Nb and V.

In Alloy 3 there are two distinct BCC phases with compositions of 26 at% Ti - 17 at% Zr - 49 at% Nb - 9 at% Mo and 41 at% Ti - 42 at% Zr - 17 at% Nb. The boundary between the two phases can be seen in the BSE image in Figure 4.4 (3) by a small change in contrast across

the image where the phase containing no Mo and depleted in Nb is at the top of the image and the phase high in Mo and Nb is at the bottom. Referring to the XRD, the two BCC phases have a very similar lattice parameter so have partially superimposed, the other phase present is Nb which can also be seen as the un-alloyed spherical shaped lighter coloured areas in Figure 4.2 (3). The interesting formation of the distinct boundary between the two phases is probably a symptom of the arc-melting process used to manufacture this sample. Therefore, since this alloy is intended to be manufactured via PBF-LB/M, the interaction between these two phases could be beneficial for alloy strength if the phases were dispersed in finer microstructural features. Hence this alloy shows potential that the refined microstructure commonly seen in AM could result in an interesting DP-HEA.

In Alloy 5, XRD shows a prominent BCC phase with a similar lattice parameter to pure Mo and 3 other less abundant BCC phases. These 3 minor phases could likely be MoTa, Cr_3Mo and a Cr-based phase. SEM shows two distinct areas of differing composition separated by a boundary across the sample, similar to that seen in Alloy 3. One of those areas, shown in Figure 4.4, has a composition of 25 at% Cr - 51 at% Nb - 14 at% Mo - 10 at% Ta and has a dendritic microstructure. The second area contains 67 at% Mo - 33 at% Ta, indicating that these elements may have reached saturation in the other phase or they could be immiscible. This area contains the main Mo BCC phase and the MoTa, whereas the Cr_3Mo and Cr-based phase are found in the dendritic area of the sample. It is possible that some of the BCC phases in this alloy are ordered phases, therefore could be brittle or compromise material properties. However the peaks corresponding to these phases are of low enough intensity in the XRD and the EDS was not able to resolve these phases exactly, hence they can only be identified as BCC but no more. Similarly to Alloy 3, this alloy also shows promise to be an interesting DP-HEA when manufactured by PBF-LB/M, if the microstructure can be refined and optimised.

Finally, Alloy 7 also has a dendritic microstructure as seen in Figure 4.4. There are slightly differing compositions in the dendritic and interdendritic regions which were 33 at% Ti - 38 at% V - 24 at% Cr - 6 at% Mo and 49 at% Ti - 27 at% V - 22 at% Cr - 2 at% Mo respectively. The interdendritic region also shows the formation of what appear to be needle-like precipitates of an unknown phase, which are likely present in such a small proportion they cannot be resolved by XRD or by EDS as they are less than 1 μm in width. There is a small peak which is attributed to un-melted Mo which can be seen in Figure 4.2, however this peak could also be associated with these precipitates, though further investigation would be needed to confirm this.

4.5.1.2 Amber Alloys

Alloys are categorised as "amber" if some peaks in the XRD pattern were unidentified despite there being a definite BCC phase present. XRD patterns for alloys 4, 6 and 9 which were categorised

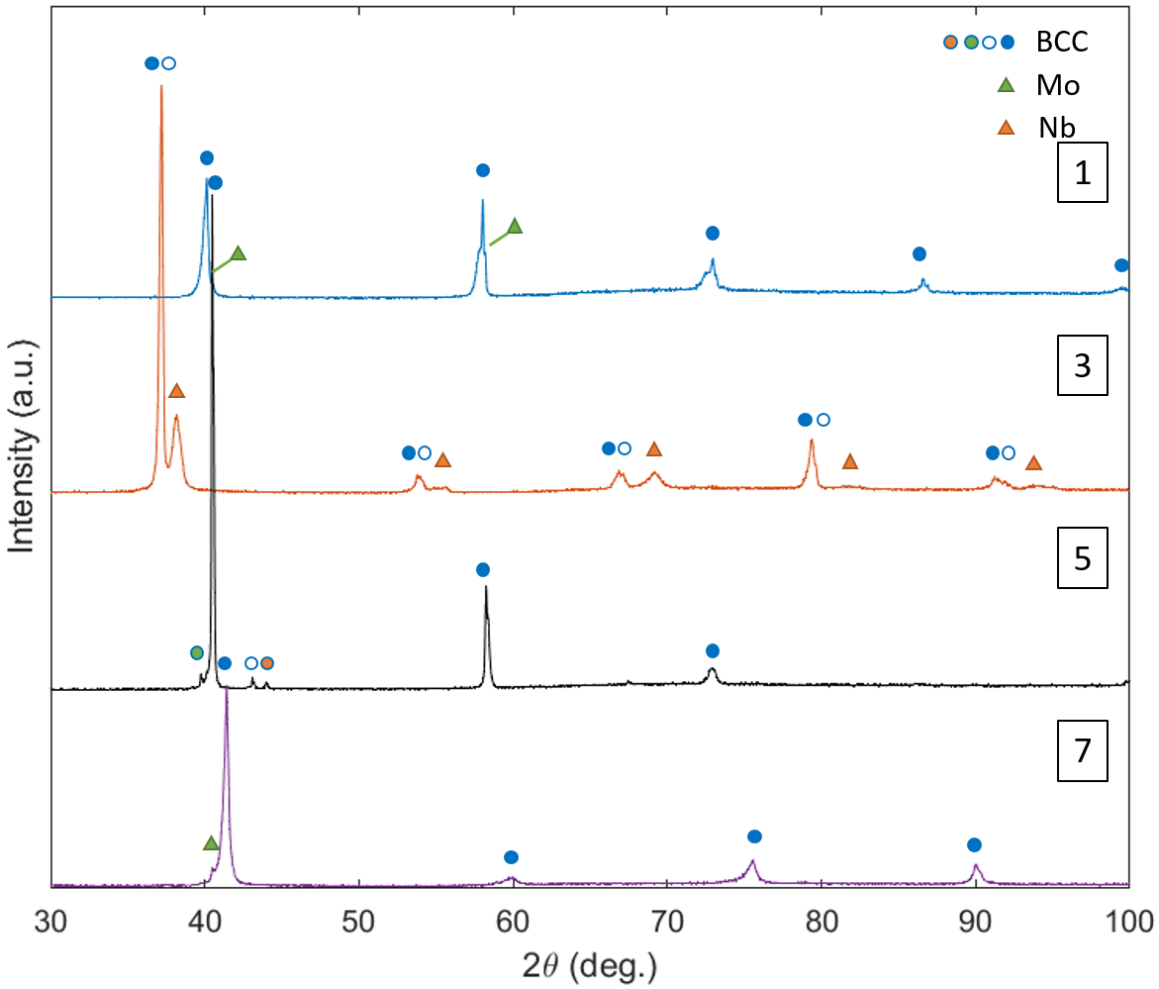

Figure 4.3: *XRD patterns of the alloys categorised as green. The peaks likely caused by un-melted particles from the arc-melting process are labelled in red. BCC peaks are labelled and lattice parameters for alloys 1, 3, 5 and 7 were* $a \approx 3.19$ *Å,* $a \approx 3.41$ *Å,* $a \approx 3.17$ *Å and* $a \approx 3.09$ *Å respectively.*

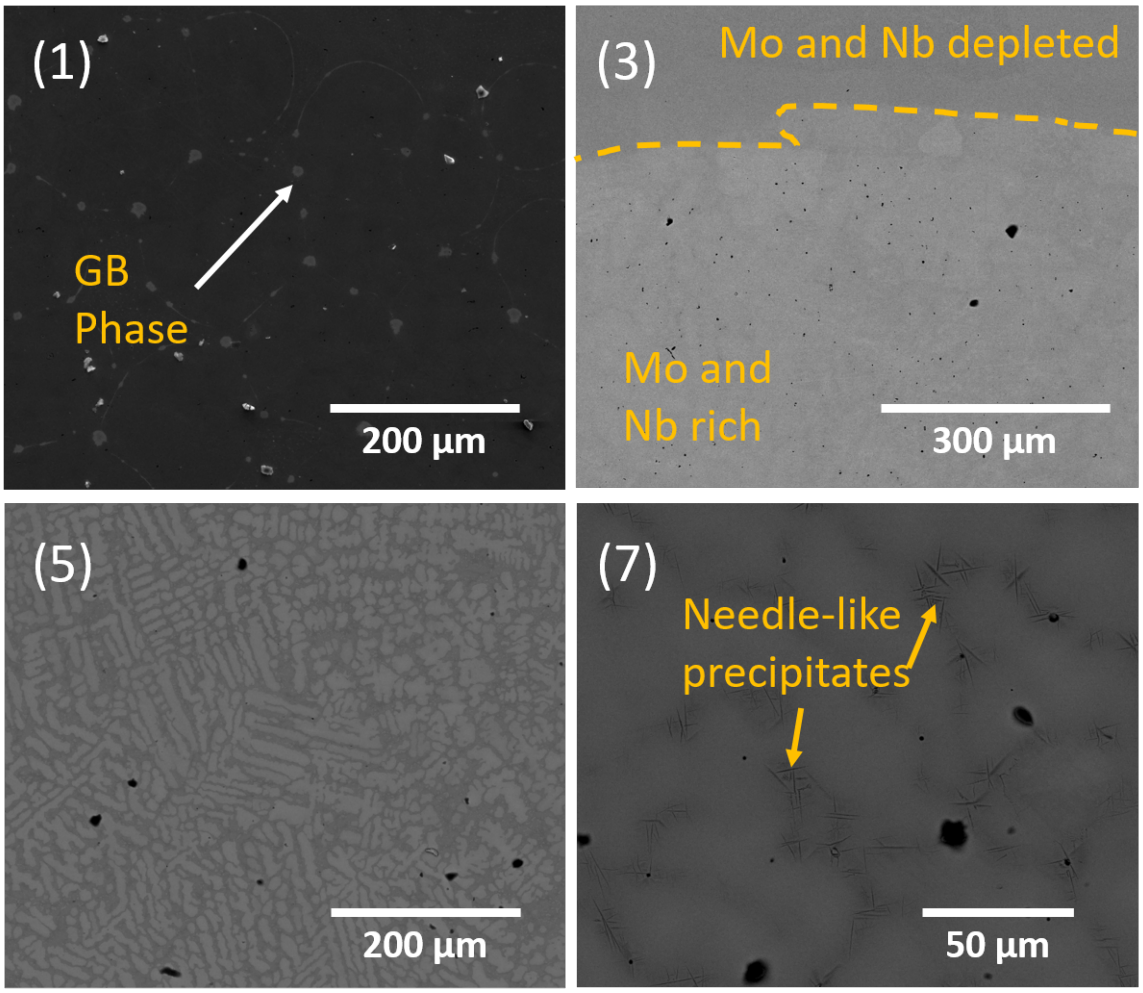

Figure 4.4: *BSE images of the alloys categorised as green. The image for each alloy is labelled with the number of that alloy. The dashed line on (3) represents the interface between phases.*

amber are shown in Figure 4.5 and the SEM images are shown in Figure 4.6.

Alloy 4 shows multiple BCC phases on the XRD pattern. Un-alloyed Ta has been identified and this is seen on the SEM image in Figure 4.2. Figure 4.6 shows a 2 phase dendritic structure in the majority of the sample with the compositions 8 at% Zr - 28 at% Nb - 36 at% Mo - 28 at% Ta and 42 at% Zr - 25 at% Nb - 22 at% Mo - 11 at% Ta. The main phase is rich in Ta but depleted in Zr and the other GB phase is rich in Zr but depleted in Ta. Not all peaks have been identified in this alloy, as there are two small peaks between $2\theta = 36^o$ and $2\theta = 40^o$, therefore this alloy was categorised as amber. It is likely those peaks could be from impurities from the polishing process or less abundant BCC phases which have superimposed to form the broadening in the other peaks in the XRD pattern. If this was the case then this alloy would be put into the green category, but due to the uncertainties, the possible re-classification this alloy would require further work.

Alloy 6 did not result in a fully alloyed microstructure as seen in Figure 4.2. There are multiple areas of differing compositions as well as some large un-melted Ta particles. Indicating some elements like Ta and Cr in this alloy were immiscible so alloying is unlikely in near equilibrium conditions. This separation and immiscibility of Cr and Ta was also observed in alloy 5. The XRD in Figure 4.5 indicates 4 different BCC phases, matching with the multiple areas of differing composition shown in Figure 4.2.

Lastly, Alloy 9 contains two completely different elements in the addition of Al and Cu which were not present in any of the other alloys. The XRD pattern for this alloy had a much lower peak intensity than the other alloys and as a result, peaks are harder to separate from noise. There appears to be three distinct phases in this alloy as shown in Figure 4.6 (9) where there are two distinct areas of differing composition and a dendritic transition zone between them. The darker phase contains 9 at% Al - 36 at% Ti - 55 at% V with no Cu detected. The transition phase contains 2 at% Al - 25 at% Ti - 66 at% V - 6 at% Cu so is depleted in Al and Cu. The lighter phase on image (9) contains 2 at%Al - 44 at% Ti - 6 at% V - 47 at% Cu so is enriched in Cu and depleted in V and Al. It is clear from these results that Cu is almost totally immiscible with Al and V in these systems, and so forming a stable solid solution phase from these elements is very unlikely. The XRD shows two BCC phases, a $AlCu_2Ti$-based FCC phase and a tetragonal γCuTi - based B2 phase, with the latter 2 phases most likely corresponding to the light coloured phase in Figure 4.6 and the BCC peaks corresponding to the other two zones.

4.5.2 Alloy Relationship to Empirical Parameters

Figure 4.7 shows examples of four different empirical parameters plotted for green, amber and red alloys: VEC, ΔS_{mix}, ΔH_{mix} and δ are used in this case. These graphs are included to illustrate whether whether the classification obtained from the experimental results correlates at

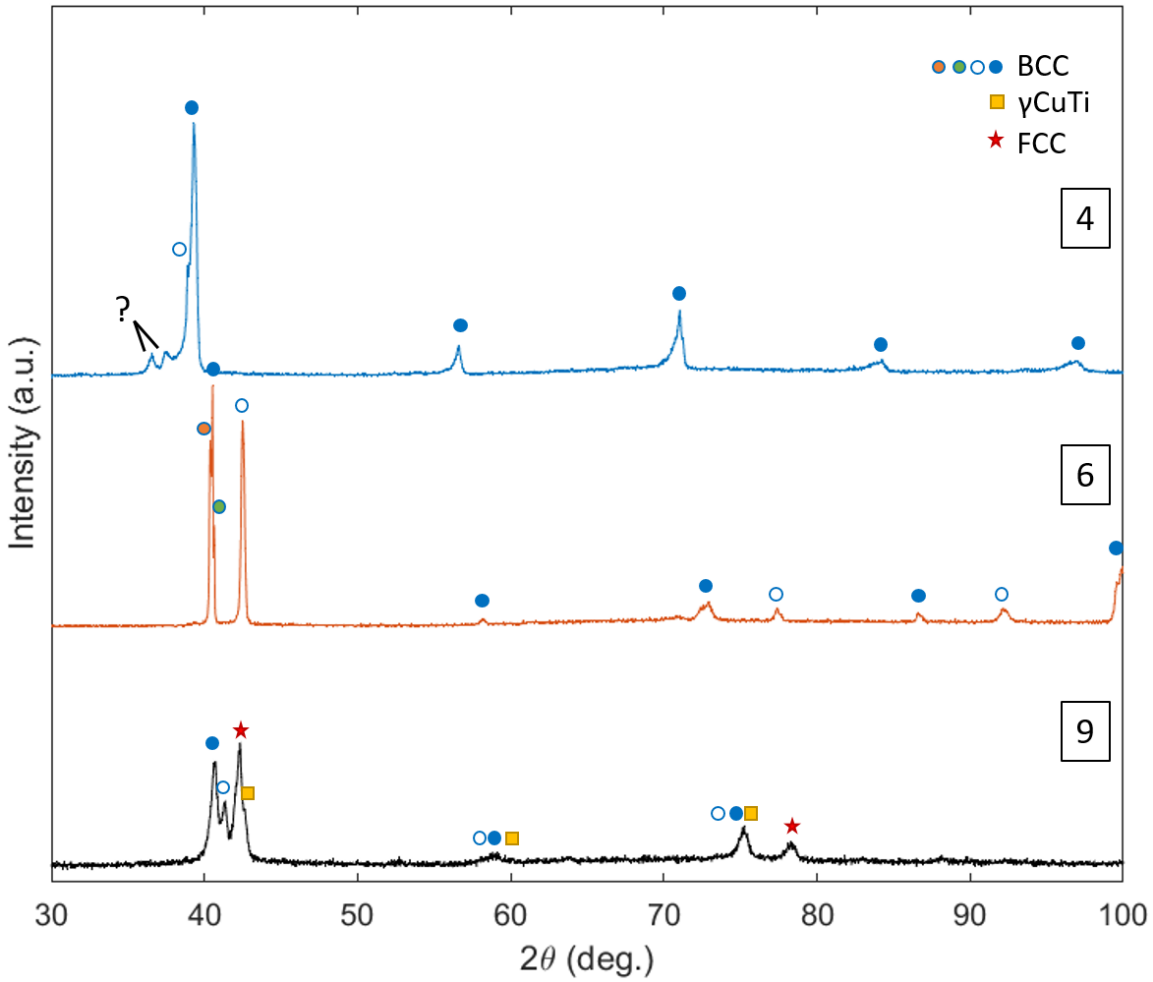

Figure 4.5: *XRD patterns of the alloys categorised as amber. The two unresolved peaks in the pattern for alloy 4 are marked with a '?'.*

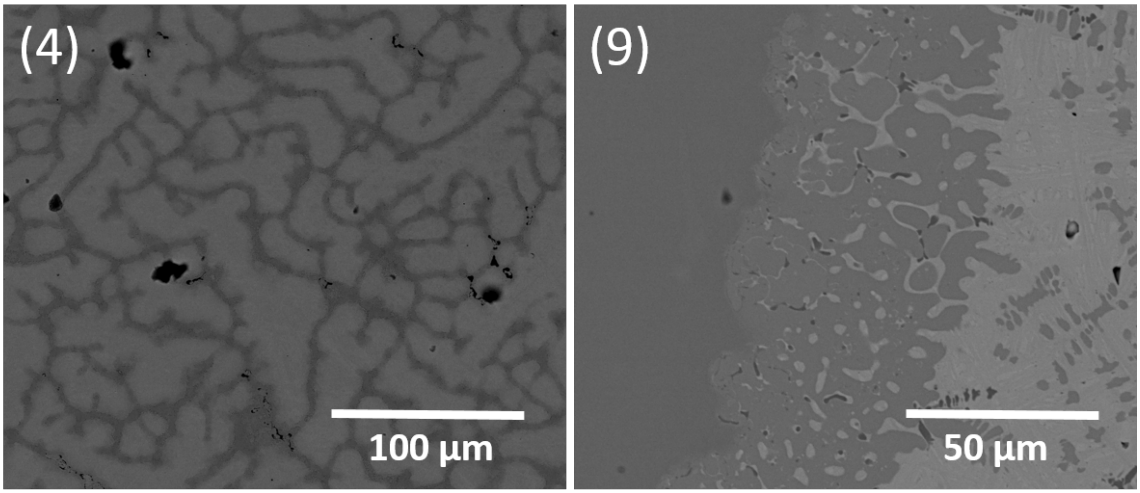

Figure 4.6: *BSE images showing the microstructure of alloys 4 and 9 categorised as amber. The image for each alloy is labelled with the number of that alloy.*

all with empirical parameters, aside from being within the limits set in the model. It is clear from these graphs that there is little to no correlation with these parameters and the microstructure seen for each alloy. Indicating there are other factors at play that are not encapsulated by the parameters used in this model, which is to be expected as the model uses some assumptions and simplifications in order to be feasible for use.

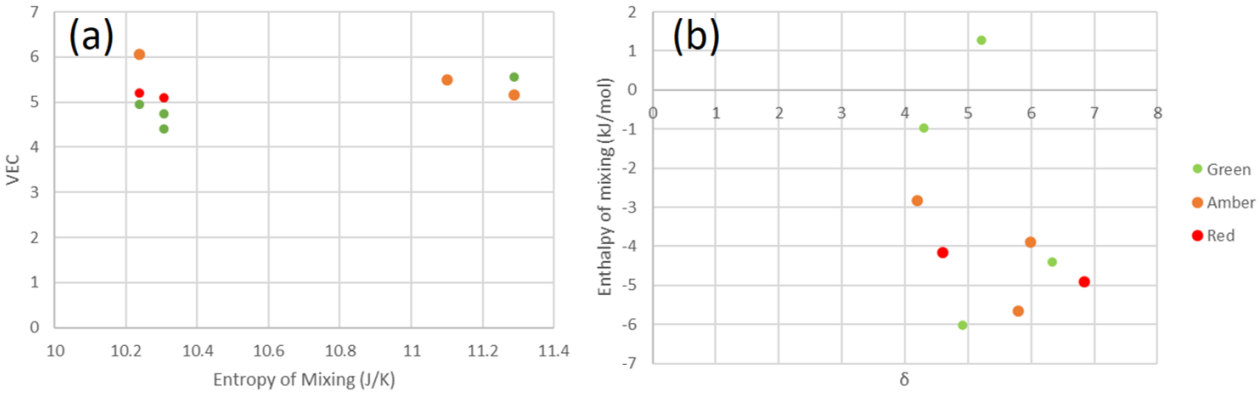

Figure 4.7: *Graphs showing values of (a) VEC and ΔS_{mix} and (b) δ and ΔH_{mix} for alloys classed green, amber or red.*

4.6 Conclusions

In this work a HEA design methodology has been introduced which uses empirical parameters to filter alloys for multi-phase solid solution formation. Different ranking configurations were used and the top three ranked alloys from each configuration were manufactured by arc-melting. The alloys which were ranked highly contained Ti, V and Mo as very prominent elements due to their high melting points.

The alloys which were manufactured successfully were then analysed by XRD and SEM/EDS in order to be able to group them into the different categories of green (BCC phases only present), amber (main BCC phases present, some peaks unidentified or of other structures or immiscible elements) or red (processing issues). Two alloys were categorised as red immediately, one because of multiple brittle fracture when being sectioned and the other because of excessive vaporisation of Mn in the arc-melting process. Four alloys were firmly categorised as green out of the seven that were manufactured successfully with the other three alloys categorised as amber. It was assessed that Alloy 4 could potentially be moved into the green category, following some further investigation. This gives the model a success rate of 44% of all alloys which were attempted to be made and 57% out of the alloys that were analysed.

The effect of empirical parameters used on the alloy category was then finally assessed and was shown to have little or no effect. Reiterating that this model uses simplified parameters to

encompass very complicated thermodynamic processes, therefore a low success rate and no correlation with empirical parameters is to be expected. In the future, it would be useful to incorporate CALPHAD methods into the modelling process to model element by element interactions, or a ML method to refine the predictions. An effort should also be made to involve modelling of what effect cooling rate could have on the alloy, as in AM cooling rates are much higher than those seen in arc-melting.

Author Contributions

Conceptualisation, L.F., I.T. and R.G.; methodology, L.F., I.T. and R.G.; investigation, L.F.; original draft preparation, L.F.; review and editing, R.G.; supervision, I.T. and R.G. funding acquisition, R.G. and I.T. All authors have read and agreed to the published version of the manuscript.

Funding

This work was supported by Science Foundation Ireland 18/EPSRC-CDT/3584, the Engineering and Physical Sciences Research Council EP/S022635/1 and the Manufacture using Advanced Powder Processes (MAPP) EPSRC Future Manufacturing Hub EP/P006566/1.

Conflicts of Interest

The authors declare no conflict of interest.

Chapter 5

Crack Susceptibility of Alloys for Additive Manufacturing

5.1 Author Contributions

Lucy Farquhar - Conceptualisation, methodology, sample manufacture via arc-melting, completion of melt tracks, sample characterisation and analysis, data analysis from samples and models, original draft preparation.
Hugh Banes - Support with methodology for finite element analysis, operation of finite element model, partial writing of Section 5.4.2 about use of the finite element model, writing - review and editing
Lova Chechik - Support with conceptualisation, design of the moving heat source model used, writing - review and editing
Alexander Goodall - Support completing the melt tracks, writing - review and editing
Felix Hofmann - Completed the TGS measurements to obtain elastic and thermal properties
Abdallah Reza - Completed the TGS measurements to obtain elastic and thermal properties
Prashant Jadhav - Design of the finite element model
Iain Todd - Conceptualisation, support with methodology, supervision
Russell Goodall - Conceptualisation, support with methodology, supervision, writing - review and editing

5.2 Background

There has been a lot of previous work looking into the onset of cracking and the associated mechanisms, largely in welding, but more recently in additive manufacturing (AM) specifically [99]. For solidification cracking there are a few indicators available, with varying degrees of accuracy, that can be used to predict cracking in any alloy, so long as solidification curves can be obtained, using CALculation of PHAse Diagrams (CALPHAD) for example [124, 125]. These solidification cracking indicators have even been used successfully with RHEAs [148]. However, when considering solid-state cracking, there are no established global indicators which can be used in a similar way for any alloy system. Solid-state cracking is usually predicted based on prior knowledge of precipitate or secondary phase formation in the given alloy system and the elements which form, inhibit or stabilise these phases. On top of that, changes in the precipitate morphology, coherency, position and grain boundary characteristics such as misorientation and tortuosity can dictate whether crack resistance is increased or decreased [104].

This chapter proposes a new empirical solid-state cracking indicator for AM based on first principles of correlating average bond energy with ductility. This solid-state cracking parameter is then used to predict the susceptibility of 4 new refractory high entropy alloys (RHEAs), resulting from the alloy design in Chapter 4 and the 3 known high entropy alloys (HEAs), which were studied in Chapter 3. Melt tracks were completed on all these HEAs to assess their suitability for laser powder bed fusion (PBF-LB/M), one of which - the $Mo_5Nb_{35}Ti_{30}V_{30}$ RHEA is further studied and developed in Chapter 6 and 7. The data from these melt tracks, forms a small database of alloys with varying crack types, providing a validation tool for the crack indicator proposed. The indicator is then also validated using 12 alloys from the literature, including very AM processable alloys such as 316L stainless steel and notoriously crack susceptible alloys such as CM247LC.

N.B. Further detail on the mathematical derivation involved in Section 5.4.1, Equation 5.3 is included in Appendix B.

Paper: Crack Susceptibility of Alloys for Additive Manufacturing

Lucy Farquhar[1], Hugh Banes[1], Lova Chechik[2], Alexander Goodall[1], Felix Hofmann[3], Abdallah Reza[3], Prashant Jadhav[1], Iain Todd[1], Russell Goodall[1]

1 – Department of Materials Science and Engineering, University of Sheffield, Sheffield S1 3JD, UK

2 – Institute of Photonic Technologies, Friedrich-Alexander-Universität Erlangen-Nürnberg, Konrad-Zuse-Str. 3/5, Erlangen, 91052, Germany

3 – Department of Engineering Science, University of Oxford, Parks Rd, Oxford, OX1 3PJ, UK

Correspondence: laufarquhar1@sheffield.ac.uk

Abstract

Additive manufacturing (AM) offers the capability to manufacture optimised parts with complex geometries. Many new alloys are being developed specifically for manufacture via AM, including alloys with completely new compositions, in previously unknown systems, such as high entropy alloys (HEAs). However due to the non-equilibrium rapid cooling conditions during AM it is difficult to predict alloy behaviour without prior knowledge of its microstructure or tendency to form secondary phases. In this work a new universal indicator for solid-state cracking is proposed, using easily-accessed parameters; elastic modulus, coefficient of thermal expansion (CTE) and a temperature change predicted by a moving heat source model. An ABAQUS subroutine was used to study the effect of CTE on the development of residual stress, finding that increased CTE could hinder the formation of high tensile stress areas and promote higher compressive stresses. A map of crack susceptibility is then formed using the new solid-state cracking indicator (SSCI) and the Kou solidification cracking indicator (SCI), mapping 7 HEAs and 12 conventional alloys. Melt tracks are also completed on arc-melted samples of the HEAs to validate the cracking behaviour predicted. The SSCI successfully predicts solid-state cracking behaviour in 17 out of the 19 alloys. Use of the SSCI as an alloy screening tool, ensuring alloys with a high predicted crack susceptibility can be identified before any AM trials, could massively reduce the time and cost of high-throughput alloy testing.

Keywords

Additive Manufacturing, Laser Powder Bed Fusion, Cracking Mechanisms, High Entropy Alloys, Solid-State Cracking, Alloy Design

5.3 Introduction

Additive manufacturing (AM) is a novel technology which builds parts layer-by-layer, allowing design freedom, which in turn permits the optimisation of part geometry and weight. In laser powder bed fusion (PBF-LB/M), powder feedstock is melted in layers in a powder bed by a laser heat source to form a consolidated solid part [249]. Material is exposed to sequential laser passes and multiple reheating cycles due to the deposition of subsequent layers and the melting of surrounding material. This is a non-equilibrium process, resulting in high cooling rates, far exceeding those seen in conventional manufacturing methods such as casting [250].

However, many high strength materials are optimised to be manufactured by conventional methods,in ways which produce microstructures with strengthening phases. For example, many nickel alloys are not conducive to being manufactured via AM due to the formation of phases such as γ' phase, which often cause cracking [251]. All alloys can suffer from common AM defects such as lack of fusion porosity and keyholes, if the PBF-LB/M parameters result in low and high volume energy density (VED) conditions respectively, but cracking during AM processing can be more challenging to overcome by changing process conditions [99]. Where it is observed, cracking can occur by many different mechanisms and for alloys that are prone to this, there is a very small or non-existent processing window where dense, un-cracked parts can be manufactured.

Due to this, more alloys are being designed with manufacturability by AM at the forefront of their design process, such as ABD-850AM and ABD-900AM [105]. Other work is attempting to assess printability of current alloys [110, 114, 116], defined by Wei as "the ability of an alloy feedstock, to be converted to a component with acceptable metallurgical, mechanical and functional requirements for a specific application" [117]. Many of these recent studies focus on porosity-based AM defects or distortion rather than cracking. The cracking indicators used for AM commonly come from welding literature, or even from casting, despite the large differences between the conditions experienced by the material in these processes [103]. Many of these cracking indicators have even been used to assess the printability of new refractory high entropy alloys (HEAs) with some success, especially for solidification cracking [148].

There are 3 main crack types commonly reported in AM processes, which are as follows:

- Solidification cracking
- Liquation cracking

- Solid-state cracking (eg. ductility dip cracking (DDC), strain age cracking (SAC) and post weld heat treatment cracking (PWHTC))

Solidification cracks form in the latter stages of solidification, due to shrinkage at grain boundaries (GBs) and interdendritic regions, where a liquid film has yet to solidify [99,103]. Hence these cracks have a dendritic jagged morphology, where each side of the crack does not match up. The main factors influencing this type of crack formation are the solidification temperature range, the cooling rate and the final inter-facial liquid morphology and composition. Consequently, there are 2 types of predictive models: metallurgical models using solidification ranges, curves and phase diagrams and thermo-mechanical models assessing the strain associated with the shrinkage [122, 123]. Examples of metallurgical models include the crack susceptibility coefficient from Clyne and Davies [125] and the Kou cracking indicator, which focuses on the final solidification stages [124]. The model proposed by Rappaz, Drezet, and Gremaud is an example of a thermo-mechanical indicator, where the critical strain rate is calculated [128].

Liquation cracking occurs in the partially melted zone (PMZ) during reheating to a temperature below the melting point of the main phase but above the melting point of the GB precipitates, causing localised melting [104]. The tensile stress developed in the AM process can result in GB tearing and separating the liquid films. In nickel alloys liquation can occur due to the γ/γ' eutectic [105], whereas more generally it occurs in alloys with wider freezing ranges, a higher fraction of liquid during freezing or with increasing GB segregation. Liquation cracking is often predicted based on composition and prior knowledge of eutectic phases which could form. Hence it is difficult to predict in alloys with unknown microstructures or phase diagrams.

Solid-state cracking can be divided into several categories. DDC occurs due a sharp reduction in ductility for many materials including austenitic stainless steels, nickel alloys and titanium alloys between 0.5 to 0.9 of the solidus temperature T_s [103]. It primarily occurs along GBs, so the presence of high angle GBs and GB precipitates can be contributing factors, however it can occur intragranularly if brittle phases are distributed within grains. It can be predicted based on the solidification range and strain induced, but in nickel alloys for example, DDC susceptibility is often predicted based on γ' or carbide content [131]. Similarly, SAC occurs specifically in the heat-affected zone of high γ' nickel alloys when aged. γ' precipitates coarsen before dislocation annihilation causing locally brittle material to be under highly stressed conditions, leading to cracking. Hence it also can be predicted by assessing γ' content. PWHTC occurs primarily in post-process heat treatments to reduce residual stresses and temper martensitic structures [103]. It is common in low-alloy steels due to the formation of carbides or in other alloys with strong precipitation reactions in heat treatment. All solid-state crack types have a very similar morphology on observation, often straight with matching sides, and are all fundamentally caused by the combination of high residual stresses and brittle phase formation. They are also all predicted

based on prior knowledge of precipitation in a given alloy system and consequently a universal indicator for formation of these types of crack has not been reported. Due to their similarity, in this work, these crack types will be considered together and will be referred to collectively as solid-state cracking.

This work proposes a new AM-specific solid-state cracking indicator which is validated using the results of melt tracks on seven HEAs, along with reported crack behaviour of conventional alloys from the literature. Along with the Kou solidification cracking indicator, a processing map is formed showing the overall predicted crack susceptibility due to solid-state and solidification cracking [124]. Using this approach as an alloy screening tool, prior to AM trials, could massively reduce the time and cost associated with testing alloys by ensuring alloys with a high predicted crack susceptibility (and therefore low printability) can be identified and removed. This approach considers only the susceptibility to solidification and solid-state cracking (the latter using the new metric); liquation cracking is excluded as it is difficult to predict without knowledge of eutectic or low melting point phase formation.

5.4 Theory and Modelling

5.4.1 Assessing Contributing Factors to Solid-State Cracking Susceptibility

Elastic constants such as the shear modulus μ, bulk modulus B and their ratio, μ/B, have been shown previously to influence material brittleness [252]. It is also known that a lower bond energy, U_0, correlates to increased toughness and ductility [253,254]. This is a useful relationship to employ in order to approximate the toughness of a material and therefore susceptibility to solid-state cracking. Figure 5.1 shows the effect of differing initial equilibrium U_0 values for Lennard-Jones potential curves on the elastic modulus E and the coefficient of thermal expansion (CTE), α_{CTE}. The Lennard-Jones potential curve for metals has been defined previously as [255]:

$$U(r) = U_0 \left[\left(\frac{r_0}{r} \right)^{12} - 2 \left(\frac{r_0}{r} \right)^{6} \right] \tag{5.1}$$

where r_0 is the distance at which the bond energy between two atoms is at a minimum, for alloys this is the average bond length and r is the bond length at a given bond energy. Assuming small deformations, the elastic modulus is calculated from the Lennard-Jones potential by [256]:

$$E = \left(\frac{\partial^2 U}{\partial r^2} \right)_{r=r_0} \tag{5.2}$$

Combining Equation 5.1 and Equation 5.2 indicates that $E \propto U_0$. Based on work by Kittel, a

measure for a material CTE is proposed using the energy required to displace a pair of atoms from their equilibrium mean separation [257]. Using a Boltzmann distribution to calculate average displacement and assuming that the anharmonic terms contributing to oscillations are small compared to the effect of temperature increase, CTE can be approximated as:

$$\alpha_{CTE} = \frac{7k_B}{48U_0} \tag{5.3}$$

where k_B is the Boltzmann constant. This indicates that in this case $\alpha_{CTE} \propto 1/U_0$. Detailed derivation of this relationship is included in Appendix B. Kirchoff's law also dictates that for a constant pressure system the change in specific enthalpy ΔH is:

$$\Delta H = c_P \Delta T \tag{5.4}$$

where c_p is specific heat capacity at constant pressure and ΔT is the change in temperature. Therefore as $\Delta H = \Delta U/mol$ and U_0 is negative, for a given amount of moles of material any increase in temperature reduces the magnitude of the bond energy $U = U_0 + \Delta U$, as depicted in Figure 5.1, thereby increasing material toughness. Therefore combining the above conclusions we can infer that:

$$U_0 \propto \frac{E}{\alpha_{CTE}\Delta T} \tag{5.5}$$

Meaning, with limited material knowledge and assessment time that this relationship can be used in screening of candidate alloys as a proxy for material toughness and crack susceptibility.

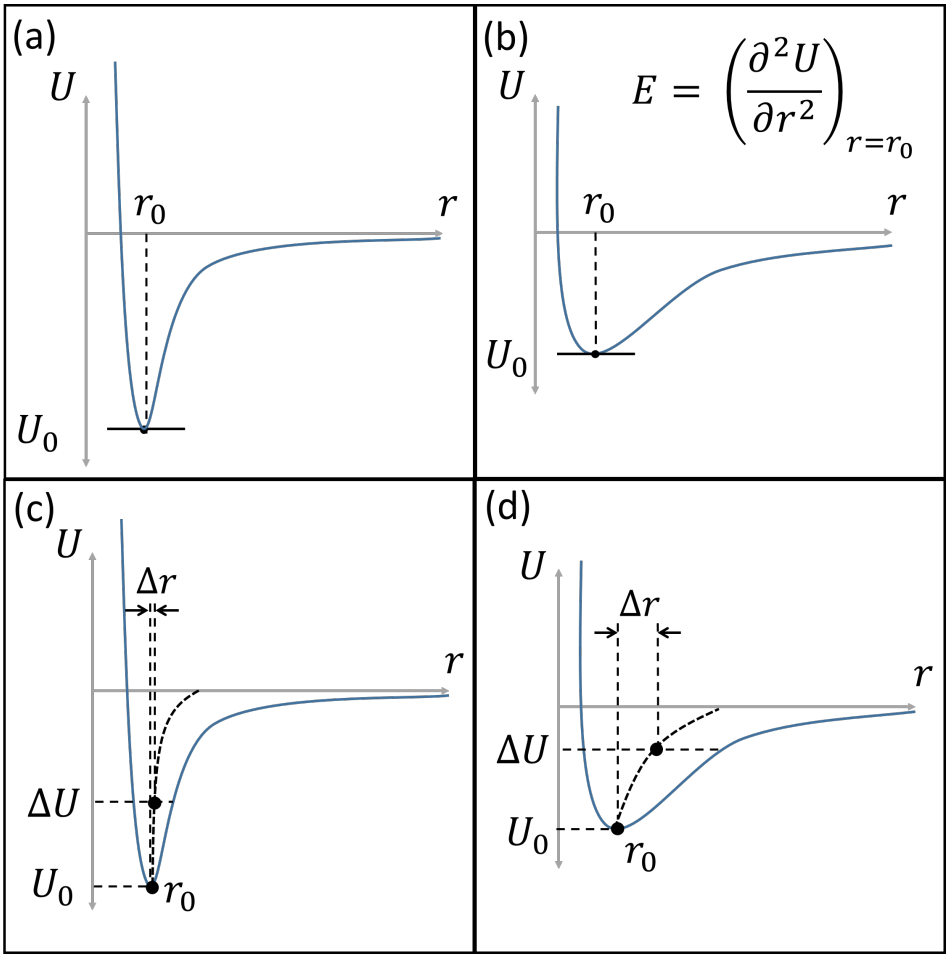

Figure 5.1: *(a) and (b) show the impact of high and low bond energy respectively on the elastic modulus, where higher bond energy results in higher instantaneous curvature at the equilibrium bond length r_0, therefore a higher elastic modulus. (c) and (d) show the impact of high and low bond energy on the CTE. At higher bond energy there is increased symmetry in the energy potential well, resulting in reduced deviation Δr from the r_0 value, and hence a reduced CTE.*

When studying comparable parameters with respect to PBF-LB/M, it has been indicated that the absolute value of the maximum longitudinal residual stress decreases as heat input increases, and doubling the heat input could reduce the residual stress by approximately 20% [118]. However, increasing the heat input leads to an increased melt pool volume and larger melt pools shrink more overall on solidification, increasing the thermal strain. This leads to distortion, as indicated by the thermal strain parameter, resulting in dimensional inaccuracy. Of course, the distortion due to the heat input does not just arise from dimensional changes associated with the liquid-solid phase change. The CTE itself describes the dimensional changes in the solid state due to fluctuations in temperature. Thermal strain and thermal stress have been found to be inversely proportional with changing heat input [118]. Much like the relationship between CTE, bond energy

and therefore ductility indicated by Equation 5.3, it is likely a relationship could exist between the stress field, corresponding tensile and compressive stresses and the CTE, as higher CTE would directly translate to an increase in thermal strain.

Confirming this hypothesis experimentally is difficult, as the CTE cannot be changed without changing materials (and so altering other parameters), and thus the effect of CTE changes cannot be monitored in isolation. Therefore, a modelling approach has been taken in order to investigate the relationship between CTE and residual stress distribution following thermal input as applied in PBF-LB/M.

5.4.2 Modelling the Effect of CTE on Residual Stress

Many models have previously been proposed to simulate the complex interactions in AM processes at different length scales and the resulting part quality and microstructure [258–260]. In this work, a finite element formulation for the heat source (representative of that in PBF-LB/M) has been used, where a single layer is melted on top of a substrate. The double-ellipsoid Goldak formulation [261] is the most commonly used formulation for heat source modelling in AM [262]. However such a formulation requires an extensive set of parameters and calibration data, which were unavailable for this work. Thus, a simple tri-variate Gaussian formulation was used while calibrating the heat source to available literature data:

$$Q_v(x,y,z) = \frac{2 * A * P}{\sigma_x \sigma_y \sigma_z (\pi)^{3/2}} * exp\left(-\frac{1}{2}\left(\frac{(x-\mu_x)^2}{\sigma_x^2} + \frac{(y-\mu_y)^2}{\sigma_y^2} + \frac{(z-\mu_z)^2}{\sigma_z^2}\right)\right) \tag{5.6}$$

Where (μ_x, μ_y, μ_z) is the position of the centre of the heat source, (x, y, z) are co-ordinates on the powder bed, A is the Absorption Efficiency of the powder bed and P is the laser power. The beam spread along the x, y, z axes are represented by the parameters $\sigma_x, \sigma_y, \sigma_z$, which are dependent on the Beam Radius (R_b) and the Penetration Depth (D_p). To reduce computational cost, simulation of the deposition process was carried out over a representative volume element (RVE). This model was then implemented as a user subroutine for ABAQUS (2021 version), allowing for prediction of both thermal history and stress evolution using ABAQUS' thermomechanical modelling process. The model uses parameters determined through calibration and validation from experimental data sources [263]. These parameters are detailed in Table 1, alongside the standard settings used for the simulations.

Table 5.1: *Model parameters and general settings for the different simulations performed.*

Constant	Value	Units
Absorption Efficiency	0.45	N/A
Beam Radius, R_b	75	µm
Penetration Depth, L_H	150	µm
Laser Power, P	195	W
Laser Speed, v	1.2	m/s
Hatch Spacing, h	30	µm
RVE Size	(1234,750)	(x,y) µm

In this model, Ti-6Al-4V was used as a base material, using the material properties employed by Lu *et al.* [264]. Two types of models were created, a single track scan, where the laser followed a single straight line (a single pass) along the centre of the RVE, and a multi-hatch scan, where the laser hatched back and forth across the entire RVE. The laser power and speed were the same as the single track case, and the hatch spacing was kept constant. The CTE values at all temperatures were varied to from 10% to 300% of the original value of Ti-6Al-4V for the single track model and from 10% to 200% for the multi-hatch models.

The resulting longitudinal, transverse and through-thickness residual stress distributions after full cooling are shown in Figure 5.2 and the maximum compressive and tensile stresses present each direction are plotted in Figure 5.3. These distributions and maximum stresses were taken halfway through the part, perpendicular to the laser scan direction x. Overall for both single and multi-track models, the residual stresses increase as the CTE increases. However, in the case of the single track and increasing CTE values, the tensile residual stress either plateaus or decreases, while the compressive stress plateaus or increases. There is no significant change in the through thickness stress with increasing CTE for either model. In the multi-hatch model, longitudinal tensile stress accumulates towards the the early hatches (on the right), indicating the reheating cycles act to reduce the tensile longitudinal stress. So over a larger part, the increased number of subsequent hatches would reduce this effect, leaving a tensile stress at the edge, which could lead to surface cracking, but without any crack propagation in the bulk due to increased compressive stress. The transverse tensile stress accumulates near the top of the layer, which would be remelted and likely reduced by the compressive stress field around melt pools of subsequent layers, as indicated by other work [118]. However in this investigation the addition of further layers was deemed to be too computationally expensive, so this could not be confirmed. These results suggest alloys with larger CTEs could initiate larger compressive stresses and reduced tensile stresses, thereby generating conditions which could inhibit solid-state crack

propagation.

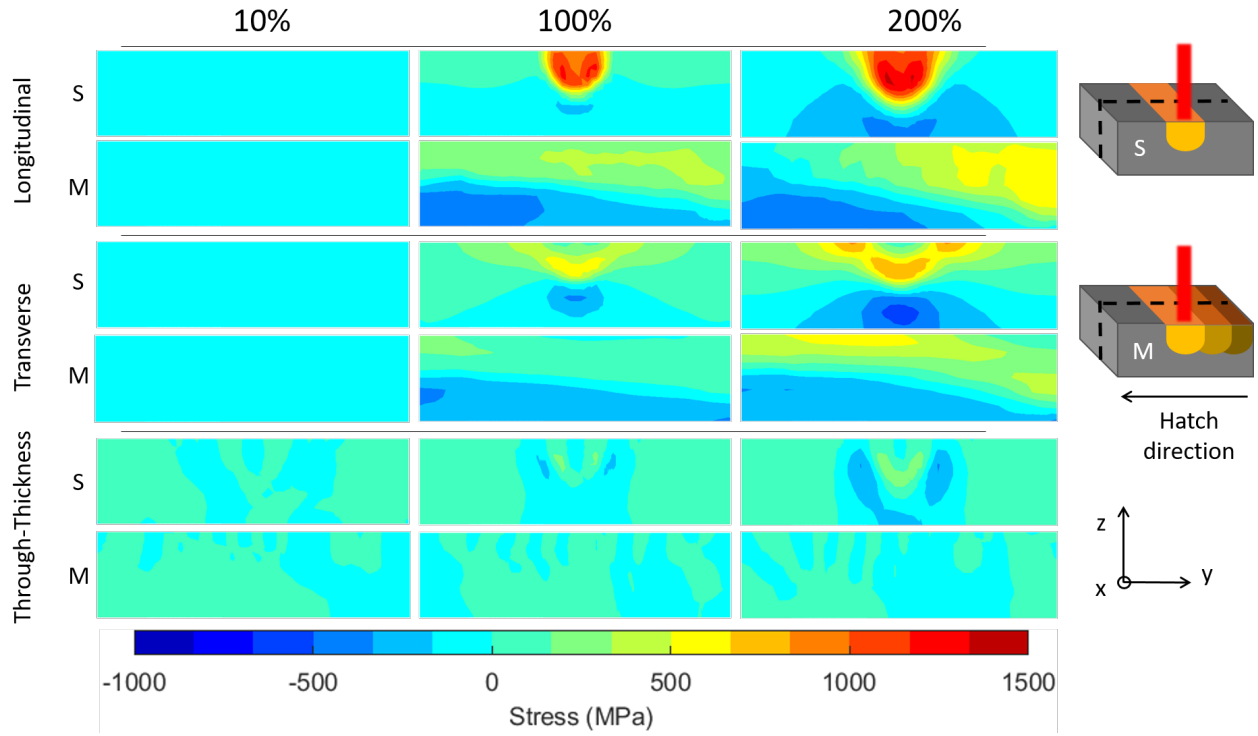

Figure 5.2: *The stress fields for CTE values of 10%, 100% and 200% of the base CTE values for Ti-6Al-4V in the longitudinal (x), transverse (y) and through-thickness directions (z) from the central z-y plane (as indicated in the schematics as a dashed line). Tensile stresses are indicated by positive values. Single hatch simulations are denoted by an S. Multi-hatch simulations are denoted by a M, and the hatch direction is from left to right.*

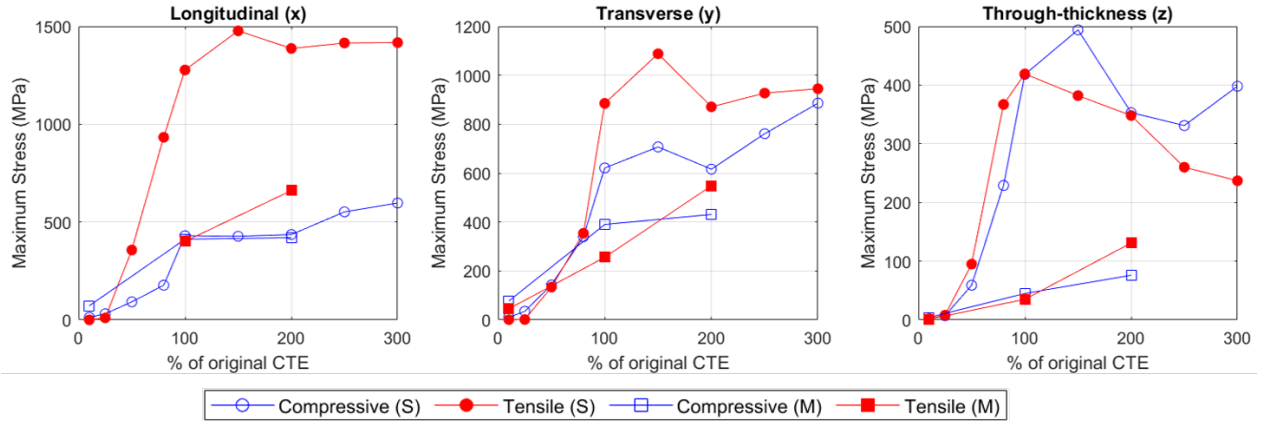

Figure 5.3: *The maximum compressive and tensile stresses for (S) single hatch and (M) multi-hatch models in the longitudinal (x), transverse (y) and through-thickness directions(y).*

5.5 Materials and Methods

5.5.1 Formulation of the Solid-State Cracking Indicator (SSCI)

Combining the beneficial factors reducing bond energy and therefore increasing ductility already outlined, an alloy with a low elastic modulus and a high CTE along with a high heat input during the AM process, results in the formulation of the SSCI is as follows:

$$SSCI = \frac{E}{\alpha_{CTE}\Delta T} \tag{5.7}$$

where E and α_{CTE} are defined at room temperature and ΔT is the average change in temperature in the melt pool.

An approximation to the average change in melt pool temperature ΔT in the PBF-LB/M process was obtained using a Rosenthal-based moving heat source model, adapted for a Gaussian beam profile [265, 266]. This exact model previously proved successful in the study of melt pool shape in laser directed energy deposition of Inconel 718 and uses the beam size of the AconityMINI PBF-LB/M system [267].

$$\Delta T = T - T_0 = \frac{2A\alpha P}{\kappa\pi^{3/2}} \int_{-\infty}^{\infty} \frac{exp\left[-2\frac{(x+vt)^2+y^2}{D_b^2+8\alpha t} - \frac{z^2}{4\alpha t}\right]}{\sqrt{\alpha t}(D_b^2+8\alpha t)} dt \tag{5.8}$$

where T is final temperature, T_0 is initial temperature, κ is thermal conductivity, α is thermal diffusivity, ρ is density, x is displacement relative to laser position, t is time and D_b is the Gaussian laser beam diameter. The coordinate system is defined in the same way as in Equation 5.6.

Currently assessments of an alloy's solid-state cracking susceptibility rely heavily on knowing the phase formation and hence mechanical and thermo-physical properties. In novel alloy development, these properties are not known and unless time is taken to measure them, they can only be approximated. Approximating material properties such as thermal conductivity or elastic modulus can be done with some accuracy for systems where there are similar, well-characterised alloys. But when developing new alloys, such as HEAs, the mixture of elements and compositions are often uncommon, so a simple rule of mixtures (ROM) based calculation may be the only option available; this can of course lead to significant errors where there is the production of new phases within the alloy. To validate the predictions made with relevant systems, the cracking susceptibility of seven HEAs are assessed alongside conventional alloys. The compositions of the HEAs and the corresponding nomenclature are shown in Table 5.2. Three of the CoCrFeNi-based HEAs are known in the literature and have been manufactured by PBF-LB/M before, while the other four are new refractory HEAs, which were designed using empirical parameters for solid-solution phase formation such as atomic size mismatch δ, for use in high temperature applications [42].

Table 5.2: *HEAs compositions used to validate the crack susceptibility analysis.*

Alloy Name	Nominal Composition (at%)	Ref
CoCrFeNi	$Co_{25}Cr_{25}Fe_{25}Ni_{25}$	[6, 248]
CoCrCuFeNi	$Co_{20}Cr_{20}Cu_{20}Fe_{20}Ni_{20}$	[248]
CoCrFeNiTi	$Co_{20}Cr_{20}Fe_{20}Ni_{20}Ti_{20}$	[248]
MoNbTiV	$Mo_5Nb_{35}Ti_{30}V_{30}$	new
MoNbTiZr	$Mo_5Nb_{30}Ti_{35}Zr_{30}$	new
MoNbTaZr	$Mo_{35}Nb_{25}Ta_{20}Zr_{20}$	new
CrMoNbTa	$Cr_{20}Mo_{35}Nb_{25}Ta_{20}$	new

Transient Grating Spectroscopy (TGS) can be used to measure thermal diffusivity and elastic modulus, using a sample with similar size and preparation requirements as for characterisation using scanning electron microscopy (SEM) [268]. This technique is used in this work to rapidly obtain accurate thermal diffusivity measurements for input to the moving heat source model and measurements of E for the SSCI. Table 5.3 shows the parameters included in the moving heat source and SSCI models and how they were found, including direct measurements, calculation of phases diagrams (CALPHAD) predictions and ROM calculations.

The power and velocity values input to the model and therefore the melt tracks are calculated by examining the energy needed to raise the temperature of the powder bed of the material to the melting temperature of the material $H_{min} = \rho c_p(T_m - T_0)$, as developed by Thomas *et al.* [110]. For most materials the energy input required for consolidated parts $E_0 = Ap/2hvl$ is 2-8 times larger than H_{min}, where h is hatch spacing and l is layer thickness. Therefore, as detailed in section 5.5.3, central power and velocity parameters satisfying $4E_0$ were chosen and using a central composite statistical design, other values varied between $2E_0 - 8E_0$.

Table 5.3: *Parameters included in the moving heat source model and SSCI and how they were found. For alloys marked as 'Eq', parameters were found using the relationship* $\alpha = \kappa/\rho c_p$.

Alloy	**Thermal Diffusivity** α **(**$\times 10^{-6} m^2/s$**)**	**Thermal Conductivity** κ (W/mK)	**Specific Heat Capacity** c_p (J/kgK)	**Melting (Solidus) Temperature** T_m (°C)	**Elastic Modulus** E (GPa)	**CTE** α_{CTE} ($\times 10^{-6} K^{-1}$)
CoCrFeNi	3.10 (TGS)	11.31 (Eq)	444 [6]	1414 [6]	147.89 (TGS)	16.5 [6]
CoCrCuFeNi	3.70 (TGS)	13.2 (Eq)	426 (ROM with [6])	1348 (ROM with [6])	125.54 (TGS)	16.5 (ROM with [6])
CoCrFeNiTi	1.96 (TGS)	6.7 (Eq)	454 (ROM with [6])	1463 (ROM with [6])	221.09 (TGS)	15.0 (ROM with [6])
MoNbTiV	4.65 (TGS)	12.6 (Eq)	407 (ROM)	1810 (CALPHAD)	115.03 (TGS)	7.90 (ROM)
MoNbTiZr	3.66 (TGS)	8.6 (Eq)	354 (ROM)	1712 (CALPHAD)	81.394 (TGS)	7.50 (ROM)
MoNbTaZr	15.0 (TGS)	36.4 (Eq)	235 (ROM)	2124 (CALPHAD)	209.69 (TGS)	5.91 (ROM)
CrMoNbTa	19.5 (TGS)	53.6 (Eq)	262 (ROM)	2186 (CALPHAD)	257.87 (TGS)	11.8 (ROM)
CoCrFeMnNi	3.47 (Eq)	13.7 [269]	490 [270]	1334 [271]	203 [25]	15.0 [25]
Inconel 718	2.81 (Eq)	9.9 [272]	435 [119]	1260 [250]	208	16.2 [273]
CM247LC	2.82 (Eq)	10.3 [274]	428 [274]	1282 [273]	235 [275]	18.2 [276]
ABD-850AM	2.16 (Eq)	10.7 (Alloyed)	587 (Alloyed)	1383 [105]	220	11.5 (Alloyed)
ABD-900AM	1.99 (Eq)	11.0 (Alloyed)	660 (Alloyed)	1305 (Alloyed)	220	11.4 (Alloyed)
Haynes282	2.88 (Haynes International)	10.3 (Haynes International)	432 (Eq)	1300 (Haynes International)	217	12.1 (Haynes International)
Waspaloy	2.60 (Eq)	11.0 (Haynes International)	520 (Haynes International)	1330 (Haynes International)	211	12.2 (Haynes International)
CMSX-4	2.50 [277]	8.7 (Eq)	400 [277]	1346 [278]	211 [279]	13.0 [280]
316L Stainless	3.90	14 .0 [281]	464 [281]	135 [281]	193	17.2 [282]
17-4PH	5.13 (Eq)	18.3 (Sandmeyer Steel)	460 (Sandmeyer Steel)	1404 (Sandmeyer Steel)	196	11.3 (Sandmeyer Steel)
Ti-6V-4Al	2.87	6.25 [281]	526 (ASM Inc.)	1605 [281]	114	8.6 (ASM Inc.)
Cp-Ti	6.95	16.4 (ASM Inc.)	523 (ASM Inc.)	1668	103.4	8.6 [283]

5.5.2 Solidification Cracking Susceptibility

Alongside the SSCI, a solidification cracking assessment is used to obtain a more comprehensive view of alloy cracking behaviour (noting that liquation cracking, relatively rarely observed in AM processing of alloys of this type, is not explicitly considered in this approach). The simplest assessment of solidification cracking is made by examining the size of the freezing range, however this does not provide specific information on the behaviour at the end of solidification, which is thought to be the most important stage in the formation of solidification cracks [103]. Therefore, the solidification cracking susceptibility of each alloy was calculated using the Kou Solidification Cracking Indicator (SCI) [124]:

$$SCI = \left| \frac{dT}{d(f_s^{1/2})} \right| \tag{5.9}$$

where f_s is the solid fraction and T is the temperature describing a Scheil solidification curve. Based on analysis of Al alloys, this value was first somewhat arbitrarily calculated for the range $0.87 < f_s < 0.94$; however other work has used different values which better fit the alloys concerned in each case [124]. Here, 3 ranges of f_s are tested and the most accurate to the cracking behaviour observed is taken forward to form an alloy processability map. The ranges are $0.8 < f_s < 0.9$, $0.9 < f_s < 0.99$ and $0.8 < f_s < 0.99$, the same used by Tang *et al.* [105].

Scheil solidification curves for each alloy were obtained using the CALPHAD software Thermocalc 2022b. The TCHEA6, TCNI11, TTTI3 and TCFE8 databases were used for the HEAs, nickel alloys, titanium alloys and steels respectively. Both the classic Scheil and Scheil with solute trapping models were used, where the solute trapping approach assumes the solidification interface velocity is faster than the diffusive speed of solutes in the liquid, which are therefore trapped as solid is formed. The velocities to achieve such effects are reported to be of the order of 10^{-2} m/s for localised diffusion and $\approx$ 1 m/s for complete solute trapping [284]. Therefore in theory, this model should better approximate conditions in PBF-LB/M, which uses laser scanning speeds close to 1 m/s, assuming the solidification interface velocity is comparable to the laser speed. Here, the models are compared for each set of alloys and their efficacy in accurately predicting solidification cracking is assessed. The SCI and SSCI then create a crack susceptibility map showing the cracking behaviour of the alloys and interaction between the crack types.

5.5.3 Melt Track Trials

To validate the predicted cracking behaviours, 3.5g samples of the 7 HEAs in Table 5.2 were arc melted using an Edmund Bühler Compact Arc Melter MAM-1. A mixture of wire and lump forms of each element were used with a minimum purity of 99.5%, supplied by Goodfellow UK. To ensure homogeneity, samples were flipped and re-melted 10 times. The arc-melted buttons were then sectioned, mounted in bakelite and ground to a P1200 finish, to ensure a plane surface, while not achieving an optically reflective surface.

XRD patterns for the HEAs can be seen in Figure 5.4. The CoCrFeNi-based alloys have a face centred cubic (FCC) matrix or main phase. CoCrFeNi has a single FCC phase, the CoCrCuFeNi alloy has a Cu-lean main FCC phase along with a Cu-rich FCC phase. CoCrFeNiTi has two main FCC phases, one which is Cr-rich and Ti-lean and one which is Ti-rich and Cr-lean, a hexagonal close packed Laves phase and a Ti_5Ni_8 rhombohedral intermetallic. There is also one small peak at a 2θ value of 41°, which has been attributed to another FCC phase but could correspond to

a phase of a different structure, as the intensity is too low to resolve other associated peaks. The refractory HEAs all have a single phase body centred cubic (BCC) structure, except for the MoNbTaZr alloy which has a two phase BCC structure.

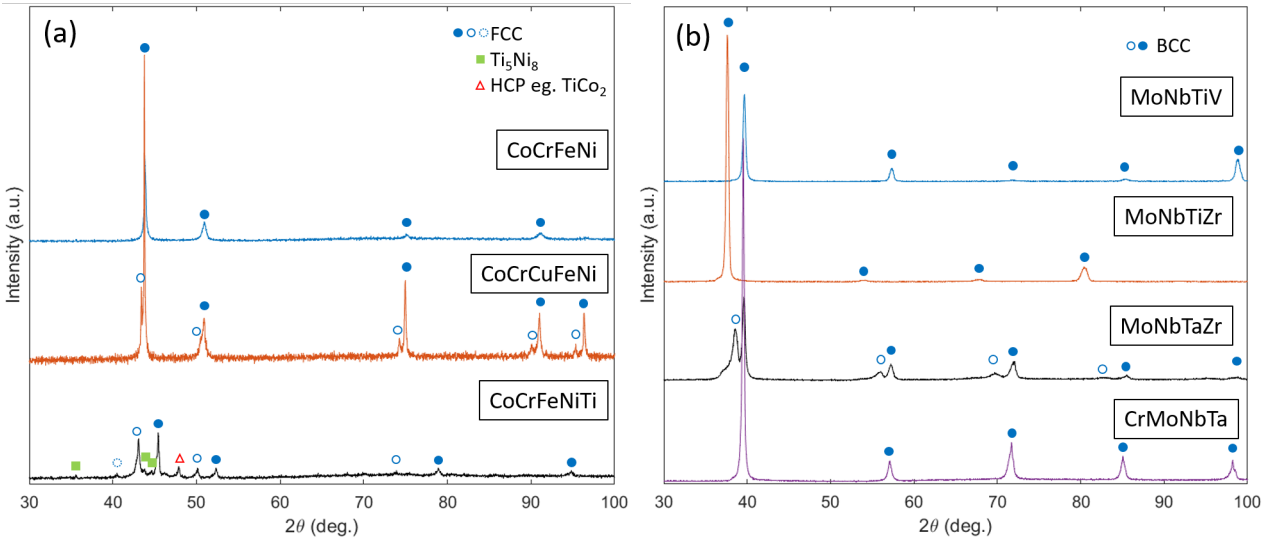

Figure 5.4: *(a) XRD of the CoCrFeNi based alloys. The CoCrFeNi and CoCrCuFeNi alloy have primary FCC phase with a lattice parameter of a = 3.580 Å, with a secondary FCC phase in the CoCrCuFeNi alloy a = 3.608 Å(with peaks at . The CoCrFeNiTi alloy has three primary FCC phases with lattice parameters of a = 3.464 Å, a = 3.628 Å and a = 3.140 Å as well as a HCP Laves phase and a Ti_5Ni_8 rhombohedral intermetallic phase. (b) XRD of the refractory HEAs. The MoNbTiV, MoNbTiZr and CrMoNbTa all have a BCC single phase with lattice parameters of a = 3.211 Å, a = 3.380 Å and a = 3.222 Å respectively. The MoNbTaZr alloy has 2 BCC phases with lattice parameters of a = 3.255 Å and a = 3.294 Å.*

Laser melt tracks were completed using an Aconity MINI PBF-LB/M system, configured to disable the powder spreading and build plate movement. The software Minitab version 20.4 was used to create a central composite statistical design of experiment where laser power and velocity were varied between 80 W - 190 W and 150 mm/s - 1643 mm/s respectively. This resulted in 9 parameter sets with differing line energies, which are the same as those used for the input to the moving heat source model for the SSCI, where the central parameters correspond to $4E_0$. A diagram of the melt tracks is shown in Figure 5.5, indicating how each parameter set included 6 hatches with a constant hatch spacing of 60 µm, to mimic the reheating cycles of subsequent hatches in PBF-LB/M. There was a spacing of 200 µm between parameter sets and each hatch is 7 mm long.

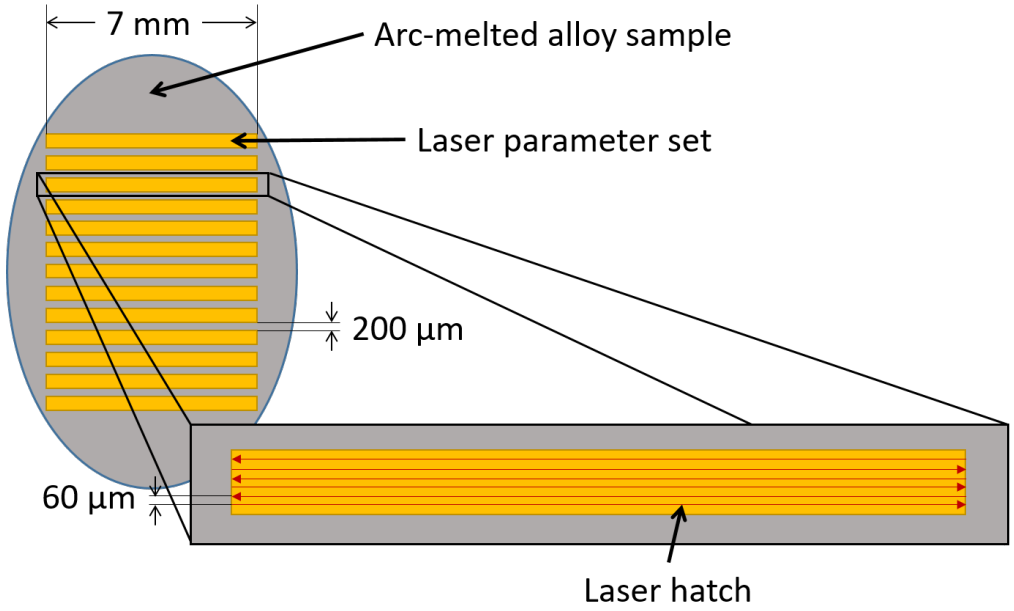

Figure 5.5: *Diagram of the melt track trials, where yellow boxes represent parameter sets and within each set there are 6 laser hatches indicated by the red arrows.*

After melting, samples were imaged from above using a Olympus BX 51 optical microscope (Clemex Vision Pro). They were then sectioned down the centre, perpendicular to the laser scanning direction, prepared using standard metallographic preparation techniques and imaged using a Inspect F50 SEM. The cracking behaviour of each alloy was visually assessed using both the planar view optical images and the SEM images of the cross sections, showing the melt pools and changes in microstructure generated by the laser. Using previously described crack characteristics, cracks were categorised into two crack types: solidification cracking and solid-state cracking. The cracking behaviour of some well known nickel and titanium alloys, steels and the CoCrFeMnNi HEA were also categorised using results from the literature. The resulting categories are shown in Section 5.6.1.

5.6 Results and Discussion

5.6.1 Melt Track Trials

Examples of solidification and solid state cracking can be seen in the CoCrFeNi-based alloys; as illustrated in Figure 5.6, CoCrCuFeNi shows solidification cracking at low line energies, as well as solid-state cracking at higher line energies, where the line energy is P/V. CoCrFeNiTi shows extensive solid-state cracking at all line energies, to the extent that it caused spallation of the surface on sectioning. CoCrFeNi showed no cracking, agreeing closely with the results when these

alloys were manufactured previously by PBF-LB/M [248].

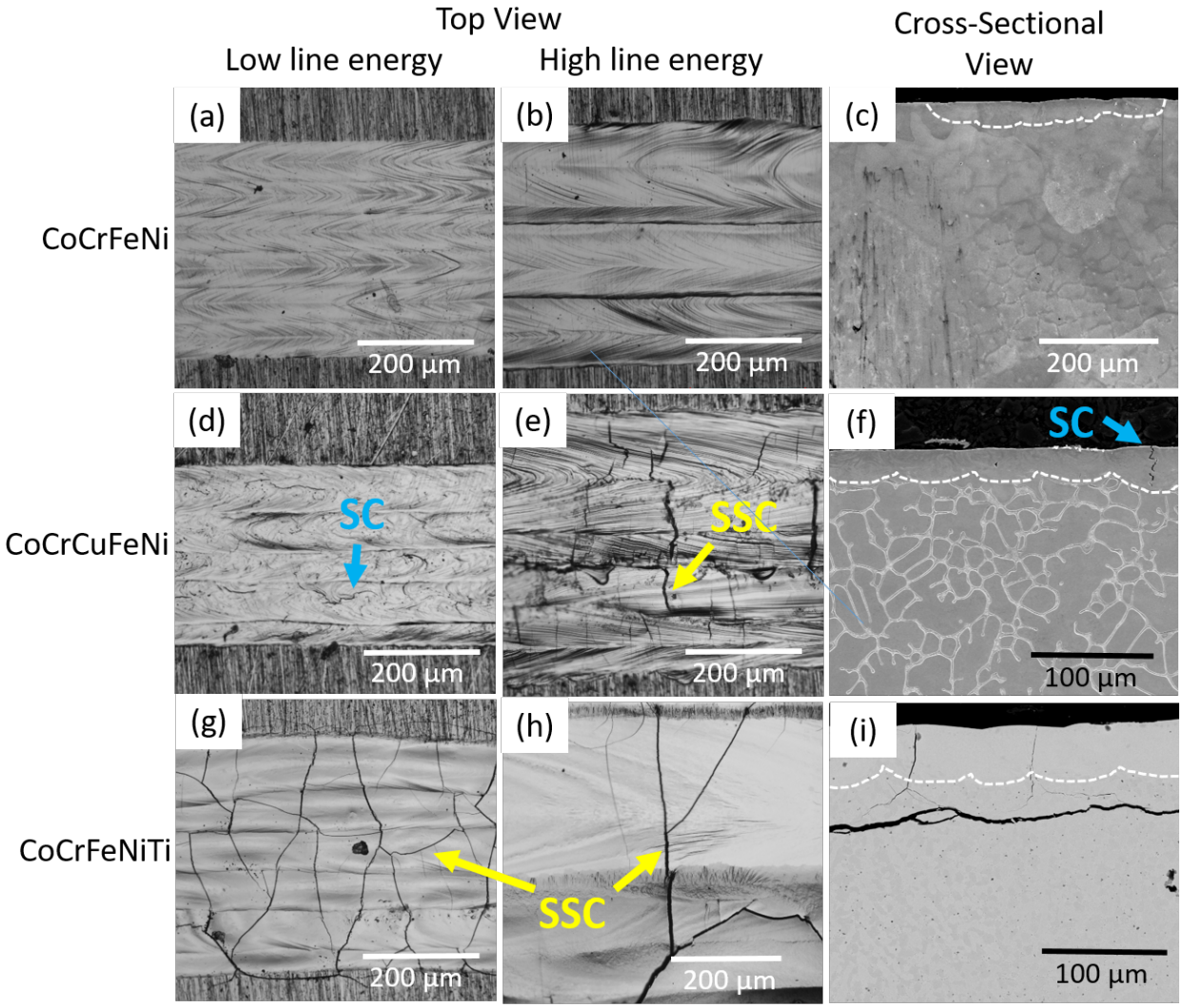

Figure 5.6: *Melt tracks on the CoCrFeNi-based alloys. The top views are optical micrographs and the cross sectional views of low energy parameters are shown as SEM micrographs taken in back-scattered electron mode. The arrows labelled SC and SSC refer to solidification cracking and solid-state cracking respectively and the white dashed lines indicate the melt pools. Solidification cracking is identified by the dendritic edges of cracks and is most often found parallel to the longitudinal direction (in the direction of laser travel). Solid state cracks are usually straight and angular with matching edges and are often found perpendicular to the longitudinal direction, due to the high longitudinal tensile residual stress remaining after laser melting in many cases.*

Both the MoNbTiV and MoNbTiZr showed no cracking and the melt tracks homogenised what was, in the previous as-cast form, a dendritic microstructure. Both MoNbTaZr and CrMoNbTa exhibit solid-state cracking behaviour for all parameters, with some less extensive solidification

cracking. A summary of the types of cracking commonly seen in each alloy, including alloys from the literature, is shown in Table 5.4.

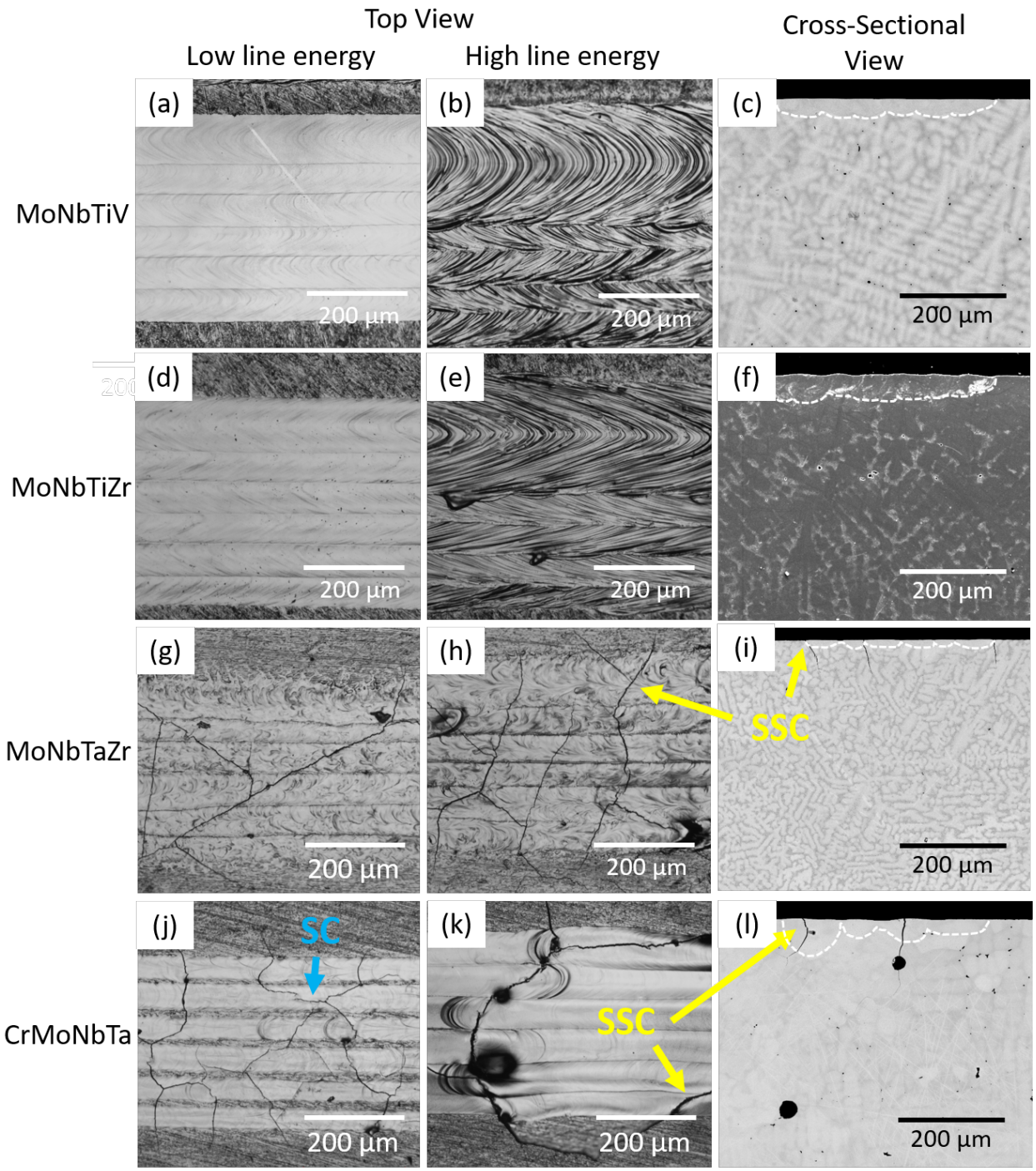

Figure 5.7: *Melt tracks on the refractory HEAs. The top views are optical micrographs and the cross sectional views of low energy parameters are shown as SEM micrographs taken in back-scattered electron mode. The arrows labelled SC and SSC refer to solidification cracking and solid-state cracking respectively and the white dashed lines indicate the melt pools. Solidification cracking is identified by the dendritic edges of cracks and is most often found parallel to the longitudinal direction (in the direction of laser travel). Solid state cracks are usually straight and angular with matching edges and are often found perpendicular to the longitudinal direction, due to the high longitudinal tensile residual stress remaining after laser melting in many cases.*

Table 5.4: *Summary of cracking types commonly reported in each alloy. MT refers to the melt track trials completed in this work.*

Alloy	Cracking Type		Source
	Solidification	Solid-State	
CoCrFeNi	N	N	MT/PBF-LB/M [6, 248]
CoCrCuFeNi	Y	Y	MT/PBF-LB/M [248]
CoCrFeNiTi	N	Y	MT/PBF-LB/M [248]
MoNbTiV	N	N	MT
MoNbTiZr	N	N	MT
MoNbTaZr	Y	Y	MT
CrMoNbTa	Y	Y	MT
CoCrFeMnNi	N	N	PBF-LB/M [176, 179, 285]
In718	N	N	PBF-LB/M [286, 287]
CM247LC	Y	Y	PBF-LB/M [105, 288–290]
ABD-850AM	N	N	PBF-LB/M [105]
ABD-900AM	N	N	PBF-LB/M [105, 291]
Haynes 282	N	N	PBF-LB/M [292, 293]
Waspaloy	Y	N	PBF-LB/M [294, 295]
CMSX-4	Y	Y	PBF-LB/M [296]
SS316L	N	N	PBF-LB/M [50, 297, 298]
17-4PH	N	Y	PBF-LB/M [299–301]
Ti-6V-4Al	N	N	PBF-LB/M [302, 303]
Cp-Ti	N	N	PBF-LB/M [304]

5.6.2 Determination of SCI parameters

According to Table 5.4, CoCrCuFeNi, MoNbTaZr, CrMoNbTa, CM247LC, Waspaloy and CMSX-4 all are prone to solidification cracking when manufactured by PBF-LB/M. Figure 5.8 shows the SCI calculated using the Scheil curves generated by the classic Scheil and solute trapping Scheil models in Thermocalc. They also both show the SCI calculated for 3 different ranges of fraction of solid f_s. For the classic Scheil SCI values, using the range $0.8 < f_s < 0.9$ accurately predicts solidification cracking in CoCrCuFeNi, MoNbTaZr and CrMoNbTa, but does not predict it in the crack prone nickel alloys. Similarly, the range $0.9 < f_s < 0.99$ also has an appreciable number of inaccuracies, including not predicting the cracking of CoCrCuFeNi, even though the cracking of CM247LC and Waspaloy are predicted. More successfully, all the solidification cracking prone HEAs have a high SCI when calculated using $0.8 < f_s < 0.99$, as does Waspaloy. However 316L

and 17-4PH steels also have high SCI using these f_s values.

In the solute trapping Scheil modelling, for all ranges of f_s, MoNbTaZr and CrMoNbTa have high SCI values but CoCrCuFeNi wrongly has extremely low SCI values. Additionally, for ranges $0.9 < f_s < 0.99$ and $0.8 < f_s < 0.99$ Waspaloy correctly has a high SCI, however so do ABD-850AM and 17-4PH which reportedly have good printability [105, 299–301]. Comparing these results and completing a ranking analysis, the classic Scheil model using $0.8 < f_s < 0.99$ was determined to produce the most accurate predictions followed by the classic Scheil using $0.8 < f_s < 0.9$. Therefore the classic Scheil model with $0.8 < f_s < 0.99$ will be used in further analysis. However, it is important to note that the inaccuracy of the SCI values calculated using the solute trapping model is likely due to the lack in quality and quantity of HEA CALPHAD databases in particular, especially in rapid solidification regimes. For this reason, in the future it is possible this method could be a much more accurate option.

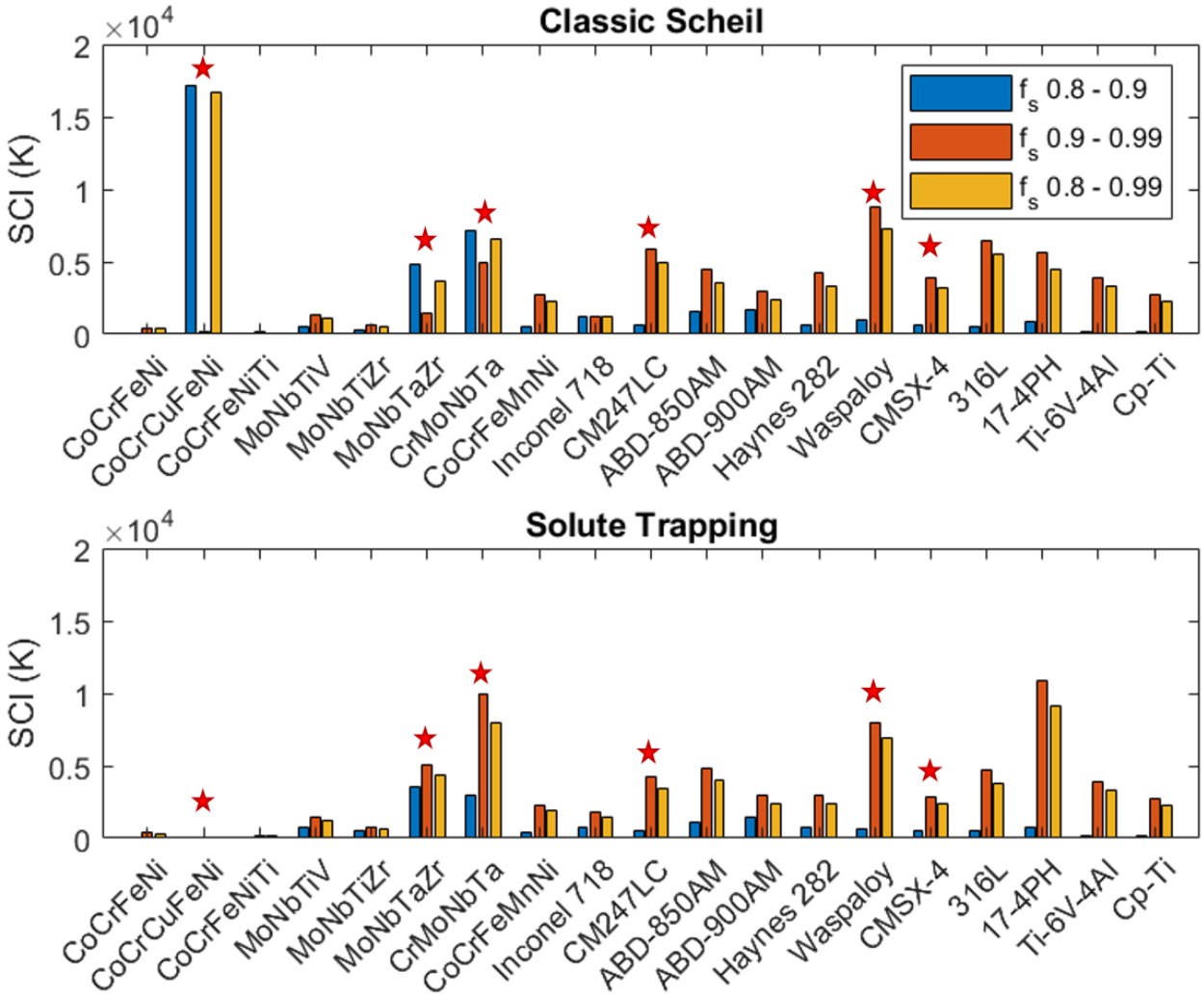

Figure 5.8: *SCI values using the classic Scheil and solute trapping models, for different f_s ranges. The alloys which show solidification cracking, either in the literature or from the melt tracks, are indicated with a red star.*

5.6.3 Crack Susceptibility Map

Figure 5.9 shows the complete crack susceptibility map, including the SSCI and SCI. In this diagram the alloys with a low crack susceptibility are clustered together in an approximate zone with SSCI $\leq 2.5 \times 10^5$ Pa and SCI ≤ 6000 K. The solid-state cracking behaviour in 5 out of 7 of the HEAs and 12 out of 12 of the conventional alloys was predicted by the SSCI. Whereas, the SCI accurately indicates solidification cracking in 3 out of the 5 alloys susceptible to solidification cracking, but inaccurately predicts 316L, 17-4PH, Ti-6V-4Al, ABD-850AM and Haynes 282 to have a similar solidification cracking susceptibility to CM247LC and CMSX-4. There is a definite clustering of non-cracking and cracking alloys suggesting an interaction or correlation between the indicators. It may be that since a high SSCI indicates a high ratio of tensile to compressive

residual stress, this also indicative of the formation of solidification cracks where high tensile stress results in interdendritic liquid film separation.

Exceptions to the success of the SSCI include CoCrFeNiTi, which contains ordered phases in small proportions, causing local solid-state cracking susceptibility, despite the global SSCI indicating resistance to solid-state cracking. The SSCI does not account for the detrimental effects of small amounts of very brittle phases on localised fracture toughness, as the large bond energy does not encapsulate this. This is especially true in new alloys if intermetallic or ordered phases are present and are particularly detrimental to ductility more than simply an engineered strengthening phase similar to the γ' phase in nickel alloys. The CoCrCuFeNi alloy is also correctly predicted to be very susceptible to solidification cracking, however it also shows some less extensive solid-state cracking which was not indicated. This is likely caused by propagation of established solidification cracks.

MoNbTaZr shows mainly solid-state cracks, however some solidification cracks are seen, mainly concentrated in the equiaxed heat affected zone at the edge of the melt tracks. The melting of the coarse, dendritic arc-melted microstructure could have caused this solidification cracking. It is expected that these solidification cracks would be less likely in PBF-LB/M as the microstructure is refined, less dendritic and with less segregation, more similar to the microstructure seen in the centre of the melt track (as the layers are equivalent to consecutive laser passes). Two well known difficult-to-process nickel alloys, CMSX-4 and CM247LC, also have a relatively low SCI values, yet still show solidification cracking according to previous work done on PBF-LB/M of these alloys [105, 288–290, 296]. It may be that locally these alloys have areas of low toughness or high levels of segregation driving this solidification cracking.

There are a few limitations to this mapping process, for HEA assessment in particular with the main one arising from using CALPHAD for the SCI. The current databases do not have a high enough quality or quantity of data for accurate analysis of some HEAs, especially those composed of more unusual element combinations. This is exacerbated when studying either novel compositions which are not CoCrFeNi-based HEAs or far from equilibrium solidification processes like the rapid solidification in AM. Because of this, as improvements in the rapid solidification part of HEA databases occur, it is expected that the solute trapping model will become more accurate than the classic Scheil model.

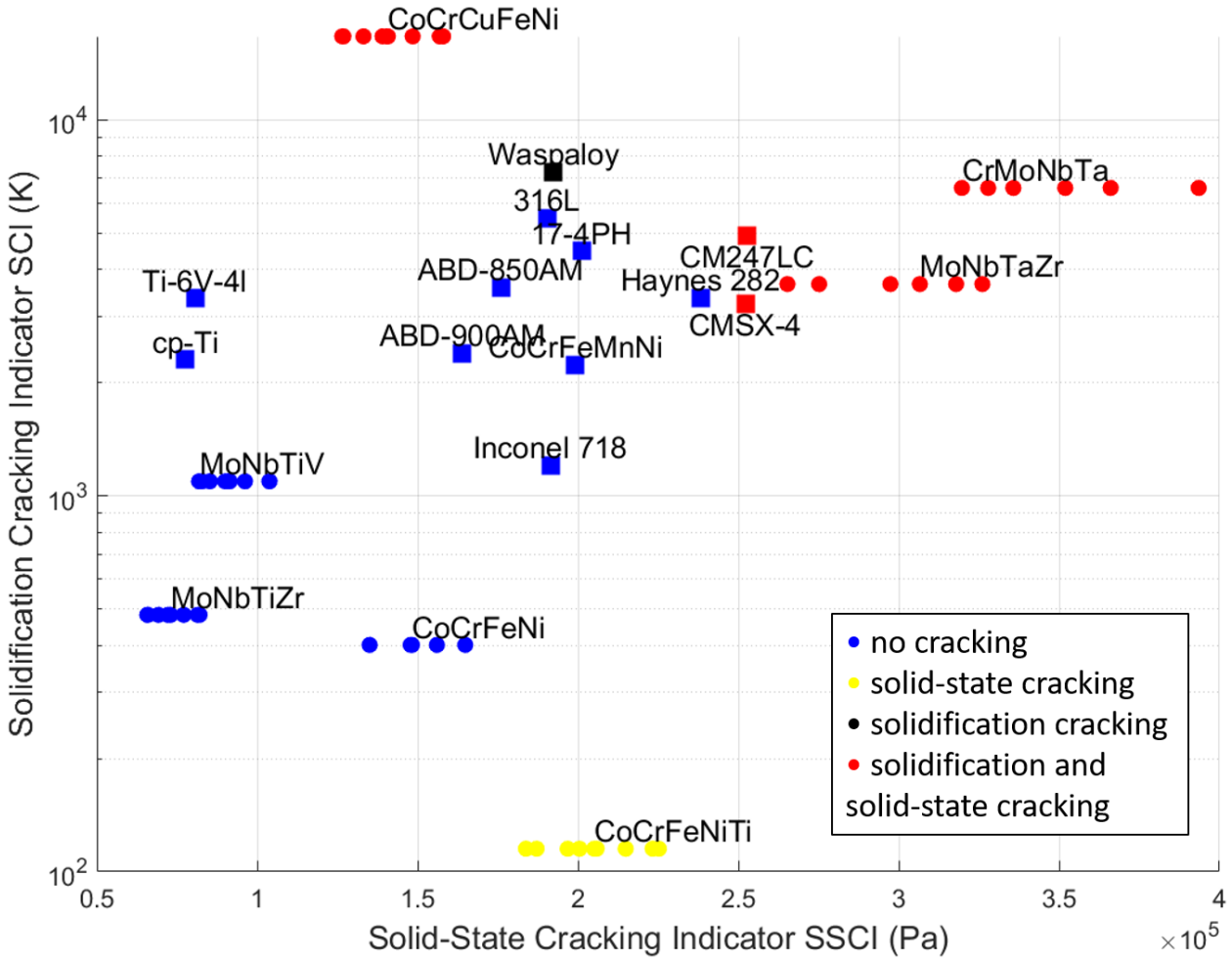

Figure 5.9: *Map of crack susceptibility for PBF-LB/M. Groups of circular markers denote new HEAs and the different parameters input to the moving heat source model for the SSCI and for the melt tracks. For simplicity, the conventional alloys and the CoCrFeMnNi HEA, only have the central parameter set shown, marked by a square.*

Despite many of the alloys discussed being quite crack susceptible, cracking in these alloys could be reduced or in some cases completely removed. Solidification cracking can be reduced by refining machine parameters to change the strain on the liquid films [289]. Residual stress can be reduced by pre-heating the substrate or changing laser scanning strategies eg. island scanning or remelting layers, thereby reducing solid-state cracking [286, 305, 306]. So consequently a high SCI or SSCI does not mean that the given alloy is completely un-processable, it indicates an inherent tendency to crack resulting in a reduced (or potentially non-existent) processing window for crack free parts. On top of this, alloys with a low SSCI value, may have a reduced crack susceptibility, but the distortion associated with a high CTE and higher heat input will often mean that parts are not dimensionally accurate or warp. Therefore, an appropriate condition and alloy would have to be selected in order to ensure reduced residual stresses and as well as distortion, acceptable for

the given application.

5.7 Conclusions

This work proposes a new indicator for solid state cracking susceptibility, based on considering the effect of average bond energy on material ductility and using thermal expansion coefficient, elastic modulus and temperature to approximate this relationship. As confirmation of the effect of varying CTE in isolation, a finite element model is used showing a positive effect on increasing compressive residual stresses compared to tensile residual stresses after being subject to the AM process. A crack susceptibility mapping method is described which shows the highly processable alloys as having SSCI $\leq 2.4 \times 10^5$ Pa and SCI ≤ 6000 K. 7 HEAs, 3 CoCrFeNi-based and 4 refractory HEAs, were subject to melt track trials to validate the crack susceptibility mapping method. The solid-state cracking behaviour of 5 out of the 7 HEAs and all 12 of the conventional alloys was predicted by the SSCI. The exceptions were the CoCrFeNiTi alloy containing several intermetallic phases, causing local brittleness which is not accurately modelled by a global parameter such as the SSCI. Along with the CoCrCuFeNi alloy where solidification cracking has likely created low-energy initiation sites for solid-state cracking propagation. Conversely, the SCI reported in the literature, accurately indicates 3 out of the 5 alloys cracking by solidification cracking, but inaccurately predicts several alloys to have similar solidification cracking susceptibility to CM247LC and CMSX-4. A clear limitation with calculating the SCI of HEAs, is due to the poor quality and quantity of thermodynamic HEA databases available for CALPHAD-based modelling, especially for AM specifically. This will likely improve with time as more experimentation is performed on more varying compositions. If improvements are made then it is feasible that the solute trapping Scheil solidification model may also become more accurate for this application rather than the classic Scheil model.

The main consideration of using the SSCI as the sole parameter to rank potential alloys for AM processability is that a low SSCI can arise from a high CTE or high heat input, which could result in more distortion in PBF-LB/M parts causing dimensional inaccuracy. So an appropriate condition would have to be selected to mitigate this as well as maintaining a low SSCI. However, despite the limitations, use of the SSCI has the potential to reduce the time and cost associated with alloy development for AM by screening alloys for crack susceptibility prior to any AM trials. A tool which would be welcomed in the the development of new alloys for AM, especially in the field of HEAs where there are often millions of potential compositions which cannot all be made experimentally.

Author Contributions

Conceptualisation, L.F., I.T. and R.G.; methodology, L.F., L.C., P.J., I.T. and R.G.; investigation, L.F., F.H., H.B., A.G., and A.R.; original draft preparation, L.F.; review and editing, A.G., L.C., F.H, H.B. and R.G.; supervision, I.T. and R.G. funding acquisition, R.G. and I.T. All authors have read and agreed to the published version of the manuscript.

Funding

This work was supported by Science Foundation Ireland 18/EPSRC-CDT/3584, the Engineering and Physical Sciences Research Council EP/S022635/1 and the Manufacture using Advanced Powder Processes (MAPP) EPSRC Future Manufacturing Hub EP/P006566/1. We wish to acknowledge the Henry Royce Institute for Advanced Materials, funded through EPSRC grants EP/R00661X/1, EP/S019367/1, EP/P02470X/1 and EP/P025285/1, for access to the Aconity3D Mini at The University of Sheffield. The authors would also like to thank Dr Katerina Christofidou for the useful discussions.

Conflicts of Interest

The authors declare no conflict of interest.

Chapter 6

Comparison of In-Situ Alloying and Pre-Alloyed Powder for the Additive Manufacture of Novel Multicomponent Alloys; example of $Mo_5Nb_{35}Ti_{30}V_{30}$

6.1 Author Contributions

Lucy Farquhar - Conceptualisation, methodology, manufacture of samples, sample preparation, data analysis, sample characterisation and analysis, writing of original draft.
Robert Snell - Support with build file design, writing - review and editing
Jonah Shrive - Operation of microscope for EBSD, support with EBSD analysis
Milo Maguire - Operation of Freeman FT4 for powder analysis
Elaine Livera - Operation of microscope for EBSD, support with EBSD analysis, writing - review and editing
Iain Todd - Supervision
Russell Goodall - Conceptualisation, support with methodology, supervision, writing - review and editing

6.2 Background

As described in Chapters 2 and 3, in-situ alloying (ISA) is extensively used for additive manufacturing (AM) of high entropy alloys (HEAs), especially for refractory HEAs (RHEAs), as manufacture

of homogeneous powder feedstock is costly and has long associated lead times. The same considerations when completing ISA applies for RHEAs as it does for other alloys, with the added difficulty that because of the high melting points of the refractory elements much higher volume energy density (VED) inputs are necessary to ensure full alloying [3]. In laser powder bed fusion (PBF-LB/M), there is also the constraint that powder must have good flow characteristics, for even deposition of powder on the substrate [202]. However, spherical refractory powders including elemental powders are difficult to obtain hence some studies have used partially non spherical powders [203, 204]. Though incomplete spreading can cause spreading defects and voids in parts, if the aim is to assess the material microstructure in AM then ISA using non spherical powders is a useful, time and cost saving approach to take. Yet the effect of powder morphology, on ISA of HEAs specifically is yet to be studied.

As ISA is often used for AM in the absence of pre-alloyed powder, there is yet to be any work reported which directly compares both methods for the same HEA system. Therefore comparing not only the alloying, but defects formed, melt pool shape, resulting microstructures and the difference in material response to process parameters is valuable. It is expected that for full alloying in ISA a higher VED is needed to melt the highest melting point elements than would perhaps be necessary for the pre-alloyed equivalent. However, if elemental particle size is small enough, the concentration of the element is low enough, the element is miscible in the melt pool or elemental mixing results in an exothermic reaction then a lower VED may be required [150]. Demonstrating that there are complex interplays involved with both processing parameters, powder properties, inherent alloy properties and binary elemental interactions.

This work very much builds on the work proposed in Chapter 3, on the effect of the additions of different elements on ISA, considering melting points, thermal properties and tendency to segregate. Instead this chapter focuses on the influence of powder quality, specifically the powder contamination, particle shape and size and the influence of these factors on the success of ISA via PBF-LB/M. The resulting samples are then compared to samples of the same RHEA when manufactured using pre-alloyed powder. The $Mo_5Nb_{35}Ti_{30}V_{30}$ RHEA manufactured here, is referred to as Alloy 1 in Chapter 4 and is one of the 2 RHEAs which showed AM processability in Chapter 5.

Paper: Comparison of in-situ alloying and pre-alloyed powder for the additive manufacture of novel multicomponent alloys; example of $Mo_5Nb_{35}Ti_{30}V_{30}$

Lucy Farquhar[1], Robert Snell[1], Jonah Shrive[1], Milo Maguire[1], Elaine Livera[1], Iain Todd[1], Russell Goodall[1]

1 – Department of Materials Science and Engineering, University of Sheffield, Sheffield S1 3JD, UK

Correspondence: laufarquhar1@sheffield.ac.uk

Abstract

Refractory high entropy alloys (RHEAs) generally show superior strength at high temperatures and consequently, due to the high melting point elements concerned, are difficult to manufacture via conventional methods. Therefore, additive manufacturing (AM) of RHEAs is gaining popularity as a method by which to produce homogeneous alloys in parts with complex geometries for many applications, especially via use of blended powders and in-situ alloying (ISA). In this work, ISA of the $Mo_5Nb_{35}Ti_{30}V_{30}$ RHEA by blending of off-the-shelf elemental powders is compared to the manufacture of the same alloy using pre-alloyed (PA) powder, via laser powder bed fusion. The resulting contamination, defects, elemental distribution, microstructural texture and grain morphology are compared for both sample types. The ISA powder resulted in higher interstitial content and gas porosity as well as un-alloyed elements at low input energies and crack-like spreading defects, caused by low powder flowability. The PA powder also showed un-alloyed Nb and Mo as well as high levels of Ta contamination. While keyholes were prevalent at high energies in the PA samples, the ISA powder suppressed keyhole formation and showed an almost homogeneous microstructure. The texture in the ISA samples is largely equiaxed due to high melting point elements acting as grain nucleation sites and grain refiners, compared to the epitaxial columnar grain growth seen when using PA powder. It is demonstrated that representative AM microstructures can be obtained using low flowability ISA powders, acknowledging that the defects, contamination, texture and optimum processing parameters will differ from the PA equivalent.

Keywords

Additive Manufacturing, Laser Powder Bed Fusion, Refractory High Entropy Alloys, In-Situ Alloying

6.3 Introduction

High entropy alloys (HEAs) were first proposed in 2004, and instead of being based on a primary element, comprise of multiple elements with similar composition. The equiatomic CoCrFeMnNi was the first HEA put forward by Cantor *et al.* [1], however a range of HEAs have since been explored, including those containing refractory elements aimed at being used for high temperature applications [20]. Refractory HEAs (RHEAs) are particularly difficult to manufacture, requiring high temperatures due to the high melting point constituent elements. Therefore, additive manufacturing (AM) is an ideal technology to manufacture these materials, through the use of a high powered, focused heat source.

Metal laser powder bed fusion (PBF-LB/M) is a process where parts are built through use of a laser sequentially melting metal powder feedstock layer-by-layer in a powder bed. Usually, this process requires the use of powders with excellent flowability and consequently spherical particle shape and narrow particle size range. However, these powders are expensive, energy intensive and time consuming to produce, especially for newly designed RHEAs containing high melting point elements, with compositions which have not been manufactured previously. In-situ alloying (ISA) offers the opportunity to manufacture these alloys quickly, using less energy and at lower cost by blending elemental powders to achieve the desired composition. ISA has been used to manufacture many different types of alloys previously, including many HEAs from the CoCrFeNi-based transition metal alloy systems [182, 216, 248, 285, 307–315]. ISA of RHEAs specifically has been studied mainly by the use of directed energy deposition (DED) [5, 153, 193–200]. However, there are few examples in the literature where RHEAs have been manufactured via ISA in PBF-LB/M [7, 203–206]. Wang *et al.* varied composition of Mo in $NbTa_{0.5}TiMo_x$ alloys using spherical elemental powders, and had difficulty with un-melted Mo particles and cracking [205]. Zhu *et al.* used a mixture of spherical and non-spherical powders to manufacture a $V_{0.5}Nb_{0.5}ZrTi$ alloy. Cracking was observed at low volumetric energy density (VED) values, but at high VED crack free parts with a mechanical strength 400 MPa higher than the as-cast form were achieved [204]. The NbMoTaW alloy was also manufactured via ISA in PBF-LB/M by Zhang *et al.* with near-spherical powders, achieving a single phase microstructure with no un-melted elements [203].

In this work the $Mo_5Nb_{35}Ti_{30}V_{30}$ HEA is manufactured by both PBF-LB/M of pre-alloyed (PA) powder and ISA of off-the-shelf elemental powders. The aim is to assess the effect of blending powders with varying particle sizes, shapes and thermal properties on flowability and consequently sample homogeneity, while comparing the results to a near "ideal" PA powder for PBF-LB/M. With the result enabling further understanding of the capabilities of ISA to properly represent the AM processing of novel alloys, and to judge its suitability for inclusion in high-throughput assessment schemes for such materials. This work specifically compares the behaviour of the Mo

(smaller, dendritic, high surface area to volume ratio) particles with the Nb (larger, angular, low surface area to volume ratio) particles, to assess the effect of particle shape and size on alloying in the PBF-LB/M process. Consequently, the microstructures and defects obtained via ISA of a powder blend with varying constituent powder quality, can be compared with those obtained by using pre-alloyed powder. The limitations of this process are then discussed, including those associated with the effects of having to use high input energies on the quality of the resulting parts. This work acts as a guide to the important factors involved in successful ISA of HEAs, in order to reduce the cost and time associated with manufacturing these alloys for early stage experimental investigation.

6.4 Materials and Methods

The elemental powders were supplied by Goodfellow Cambridge, UK. Due to low availability of suitable stock powders, the Ti powder has a uniform spherical particle shape but the other powders are non-spherical. The corresponding PA powder was produced by multiple melting in a cold copper crucible, crushing and radio-frequency plasma spherodisation and was supplied by Metal Powder Emergence, UK. All powders were sieved through a 52 µm sieve before characterisation or mixing of the blended powder. Mixing was done by manually tumbling the powder blend on multiple axes for 15 minutes. All specimens were manufactured using an Aconity3d Mini PBF-LB/M machine, using a Gaussian laser beam, with a laser spot size of 70 µm and a maximum laser power of 200W. 5mm $\times$ 5mm $\times$ 8mm cubic samples were manufactured on a Ti-6V-4Al substrate, with a tapered pyramidal underside allowing for easy removal from the build plate, depicted in Figure 6.2. The laser scanning velocity was varied from 300 - 600 mm/s, the hatch spacing was varied from 20 - 60 µm, the laser power and layer height were kept constant at 190 W and 30 µm respectively. All samples were sectioned parallel to the build direction and were analysed in the as-built state. After polishing, the optical density and defects in the samples were characterised using an Olympus BX 51 optical microscope (Clemex Vision Pro) along with image analysis using ImageJ [236].

The particle size distribution (PSD) for each elemental powder, the blended powder and the PA powder was analysed using a laser diffraction particle size analyser (Mastersizer 2000, Malvern, UK). Powder flowability characteristics were determined based on shear flow tests using an FT4 powder rheometer (Freeman Technology, UK), with a 30 mm diameter vessel and a 23.5 mm impeller, used with the standard stability and variable flow rate test method. Inductively coupled plasma optical emission spectroscopy (ICP-OES) was used to assess metallic element content on the elemental, blended and PA powders. The content of O and N was found using thermoconductivity and infra-red (IR) absorption (Eltra ONH 2000 Analyser) and the C content

was found using combustion/IR analysis. All bulk elemental analysis was carried out by Sheffield Assay Office, UK using the ATM167, ATM149 and ATM82 standards. Phase characterisation of the as-built samples was done by X-ray diffraction (XRD) on a Bruker D2 Phaser Diffractomer using a Cu K_α ($\lambda = 1.54$ Å) radiation source. Scanning electron microscopy (SEM) and energy dispersive X-ray spectroscopy (EDS) were carried out on the powders and as-built samples using a FEI Inspect F50 SEM, with a working distance of approximately 10 mm, where the accelerating voltage and spot size were 20 kV and 3.5 respectively. Electron backscattered diffraction (EBSD) was conducted using a JEOL 7900F field emission gun (FEG)-SEM, equipped with an Oxford Instruments symmetry detector. An accelerating voltage of 20 kV and step size of 0.4 µm was used to characterise texture. MTEX software was used to denoise the maps and extract pole figures [316].

6.5 Results and Discussion

6.5.1 Powder Analysis

The elemental powders used for this work were obtained off-the-shelf, as this would be the approach required to ensure quick lead times and lower costs in general high throughput alloy development work. Consequently, only the Ti powder has a uniform spherical particle shape, Nb and V powders contain irregular angular particles and the Mo powder has complex dendritic type particles [317]. The PSDs and powder morphologies are shown in Figure 6.1 with the percentiles detailed in Table 6.1, where it shows, for the non-spherical powders, there are still particles present with dimensions larger than 52 µm. These non-spherical particle shapes could affect many important factors within the PBF-LB/M process including flowability, laser absorptivity, melt pool dynamics, elemental segregation and homogeneity [203]. Nb has significantly larger D_{50} and D_{90} values then the other elemental powders and is one of the two higher melting point elements in the alloy along with Mo, reducing its laser absorptivity as well as flowability. Assuming uniform spreading, particle shape and size can influence the success of the alloying itself. This is because larger particles of higher melting point elements like Nb might not melt, dissolve or be carried by the fluid flow in the melt pool. Comparatively, particles with a similar melting point but higher surface area to volume ratio, such as the Mo powder in this work, could be more effectively incorporated. The elemental blend powder shows good mixing of the constituent elements and has a comparable PSD to that of the pre-alloyed powder, however blending varying particle shapes and sizes at these proportions impacts powder flowability, as indicated in Table 6.3, resulting in differing spreading behaviour in PBF-LB/M.

The pre-alloyed powder contains spherical particles however after sieving, some particles larger

Table 6.1: *Particle shape, PSD, melting points and boiling points for each of the elemental powders, the ISA blend and PA powders. The melting (solidus) and boiling points of the alloy are estimated by a rule-of-mixtures calculation as the actual values are unknown.*

Powder	Particle shape	D_{10} (µm)	D_{50} (µm)	D_{90} (µm)	Melting point (°C)	Boiling point (°C)
Mo	dendritic	11.7	30	65.7	2622	4639
Nb	angular	15.3	36.1	70.9	2477	4741
Ti	spherical	21.9	31.9	45.6	1670	3287
V	angular	15.1	31.5	54.3	1910	3407
ISA	all of above	14.7	31.6	60.6	2072	3900
PA	spherical	11.9	28	57.3	2072	3900

than 52 µm still remain, most likely due to the agglomeration of particles which are below 15 µm or due to elliptical particles, both of which are seen in Figure 6.1. The composition of this powder varies from the nominal composition. Some particles show high amounts of Nb varying from the nominal composition of 35 at% up to 75 at%. This is usually accompanied by an increase of Mo content in the same particles to 8 - 10 at%. There is also some Ta present in the powder, most likely from contamination in the manufacturing process, where some isolated particles contain up to 49 at% Ta, with a near nominal composition of the rest of the constituent elements.

The powder analysis in this work is reported in Table 6.3, where the PA powder is shown to have much more fluidity. This is expected due to the reduced basic flow energy (BFE) and specific energy (SE), and increased conditioned bulk density (CBD). However, compared to many powders reported in the literature, the PA powder has SE and BFE values on the higher end and CBD on the lower end of acceptable ranges, attributed to the presence of fine particles below 15 µm causing increased cohesion [318, 319]. The ISA powder has SE and BFE much higher and CBD much lower than previously reported ranges for AM, indicating higher cohesion and lower packing density than other powders reported. It also shows more variability, as indicted by the stability index (SI), due to the non-uniform powder properties to be expected from a blend of four different powders. It is worth noting that determination of these parameters does not necessarily have any bearing on spreadability in an PBF-LB/M process, as has been indicated previous in work on the SE and flow rate index (FRI) [320]. However, they do provide useful insight into the powder behaviour and the influence of particle shape and size on powder properties more generally.

Elemental analysis for the powders is displayed in Table 6.2. Each of the elemental powders shows a high purity of above 99.6 wt%, despite having relatively high O content. V is the exception to this having a purity of 96.2 wt% and a very high O concentration of 3.69 wt%, meaning much

Table 6.2: *Bulk elemental analysis of the isolated elemental powders, the blended ISA powder and the PA powder. All compositions are given in wt%. The nominal composition of the target alloy in wt% is* $Mo_{7.2}Nb_{48.6}Ti_{21.4}V_{22.8}$.

Powder	Mo	Nb	Ti	V	Ta	O	N	C
Mo	99.6	0.026	0.054	0.049	-	0.200	0.004	0.001
Nb	<0.02	99.7	<0.02	<0.02	-	0.260	0.006	0.003
Ti	<0.02	<0.02	99.8	0.05	-	0.087	0.027	0.012
V	0.033	0.047	0.022	96.2	-	3.69	0.040	0.007
ISA blend	6.39	49.4	22.4	21.0	-	0.700	0.012	0.005
PA	7.47	50.2	20.8	21.3	0.31	0.073	0.091	0.086

Table 6.3: *Measured basic flow energy (BFE), specific energy (SE), flow rate index (FRI), stability index (SI) and conditioned bulk density (CBD) for the PA and ISA powders. The errors given are the standard deviations of the calculated mean value reported.*

Powder	BFE (mJ)	SE (mJ/g)	FRI	SI	CBD (g/ml)
ISA	936.33 ±18.12	5.96 ±0.10	1.29 ±0.02	1.05 ±0.08	2.07 ±0.02
PA	611.17 ±4.72	3.23 ±0.02	1.22 ±0.01	0.99 ±0.04	3.55 ±0.02

of the powder analysed has oxidised. The measured level of O content has likely been increased by the length of storage time of the analysed powder, as the V powder blended for this work was used for PBF/LB-M within a month of receiving it from the supplier, and elemental analysis was completed months after this. However the results clearly show that the V powder used will make the largest contribution to O contamination in the ISA samples. The O contamination results in the ISA powder containing almost an order of magnitude more O than the PA. This means that even though the ISA contains less C and N than the PA, there could be substantial effects of interstitial O in the ISA samples, including embrittlement and cracking. The results in Table 6.2, also show the presence of high levels of Ta in the PA powder. This shows that even with high costs and lead times, bespoke small batch creation of PA powders of this type does not necessarily guarantee perfect composition. It is also worth noting that the elemental Nb powder contains a negligible amount of Mo. However, in the EDS of the powder blend in Figure 6.1, the indication of the presence of Mo in the Nb powder is due to overlapping peaks in the EDS pattern, not due to high levels of Mo in the Nb powder.

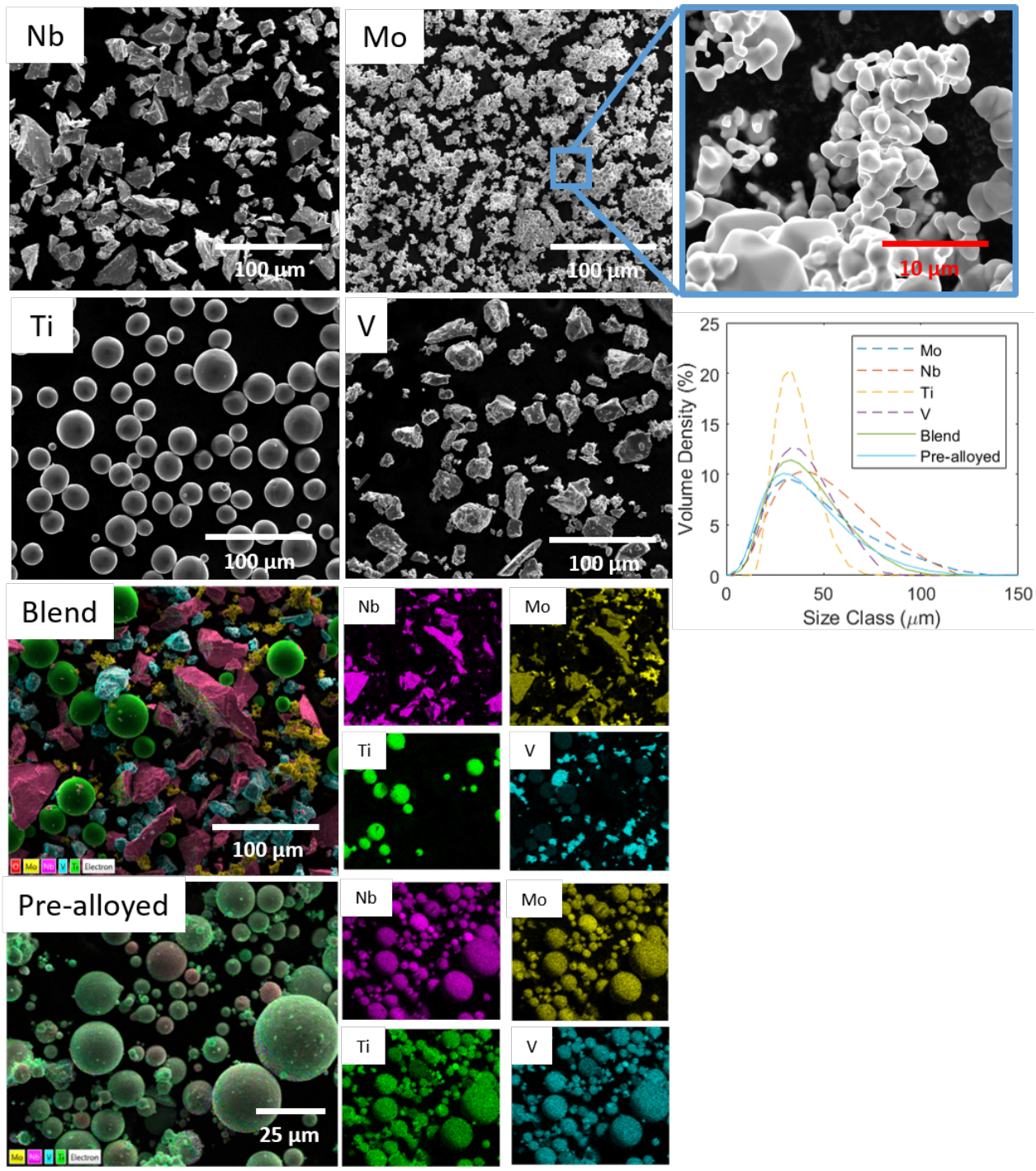

Figure 6.1: *Scanning electron images showing the individual elemental powders, the blend of elemental powders and the pre-alloyed powder with EDS maps showing the elemental distributions. The graph also shows the particle size distributions for all the powders after sieving.*

6.5.2 Sample Manufacture and Defects

Images of both the builds are shown in Figure 6.2, where it shows that both powders produced consolidated parts. There is, however, the appearance of a black-coloured impurity visible on some of the ISA parts, most likely due to the increased contamination indicated by elemental analysis. When sectioned, some of the ISA parts, notably those clustered towards the sides and back of the build plate (furthest from the powder supply system), showed lack of fusion-type porosity despite high VED values. It is believed this was caused by incomplete powder spreading in these areas, as a result of the low flowability of the ISA powder. Therefore, only parts located near the front and centre of the build plate were selected for further analysis, ensuring that the distribution of elements and powder spreading was as homogeneous as possible in the analysed parts. Figure 6.2 also shows optical images of the cross-sections of representative low, medium and high volume energy density (VED) parameter sets. Here $VED = P/vlh$, where P is laser powder, v is laser scanning velocity, h is hatch spacing and l is layer thickness. The parameters for each VED value and corresponding optical densities for each powder type can be found in Table 6.4.

The PA samples show gas porosity at low VED values as well as the increasing formation of keyholes at higher VED values, which is consistent with literature [321]. Keyholes, usually between 10 to 50 µm in size, are a common AM defect due to the trapping of vaporised material by unstable keyhole-type melt pool formation, and increase in quantity at higher VED [99]. Gas porosity is most commonly caused by the entrapment of gases which are supersaturated in the melt pool and the resulting pores are usually on the order of 5 to 20 µm. It is mitigated by increasing VED to ensure slower cooling rates and time for gas to escape while material is molten [100]. The ISA samples show both of these types of porosity, however the pores are generally smaller, suggesting a higher prevalence of gas porosity than keyhole formation. This could be due to the presence of un-melted particles of Nb, and to some extent Mo, depleting those elements in the base composition, thereby causing vaporisation of the lower melting point Nb- and Mo-depleted composition. It could also be caused by a higher entrainment of gas or moisture within the ISA powder, which could in part be due to the poor packing caused by the mixture of particle shapes or potential porosity within the powder.

The presence of large powder particles has also been shown previously to create shallow, wider melt pools, thereby reducing the tendency for keyhole formation, explaining why keyhole porosity is not prevalent [322]. The level of gas porosity in the ISA samples does, however, remain fairly constant, with the difference in optical densities more obviously being caused by the formation of crack-like defects. It is likely these defects are caused by either partial powder spreading, or the presence of solid-state cracks, forming due to the embrittlement caused by increased interstitial element content. The latter is exacerbated by un-melted powder particles that provide crack-initiation sites that are not present in the PA samples. Due to the combined result of these

Table 6.4: *Process parameters and densities for PA and ISA samples at low, medium and high VED. The optical density of un-melted Nb in the ISA samples is obtained by image thresholding in ImageJ, due to the differing contrast on backscattered electron (BSE) images, examples of which are shown in Figure 6.3.*

Sample Input Energy	Power (W)	Scanning Speed (mms^{-1})	Hatch Spacing (µm)	VED (Jmm^{-3})	Density ISA (%)	Density PA (%)	Un-alloyed Nb ISA (%)
Low	190	600	45	234.57	96.44	99.70	4.81
Medium	190	450	35	402.12	91.69	97.69	2.26
High	190	400	20	791.67	94.76	96.35	0.56

effects, the density of these defects is similar for all the ISA samples at different energies, despite increased alloying of high melting temperature particles in higher energy samples. However the combination of gas porosity, some keyholes and crack-like defects has resulted in the medium energy sample exhibiting the lowest relative density overall.

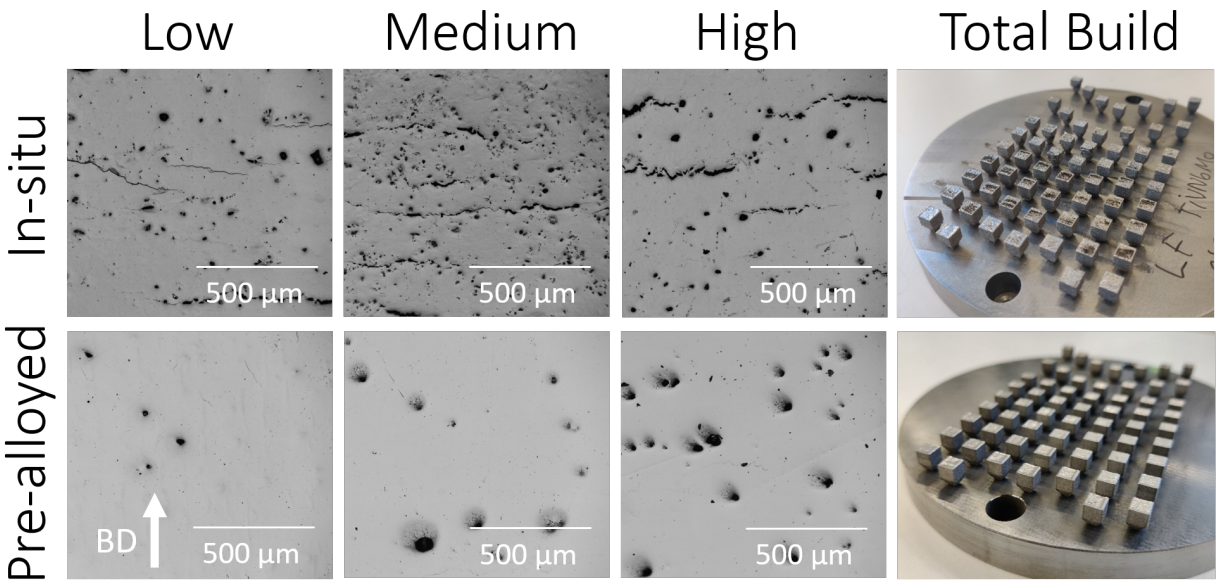

Figure 6.2: *Cross-sectional optical images of ISA and PA samples at different input energies showing the difference in defects, where the build direction (BD) is vertical for all images as indicated. An image of the total build plate is also shown for both of the powder types.*

6.5.3 Microstructure

6.5.3.1 Elemental distribution

Figure 6.3 shows the elemental distributions for the ISA and PA samples for the low, medium and high VED parameter sets. In all the PA samples, there is largely a single phase of the nominal composition, however in the medium VED sample there is the appearance of a Nb-Mo based spherical secondary phase. This type of secondary phase was seen in many others analysed, showing increased Nb-Mo content. This is very likely due to the in-homogeneity in the PA powder, where some particles have increased Nb-Mo concentrations. At low or medium VED, these are not fully alloyed into the main phase due to their increased melting points compared to that of the base composition. Nb and Mo have melting points of 2477 °C and 2622 °C respectively, whereas the predicted solidus temperature of the nominal composition is 2072 °C, as shown in Table 6.1. Since the main phase here is likely slightly depleted in Mo and Nb, the solidus temperature in this phase may be even lower than the predicted nominal solidus temperature. Un-melted Ta-based particles, present due to contamination in the powder, were also seen in the microstructure of some samples, but not in the particular cross-sections of the samples detailed in this work.

In the ISA case, the approximate area percentage of the sample image which taken up by un-melted or un-alloyed Nb is given in Table 6.4, where it shows that the fraction decreases as the energy input increases. This is expected as increased VED means either the material is at increased temperature for longer time periods, or it is remelted more times (due to reduced scanning velocity and hatch spacing). Therefore, higher melting point elements like Nb have more time to melt or dissolve into the melt pool. It is hypothesized in the literature that a negative enthalpy of mixing of the elements means less energy should be necessary as input by the process to aid with melting than is needed with pre-alloyed powder. As if the reaction of mixing itself is exothermic, therefore providing more heat, this can increase alloying [323]. However, as the mixing enthalpy for this alloy is only slightly negative at -0.96 kJ/mol (calculated by the Miedema model [242]), this reaction does not supply sufficient energy to melt the Nb and Mo. In the low VED sample there are areas of high concentration of all elements, including Ti and V, indicating that there has been insufficient time to allow for diffusion. The compositional variation of Ti and V reduces at higher energies; however, the high concentration areas of Ti and V tend to coincide, especially in the medium energy sample. This indicates that Ti and V behave in a similar manner both in the melt pool and on solidification. This could be due to these elements possessing similar densities and PSD (despite having different particle shapes), so therefore having similar buoyancy forces within the melt pool as well as the most similar melting points. This indicates they are melting before Mo and Nb and therefore mixing prior to the incorporation of those elements.

Mo and Nb have comparable melting points at 2623 °C and 2477 °C respectively, however

in this work there is proportionally much more un-melted or un-alloyed Nb present in the ISA samples. This is likely for a few reasons, the Nb particles are larger on average than the Mo particles, as well as having a much smaller surface area to volume ratio due to their angular shape vs the dendritic shape of the Mo. This shape difference means that the Mo will dissolve more readily in the melt pool at lower temperatures than the Nb particles. It is also hypothesized that the large size of the Nb, with particles of comparable dimensions to the beam spot size, will mean that particles are not easily carried in the generated Marangoni flow of the melt pool, resulting in Nb particles getting trapped at the bottom of the melt pool [324, 325]. The large size of Nb particles also means that its laser absorptivity is reduced compared to other smaller particles, meaning it is much more reliant on dissolving in molten material to become alloyed [203]. Lastly, the Mo is at a much lower concentration in the nominal composition than Nb, meaning that for Mo, there is less chance of the surrounding material being saturated on melting. So there is a higher driving force for dissolving the Mo into solution. Meanwhile, the high concentration of Nb means a much higher energy input and time is needed to alloy the Nb into solution anyway, even without the reduced surface area to volume ratio of the particles.

The lack of alloying of Nb, compared to Mo, emphasizes the importance of particle size and shape in the ISA process. In order to successfully alloy high melting point elements, either a small particle size or a highly irregular particle shape with a high surface area to volume ratio is desired to promote alloying at lower temperatures. It is also helpful if the high melting point elements have a lower composition within the alloy, both so the element is easily dissolved and so the small or irregular particle shapes and sizes do not impede powder spreading or increase cohesion. Although, of course, where the purpose is to experimentally explore new alloys, this is not always possible [322]. Otherwise a high VED input is needed to alloy higher proportions of larger particles, however this has implications for the formation of other defects at high temperatures.

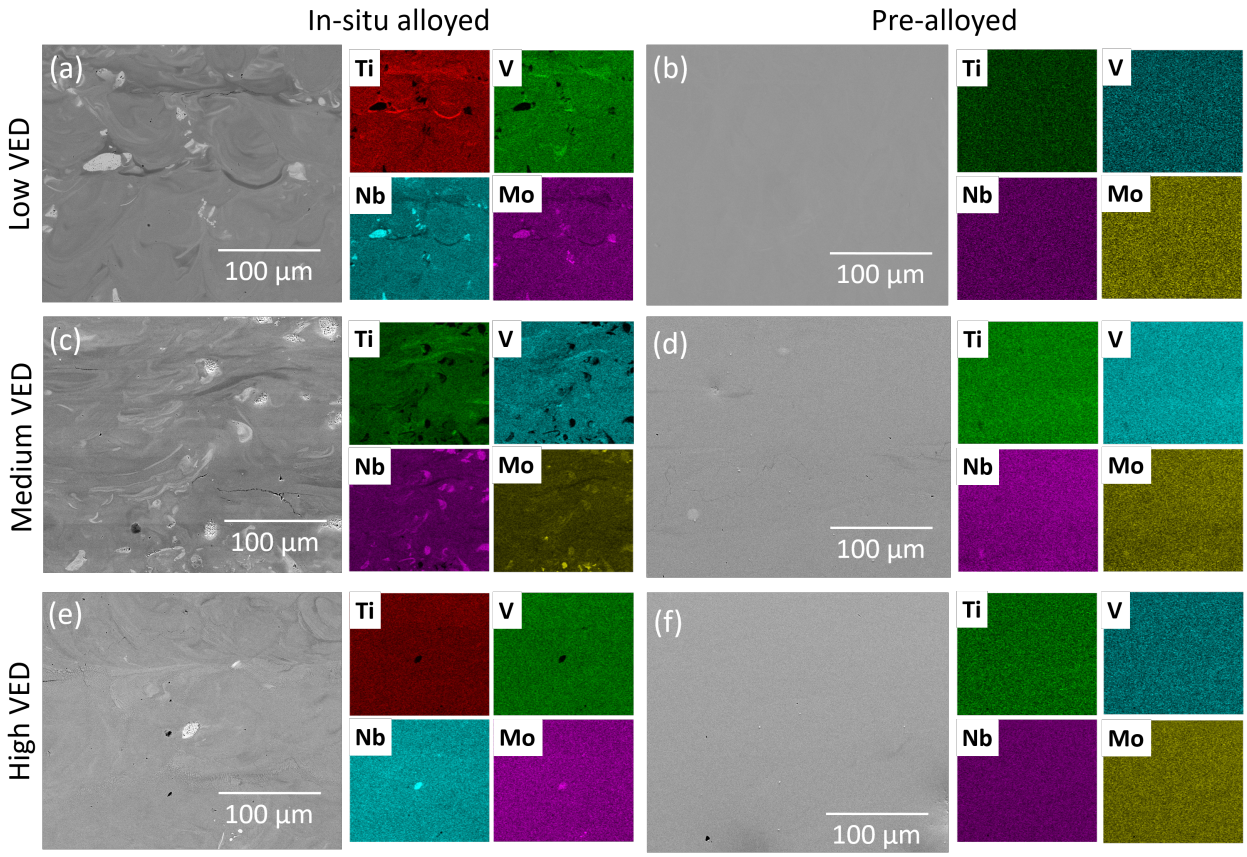

Figure 6.3: *BSE images and elemental EDS maps for the PA and ISA samples for the low, medium and high VED parameter sets. The un-melted Nb particles are also shown in the EDS as containing Mo (as with the Nb powder), an un-melted elemental Mo particle can be identified where Mo and no Nb is present.*

6.5.3.2 Phase Characterisation and Texture

XRD of the low energy samples, shown in Figure 6.4, indicates that both sample types have a body-centred cubic (BCC) microstructure with a lattice parameter of 3.211 Å. The ISA sample has a small peak consistent with the expected peak position of pure Nb, due to the un-alloyed Nb observed in the microstructure. The EBSD IPF-Y maps and pole figure of the low energy PA sample shows columnar grains, with a strong texture in the <100> direction, which is the build direction in this case. This is typical of samples manufactured by AM, especially those in keyhole mode melting, which this sample is, according to the defect formation reported in Figure 6.2. Since all higher energy PA samples showed extensive keyhole porosity, it is expected that they show similar microstructural texture. Conversely the EBSD map for the low energy ISA sample shows an equiaxed microstructure consistent with that seen in the literature in other cases of ISA in DED [7, 141]. This is attributed to the higher melting point elements acting as heterogeneous

nucleation sites for solidification, therefore removing the <100> texture which usually occurs due to epitaxial grain growth when solidification is driven by thermal gradient.

In the high VED ISA sample, an equiaxed microstructure is also observed, as shown in Figure 6.4(b), however the microstructure is noticeably less refined than the low VED sample. The grain size distributions by area percentage are shown in Figure 6.5, where it can be seen that in the high energy ISA sample there are some larger, slightly elongated grains similar to those in the PA sample, indicating the larger melt pools caused by higher VED input. The level of un-melted Nb in the high VED ISA sample is significantly reduced compared to the low VED, as indicated by the EDS maps in Figure 6.4. This decrease in un-melted Nb perhaps explains why there are more elongated grains present in the high VED ISA sample, as there are less sites for heterogeneous nucleation of growth of smaller grains. However, the overall texture is not significantly affected, indicating that there is still not a transition to keyhole mode melting even at high VED input, which would promote columnar grain growth [326]. The larger Nb particles, present in the powder blend, likely inhibited fluid flow in the melt pool even before melting and therefore still hindered this transition. This indicates that, because of this effect, if the VED is further increased, all the high melting point elements could be fully alloyed without extensive keyhole porosity formation, an effect similar to that reported by Spurek et al in PA steel powder [322]. However, once full melting is achieved, the effect of equiaxed grain nucleation due to these powder particles could be reduced. Hypothetically, if the lower melting point elements instead had larger particle sizes compared to the higher melting point elements, then it is possible that keyhole formation could be suppressed while also allowing full alloying of the high melting point element particles, thus allowing further control of melt pool shape, keyhole porosity as well as grain morphology and grain size.

Grain-boundary (GB) misorientation maps and histograms for the low and high VED ISA samples and low VED PA sample are also shown in Figure 6.5. The VED PA sample shows a much higher frequency of low angle GBs than the equivalent ISA sample, and these low angle GBs are mainly distributed along the elongated columnar grains, with high angle GBs found where there are small areas of equiaxed grain formation, giving an almost bimodal GB misorientation distribution. Both the ISA samples show an increased frequency of higher angle GB misorientations and a reduction in low angle GB misorientations compared to PA. The ISA samples also show a more normal distribution of misorientations, indicative of their isotropic microstructures.

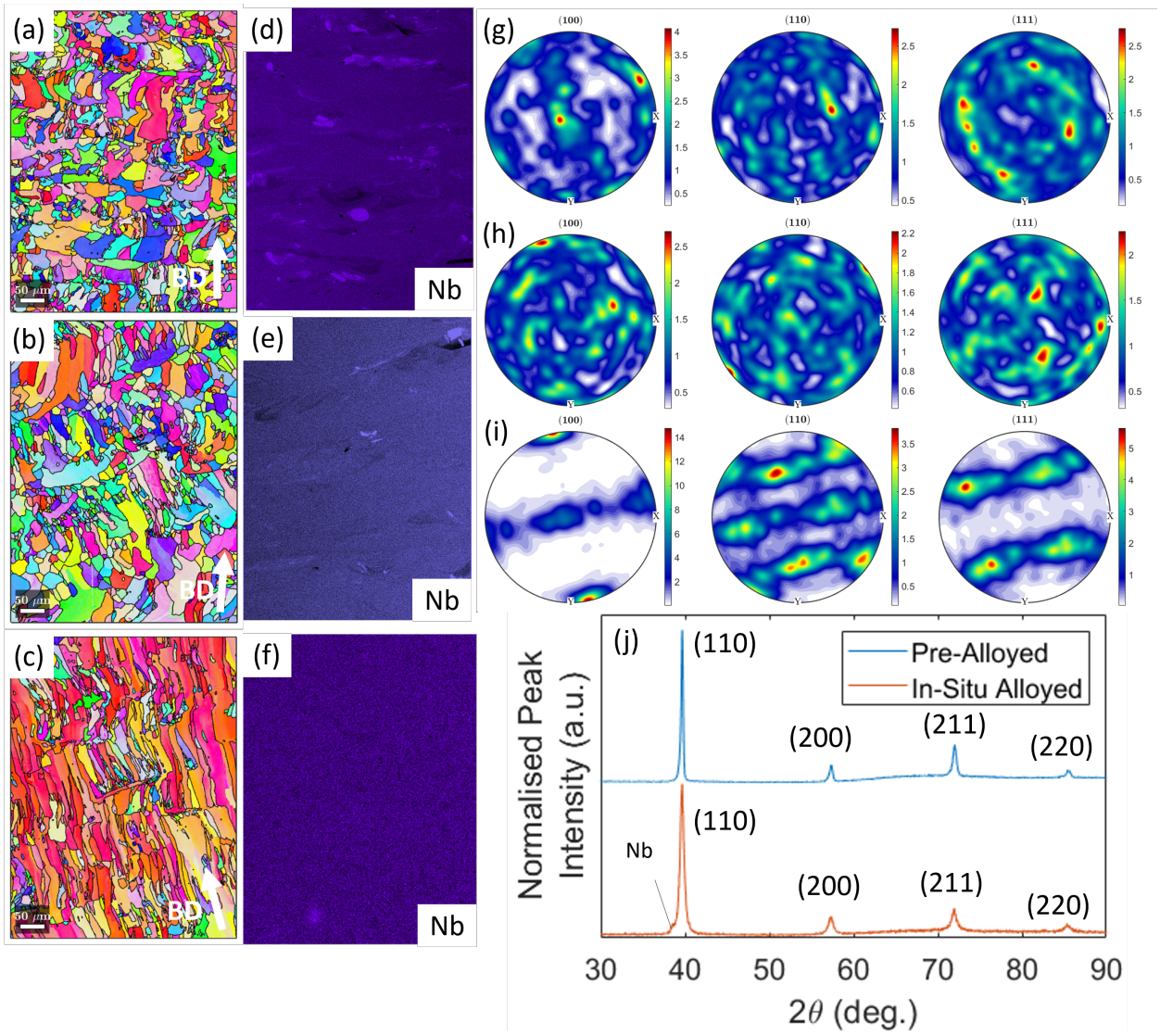

Figure 6.4: *(a), (b) and (c) EBSD IPF-Y maps of the low and high VED ISA samples and the low VED PA sample respectively. (d), (e) and (f) EDS maps for Nb in the low and high VED ISA samples and the low VED PA sample respectively. (g), (h) and (i) pole figures for the low and high VED ISA and low VED PA samples respectively, calculated from the EBSD maps for the same samples. (j) Normalised XRD patterns for the low VED PA and ISA samples. BD here indicates build direction which also corresponds to the <100> direction in this images.*

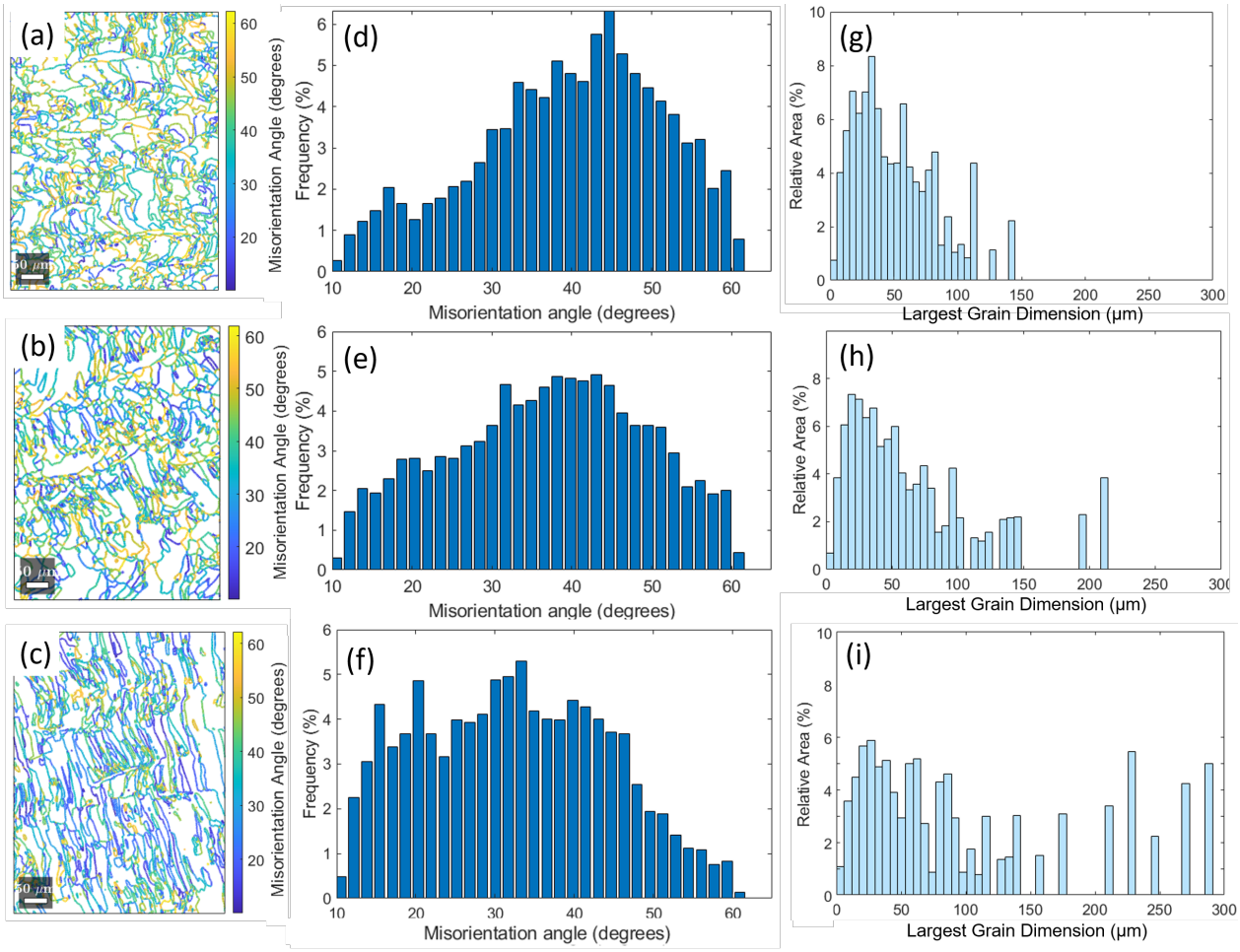

Figure 6.5: *(a), (b) and (c) GB misorientation maps for the low and high VED ISA and low VED PA samples respectively. (d), (e) and (f) Misorientation histograms for the low and high VED ISA and low VED PA samples respectively. (g), (h) and (i) Graphs of the relative area percentage occupied by grains of differing size for the low and high VED ISA and low VED PA samples respectively.*

6.6 Conclusions

The purpose of this work was to evaluate the success of in-situ alloying as an accelerated, cost and energy saving manufacturing method for the development of new RHEAs and similar alloys. Two powders were used and their results compared; a blend of elemental powders of varying particle size and shape and a pre-alloyed powder of the same composition. The powder shapes, sizes and flowability were measured and correlated with the resulting part qualities and defects observed. The extent of alloying of high melting point elements was also discussed, emphasising the importance of reduced particle size and/or irregular particle shapes on alloying, by increasing surface area to volume ratio. The effect that these elements have on the microstructure, including

grain size, shape and texture was also reported. The following points summarise the key findings of this work:

- Both the ISA and PA powder had comparable PSDs, however their flowability was measured to be significantly different. This was due to the mixture of different particle shapes and sizes present in the ISA powder causing increased cohesion and reduced packing density.
- Elemental analysis confirmed O contamination an order of magnitude higher in the ISA powder compared to the PA. This stemmed from the use of elemental V, meaning the ISA particles will contain a much higher level of interstitial O. There were also high levels of Ta contamination reported in the PA powder.
- Between the powders, there were differences in part quality and defect formation in the built samples. The ISA parts showed the formation of extensive gas porosity attributed to entrapped gas or vaporisation of lower melting point elements. There was also the formation of crack-like defects which could be due to incomplete powder spreading, the formation of cracks initiated from un-melted particles, or embrittlement caused by increased interstitial O contamination. The PA parts showed typical keyhole and gas porosity formation.
- The PA parts contained Nb-Mo spherical precipitates due to inhomogeneity in the powder. In the ISA parts, the dendritic shape, resulting in an increased surface area to volume ratio, of Mo particles meant they dissolved in the melt pool more readily than the angular Nb particles. The volume of un-melted Nb reduced with the use of high VED parameters, creating a single phase microstructure, while also suppressing keyhole formation due the presence of large powder particles. However, this is only possible as the boiling points of the other elements in the alloy are sufficiently high.
- ISA resulted in equiaxed grain growth due to heterogeneous nucleation on un-melted, or partially melted, high melting point element particles, whereas the PA parts showed a typical AM columnar grain structure with a texture in the <100> direction. Larger grains were formed in the high VED ISA sample compared to the low VED, due to the reduced amount of un-melted high melting point elements providing sites for grain nucleation.
- Overall, it was shown that representative, near fully alloyed microstructures can be obtained by using ISA of low flowability powders, with consideration that the defect formation, contamination, processing parameters and texture will all be different than that of a PA equivalent. Utilising ISA also means the melt pool shape, grain morphology and grain size can be modified through the effects of unusual powder shapes and sizes. Use of such an approach thereby reduces the cost and time associated with assessing processability

of new HEAs for PBF-LB/M, while also offering the opportunity to modify the resulting microstructure.

Author Contributions

Conceptualisation, L.F., I.T. and R.G.; methodology, L.F., R.S., I.T. and R.G.; investigation, L.F., J.S., and M.M.; software, E.L.; original draft preparation, L.F.; review and editing, R.S., E.L., and R.G.; supervision, I.T. and R.G. funding acquisition, R.G. and I.T. All authors have read and agreed to the published version of the manuscript.

Funding

This work was supported by Science Foundation Ireland 18/EPSRC-CDT/3584, the Engineering and Physical Sciences Research Council EP/S022635/1 and the Manufacture using Advanced Powder Processes (MAPP) EPSRC Future Manufacturing Hub EP/P006566/1. We wish to acknowledge the Henry Royce Institute for Advanced Materials, funded through EPSRC grants EP/R00661X/1, EP/S019367/1, EP/P02470X/1 and EP/P025285/1, for access to the Aconity3D Mini at The University of Sheffield.

Conflicts of Interest

The authors declare no conflict of interest.

Chapter 7

Carbonitride Strengthening of $Mo_5Nb_{35}Ti_{30}V_{30}$ Refractory High Entropy Alloy Manufactured by Laser Powder Bed Fusion

7.1 Author Contributions

Lucy Farquhar - Conceptualisation, methodology, manufacture of samples, sample prep, data analysis, sample characterisation and analysis, writing of original draft.
Jonah Shrive - Operation of microscope for EBSD, support with EBSD analysis
Robert Snell - Support with build file design, writing - review and editing
Elaine Livera - Operation of microscope for EBSD, support with EBSD analysis, writing - review and editing
Luke Jones - Operation of compression testing machine, assistance in writing methodology for compression testing
Hassan Ghadbeigi - Academic lead of compression testing lab
Iain Todd - Supervision
Russell Goodall - Conceptualisation, support with methodology, supervision, writing - review and editing

7.2 Background

Resistance of refractory high entropy alloys (RHEAs) to interstitial infiltration and oxidation is an area of particular interest, as RHEAs are proposed as a potential option to supersede superalloys for high temperature applications [3]. Infiltration of interstitials is usually considered to be detrimental to material properties, especially when uncontrolled at extremely high temperatures. However there are some examples of where interstitial infiltration has been used to the benefit of material properties, in forming protective oxide coatings for example, which prevent further oxidation [327].

A drawback of much high entropy alloy (HEA) research is that many alloys are only reported in the as-cast state, or in the case of AM in the as-built state, therefore not exploring the stability of the phases present. Therefore this work initially aimed to apply a heat treatment to the $Mo_5Nb_{35}Ti_{30}V_{30}$ RHEA in order to assess the stability of its single phase body centred cubic (BCC) microstructure. After heat treatment it became apparent that there had been some atmospheric infiltration that had resulted in secondary phase precipitation, causing the formation of TiCN, a phase which has previously been used to strengthen CoCrFeNi-based HEAs as well as other alloys [328]. Although in the present work it was an unintended consequence of an imperfect inert atmosphere, the precipitation of this secondary phase has positive benefit on mechanical properties and the interstitial infiltration in the BCC matrix increases the compressive strength.

As described in Chapter 2, secondary phase precipitation in RHEAs is an area of interest, with many phases from B2 and Laves phases, to carbides and silicides purposefully precipitated to improve alloy properties. A combination of precipitating beneficial amounts of these phases in conjunction with exposure to low level atmospheric infiltration is something which to the author's knowledge has not been studied for HEAs previously.

N.B. Compression curves for all tests are included in Appendix C.

Paper: Carbonitride strengthening of $Mo_5Nb_{35}Ti_{30}V_{30}$ refractory high entropy alloy manufactured by laser powder bed fusion

Lucy Farquhar[1], Jonah Shrive[1], Robert Snell[1], Elaine Livera[1], Luke Jones[2], Hassan Ghadbeigi[2], Iain Todd[1], Russell Goodall[1]

1 – Department of Materials Science and Engineering, University of Sheffield, Sheffield S1 3JD, UK

2 – Department of Mechanical Engineering, University of Sheffield, Sheffield S1 3JD, UK

Correspondence: laufarquhar1@sheffield.ac.uk

Abstract

Previous research into refractory high entropy alloys (RHEAs) often focused on optimising alloys with solid solution phases by adjusting elemental compositions and refining microstructure. To be suitable for critical structural applications, formation of secondary phases, such as those seen in the microstructures of many superalloys, is an area which is still in the early stages of exploration for RHEAs. In this work, a new $Mo_5Nb_{35}Ti_{30}V_{30}$ RHEA is manufactured via laser powder bed fusion and subsequently heat treated, inducing the formation of a TiCN phase, initially on cell and grain boundaries (GBs) after 1 hour. After prolonged 24 hour heat treatment the TiCN on the GBs coarsens and the cellular substructure is removed. Samples are then compression tested, all showing ductile failure. Due to the strengthening caused by interstitial elements in the body centred cubic (BCC) matrix phase and micron scale TiCN on GBs, the 24 hour heat-treated samples showed increased compressive strength and similar ductility compared to the as-built samples. TiCN largely grows at a 45° angle from the BCC matrix phase, hence Kernel average misorientation (KAM) maps show dislocation pile up at the phase boundaries and at the high angle grain boundaries in the recovered microstructure. Susceptibility of RHEAs to interstitial infiltration is a concern in the RHEA field, however this work shows that, if controlled, exposure to these elements can result in beneficial dual-phase microstructures and improved material properties as a result.

Keywords

Additive Manufacturing, Laser Powder Bed Fusion, Refractory High Entropy Alloys, Mechanical Properties, Microstructure

7.3 Introduction

High entropy alloys (HEAs) were first proposed in 2004 and are known for their microstructural stability and retained mechanical properties at elevated or cryogenic temperatures [1,2]. They were first defined as containing 5 - 13 elements at 5 - 35 at%, however this definition has since expanded to include differing numbers of elements and compositional variations outside this range. The first refractory HEAs (RHEAs) were proposed in 2010 and have been explored for their potential, in particular for high temperature applications [20]. However, RHEAs are especially difficult to manufacture by conventional methods due to the high melting points of the elements concerned and their susceptibility to oxidation [329]. Vacuum arc-melting has previously been the preferred route to manufacture these materials [63, 64, 330, 331], but more recently additive manufacturing (AM) has gained popularity as a method by which to produce homogeneous RHEAs [3, 151, 154]. AM also offers the advantage of being able to create near-net shape components, reducing the amount of machining required, and providing a benefit as refractory metals typically are difficult to machine by conventional machining methods [170].

In AM, parts are built up layer by layer allowing geometries that are not manufacturable by traditional means and reduced material wastage. Laser powder bed fusion (PBF-LB/M) is a type of AM process where parts are built by sequentially melting layers of powder deposited in a powder bed using thermal energy supplied by a focused high-powered laser beam. Few RHEAs have been manufactured using this method and where they have, it is often through the use of blended elemental powders due to the cost and difficulty associated with manufacture of bespoke RHEA powder [7, 203–206]. Very few publications have therefore manufactured RHEAs via PBF-LB/M with pre-alloyed powders, with only a few using optimised spherical powders [207–209].

Generally, HEAs were initially appealing as a research area due to the expectation of their tendency to form single solid solution phases, stabilised by high mixing entropy. But more recently, efforts have been made to initiate the formation of beneficial precipitates and secondary phases in RHEAs, such as carbides and nitrides, to increase strength, while maintaining the ductility afforded by a solid solution phase [73–75, 77–79, 85, 87]. However, using AM in isolation or even along with post-process heat treatment to produce carbide or nitride secondary phases in RHEAs is still not common practice [76, 173, 332]

In this work a $Mo_5Nb_{35}Ti_{30}V_{30}$ RHEA is manufactured via PBF-LB/M. Resulting samples are

then subjected to heat treatment, to reduce residual stress and to recrystallise cellular substructures, but also to promote the formation and growth of a secondary carbonitride phase TiCN, caused by atmospheric infiltration. These samples, along with samples in the as-built condition are compression tested to assess the effect of the precipitated TiCN phase and interstitial elements on strength and ductility. The work reported here illustrates that although infiltration of atmospheric impurities is often detrimental to material properties, the controlled exposure to small amounts of interstitials and secondary phase formers during heat treatment can result in enhanced mechanical performance of RHEAs.

7.4 Materials and Methods

The powder feedstock in this work was produced by multiple melting in a cold copper crucible, followed by crushing and radio-frequency plasma spherodisation by Metal Powder Emergence, UK. The powder was sieved through a 52 μm sieve prior to use, All specimens were manufactured using the reduced build volume adaptation on an Aconity3D Mini PBF-LB/M machine, with a laser spot size of 70 μm and a maximum laser power of 190 W in an inert argon atmosphere. 8 mm $\times$ 8 mm cylindrical samples were manufactured on a 55 mm diameter Ti-6V-4Al substrate for compression and microstructural analysis. Prior to this work an iterative statistical design of experiment was completed in order to obtain optimal PBF-LB/M parameters to ensure nominally dense parts. The resulting parameters which are used in this work are: laser scanning velocity 600 mm/s, hatch spacing of 17 μm, power 190 W, layer height of 30 μm and a hatch rotation angle of 67°. After removal from the substrate, five samples were left in the as-built (AB) condition while others were heat treated. Heat treatments were completed in an inert furnace with argon gas flow and a Ti getter, where samples were put into a pre-heated furnace and then furnace cooled. Five samples received a 1 hour heat treatment (1HT) at 1200°C to reduce residual stress and five other samples were heat-treated for 24 hours (24HT) at 1200°C to attempt recrystallisation and possible secondary phase precipitation. Quasi-static compression testing on the samples was completed using a 250 kN capacity Schenck servo-hydraulic Universal Test Machine, with a fixed crosshead displacement rate such that a strain rate of 0.001 s^{-1} was achieved in the elastic region. Four samples of each type were compressed parallel to the build direction. Samples were placed centrally in custom manufactured compression platens with a diameter of 50 mm and a surface hardness greater than 400 HV. The platens were lubricated with machine oil to reduce barrelling. The test was stopped when the load exceeded 200 kN. For microstructural characterisation, all samples, including those compression tested, were sectioned parallel to the compression/build direction and were prepared using standard material grinding and polishing methods.

The particle size distribution (PSD) for the powder was analysed using a laser diffraction par-

ticle size analyser (Mastersizer 2000, Malvern, UK). Inductively coupled plasma optical emission spectroscopy (ICP-OES) was used to assess metallic element content of the powder, AB and heat-treated samples. O and N content was found using thermoconductivity and infra-red (IR) absorption (Eltra ONH 2000 Analyser) and the C content was obtained using combustion/IR analysis. All bulk elemental analysis was done by Sheffield Assays, UK following the ATM167, ATM149 and ATM82 standards. Phase characterisation was performed by X-ray diffraction (XRD) on a Bruker D2 Phaser Diffractomer using a Cu K_α ($\lambda = 1.54$ Å) radiation source. Scanning electron microscopy (SEM) was carried out on the AB and heat-treated samples before compression, using a FEI Inspect F50 SEM. Analysis was completed with a working distance of approximately 10 mm, where the accelerating voltage and spot size were 20kV and 3.5 respectively. Electron backscattered diffraction (EBSD) and energy dispersive X-ray spectroscopy (EDS) was conducted using a JEOL 7900F field emission gun (FEG)-SEM, equipped with an Oxford Instrument's symmetry detector. An accelerating voltage of 20 kV was used, along with a step size of 0.4 µm, to characterise texture and a step size of 0.018 µm to study precipitate formation. Grain reconstruction was performed using MTEX software with low and high angle grain boundary (HAGB) thresholds of 3° and 10° respectively [316]. Inverse pole figure (IPF) maps, pole figures and kernel average misorientation (KAM) maps were produced from the reconstructed data.

7.5 Results and Discussion

7.5.1 Powder Analysis

As can be seen in Figure 7.1, the powder is largely spherical, however some smaller clusters of satellite particles are present. These smaller particles are reflected in the PSD, which also indicate the presence of particles above 52 µm, despite being sieved prior to use. The percentile D_{10}, D_{50} and D_{90} values for the PSD, are 11.9 µm, 28.0 µm and 57.3 µm respectively. The larger particles are most likely caused by agglomerates of the finer particles, or by elliptical particles that are able to pass through the sieve. These have two dimensions below the mesh size due to incomplete spherodisation in the powder production process. Nb and Mo rich particles, which deviate from the nominal composition, are also present in the powder. In some particles, the Nb and Mo content reaches up to 75 at% and 10 at% respectively, with Ti and V compositions remaining constant throughout.

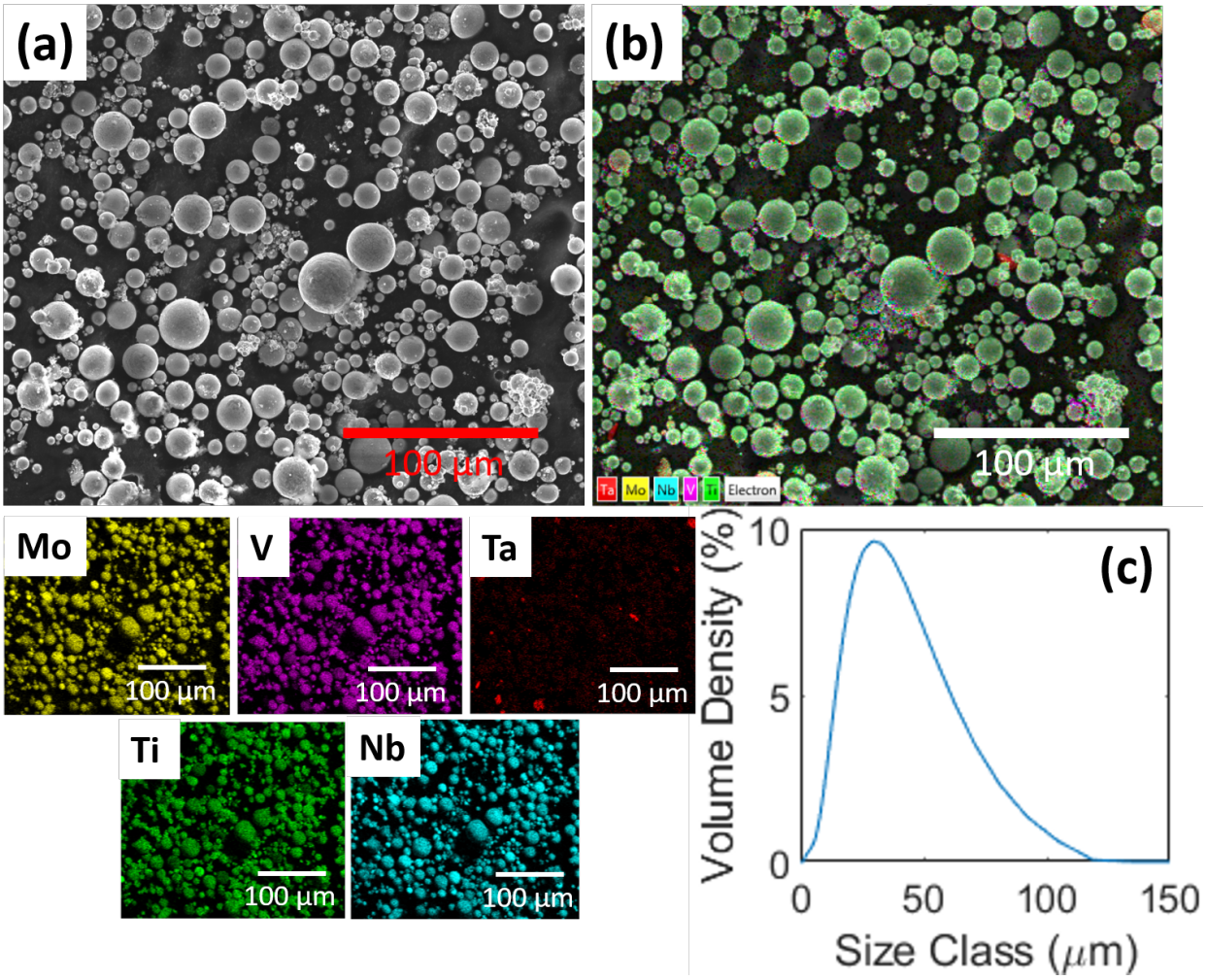

Figure 7.1: *(a) Backscattered electron (BSE) image showing the powder feedstock used, (b) Overlaid EDS map showing the elemental distributions, along with maps for each element in the nominal composition as well as the contaminating Ta, (c) PSD for the powder.*

7.5.2 Bulk elemental analysis

ICP-OES results for the powder and all bulk samples are shown in Table 7.1. The values of measured composition for the constituent elements are all within 2 wt% of the nominal composition with Nb showing the greatest deviation. There is a high level of O, N and C reported, which could cause the formation of pores, balling, cracking or microstructural variability that would not otherwise be present without these interstitial elements [333–335]. RHEA powders such as this are difficult to manufacture due to the high temperatures needed for melting as well as their tendency to oxidise. Therefore, it is likely that the crushing and spherodisation manufacturing route introduced more O into the powder than other routes, such as electrode induction gas

atomisation (EIGA), would have [336]. However, the contamination of O, and particularly N, could also be due to prolonged storage of the powder before ICP-OES was conducted (a period of 9 months storage after manufacture), therefore not giving an accurate representation of the O and N content of the manufactured samples.

The powder, and therefore also the corresponding bulk samples, also contain approximately 0.3 wt% Ta contamination, which has been introduced in the manufacturing process. After further analysis some Ta-rich powder particles were found in the powder feedstock as shown in Figure 7.1. After PBF-LB/M, the AB sample shows a small increase in O, N and C content, which is typical after an AM process [333]. The O content also increases with increasing heat treatment time, due to the infiltration of atmospheric gases. According to these results, both the C and N increase after 1HT, and then reduce after 24HT, which is unexpected, as further results in this work indicate an increase in these elements, due to the precipitation and coarsening of the TiCN phase. There are many potential reasons for this, including a change in the composition of the heat treatment atmosphere between the two heat treatments, therefore the discrepancy between these results is likely within the margin of error for detection of these elements.

Table 7.1: *Elemental composition of the powder feedstock, AB, 1HT and 24HT samples, compared with the nominal composition, including entrained O, N and C.*

Element (wt%)	**Mo**	**Nb**	**Ti**	**V**	**Ta**	**O**	**N**	**C**
Nominal	7.16	48.6	21.4	22.8	-	-	-	-
Powder	7.47	50.2	20.8	21.3	0.31	0.073	0.091	0.086
AB	7.56	50.6	20.4	21.1	0.35	0.13	0.13	0.097
1HT	7.65	51.0	19.9	20.8	0.32	0.27	0.23	0.093
24HT	7.64	51.3	19.7	20.6	0.34	0.45	0.18	0.083

7.5.3 Microstructure

Figure 7.2 shows EBSD maps and pole figures for the AB, 1HT and 24HT samples. The AB sample shows epitaxial columnar grain growth, typical of AM processes, resulting in a texture in the <100> direction, which here aligns with the build direction in these images. The texture of the samples reduces with heat treatment time, however it has not been completely removed and is still partially present in the 24HT sample.

As well as partial re-crystallisation, XRD scan results, shown in Figure 7.3 indicate that all samples have a main body centred cubic (BCC) phase with a lattice parameter between 3.210 and 3.224 Å. The peak corresponding to the (200) plane in the AB sample has a lower peak intensity due to sample orientation in the XRD scan, as the EBSD does not indicate a change in

grain orientation substantial enough to cause this reduction. The samples show the appearance of small peaks at 35.6° and 42.4° after heat treatment, corresponding to the onset of formation of a secondary phase. The EBSD phase maps and EDS results for the 24HT sample are shown in Figure 7.4, where the secondary phase has formed on the GBs of the BCC matrix grains. These phases have been identified as a solid solution of both TiC and TiN which both have very similar peak positions and are both face-centred cubic (FCC) structures, otherwise known as TiC_xN_{1-x}, here referred to as TiCN. Phase maps for the 1HT and 24HT samples in Figure 7.4, confirm the formation of this FCC TiCN phase. The exact level of C and N content in this phase was unable to be resolved with EDS, as the precipitates are less than 1 µm in size, however broadly speaking Ti content stays consistently between 26 at% to 30 at%, while C and N remain elevated above the content in the surrounding phase.

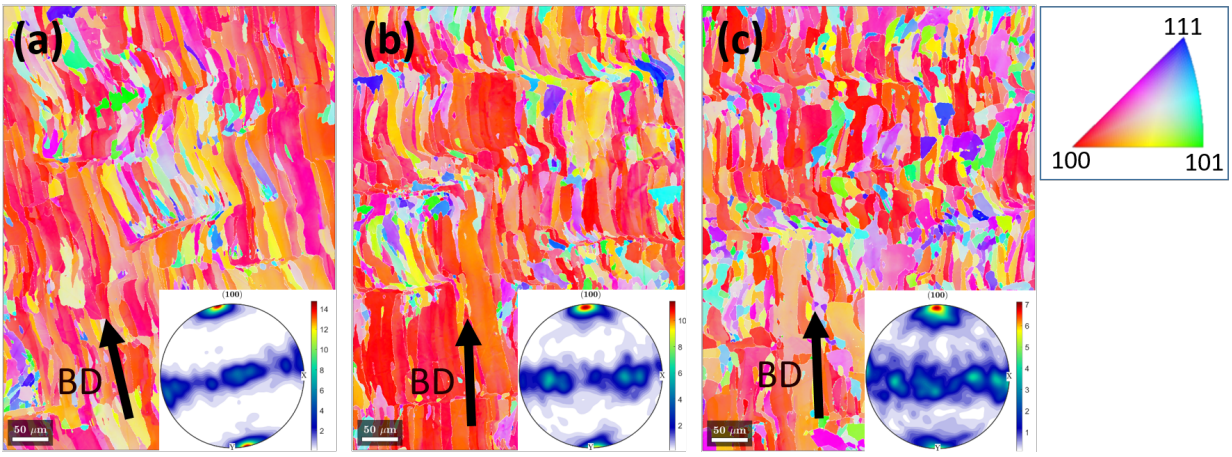

Figure 7.2: *EBSD inverse pole figure (IPF-Y) images and corresponding (100) pole figures for (a) as-built, (b) 1HT and (c) 24HT, showing microstructural texture and the onset of grain recrystallisation. BD here stands for build direction from the PBF-LB/M process.*

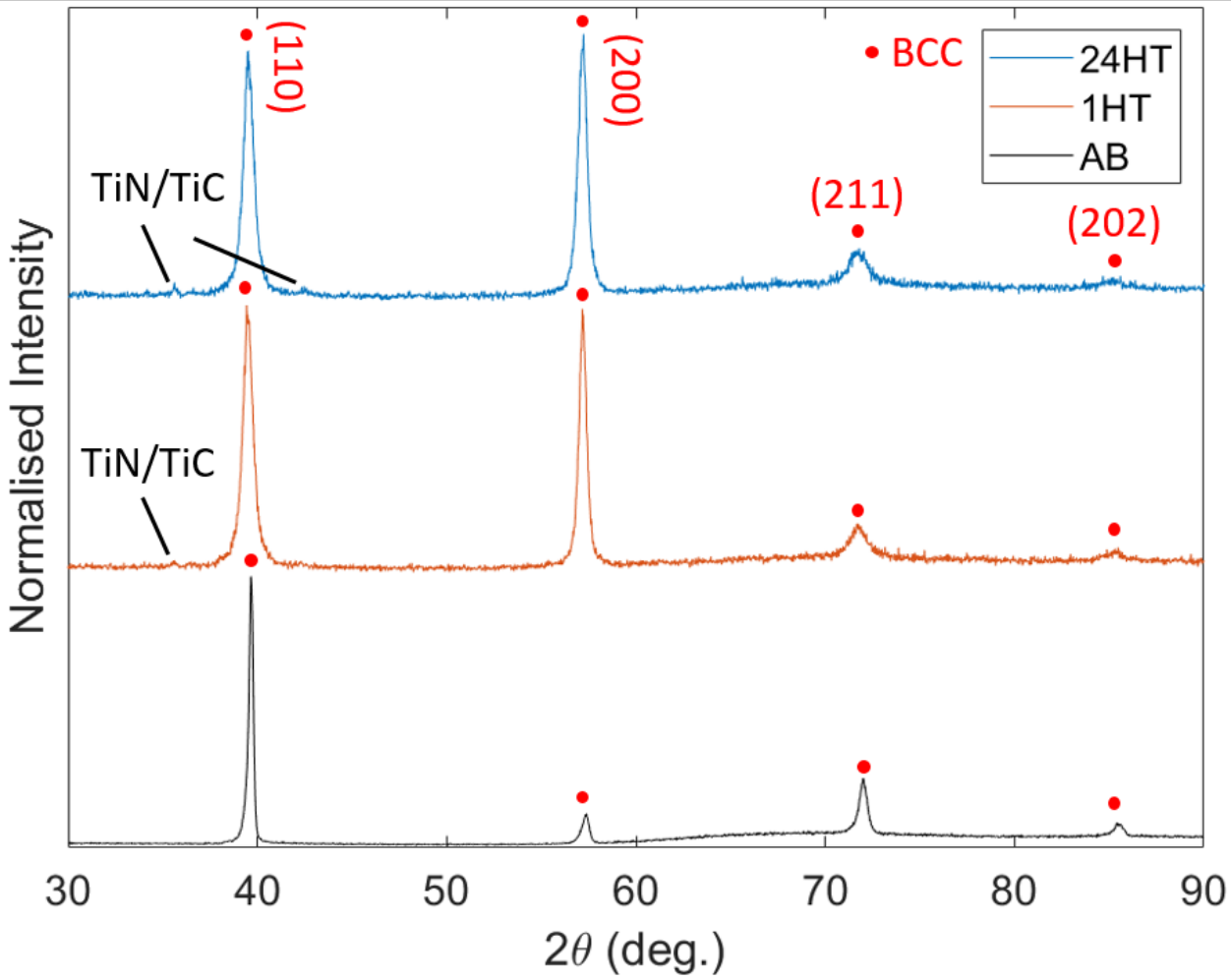

Figure 7.3: *XRD patterns of the AB, 1HT and 24HT samples, showing the onset of the formation of TiCN.*

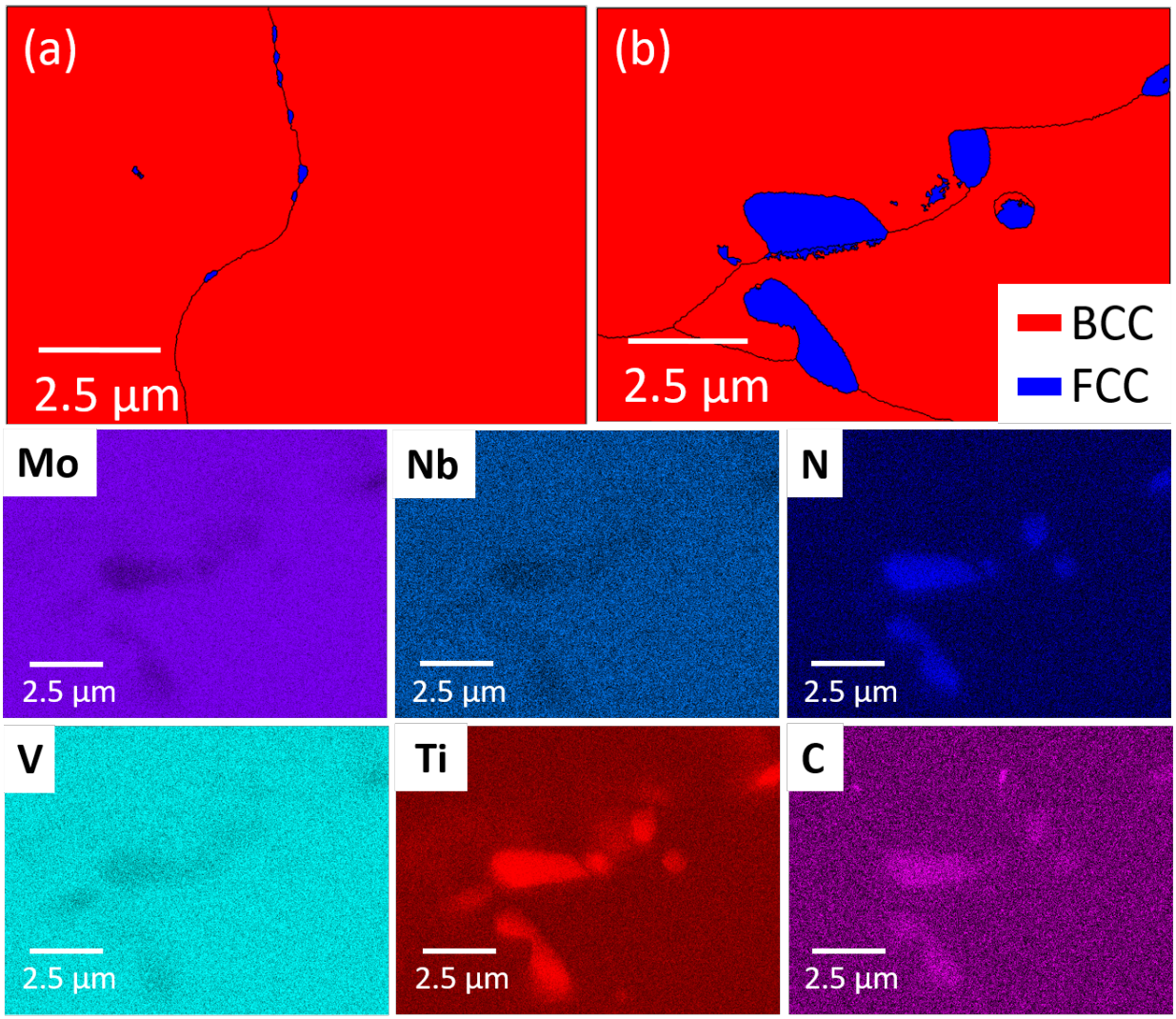

Figure 7.4: *(a) Phase maps of the 1HT, showing the start of the formation of FCC TiCN. (b) Phase map of the coarsened GB TiCN phase in the 24HT sample, along with EDS maps showing the distribution of elements in the nominal composition, as well as N and C in the TiCN phase.*

Figure 7.5 shows the secondary phase precipitation and growth after differing heat treatment times. The AB sample shows the formation of dislocation cells within grains, the size and shape of which correspond with the position in the melt pool. But no precipitation of a secondary phase. After heat treatment for 1 hour, the secondary phase has begun to precipitate on the GBs and partially on the cell boundaries (CBs), which have not yet recrystallised, a phenomenon seen previous in heat-treated nickel-based alloy samples made by PBF-LB/M [337, 338]. The size of the TiCN precipitates on the CBs varies significantly between 10 - 600 nm in size, following the pattern of cells left by the solidification of successive melt pools and are finely dispersed with a needle-like shape on the CBs. The TiCN present on GBs is clustered and interconnected, with

sizes from 100 nm - 1 µm as seen in Figure 7.4.

In the 24HT sample, the dislocation cells have recovered leaving a small number of larger remaining intragranular secondary phase particles. However, the majority of these precipitates have likely dissolved into the matrix phase forming interstitials in the BCC lattice, or have diffused to GBs; EDS was however unable to resolve the change in C content. Due to the diffusion and infiltration of further N and C, the secondary phase has coarsened and is now most often present on GBs, and the size of the TiCN is now between 1 µm - 4 µm in length.

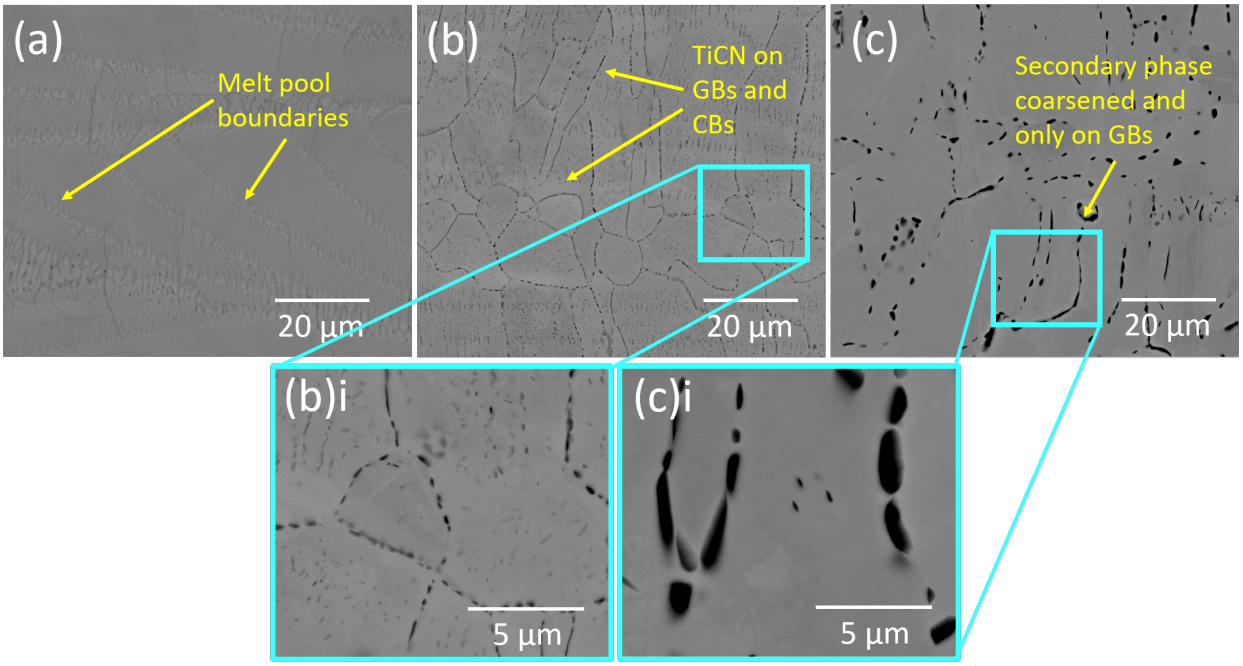

Figure 7.5: *BSE images of the (a) AB, (b) 1HT and (c) 24HT samples showing the formation and evolution of the secondary phase and the recovery of the cellular microstructure. (b)i and (c)i show high magnification BSE images of the shape and size of TiCN precipitation in the 1HT and 24HT samples respectively.*

An example of the TiCN precipitates in the 24HT sample and the corresponding GB misorientation map is shown in Figure 7.6. In the misorientation histogram there is a high intensity peak at 45° showing the prevalence of this angle of misorientation between grains. Considering the misorientation map, this angle likely corresponds to the growth of the TiCN secondary phase from the BCC phase. Consideration of atomic structures between these two phases, shown in Figure 7.6 give evidence of a structural correspondence at this angle. A growth mechanism for the TiCN phase is proposed in the schematic shown in Figure 7.6 (d), where the FCC phases grow from the $\{110\}$ plane in the BCC matrix phase, to become the $\{100\}$ plane in the FCC phase. For this to achieve a 45° misorientation with correspondence of the atomic sites with a BCC phase of given lattice parameter a, the lattice parameter of the FCC phase must be approximately equivalent to

$a\sqrt{2}$. Here the lattice parameter of the BCC phase is approximately 3.22 Å so $a\sqrt{2} = 4.55$ Å. The lattice parameter of the TiCN phase in this case is between $a_{FCC} = 4.24$ Å (TiN) or $a_{FCC} = 4.33$ Å (TiC). It can therefore be suggested that the TiCN often nucleates on GBs of BCC grains and grows into a neighbouring grain, resulting in 45° GB on one edge of an elongated FCC grain. Alternatively, where diffusion to the GB has not occurred after the annealing of the cellular microstructure, TiCN has formed with a 45° total misorientation from the surrounding grain.

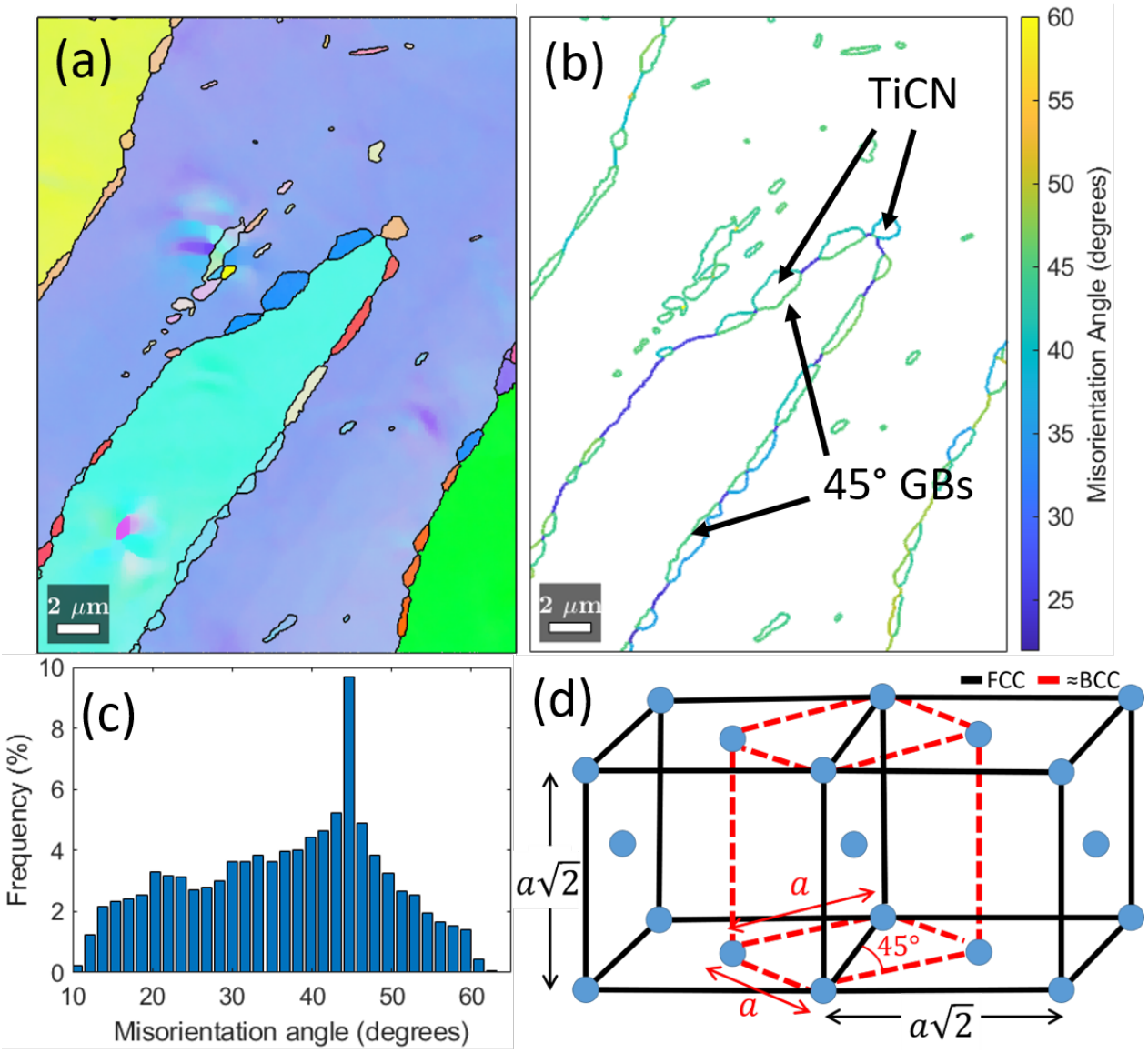

Figure 7.6: *(a) EBSD IPF-Y map of 24HT sample and the GB TiCN secondary phase present. (b) Map of GB misorientations in the 24HT sample. (c) Misorientation histogram for the EBSD image of the 24HT samples shown in Figure 7.2, with a peak at 45° corresponding the secondary phase growth direction. (d) Schematic of the growth mechanism of the FCC TiCN phase from the BCC matrix phase.*

7.5.4 Mechanical behaviour under compression

Representative true stress vs. true strain curves and the corresponding yield strength values for the AB, 1HT and 24HT samples are illustrated in Figure 7.7. All samples exhibited ductile failure and all reached the force limit of the compression test equipment used at 200 kN, with the heat treated samples showing some spallation of surface oxides at higher strains. The AB sample has a high mean yield strength of 1179 MPa, due to the hierarchical microstructure present, including melt pools, columnar grains, cellular sub-structures and high dislocation density, all of which impede dislocation motion [177]. However as many of these structures are still present in the other samples, it is thought that the high strength is also influenced by the residual stress commonly induced during AM. Due to the AM processing, high tensile stresses are induced at the edges of the part and compressive stresses are induced at the centre [249, 305, 339]. Therefore the high initial residual tensile stresses within the parts may be resulting in an apparent increase in the compressive strength [340].

The 1HT sample has a texture much the same as the AB sample and retains the cellular sub-structures, along with the onset of precipitation on GBs and CBs. In theory this alone should result in an increased strength, due to secondary phase strengthening and increased GB misorientation. However the mean yield strength of this sample is 960 MPa, a reduction compared to the AB sample. This is likely due to the reduction in residual stresses resulting from even a short heat treatment [341]. The initial hardening rate of this sample is similar to that of the AB sample, indicating that these samples are plastically deforming via the same dislocation slip mechanisms and that the nano precipitation of the secondary phase is having very little effect on creating dislocation pile up. However, due to the reduced yield stress the total strain of the sample at 200 kN is comparable to that achieved by the 24HT sample.

In the 24HT sample, the cellular substructure has been completely removed and the secondary TiCN phase has coarsened and resides mostly on GBs. This sample has a vastly reduced dislocation density compared to the other samples, leading to an increase in ductility and reduction in hardening rate. However the increase in TiCN concentration indicated by XRD as well as the infiltration of interstitial contaminants such as O, C and N, has meant that the material also has an increased compressive yield strength of 1213 MPa, surpassing that of the AB samples.

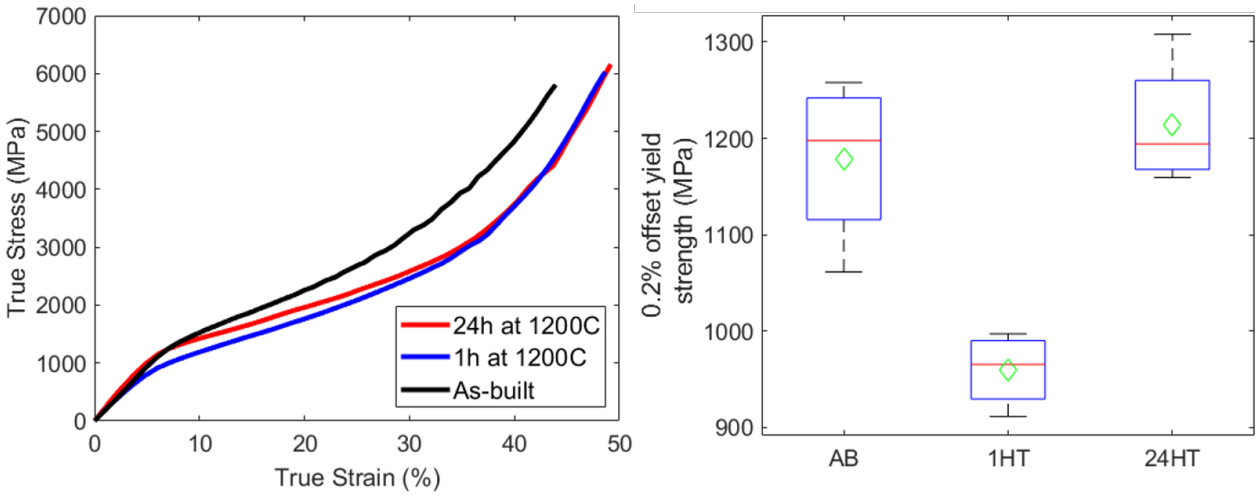

Figure 7.7: *Example true stress vs. true strain curves for compression of the AB, 1HT and 24HT samples and boxplots for the 0.2% Offset compressive yield stress for each sample type. Median values are shown with a red line and mean values are shown by a green diamond.*

7.5.5 Deformed Microstructure

EBSD and kernel average misorientation (KAM) maps for the AB, 1HT and 24HT samples are shown in Figure 7.8. Each of the 3 samples show shearing of the grains present at 45°, consistent with the angle of maximum shear stress in uni-axial compression. The AB sample displays the CBs indicated by the oval structures within grains with higher KAM values. The high level of misorientation and therefore dislocations still distributed throughout this sample due to the cells, explains the high strength and reduced ductility shown in the compression curve as the motion of dislocations is impeded. The level of non-indexed areas and KAM at GBs in the AB sample is also reduced compared to the heat treated samples, indicating there is less dislocation build up in those areas.

The 1HT sample has a much higher average KAM and much more non-indexed areas compared to the other samples. There is also a slight development from the oval shaped cell morphology seen in the KAM for the AB sample, although this could be attributed to the grains which are imaged. Due to the relief of residual stress to reduce the yield strength, for the same maximum load, there is an increase in plastic deformation consistent with the compression curve, ending in a strain of 63 % compared to 55% for the AB sample. The fine nano-TiCN secondary phase precipitates also create HAGBs and barriers within grains which increase the number of isolated dislocation pile ups which is reflected in the non indexed pixels in this sample. Therefore there are no micro-scale dislocation pile ups which traverse a whole grain on the same plane as there are in the 24HT sample. However despite the strengthening effect commonly associated by these

types of precipitates and slight interstitial infiltration, the effect of reduced residual stress has had a larger influence causing a reduced yield strength.

In the 24HT sample, there are bands of increased misorientation and therefore increased slip across grains which were previously recovered, removing the cellular structures. These bands correspond to the <111> direction, the predominant slip direction in BCC materials [342]. This explains why there extensive 45° slip bands in grains 1 and 2, but little deformation in grain 3, as the critical resolved shear stress for 1 and 2 is higher for those grains which are more aligned with the <111> direction. The enhanced ductility of this sample is due to the unimpeded dislocation motion within the recrystallised grains, which also explains why the highest KAM contrast is found interconnected to the GBs. After slip within the grains, dislocation pile up is due to either the coarse TiCN secondary phase particles, or HAGBs, which are more predominant in a sample which is partially recrystallised compared to the AB sample. This analysis confirms that substantial strengthening must come from both the increased TiCN content and interstitial solid-solution strengthening in the BCC lattice, and the increasing ductility is due to the removal of the cell structures.

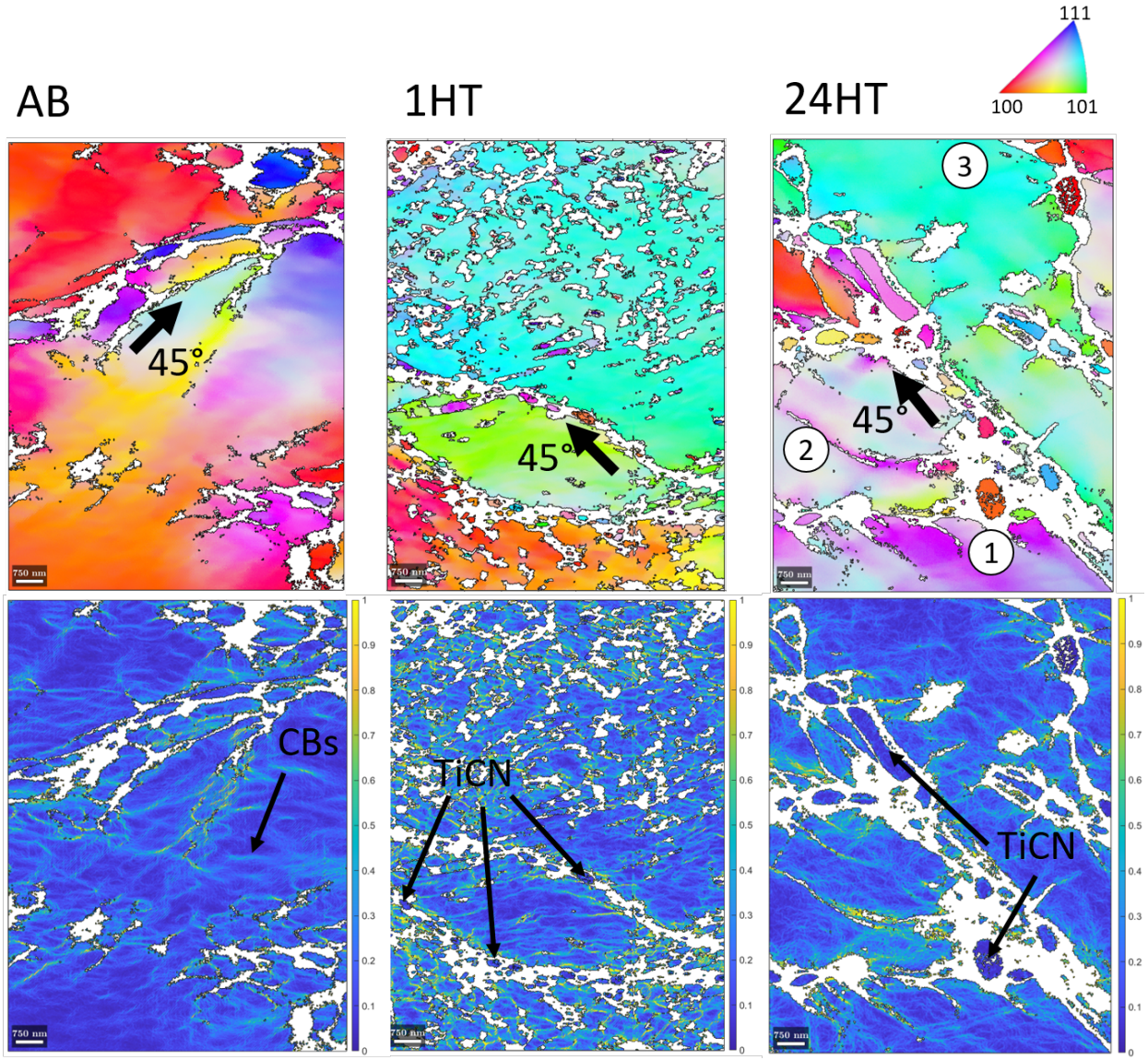

Figure 7.8: *EBSD IPF-Y images and KAM maps showing the deformed microstructures of the AB, 1HT and 24HT samples. The white areas represent non-indexed pixels, due to extensive misorientation within the step size used. The vertical direction in these images corresponds to both the build direction and the compression direction. The colourbar for the KAM maps represents the KAM angle in degrees and the shear slip angle of 45° is also indicated.*

7.6 Conclusions

In this work, the new RHEA $Mo_5Nb_{35}Ti_{30}V_{30}$ was manufactured via PBF-LB/M and heat treated. A secondary phase precipitated after heat treatments, due to the partial infiltration of N and C, creating fine precipitates after 1 hour and coarse GB precipitates after 24 hours at 1200°. The

corresponding samples were compression tested and the results analysed along with the deformed microstructure. The key findings are summarised as follows:

- Pre-alloyed powder was used to manufacture samples which were then heat treated to reduce residual stress, recover the cellular microstructure, achieve a reduction in texture, and precipitate secondary phases.
- Infiltration of atmospheric impurities in the heat treatment resulted in the precipitation of a TiCN secondary phase in heat treated samples with varying C and N content, as confirmed by XRD and EBSD phase analysis and bulk elemental analysis. The level of interstitial O also increased with heat treatment time.
- A fine TiCN phase precipitated on the CBs and GBs on the 100 nm scale in the 1HT sample, while in the 24HT sample, after removal of the sub-structures, the TiCN diffused, increase in concentration and coarsened on GBs to a micron scale.
- The FCC TiCN preferentially grows at a 45° angle on the GBs of the BCC matrix phase, creating a HAGB between the phases.
- Compression testing showed that for 24HT the increased amount of TiCN and interstitial elemental content resulted in increased compressive strength while the ductility increased due to removal of cells and coarsening of the TiCN when compared to the AB samples.
- The infiltration of interstitial elements, often thought of as deleterious especially to refractory materials, has here been shown to enhance material strength without compromising ductility. Thereby using the affinity of RHEAs to react with atmospheric interstitial elements as an advantageous way to strengthen these types of alloys.

Author Contributions

Conceptualisation, L.F., I.T. and R.G.; methodology, L.F., R.S., I.T. and R.G.; investigation, L.F., J.S., L.J., H.G. and M.M.; software, E.L.; original draft preparation, L.F.; review and editing, R.S., E.L., and R.G.; supervision, I.T. and R.G. funding acquisition, R.G. and I.T. All authors have read and agreed to the published version of the manuscript.

Funding

This work was supported by Science Foundation Ireland 18/EPSRC-CDT/3584, the Engineering and Physical Sciences Research Council EP/S022635/1 and the Manufacture using Advanced Powder Processes (MAPP) EPSRC Future Manufacturing Hub EP/P006566/1. We wish to acknowledge the Henry Royce Institute for Advanced Materials, funded through EPSRC grants EP/R00661X/1, EP/S019367/1, EP/P02470X/1 and EP/P025285/1, for access to the Aconity3D Mini at The University of Sheffield.

Conflicts of Interest

The authors declare no conflict of interest.

Chapter 8

Conclusions

This project aimed to design and develop tools to assist with high throughput alloy development for alloys suitable for additive manufacturing (AM), using high entropy alloys (HEAs) as an example of a group of alloys showing promise for many applications. Where methods were already described in literature, these methods have been explored for their success and limitations when used with HEAs, such as in-situ alloying (ISA). Where a method which could be applied for HEA systems did not exist, such as a solid-state cracking indicator, a new method was proposed, which could be globally applied to any alloy system.

Chapters 3 and 6 focused specifically on ISA and the considerations required for successful production of homogeneous HEAs via this method. Chapter 3, explored the effect of adding different elemental powders to a base CoCrFeNi powder. The additions of Cu and Ti result in the formation of vastly different microstructures and phases when manufactured by conventional methods, and this was reflected in the samples manufactured by AM. If an element caused segregation in a arc-melted sample then similar phases were found to occur in AM, but on top of this the alloying of that additional element is hindered by the inherent tendency to segregate and miscibility of that element in the matrix phase, such as with the CoCrCuFeNi alloy. Unsurprisingly, binary interactions between elements often result in brittle intermetallic phase formation, such as TiNi in the CoCrFeNiTi, resulting in extensive cracking, exacerbated by the availability of un-alloyed elemental Ti, providing sites for crack initiation. The other consideration of importance is the melting temperature of the elemental addition compared with the base powder. If the elemental melting temperature is considerably less than the base powder than this could cause gas porosity or excessive vaporisation resulting in deviation from the nominal composition. If the elemental melting temperature is higher, then a much higher volumetric energy density (VED) is required to initiate alloying to avoid un-melted elements.

Empirical parameters such as atomic size mismatch δ and the enthalpy of mixing ΔH_{mix} are used to predict solid-solution phase formation for a pool of over a million quaternary HEAs in

Chapter 4. Alloys were filtered through limits set on the parameters for multi-phase solid-solution formation, as well as melting temperature, melting temperature range and density. The top 9 ranked alloys were then manufactured via arc-melting resulting in 4 alloys which had single or multi-phase BCC solid-solution phases, 3 alloys with complex intermetallic or unidentified phases and 2 alloys which had manufacturing issues and were not produced in a well-alloyed form. Despite the low success rate of this approach, new alloys in relatively unexplored compositional spaces were predicted successfully, suggesting many new alloys which were then explored in Chapter 5, for their AM processability.

Chapter 5 concerns predicting the cracking behaviour of alloys for additive manufacturing. Along with use of the Kou solidification cracking indicator (SCI), a new solid-state cracking indicator, based on considering the effect of bond energy on toughness (SSCI), is introduced. This cracking parameter is then validated based on melt tracks completed on arc-melted samples of 4 of the alloys produced in Chapter 4 and the CoCrFeNi-based alloys in Chapter 3, as well as 12 alloys from literature with varying AM processability. The SSCI successfully predicts the cracking behaviour in all 12 of conventional alloys from literature and 5 out of 7 of the HEAs. There are limitations on the SSCI for two reasons. The first is that if the alloy is susceptible to solidification cracking, such as the CoCrCuFeNi alloy, then this can also often result in the initiation solid-state cracks. If extensive solidification cracking is present then the stress fields experienced in AM may be enough to propagate solid-state cracks further, which may not have been the case had those solidification cracks not been there. The second reason is that the SSCI relies on bulk material properties such as elastic modulus, therefore if there are even small amounts of brittle phases with vastly different properties, then this can compromise crack resistance, despite not being indicated by bulk properties. This seems to apply mainly to alloys with extremely deleterious non-optimised phases which severely compromise ductility, despite the presence of a more ductile phase, such as the CoCrFeNiTi alloy with multiple intermetallic phases in a face centred cubic (FCC) matrix.

In Chapter 6, the effect of powder size, shape and contamination on ISA is considered for the $Mo_5Nb_{35}Ti_{30}V_{30}$ refractory HEA (RHEA) and the corresponding samples are compared with those manufactured from pre-alloyed powder. In the powder blend, only the Ti powder was spherical, compromising the powder flowability, likely causing crack-like defects in the samples. However, due to the size and shape of the Mo powder compared to the large angular Nb particles, the Mo was almost homogeneously distributed despite having a higher melting point than Nb. The powder blend also had much higher O contamination than the pre-alloyed powder, mainly due to the O contamination of the elemental V. Typical of many RHEA powders, where full alloying is difficult due to the high temperatures involved, the pre-alloyed powder contained in-homogeneous powder particles with high levels of Nb-Mo and other particles with high Ta content. The VED required for alloying of the blend powder was significantly higher than that required for high density parts

in the pre-alloyed powder, which also did not show a fully homogeneous microstructure due to the Nb-Mo enriched particles. Similar to many other studies on ISA, the resulting microstructure for the powder blend was equiaxed due to nucleation of grain growth on high melting point element particles, compared to the <100> texture in the pre-alloyed samples, resulting in smaller grains but higher grain boundary misorientations. It was demonstrated that representative microstructures can be obtained by using off-the-shelf low flowability powders, while considering the defects, contamination, processing parameters and texture will differ from the pre-alloyed equivalent.

Following the manufacture of $Mo_5Nb_{35}Ti_{30}V_{30}$ RHEA in Chapter 6, Chapter 7, concerns post-process heat-treatment and compression testing to ascertain mechanical properties. It was found that due to atmospheric infiltration, nano-scale TiCN precipitated on cell and grain boundaries, coarsening to a micron scale after a longer heat treatment time. When compression tested it was found that after 1 hour heat treatment, the yield strength reduced due to the reduction in residual stress but after 24 hour heat treatment, there was an increase in the compressive strength and no reduced ductility. This can be attributed to a few factors: removal of the cellular substructure increasing ductility, the coarser TiCN phase pinning grain boundaries and impeding dislocation motion increasing strength and the content of interstitial elements (C, N and O) in the BCC matrix contributing to increased strength. Illustrating that when controlled, atmospheric infiltration, often seen as detrimental to material properties especially for refractory materials, can result in an improvement in material properties.

Overall, this thesis has illustrated that accelerated alloy development for AM still requires extensive experimentation, however there are some predictive methods and alternative investigations which can be used to reduce the time and cost. ISA is here proposed as a viable alternative by which to produce representative microstructures via AM, if the considerations involving elemental interactions and powder characteristics outlined here are employed. Predictive parameters for cracking can also be applied to new HEAs with some confidence in order to assess AM processability without manufacture of powder, while considering the limitations of alloys with extremely brittle phases and the interplay between cracking mechanisms. RHEAs for high temperature applications need to be designed with stable multi-phase microstuctures, therefore an insight into the precipitation of secondary phases in post processing was outlined in this work. Though once alloy databases are improved in quality and quantity, the design of alloys with these microstructures can be accelerated to find even more complex and effective alloy systems.

Chapter 9

Future Work

There is a broad scope of work which could possibly follow on from this thesis:

- Development of knowledge about TiCN precipitation in the $Mo_5Nb_{35}Ti_{30}V_{30}$ RHEA. This would include heat treatment trials with controlled infiltration of atmospheric gases, in order to see the development of the precipitates and understand their growth more thoroughly. This could also help in understanding the limits of improvements in mechanical performance caused by atmospheric infiltration and at what point the effects would start to become deleterious to mechanical properties. Studies into the precipitation of TiCN by feeding with pure N gas or with the addition of C, in the form of TiC for example, would be useful to understand the impact of the TiCN or TiN/TiC in isolation of the infiltration of O or other atmospheric elements.

- Investigate the stability of the BCC single phase of the $Mo_5Nb_{35}Ti_{30}V_{30}$, in a vacuum furnace without infiltration of interstitial elements. This would be useful to understand if BCC phase decomposition occurs if held at high temperatures for prolonged periods. A heat-treatment trial in a high vacuum atmosphere would also reveal the heat-treatment time and temperature necessary for grain growth in pre-alloyed powder samples.

- Further exploration is also required into the mechanical properties of the $Mo_5Nb_{35}Ti_{30}V_{30}$ RHEA. High temperature tensile testing is necessary to investigate whether strength is retained at high temperatures as it is with many other RHEA systems. Fractography would also be useful to be able to understand the fracture mechanisms to gain insight into how to optimise further the morphology of the precipitates and microstructure.

- Understand more about the limits of AM processability of the $Mo_5Nb_{35}Ti_{30}V_{30}$ RHEA. This could include assessing suitability for heat exchanger applications by building of thin walled samples and assessing the effect of residual stress.

- Investigate further the effect of ISA on part post-processing, including whether full homogenisation is possible after partial alloying the AM process, possibly investigating hot isostatic pressing (HIP) of ISA microstructures.

More generally in the HEA field moving forward, the focus is likely to be on reporting of HEAs in the as-cast and homogenised forms to ensure that databases contain accurate information about alloy stability. This should in turn make ML and CALPHAD modelling of HEA systems more accurate, therefore making high-throughput alloy design more efficient and allowing accurate assessment of orders of magnitude more compositions. On top of this, as more HEAs are manufactured by AM then the accuracy of predictions for HEA behaviour will also improve, as understanding of the effect of fast cooling rates and multiple heating cycles have on different HEA systems.

Many new RHEAs manufactured by AM and reported in the as-built state are reported with exceptional material properties. However it is likely that many of these microstructures formed are metastable. Since many potential applications for RHEAs involve high temperatures, it is essential that these microstructures are explored after post-processing and prolonged periods at high temperatures.

Chapter 10

Bibliography

[1] B. Cantor, I. T.H. Chang, P. Knight, and A. J.B. Vincent. Microstructural development in equiatomic multicomponent alloys. *Materials Science and Engineering A*, 375-377(1-2 SPEC. ISS.):213–218, 2004.

[2] Jien Wei Yeh, Swe Kai Chen, Su Jien Lin, Jon Yiew Gan, Tsung Shune Chin, Tao Tsung Shun, Chun Huei Tsau, and Shou Yi Chang. Nanostructured high-entropy alloys with multiple principal elements: Novel alloy design concepts and outcomes. *Advanced Engineering Materials*, 6(5):299–303, 2004.

[3] Wei Xiong, Amy X.Y. Guo, Shuai Zhan, Chain Tsuan Liu, and Shan Cecilia Cao. Refractory high-entropy alloys: A focused review of preparation methods and properties, 4 2023.

[4] Hui Zhang, Ye Pan, and Yi Zhu He. Synthesis and characterization of FeCoNiCrCu high-entropy alloy coating by laser cladding. *Materials and Design*, 32(4):1910–1915, 2011.

[5] Henrik Dobbelstein, Magnus Thiele, Evgeny L. Gurevich, Easo P. George, and Andreas Ostendorf. Direct metal deposition of refractory high entropy alloy MoNbTaW. In *Physics Procedia*, volume 83, pages 624–633. Elsevier B.V., 2016.

[6] Yevgeni Brif, Meurig Thomas, and Iain Todd. The use of high-entropy alloys in additive manufacturing. *Scripta Materialia*, 99:93–96, 2015.

[7] Hang Zhang, Wang Xu, Yunjing Xu, Zhongliang Lu, and Dichen Li. The thermal-mechanical behavior of WTaMoNb high-entropy alloy via selective laser melting (SLM): experiment and simulation. *International Journal of Advanced Manufacturing Technology*, 96(1-4):461–474, 2018.

[8] Shuying Chen, Yang Tong, and Peter K. Liaw. Additive manufacturing of high-entropy alloys: A review, 12 2018.

[9] B. E. MacDonald, Z. Fu, B. Zheng, W. Chen, Y. Lin, F. Chen, L. Zhang, J. Ivanisenko, Y. Zhou, H. Hahn, and E. J. Lavernia. Recent Progress in High Entropy Alloy Research. *Jom*, 69(10):2024–2031, 2017.

[10] F. Otto, Y. Yang, H. Bei, and E. P. George. Relative effects of enthalpy and entropy on the phase stability of equiatomic high-entropy alloys. *Acta Materialia*, 61(7):2628–2638, 2013.

[11] Zhiming Li, Konda Gokuldoss Pradeep, Yun Deng, Dierk Raabe, and Cemal Cem Tasan. Metastable high-entropy dual-phase alloys overcome the strength-ductility trade-off. *Nature*, 534(7606):227–230, 2016.

[12] S. J. Sun, Y. Z. Tian, H. R. Lin, X. G. Dong, Y. H. Wang, Z. J. Zhang, and Z. F. Zhang. Enhanced strength and ductility of bulk CoCrFeMnNi high entropy alloy having fully recrystallized ultrafine-grained structure. *Materials and Design*, 133:122–127, 11 2017.

[13] S. W. Xin, M. Zhang, T. T. Yang, Y. Y. Zhao, B. R. Sun, and T. D. Shen. Ultrahard bulk nanocrystalline VNbMoTaW high-entropy alloy. *Journal of Alloys and Compounds*, 769:597–604, 11 2018.

[14] Wenyi Huo, Xiaodong Liu, Shuyong Tan, Feng Fang, Zonghan Xie, Jianku Shang, and Jianqing Jiang. Ultrahigh hardness and high electrical resistivity in nano-twinned, nanocrystalline high-entropy alloy films. *Applied Surface Science*, 439:222–225, 5 2018.

[15] Oleg N. Senkov, Daniel B. Miracle, Kevin J. Chaput, and Jean Philippe Couzinie. Development and exploration of refractory high entropy alloys - A review, 2018.

[16] Bernd Gludovatz, Anton Hohenwarter, Dhiraj Catoor, Edwin H. Chang, Easo P. George, and Robert O. Ritchie. A fracture-resistant high-entropy alloy for cryogenic applications. *Science*, 345(6201):1153–1158, 2014.

[17] R. B. Nair, H. S. Arora, Sundeep Mukherjee, S. Singh, H. Singh, and H. S. Grewal. Exceptionally high cavitation erosion and corrosion resistance of a high entropy alloy. *Ultrasonics Sonochemistry*, 41:252–260, 3 2018.

[18] S. Shuang, Z. Y. Ding, D. Chung, S. Q. Shi, and Y. Yang. Corrosion resistant nanostructured eutectic high entropy alloy. *Corrosion Science*, 164, 3 2020.

[19] B. Gorr, M. Azim, H. J. Christ, T. Mueller, D. Schliephake, and M. Heilmaier. Phase equilibria, microstructure, and high temperature oxidation resistance of novel refractory high-entropy alloys. *Journal of Alloys and Compounds*, 624:270–278, 3 2015.

[20] O. N. Senkov, G. B. Wilks, D. B. Miracle, C. P. Chuang, and P. K. Liaw. Refractory high-entropy alloys. *Intermetallics*, 18(9):1758–1765, 9 2010.

[21] Y. D. Wu, Y. H. Cai, X. H. Chen, T. Wang, J. J. Si, L. Wang, Y. D. Wang, and X. D. Hui. Phase composition and solid solution strengthening effect in TiZrNbMoV high-entropy alloys. *Materials and Design*, 83:651–660, 10 2015.

[22] Woei Ren Wang, Wei Lin Wang, Shang Chih Wang, Yi Chia Tsai, Chun Hui Lai, and Jien Wei Yeh. Effects of Al addition on the microstructure and mechanical property of Al xCoCrFeNi high-entropy alloys. *Intermetallics*, 26:44–51, 7 2012.

[23] Woei Ren Wang, Wei Lin Wang, and Jien Wei Yeh. Phases, microstructure and mechanical properties of AlxCoCrFeNi high-entropy alloys at elevated temperatures. *Journal of Alloys and Compounds*, 589:143–152, 3 2014.

[24] Walter Steurer. Single-phase high-entropy alloys – A critical update. *Materials Characterization*, 162(October 2019):110179, 2020.

[25] G. Laplanche, P. Gadaud, O. Horst, F. Otto, G. Eggeler, and E.P. George. Temperature dependencies of the elastic moduli and thermal expansion coefficient of an equiatomic, single-phase CoCrFeMnNi high-entropy alloy. *Journal of Alloys and Compounds*, 623:348–353, 2 2015.

[26] P.P. Bhattacharjee, G.D. Sathiaraj, M. Zaid, J.R. Gatti, Chi Lee, Che-Wei Tsai, and Jien-Wei Yeh. Microstructure and texture evolution during annealing of equiatomic CoCrFeMnNi high-entropy alloy. *Journal of Alloys and Compounds*, 587:544–552, 2 2014.

[27] Bingfeng Wang, Ao Fu, Xiaoxia Huang, Bin Liu, Yong Liu, Zezhou Li, and Xiang Zan. Mechanical Properties and Microstructure of the CoCrFeMnNi High Entropy Alloy Under High Strain Rate Compression. *Journal of Materials Engineering and Performance*, 25(7):2985–2992, 2016.

[28] F. Otto, A. Dlouhý, Ch Somsen, H. Bei, G. Eggeler, and E. P. George. The influences of temperature and microstructure on the tensile properties of a CoCrFeMnNi high-entropy alloy. *Acta Materialia*, 61(15):5743–5755, 2013.

[29] G. Laplanche, O. Horst, F. Otto, G. Eggeler, and E. P. George. Microstructural evolution of a CoCrFeMnNi high-entropy alloy after swaging and annealing. *Journal of Alloys and Compounds*, 647:548–557, 2015.

[30] F. Otto, N. L. Hanold, and E. P. George. Microstructural evolution after thermomechanical processing in an equiatomic, single-phase CoCrFeMnNi high-entropy alloy with special focus on twin boundaries. *Intermetallics*, 54:39–48, 2014.

[31] B. Schuh, F. Mendez-Martin, B. Völker, E.P. George, H. Clemens, R. Pippan, and A. Hohenwarter. Mechanical properties, microstructure and thermal stability of a nanocrystalline CoCrFeMnNi high-entropy alloy after severe plastic deformation. *Acta Materialia*, 96:258–268, 9 2015.

[32] E. J. Pickering, R. Muñoz-Moreno, H. J. Stone, and N. G. Jones. Precipitation in the equiatomic high-entropy alloy CrMnFeCoNi. *Scripta Materialia*, 113:106–109, 2016.

[33] J.Y. He, C. Zhu, D.Q. Zhou, W.H. Liu, T.G. Nieh, and Z.P. Lu. Steady state flow of the FeCoNiCrMn high entropy alloy at elevated temperatures. *Intermetallics*, 55:9–14, 12 2014.

[34] William Hume-Rothery. The structure of metals and alloys. *Indian Journal of Physics*, 11:74, 1969.

[35] I. Toda-Caraballo, J. S. Wróbel, S. L. Dudarev, D. Nguyen-Manh, and P. E.J. Rivera-Díaz-Del-Castillo. Interatomic spacing distribution in multicomponent alloys. *Acta Materialia*, 97:156–169, 7 2015.

[36] F H Herbstein, B S Borie, and B L Averbach. Local atomic displacements in solid solutions. *Acta Crystallographica*, 9(5):466–471, 5 1956.

[37] Sergiy V Divinski, Alexander V Pokoev, Neelamegan Esakkiraja, and Aloke Paul. A mystery of" sluggish diffusion" in high-entropy alloys: the truth or a myth? *Diffusion foundations*, 17:69–104, 2018.

[38] Jien Wei Yeh. Physical Metallurgy of High-Entropy Alloys. *Jom*, 67(10):2254–2261, 2015.

[39] S Ranganathan. Alloyed pleasures: Multimetallic cocktails. Technical Report 10, 2003.

[40] Yong Zhang, Ting Ting Zuo, Zhi Tang, Michael C. Gao, Karin A. Dahmen, Peter K. Liaw, and Zhao Ping Lu. Microstructures and properties of high-entropy alloys. *Progress in Materials Science*, 61(November 2013):1–93, 2014.

[41] Y. F. Ye, C. T. Liu, and Y. Yang. A geometric model for intrinsic residual strain and phase stability in high entropy alloys. *Acta Materialia*, 94:152–161, 2015.

[42] Yong Zhang, Yun Jun Zhou, Jun Pin Lin, Guo Liang Chen, and Peter K. Liaw. Solid-solution phase formation rules for multi-component alloys. *Advanced Engineering Materials*, 10(6):534–538, 2008.

[43] Ming Hung Tsai, Jian Hong Li, An Chen Fan, and Pei Hua Tsai. Incorrect predictions of simple solid solution high entropy alloys: Cause and possible solution. *Scripta Materialia*, 127:6–9, 2017.

[44] Sheng Guo and C.T. Liu. Phase stability in high entropy alloys: Formation of solid-solution phase or amorphous phase. *Progress in Natural Science: Materials International*, 21(6):433–446, 12 2011.

[45] X. Yang and Y. Zhang. Prediction of high-entropy stabilized solid-solution in multi-component alloys. *Materials Chemistry and Physics*, 132(2-3):233–238, 2012.

[46] Anil Kumar Singh, Nitesh Kumar, Akanksha Dwivedi, and Anandh Subramaniam. A geometrical parameter for the formation of disordered solid solutions in multi-component alloys. *Intermetallics*, 53:112–119, 2014.

[47] Sheng Guo, Qiang Hu, Chun Ng, and C. T. Liu. More than entropy in high-entropy alloys: Forming solid solutions or amorphous phase. *Intermetallics*, 41:96–103, 2013.

[48] Xi Jin, Yang Zhou, Lu Zhang, Xingyu Du, and Bangsheng Li. A novel Fe20Co20Ni41Al19 eutectic high entropy alloy with excellent tensile properties. *Materials Letters*, 216:144–146, 2018.

[49] Ka Ram Lim, Kwang Seok Lee, Jun Seo Lee, Jin Yeon Kim, Hye Jung Chang, and Young Sang Na. Dual-phase high-entropy alloys for high-temperature structural applications. *Journal of Alloys and Compounds*, 728:1235–1238, 2017.

[50] Thomas Niendorf, Thomas Wegener, Zhiming Li, and Dierk Raabe. Unexpected cyclic stress-strain response of dual-phase high-entropy alloys induced by partial reversibility of deformation. *Scripta Materialia*, 143:63–67, 2018.

[51] Yung-ta Chen, Yao-jen Chang, Hideyuki Murakami, and Stéphane Gorsse. Scripta Materialia Designing high entropy superalloys for elevated temperature application. *Scripta Materialia*, 187:177–182, 2020.

[52] E. J. Pickering and N. G. Jones. High-entropy alloys: a critical assessment of their founding principles and future prospects. *International Materials Reviews*, 61(3):183–202, 2016.

[53] Easo P. George, Dierk Raabe, and Robert O. Ritchie. High-entropy alloys, 8 2019.

[54] D. B. Miracle and O. N. Senkov. A critical review of high entropy alloys and related concepts. *Acta Materialia*, 122:448–511, 2017.

[55] Jia li Zhou, Yan hai Cheng, Yong xiong Chen, and Xiu bing Liang. Composition design and preparation process of refractory high-entropy alloys: A review, 6 2022.

[56] Stéphane Gorsse and Oleg N. Senkov. About the reliability of CALPHAD predictions in multicomponent systems. *Entropy*, 20(12), 12 2018.

[57] Stéphane Gorsse and Franck Tancret. Current and emerging practices of CALPHAD toward the development of high entropy alloys and complex concentrated alloys. *Journal of Materials Research*, 33(19):2899–2923, 2018.

[58] O. N. Senkov, J. D. Miller, D. B. Miracle, and C. Woodward. Accelerated exploration of multi-principal element alloys for structural applications. *Calphad: Computer Coupling of Phase Diagrams and Thermochemistry*, 50:32–48, 9 2015.

[59] O. N. Senkov, J. D. Miller, D. B. Miracle, and C. Woodward. Accelerated exploration of multi-principal element alloys with solid solution phases. *Nature Communications*, 6, 2015.

[60] Xianglin Liu, Jiaxin Zhang, and Zongrui Pei. Machine learning for high-entropy alloys: Progress, challenges and opportunities, 1 2023.

[61] Xianglin Liu, Zongrui Pei, and Markus Eisenbach. Dislocation core structures and Peierls stresses of the high-entropy alloy NiCoFeCrMn and its subsystems. *Materials and Design*, 180, 10 2019.

[62] Yegi Vamsi Krishna, Ujjawal Kumar Jaiswal, and Rahul M. R. Machine learning approach to predict new multiphase high entropy alloys. *Scripta Materialia*, 197, 5 2021.

[63] O. N. Senkov, G. B. Wilks, J. M. Scott, and D. B. Miracle. Mechanical properties of Nb25Mo25Ta25W25 and V20Nb20Mo 20Ta20W20 refractory high entropy alloys. *Intermetallics*, 19(5):698–706, 2011.

[64] J. P. Couzinié, G. Dirras, L. Perrière, T. Chauveau, E. Leroy, Y. Champion, and I. Guillot. Microstructure of a near-equimolar refractory high-entropy alloy. *Materials Letters*, 126:285–287, 7 2014.

[65] Dong Xu Qiao, Hui Jiang, Xiao Xue Chang, Yi Ping Lu, and Ting Ju Li. Microstructure and mechanical properties of VTaTiMoAlx refractory high entropy alloys. In *Materials science forum*, volume 898, pages 638–642. Trans Tech Publ, 2017.

[66] Mohamed El Garah, Driss Soubane, and Frederic Sanchette. Review on mechanical and functional properties of refractory high-entropy alloy films by magnetron sputtering. *Emergent Materials*, 12 2023.

[67] Sajid Alvi, Dariusz M. Jarzabek, Mojtaba Gilzad Kohan, Daniel Hedman, Piotr Jenczyk, Marta Maria Natile, Alberto Vomiero, and Farid Akhtar. Synthesis and Mechanical Characterization of a CuMoTaWV High-Entropy Film by Magnetron Sputtering. *ACS Applied Materials and Interfaces*, 12(18):21070–21079, 5 2020.

[68] Byungchul Kang, Junho Lee, Ho Jin Ryu, and Soon Hyung Hong. Microstructure, mechanical property and Hall-Petch relationship of a light-weight refractory Al0. 1CrNbVMo high entropy alloy fabricated by powder metallurgical process. *Journal of Alloys and Compounds*, 767:1012–1021, 2018.

[69] N. Yu Yurchenko, N. D. Stepanov, S. V. Zherebtsov, M. A. Tikhonovsky, and G. A. Salishchev. Structure and mechanical properties of B2 ordered refractory AlNbTiVZrx (x = 0–1.5) high-entropy alloys. *Materials Science and Engineering: A*, 704:82–90, 9 2017.

[70] Sebastian A. Kube, Carolina Frey, Chiyo McMullin, Ben Neuman, Kaitlyn M. Mullin, and Tresa M. Pollock. Navigating the BCC-B2 refractory alloy space: Stability and thermal processing with Ru-B2 precipitates. *Acta Materialia*, 265:119628, 2 2024.

[71] Eric A. Lass. On the Thermodynamics and Phase Transformation Pathways in BCC-B2 Refractory Compositionally Complex Superalloys. *Metallurgical and Materials Transactions A: Physical Metallurgy and Materials Science*, 53(12):4481–4498, 12 2022.

[72] Yuan Liu, Yan Zhang, Heng Zhang, Naijuan Wang, Xiang Chen, Huawei Zhang, and Yanxiang Li. Microstructure and mechanical properties of refractory HfMo0.5NbTiV0.5Sixhigh-entropy composites. *Journal of Alloys and Compounds*, 694:869–876, 2017.

[73] H. T. He, J. X. Fang, J. X. Wang, T. Sun, Z. Yang, B. Ma, H. T. Chen, and M. Wen. Carbide-reinforced Re0.1Hf0.25NbTaW0.4 refractory high-entropy alloy with excellent room and elevated temperature mechanical properties. *International Journal of Refractory Metals and Hard Materials*, 116, 11 2023.

[74] Shiyu Wu, Dongxu Qiao, Hongliang Zhao, Jun Wang, and Yiping Lu. A novel NbTaW0.5 (Mo2C)x refractory high-entropy alloy with excellent mechanical properties. *Journal of Alloys and Compounds*, 889, 1 2022.

[75] Shiyu Wu, Dongxu Qiao, Haitao Zhang, Junwei Miao, Hongliang Zhao, Jun Wang, Yiping Lu, Tongmin Wang, and Tingju Li. Microstructure and mechanical properties of CxHf0.25NbTaW0.5 refractory high-entropy alloys at room and high temperatures. *Journal of Materials Science and Technology*, 97:229–238, 1 2022.

[76] Jintao Xu, Ran Duan, Kai Feng, Chengcheng Zhang, Qingjun Zhou, Pan Liu, and Zhuguo Li. Enhanced strength and ductility of laser powder bed fused NbMoTaW refractory high-entropy alloy via carbon microalloying. *Additive Manufacturing Letters*, 3, 12 2022.

[77] Joshua A. Smeltzer, B. Chad Hornbuckle, Anit K. Giri, Kristopher A. Darling, Martin P. Harmer, Helen M. Chan, and Christopher J. Marvel. Nitrogen-induced hardening of refractory high entropy alloys containing laminar ordered phases. *Acta Materialia*, 211, 6 2021.

[78] Yusheng Tian, Wenzhe Zhou, Mingxu Wu, Hua Luo, Qingbiao Tan, Guoliang Zhu, Anping Dong, Da Shu, and Baode Sun. Microstructure and mechanical properties of in-situ nitride-reinforced refractory high-entropy alloy TiZrHfNbTa matrix composites. *Journal of Alloys and Compounds*, 915, 9 2022.

[79] Yixing Wan, Yanhai Cheng, Yongxiong Chen, Zhibin Zhang, Yanan Liu, Haijun Gong, Baolong Shen, and Xiubing Liang. A Nitride-Reinforced NbMoTaWHfN Refractory High-Entropy Alloy with Potential Ultra-High-Temperature Engineering Applications. *Engineering*, 2023.

[80] Olivia F. Dippo, Neda Mesgarzadeh, Tyler J. Harrington, Grant D. Schrader, and Kenneth S. Vecchio. Bulk high-entropy nitrides and carbonitrides. *Scientific Reports*, 10(1), 12 2020.

[81] Rui Xuan Li, Jun Wei Qiao, Peter K. Liaw, and Yong Zhang. Preternatural Hexagonal High-Entropy Alloys: A Review, 8 2020.

[82] V. Soni, B. Gwalani, T. Alam, S. Dasari, Y. Zheng, O. N. Senkov, D. Miracle, and R. Banerjee. Phase inversion in a two-phase, BCC+B2, refractory high entropy alloy. *Acta Materialia*, 185:89–97, 2 2020.

[83] V. Soni, O. N. Senkov, J. P. Couzinie, Y. Zheng, B. Gwalani, and R. Banerjee. Phase stability and microstructure evolution in a ductile refractory high entropy alloy Al10Nb15Ta5Ti30Zr40. *Materialia*, 9, 3 2020.

[84] Lu Wang, Xia Li, Hongwei Niu, Lin Yang, Mingqin Xu, and Jiaojiao Yi. Effect of Cr Incorporation on the Mechanical Properties of HfMoTiZrCr, HfMoNbZrCr, and HfMoNbTiCr Refractory High-Entropy Alloys. *Metals and Materials International*, 28(10):2413–2421, 10 2022.

[85] Yaxiong Guo, Huilin Wang, and Qibin Liu. Microstructure evolution and strengthening mechanism of laser-cladding MoFexCrTiWAlNby refractory high-entropy alloy coatings. *Journal of Alloys and Compounds*, 834, 9 2020.

[86] Yichen Wang, Tamás Csanádi, Hangfeng Zhang, Ján Dusza, and Michael J. Reece. Synthesis, microstructure, and mechanical properties of novel high entropy carbonitrides. *Acta Materialia*, 231, 6 2022.

[87] Ruixin Wang, Yu Tang, Zhifeng Lei, Yuanlin Ai, Zhixing Tong, Shun Li, Yicong Ye, and Shuxin Bai. Achieving high strength and ductility in nitrogen-doped refractory high-entropy alloys. *Materials and Design*, 213, 1 2022.

[88] ASTM International. F2792-12a - Standard Terminology for Additive Manufacturing Technologies. *Rapid Manufacturing Association*, pages 10–12, 2013.

[89] Nahum Travitzky, Alexander Bonet, Benjamin Dermeik, Tobias Fey, Ina Filbert-Demut, Lorenz Schlier, Tobias Schlordt, and Peter Greil. Additive Manufacturing of Ceramic-Based Materials. *Advanced Engineering Materials*, 16(6):729–754, 2014.

[90] John O Milewski. Additive Manufacturing Metal, the Art of the Possible. In *Additive Manufacturing of Metals: From Fundamental Technology to Rocket Nozzles, Medical Implants, and Custom Jewelry*, pages 7–33. Springer International Publishing, Cham, 2017.

[91] Additive manufacturing — General principles — Fundamentals and vocabulary. *ISO/ASTM 52900:2021*, 2021.

[92] Martin Leary. Chapter 13 - Binder jetting. In Martin Leary, editor, *Design for Additive Manufacturing*, Additive Manufacturing Materials and Technologies, pages 335–339. Elsevier, 2020.

[93] Ambrish Singh, Sajan Kapil, and Manas Das. A comprehensive review of the methods and mechanisms for powder feedstock handling in directed energy deposition. *Additive Manufacturing*, 35:101388, 2020.

[94] Samira Gruber, Christian Grunert, Mirko Riede, Elena López, Axel Marquardt, Frank Brueckner, and Christoph Leyens. Comparison of dimensional accuracy and tolerances of powder bed based and nozzle based additive manufacturing processes. *Journal of Laser Applications*, 32(3), 8 2020.

[95] Ana Vafadar, Ferdinando Guzzomi, Alexander Rassau, and Kevin Hayward. Advances in metal additive manufacturing: A review of common processes, industrial applications, and current challenges, 2 2021.

[96] E. O. Olakanmi, R. F. Cochrane, and K. W. Dalgarno. Densification mechanism and microstructural evolution in selective laser sintering of Al-12Si powders. *Journal of Materials Processing Technology*, 211(1):113–121, 1 2011.

[97] J. P. Oliveira, A. D. LaLonde, and J. Ma. Processing parameters in laser powder bed fusion metal additive manufacturing. *Materials and Design*, 193, 8 2020.

[98] Ritam Pal and Amrita Basak. Linking Powder Properties, Printing Parameters, Post-Processing Methods, and Fatigue Properties in Additive Manufacturing of AlSi10Mg. *Alloys*, 1(2):149–179, 7 2022.

[99] M. C. Brennan, J. S. Keist, and T. A. Palmer. Defects in Metal Additive Manufacturing Processes. *Journal of Materials Engineering and Performance*, 30(7):4808–4818, 7 2021.

[100] Leijun Li. Repair of directionally solidified superalloy GTD-111 by laser-engineered net shaping. *Journal of Materials Science*, 41(23):7886–7893, 12 2006.

[101] Sagar Patel and Mihaela Vlasea. Melting modes in laser powder bed fusion. *Materialia*, 9:100591, 2020.

[102] Ming Tang, P. Chris Pistorius, and Jack L. Beuth. Prediction of lack-of-fusion porosity for powder bed fusion. *Additive Manufacturing*, 14:39–48, 3 2017.

[103] John C Lippold. *Welding metallurgy and weldability*. John Wiley & Sons, 2014.

[104] Sindo Kou. Solidification and liquation cracking issues in welding. *JOM*, 55(6):37–42, 2003.

[105] Yuanbo T. Tang, Chinnapat Panwisawas, Joseph N. Ghoussoub, Yilun Gong, John W.G. Clark, André A.N. Németh, D. Graham McCartney, and Roger C. Reed. Alloys-by-design: Application to new superalloys for additive manufacturing. *Acta Materialia*, 202:417–436, 2021.

[106] Aditad Vasinonta, Jack L. Beuth, and Michelle L. Griffith. A process map for consistent build conditions in the solid freeform fabrication of thin-walled structures. *Journal of Manufacturing Science and Engineering, Transactions of the ASME*, 123(4):615–622, 2001.

[107] Srikanth Bontha, Nathan W. Klingbeil, Pamela A. Kobryn, and Hamish L. Fraser. Thermal process maps for predicting solidification microstructure in laser fabrication of thin-wall structures. *Journal of Materials Processing Technology*, 178(1-3):135–142, 9 2006.

[108] Eric A. Jägle, Zhendong Sheng, Liang Wu, Lin Lu, Jeroen Risse, Andreas Weisheit, and Dierk Raabe. Precipitation Reactions in Age-Hardenable Alloys During Laser Additive Manufacturing. *JOM*, 68(3):943–949, 3 2016.

[109] Umberto Scipioni Bertoli, Alexander J. Wolfer, Manyalibo J. Matthews, Jean Pierre R. Delplanque, and Julie M. Schoenung. On the limitations of Volumetric Energy Density as a design parameter for Selective Laser Melting. *Materials and Design*, 113:331–340, 1 2017.

[110] Meurig Thomas, Gavin J. Baxter, and Iain Todd. Normalised model-based processing diagrams for additive layer manufacture of engineering alloys. *Acta Materialia*, 108:26–35, 4 2016.

[111] D. B. Hann, J. Iammi, and J. Folkes. A simple methodology for predicting laser-weld properties from material and laser parameters. *Journal of Physics D: Applied Physics*, 44(44), 11 2011.

[112] Wayne E. King, Holly D. Barth, Victor M. Castillo, Gilbert F. Gallegos, John W. Gibbs, Douglas E. Hahn, Chandrika Kamath, and Alexander M. Rubenchik. Observation of keyhole-mode laser melting in laser powder-bed fusion additive manufacturing. *Journal of Materials Processing Technology*, 214(12):2915–2925, 2014.

[113] Johannes Trapp, Alexander M. Rubenchik, Gabe Guss, and Manyalibo J. Matthews. In situ absorptivity measurements of metallic powders during laser powder-bed fusion additive manufacturing. *Applied Materials Today*, 9:341–349, 2017.

[114] T. Mukherjee, J. S. Zuback, A. De, and T. DebRoy. Printability of alloys for additive manufacturing. *Scientific Reports*, 6:1–8, 2016.

[115] Robert James Deffley. Development of Processing Strategies for the Additive Layer Manufacture of Aerospace Components in Inconel 718. *PhD Dissertation*, (January), 2012.

[116] Luke Johnson, Mohamad Mahmoudi, Bing Zhang, Raiyan Seede, Xueqin Huang, Janine T. Maier, Hans J. Maier, Ibrahim Karaman, Alaa Elwany, and Raymundo Arróyave. Assessing printability maps in additive manufacturing of metal alloys. *Acta Materialia*, 176:199–210, 9 2019.

[117] H. L. Wei, T. Mukherjee, W. Zhang, J. S. Zuback, G. L. Knapp, A. De, and T. DebRoy. Mechanistic models for additive manufacturing of metallic components, 2 2021.

[118] T. Mukherjee, W. Zhang, and T. DebRoy. An improved prediction of residual stresses and distortion in additive manufacturing. *Computational Materials Science*, 126:360–372, 1 2017.

[119] John Romano, Leila Ladani, and Magda Sadowski. Laser Additive Melting and Solidification of Inconel 718: Finite Element Simulation and Experiment. *JOM*, 68(3):967–977, 2016.

[120] H. C. Basoalto, C. Panwisawas, Y. Sovani, M. J. Anderson, R. P. Turner, B. Saunders, and J. W. Brooks. A computational study on the three-dimensional printability of precipitate-strengthened nickel-based superalloys. *Proceedings of the Royal Society A: Mathematical, Physical and Engineering Sciences*, 474(2220), 12 2018.

[121] Zhibo Luo and Yaoyao Zhao. Efficient thermal finite element modeling of selective laser melting of Inconel 718. *Computational Mechanics*, 65(3):763–787, 3 2020.

[122] Lova Chechik, Katerina A. Christofidou, Lucy Farquhar, Martin Tse, Gavin Baxter, and Iain Todd. Tools for the Assessment of the Laser Printability of Nickel Superalloys. *Metallurgical and Materials Transactions A: Physical Metallurgy and Materials Science*, 54(6):2421–2437, 6 2023.

[123] D G Eskin and L Katgerman. A quest for a new hot tearing criterion. *Metallurgical and Materials Transactions A*, 38:1511–1519, 2007.

[124] S. Kou. A simple index for predicting the susceptibility to solidification cracking. *Welding Journal*, 94(12):374s–388s, 2015.

[125] T.W. Clyne and G.J. Davies. Solidification and Casting of Metals. pages 275–278. Sheffield, 1977.

[126] L Katgerman. A Mathematical Model for Hot Cracking of Aluminum Alloys During D.C. Casting. *JOM*, 34(2):46–49, 1982.

[127] Taishi Matsushita, Mohammadreza Zamani, Andrej Kump, and Anders E.W. Jarfors. Evaluation of the Critical Times for the Crack Susceptibility Coefficient Calculation. *International Journal of Metalcasting*, 2023.

[128] M Rappaz, J.-M Drezet, and M Gremaud. A New Hot-Tearing Criterion. Technical report, 1999.

[129] Eric A Ott, Jon Groh, and Howard Sizek. Metals Affordability Initiative: Application of Allvac alloy 718Plus® for aircraft engine static structural components. *Superalloys*, 718:625–706, 2005.

[130] Luke N Carter, Moataz M Attallah, and Roger C Reed. Laser Powder Bed Fabrication of Nickel-Base Superalloys: Influence of Parameters; Characterisation, Quantification and Mitigation of Cracking. 2012.

[131] G A Young, T E Capobianco, M A Penik, B W Morris, and J J McGee. The mechanism of ductility dip cracking in nickel-chromium alloys. *Welding Journal-New York-*, 87(2):31, 2008.

[132] K. Nishimoto, K. Saida, and H. Okauchi. Microcracking in multipass weld metal of alloy 690 Part 1 - Microcracking susceptibility in reheated weld metal. *Science and Technology of Welding and Joining*, 11(4):455–461, 7 2006.

[133] A. J. Ramirez and J. C. Lippold. High temperature behavior of Ni-base weld metal Part II - Insight into the mechanism for ductility dip cracking. *Materials Science and Engineering: A*, 380(1-2):245–258, 8 2004.

[134] Ramirez A and J C Lippold. New Insight into the Mechanism of Ductility-Dip Cracking in Ni-base Weld Metals. In Horst Böllinghaus Thomas }and Herold, editor, *Hot Cracking Phenomena in Welds*, pages 19–41. Springer Berlin Heidelberg, Berlin, Heidelberg, 2005.

[135] Hyo Ik Ahn, Sang Hoon Jeong, Hyun Hak Cho, and Hae Woo Lee. Ductility-dip cracking susceptibility of Inconel 690 using Nb content. *Journal of Alloys and Compounds*, 783:263–271, 4 2019.

[136] M G Collins, A J Ramirez, and J C Lippold. An Investigation of Ductility-Dip Cracking in Nickel-Based Weld Metals-Part III The characteristics of we/d-meta/ grain boundaries associated with e/evated-temperature fracture are investigated. Technical report, 2004.

[137] Ping Yu, Justin Morrow, and Sindo Kou. Resistance of Austenitic Stainless Steels to Ductility-Dip Cracking: Mechanisms. *Welding Journal*, 100(09):291–301, 9 2021.

[138] T. M. Pollock, A. J. Clarke, and S. S. Babu. Design and Tailoring of Alloys for Additive Manufacturing. *Metallurgical and Materials Transactions A: Physical Metallurgy and Materials Science*, 51(12):6000–6019, 2020.

[139] Sean P. Murray, Kira M. Pusch, Andrew T. Polonsky, Chris J. Torbet, Gareth G.E. Seward, Ning Zhou, Stéphane A.J. Forsik, Peeyush Nandwana, Michael M. Kirka, Ryan R. Dehoff, William E. Slye, and Tresa M. Pollock. A defect-resistant Co–Ni superalloy for 3D printing. *Nature Communications*, 11(1), 12 2020.

[140] Freddie Markanday, Gareth Conduit, Bryce Conduit, Julia Pürstl, Katerina Christofidou, Lova Chechik, Gavin Baxter, Christopher Heason, and Howard Stone. Design of a Ni-based superalloy for laser repair applications using probabilistic neural network identification. *Data-Centric Engineering*, 3(2), 10 2022.

[141] Marco Simonelli, Nesma T. Aboulkhair, Philip Cohen, James W. Murray, Adam T. Clare, Chris Tuck, and Richard J.M. Hague. A comparison of Ti-6Al-4V in-situ alloying in Selective Laser Melting using simply-mixed and satellited powder blend feedstocks. *Materials Characterization*, 143:118–126, 9 2018.

[142] S. Mereddy, M. J. Bermingham, D. H. StJohn, and M. S. Dargusch. Grain refinement of wire arc additively manufactured titanium by the addition of silicon. *Journal of Alloys and Compounds*, 695:2097–2103, 2017.

[143] S. Mereddy, M. J. Bermingham, D. Kent, A. Dehghan-Manshadi, D. H. StJohn, and M. S. Dargusch. Trace Carbon Addition to Refine Microstructure and Enhance Properties of Additive-Manufactured Ti-6Al-4V. *JOM*, 70(9):1670–1676, 9 2018.

[144] Timothy M. Smith, Christopher A. Kantzos, Nikolai A. Zarkevich, Bryan J. Harder, Milan Heczko, Paul R. Gradl, Aaron C. Thompson, Michael J. Mills, Timothy P. Gabb, and John W. Lawson. A 3D printable alloy designed for extreme environments. *Nature*, 2023.

[145] B. D. Conduit, T. Illston, S. Baker, D. Vadegadde Duggappa, S. Harding, H. J. Stone, and G. J. Conduit. Probabilistic neural network identification of an alloy for direct laser deposition. *Materials and Design*, 168, 4 2019.

[146] M. J. Bermingham, D. H. StJohn, J. Krynen, S. Tedman-Jones, and M. S. Dargusch. Promoting the columnar to equiaxed transition and grain refinement of titanium alloys during additive manufacturing. *Acta Materialia*, 168:261–274, 4 2019.

[147] Duyao Zhang, Dong Qiu, Mark A. Gibson, Yufeng Zheng, Hamish L. Fraser, David H. StJohn, and Mark A. Easton. Additive manufacturing of ultrafine-grained high-strength titanium alloys. *Nature*, 576(7785):91–95, 12 2019.

[148] Kaitlyn M. Mullin, Carolina Frey, James Lamb, Sophia K. Wu, McLean P. Echlin, and Tresa M. Pollock. Rapid screening of single phase refractory alloys under laser melting conditions. *Materials & Design*, 238:112726, 2 2024.

[149] Yong Jie Hu, Aditya Sundar, Shigenobu Ogata, and Liang Qi. Screening of generalized stacking fault energies, surface energies and intrinsic ductile potency of refractory multi-component alloys. *Acta Materialia*, 210, 5 2021.

[150] S. L. Sing, S. Huang, G. D. Goh, G. L. Goh, C. F. Tey, J. H.K. Tan, and W. Y. Yeong. Emerging metallic systems for additive manufacturing: In-situ alloying and multi-metal processing in laser powder bed fusion. *Progress in Materials Science*, 119, 6 2021.

[151] Tomer Ron, Amnon Shirizly, and Eli Aghion. Additive Manufacturing Technologies of High Entropy Alloys (HEA): Review and Prospects, 3 2023.

[152] José M. Torralba and Mónica Campos. High entropy alloys manufactured by additive manufacturing. *Metals*, 10(5):1–15, 2020.

[153] Michael A Melia, Shaun R Whetten, Raymond Puckett, Morgan Jones, Michael J Heiden, Nicolas Argibay, and Andrew B Kustas. High-throughput additive manufacturing and characterization of refractory high entropy alloys. *Applied Materials Today*, 19:100560, 2020.

[154] Ahmad Ostovari Moghaddam, Nataliya A. Shaburova, Marina N. Samodurova, Amin Abdollahzadeh, and Evgeny A. Trofimov. Additive manufacturing of high entropy alloys: A practical review. *Journal of Materials Science and Technology*, 77:131–162, 2021.

[155] T. Wang, Y. Y. Zhu, S. Q. Zhang, H. B. Tang, and H. M. Wang. Grain morphology evolution behavior of titanium alloy components during laser melting deposition additive manufacturing. *Journal of Alloys and Compounds*, 632:505–513, 5 2015.

[156] Tianlong Zhang and Chain Tsuan Liu. Design of titanium alloys by additive manufacturing: A critical review, 1 2022.

[157] T. M. Smith, A. C. Thompson, T. P. Gabb, C. L. Bowman, and C. A. Kantzos. Efficient production of a high-performance dispersion strengthened, multi-principal element alloy. *Scientific Reports*, 10(1), 12 2020.

[158] K. Zhang, X. Tian, M. Bermingham, J. Rao, Q. Jia, Y. Zhu, X. Wu, S. Cao, and A. Huang. Effects of boron addition on microstructures and mechanical properties of Ti-6Al-4V manufactured by direct laser deposition. *Materials and Design*, 184, 12 2019.

[159] Marco Simonelli, David Graham McCartney, Pere Barriobero-Vila, Nesma T. Aboulkhair, Yau Yau Tse, Adam Clare, and Richard Hague. The Influence of Iron in Minimizing the Microstructural Anisotropy of Ti-6Al-4V Produced by Laser Powder-Bed Fusion. *Metallurgical and Materials Transactions A: Physical Metallurgy and Materials Science*, 51(5):2444–2459, 5 2020.

[160] Jian Gou, Zhijiang Wang, Shengsun Hu, Junqi Shen, Yinbao Tian, Guancheng Zhao, and Youquan Chen. Effects of trace Nb addition on microstructure and properties of Ti–6Al–4V thin-wall structure prepared via cold metal transfer additive manufacturing. *Journal of Alloys and Compounds*, 829, 7 2020.

[161] Nan Kang, Pierre Coddet, Lucas Dembinski, Hanlin Liao, and Christian Coddet. Microstructure and strength analysis of eutectic Al-Si alloy in-situ manufactured using selective laser melting from elemental powder mixture. *Journal of Alloys and Compounds*, 691:316–322, 2017.

[162] P. Wang, L. Deng, K. G. Prashanth, S. Pauly, J. Eckert, and S. Scudino. Microstructure and mechanical properties of Al-Cu alloys fabricated by selective laser melting of powder mixtures, 2 2018.

[163] Qian Wang, Changjun Han, Tomasz Choma, Qingsong Wei, Chunze Yan, Bo Song, and Yusheng Shi. Effect of Nb content on microstructure, property and in vitro apatite-forming capability of Ti-Nb alloys fabricated via selective laser melting. *Materials and Design*, 126:268–277, 7 2017.

[164] Sheng Huang, Swee Leong Sing, Geoff de Looze, Robert Wilson, and Wai Yee Yeong. Laser powder bed fusion of titanium-tantalum alloys: Compositions and designs for biomedical applications. *Journal of the Mechanical Behavior of Biomedical Materials*, 108, 8 2020.

[165] Edward Chlebus, Bogumiła Kuźnicka, Robert Dziedzic, and Tomasz Kurzynowski. Titanium alloyed with rhenium by selective laser melting. *Materials Science and Engineering: A*, 620:155–163, 1 2015.

[166] C. Wang, X. P. Tan, Z. Du, S. Chandra, Z. Sun, C. W.J. Lim, S. B. Tor, C. S. Lim, and C. H. Wong. Additive manufacturing of NiTi shape memory alloys using pre-mixed powders. *Journal of Materials Processing Technology*, 271:152–161, 9 2019.

[167] Baicheng Zhang, Jing Chen, and Christian Coddet. Microstructure and transformation behavior of in-situ shape memory alloys by selective laser melting Ti-Ni mixed powder. *Journal of Materials Science and Technology*, 29(9):863–867, 9 2013.

[168] N. Kang, M. El Mansori, F. Guittonneau, H. Liao, Y. Fu, and E. Aubry. Controllable mesostructure, magnetic properties of soft magnetic Fe-Ni-Si by using selective laser melting from nickel coated high silicon steel powder. *Applied Surface Science*, 455:736–741, 10 2018.

[169] Ming Hung Tsai and Jien Wei Yeh. High-entropy alloys: A critical review. *Materials Research Letters*, 2(3):107–123, 2014.

[170] Mike Olsson, Ville Akujärvi, Jan Eric Ståhl, and Volodymyr Bushlya. Cryogenic and hybrid induction-assisted machining strategies as alternatives for conventional machining of refractory tungsten and niobium. *International Journal of Refractory Metals and Hard Materials*, 97, 6 2021.

[171] Neng Li, Shuai Huang, Guodong Zhang, Renyao Qin, Wei Liu, Huaping Xiong, Gongqi Shi, and Jon Blackburn. Progress in additive manufacturing on new materials: A review, 2 2019.

[172] Jinyeon Kim, Akane Wakai, and Atieh Moridi. Materials and manufacturing renaissance: Additive manufacturing of high-entropy alloys, 8 2020.

[173] Farahnaz Haftlang and Hyoung Seop Kim. A perspective on precipitation-hardening high-entropy alloys fabricated by additive manufacturing, 12 2021.

[174] Xiaopeng Li. Additive Manufacturing of Advanced Multi-Component Alloys: Bulk Metallic Glasses and High Entropy Alloys, 5 2018.

[175] Jianhua Yao, Ziqing Weng, Gang Dong, and Lijing Yang. Microstructure and hardness of FeCrNiCoMn high-entropy alloy coating prepared by laser cladding with pre-alloyed gas atomized powder. *ICALEO 2013 - 32nd International Congress on Applications of Lasers and Electro-Optics*, 480(2013):480–486, 2013.

[176] Ruidi Li, Pengda Niu, Tiechui Yuan, Peng Cao, Chao Chen, and Kechao Zhou. Selective laser melting of an equiatomic CoCrFeMnNi high-entropy alloy: Processability, non-equilibrium microstructure and mechanical property. *Journal of Alloys and Compounds*, 746:125–134, 2018.

[177] Z. G. Zhu, Q. B. Nguyen, F. L. Ng, X. H. An, X. Z. Liao, P. K. Liaw, S. M.L. Nai, and J. Wei. Hierarchical microstructure and strengthening mechanisms of a CoCrFeNiMn high entropy alloy additively manufactured by selective laser melting. *Scripta Materialia*, 154:20–24, 2018.

[178] Y. Chew, G. J. Bi, Z. G. Zhu, F. L. Ng, F. Weng, S. B. Liu, S. M.L. Nai, and B. Y. Lee. Microstructure and enhanced strength of laser aided additive manufactured CoCrFeNiMn high entropy alloy. *Materials Science and Engineering A*, 744(December 2018):137–144, 2019.

[179] Young Kyun Kim, Jungho Choe, and Kee Ahn Lee. Selective laser melted equiatomic CoCrFeMnNi high-entropy alloy: Microstructure, anisotropic mechanical response, and multiple strengthening mechanism. *Journal of Alloys and Compounds*, 805:680–691, 2019.

[180] Shuo Xiang, Hengwei Luan, Jian Wu, Ke Fu Yao, Jinfeng Li, Xue Liu, Yanzhong Tian, Wenlue Mao, Hua Bai, Guomin Le, and Qiang Li. Microstructures and mechanical properties of CrMnFeCoNi high entropy alloys fabricated using laser metal deposition technique. *Journal of Alloys and Compounds*, 773:387–392, 2019.

[181] Chengcheng Zhang, Kai Feng, Hiroyuki Kokawa, Bolun Han, and Zhuguo Li. Cracking mechanism and mechanical properties of selective laser melted CoCrFeMnNi high

entropy alloy using different scanning strategies. *Materials Science and Engineering A*, 789(May):139672, 2020.

[182] Peng Chen, Sheng Li, Yinghao Zhou, Ming Yan, and Moataz M. Attallah. Fabricating CoCrFeMnNi high entropy alloy via selective laser melting in-situ alloying. *Journal of Materials Science and Technology*, 43:40–43, 2020.

[183] V. Ocelík, N. Janssen, S. N. Smith, and J. Th M. De Hosson. Additive Manufacturing of High-Entropy Alloys by Laser Processing. *Jom*, 68(7):1810–1818, 2016.

[184] Jithin Joseph, Tom Jarvis, Xinhua Wu, Nicole Stanford, Peter Hodgson, and Daniel Mark Fabijanic. Comparative study of the microstructures and mechanical properties of direct laser fabricated and arc-melted AlxCoCrFeNi high entropy alloys. *Materials Science and Engineering A*, 633:184–193, 2015.

[185] Wenqian Wu, Rui Zhou, Bingqiang Wei, Song Ni, Yong Liu, and Min Song. Nanosized precipitates and dislocation networks reinforced C-containing CoCrFeNi high-entropy alloy fabricated by selective laser melting. *Materials Characterization*, 144(July):605–610, 2018.

[186] Tadashi Fujieda, Hiroshi Shiratori, Kosuke Kuwabara, Mamoru Hirota, Takahiko Kato, Kenta Yamanaka, Yuichiro Koizumi, Akihiko Chiba, and Seiichi Watanabe. CoCrFeNiTi-based high-entropy alloy with superior tensile strength and corrosion resistance achieved by a combination of additive manufacturing using selective electron beam melting and solution treatment. *Materials Letters*, 189(September 2016):148–151, 2017.

[187] Tadashi Fujieda, Meichuan Chen, Hiroshi Shiratori, Kosuke Kuwabara, Kenta Yamanaka, Yuichiro Koizumi, Akihiko Chiba, and Seiichi Watanabe. Mechanical and corrosion properties of CoCrFeNiTi-based high-entropy alloy additive manufactured using selective laser melting. *Additive Manufacturing*, 25(June 2018):412–420, 2019.

[188] Tadashi Fujieda, Hiroshi Shiratori, Kosuke Kuwabara, Takahiko Kato, Kenta Yamanaka, Yuichiro Koizumi, and Akihiko Chiba. First demonstration of promising selective electron beam melting method for utilizing high-entropy alloys as engineering materials. *Materials Letters*, 159:12–15, 2015.

[189] Jie Ren, Yin Zhang, Dexin Zhao, Yan Chen, Shuai Guan, Yanfang Liu, Liang Liu, Siyuan Peng, Fanyue Kong, Jonathan D Poplawsky, Guanhui Gao, Thomas Voisin, Ke An, Y Morris Wang, Kelvin Y Xie, Ting Zhu, and Wen Chen. Strong yet ductile nanolamellar high-entropy alloys by additive manufacturing. *Nature*, 608(7921):62–68, 2022.

[190] Mina Zhang, Xianglin Zhou, Xiangnan Yu, and Jinghao Li. Synthesis and characterization of refractory TiZrNbWMo high-entropy alloy coating by laser cladding. *Surface and Coatings Technology*, 311:321–329, 2 2017.

[191] Nathan Ley, Sameehan S. Joshi, Baozhuo Zhang, Yee Hsien Ho, Narendra B. Dahotre, and Marcus L. Young. Laser coating of a CrMoTaWZr complex concentrated alloy onto a H13 tool steel die head. *Surface and Coatings Technology*, 348:150–158, 8 2018.

[192] Lin Chen, Xiaowei Zhang, Yueyi Wang, Xuanhong Hao, and Hongxi Liu. Microstructure and elastic constants of AlTiVMoNb refractory high-entropy alloy coating on Ti6Al4V by laser cladding. *Materials Research Express*, 6(11), 10 2019.

[193] Florian Huber, Dominic Bartels, and Michael Schmidt. In situ alloy formation of a wmotanbv refractory metal high entropy alloy by laser powder bed fusion (Pbf-lb/m). *Materials*, 14(11), 6 2021.

[194] Henrik Dobbelstein, Evgeny L. Gurevich, Easo P. George, Andreas Ostendorf, and Guillaume Laplanche. Laser metal deposition of a refractory TiZrNbHfTa high-entropy alloy. *Additive Manufacturing*, 24:386–390, 12 2018.

[195] I. Kunce, M. Polanski, and J. Bystrzycki. Microstructure and hydrogen storage properties of a TiZrNbMoV high entropy alloy synthesized using Laser Engineered Net Shaping (LENS). *International Journal of Hydrogen Energy*, 39(18):9904–9910, 6 2014.

[196] Henrik Dobbelstein, Evgeny L. Gurevich, Easo P. George, Andreas Ostendorf, and Guillaume Laplanche. Laser metal deposition of compositionally graded TiZrNbTa refractory high-entropy alloys using elemental powder blends. *Additive Manufacturing*, 25:252–262, 1 2019.

[197] Michael Moorehead, Kaila Bertsch, Michael Niezgoda, Calvin Parkin, Mohamed Elbakhshwan, Kumar Sridharan, Chuan Zhang, Dan Thoma, and Adrien Couet. High-throughput synthesis of Mo-Nb-Ta-W high-entropy alloys via additive manufacturing. *Materials and Design*, 187:108358, 2020.

[198] Qingyu Li, Hang Zhang, Dichen Li, Zihao Chen, Sheng Huang, Zhongliang Lu, and Haoqi Yan. W x NbMoTa refractory high-entropy alloys fabricated by laser cladding deposition. *Materials*, 12(3), 2 2019.

[199] Yongyun Zhang, Bailiang Qin, Di Ouyang, Lin Liu, Chuangshi Feng, Yuqiang Yan, Shulong Ye, Haibo Ke, K.C. Chan, and Weihua Wang. Strong yet ductile refractory high entropy alloy fabricated via additive manufacturing. *Additive Manufacturing*, 81:104009, 2 2024.

[200] Shuyuan Gou, Mingyu Gao, Yunzhu Shi, Shunchao Li, Youtong Fang, Xinhuan Chen, Huaican Chen, Wen Yin, Jiabin Liu, Zhifeng Lei, and Hongtao Wang. Additive manufacturing of ductile refractory high-entropy alloys via phase engineering. *Acta Materialia*, 248, 4 2023.

[201] Yansong Zhang, Huaming Wang, Yanyan Zhu, Shuquan Zhang, Fang Cheng, Junwei Yang, Bing Su, and Chen Yang. High specific yield strength and superior ductility of a lightweight refractory high-entropy alloy prepared by laser additive manufacturing. *Additive Manufacturing*, 77, 9 2023.

[202] Silvia Vock, Burghardt Klöden, Alexander Kirchner, Thomas Weißgärber, and Bernd Kieback. Powders for powder bed fusion: a review, 12 2019.

[203] Hang Zhang, Yizhen Zhao, Sheng Huang, Shuo Zhu, Fu Wang, and Dichen Li. Manufacturing and analysis of high-performance refractory high-entropy alloy via selective laser melting (SLM). *Materials*, 12(5), 2019.

[204] Peng Zhu, Yao Yu, Cheng Zhang, Qingjun Zhou, Bailing An, Rong Guo, K. C. Chan, and Lin Liu. V0.5Nb0.5ZrTi refractory high-entropy alloy fabricated by laser addictive manufacturing using elemental powders. *International Journal of Refractory Metals and Hard Materials*, 113, 6 2023.

[205] Fei Wang, Tiechui Yuan, Ruidi Li, Shiqi Lin, Pengda Niu, and Valentino Cristino. Effect of Mo on the morphology, microstructure and mechanical properties of NbTa0.5TiMox refractory high entropy alloy fabricated by laser powder bed fusion using elemental mixed powders. *International Journal of Refractory Metals and Hard Materials*, 111, 2 2023.

[206] Jianglong Cai, Hang Zhang, Lin Wang, Xiaoyu Sun, Xuebo Xu, Xin Guo, and Dichen Li. Design and coherent strengthening of ultra-high strength refractory high entropy alloys based on laser additive manufacturing. *Materials Science and Engineering: A*, 886, 10 2023.

[207] Chang Liu, Keyan Zhu, Wangwang Ding, Yu Liu, Gang Chen, and Xuanhui Qu. Additive manufacturing of WMoTaTi refractory high-entropy alloy by employing fluidised powders. *Powder Metallurgy*, 65(5):413–425, 2022.

[208] Pengfei Gu, Tengbo Qi, Lan Chen, Tong Ge, and Xudong Ren. Manufacturing and analysis of VNbMoTaW refractory high-entropy alloy fabricated by selective laser melting. *International Journal of Refractory Metals and Hard Materials*, 105, 6 2022.

[209] Ozkan Gokcekaya, Takuya Ishimoto, Yuki Nishikawa, Yong Seong Kim, Aira Matsugaki, Ryosuke Ozasa, Markus Weinmann, Christoph Schnitter, Melanie Stenzel, Hyoung Seop

Kim, Yoshitsugu Miyabayashi, and Takayoshi Nakano. Novel single crystalline-like non-equiatomic TiZrHfNbTaMo bio-high entropy alloy (BioHEA) developed by laser powder bed fusion. *Materials Research Letters*, 11(4):274–280, 2023.

[210] Z. Wu, H. Bei, F. Otto, G. M. Pharr, and E. P. George. Recovery, recrystallization, grain growth and phase stability of a family of FCC-structured multi-component equiatomic solid solution alloys. *Intermetallics*, 46:131–140, 2014.

[211] G. A. Salishchev, M. A. Tikhonovsky, D. G. Shaysultanov, N. D. Stepanov, A. V. Kuznetsov, I. V. Kolodiy, A. S. Tortika, and O. N. Senkov. Effect of Mn and v on structure and mechanical properties of high-entropy alloys based on CoCrFeNi system. *Journal of Alloys and Compounds*, 591:11–21, 2014.

[212] C. Zhang, G. J. Chen, and P. Q. Dai. Evolution of the microstructure and properties of laser-clad FeCrNiCoBx high-entropy alloy coatings. *Materials Science and Technology (United Kingdom)*, 32(16):1666–1672, 2016.

[213] Piyanut Muangtong, Aphichart Rodchanarowan, Duangrudee Chaysuwan, Narong Chanlek, and Russell Goodall. The corrosion behaviour of CoCrFeNi-x (x = Cu, Al, Sn) high entropy alloy systems in chloride solution. *Corrosion Science*, 172(May):108740, 2020.

[214] Zengcheng Qiu, Chengwu Yao, Kai Feng, Zhuguo Li, and Paul K. Chu. Cryogenic deformation mechanism of CrMnFeCoNi high-entropy alloy fabricated by laser additive manufacturing process. *International Journal of Lightweight Materials and Manufacture*, 1(1):33–39, 2018.

[215] Shuo Xiang, Jinfeng Li, Hengwei Luan, Abdukadir Amar, Siyuan Lu, Kun Li, Lei Zhang, Xue Liu, Guomin Le, Xiaoying Wang, Fengsheng Qu, Wei Zhang, Dou Wang, and Qiang Li. Effects of process parameters on microstructures and tensile properties of laser melting deposited CrMnFeCoNi high entropy alloys. *Materials Science and Engineering A*, 743(November 2018):412–417, 2019.

[216] Mehmet Cagirici, Pan Wang, Fern Lan Ng, Mui Ling Sharon Nai, Jun Ding, and Jun Wei. Additive manufacturing of high-entropy alloys by thermophysical calculations and in situ alloying. *Journal of Materials Science and Technology*, 94:53–66, 2021.

[217] Yaqi Wu, Peter K. Liaw, and Yong Zhang. Preparation of bulk tizrnbmov and nbtialtav high-entropy alloys by powder sintering. *Metals*, 11(11):1–12, 2021.

[218] Y. Kuzminova, D. Firsov, A. Dudin, S. Sergeev, A. Zhilyaev, A. Dyakov, A. Chupeeva, A. Alekseev, D. Martynov, I. Akhatov, and S. Evlashin. The effect of the parameters of the

powder bed fusion process on the microstructure and mechanical properties of CrFeCoNi medium-entropy alloys. *Intermetallics*, 116(July 2019):106651, 2020.

[219] Zhongji Sun, Xipeng Tan, Chengcheng Wang, Marion Descoins, Dominique Mangelinck, Shu Beng Tor, Eric A. Jägle, Stefan Zaefferer, and Dierk Raabe. Reducing hot tearing by grain boundary segregation engineering in additive manufacturing: example of an AlxCoCrFeNi high-entropy alloy. *Acta Materialia*, 204:116505, 2021.

[220] Pan Wang, Pengfei Huang, Fern Lan Ng, Wai Jack Sin, Shenglu Lu, Mui Ling Sharon Nai, Zhi Li Dong, and Jun Wei. Additively manufactured CoCrFeNiMn high-entropy alloy via pre-alloyed powder. *Materials and Design*, 168:107576, 2019.

[221] Pengda Niu, Ruidi Li, Shuya Zhu, Minbo Wang, Chao Chen, and Tiechui Yuan. Hot cracking, crystal orientation and compressive strength of an equimolar CoCrFeMnNi high-entropy alloy printed by selective laser melting. *Optics and Laser Technology*, 127(July 2019):106147, 2020.

[222] Zhenlin Xu, Hui Zhang, Weihuo Li, Aiqin Mao, Lin Wang, Guangsheng Song, and Yizhu He. Microstructure and nanoindentation creep behavior of CoCrFeMnNi high-entropy alloy fabricated by selective laser melting. *Additive Manufacturing*, 28(April):766–771, 2019.

[223] P. D. Niu, R. D. Li, T. C. Yuan, S. Y. Zhu, C. Chen, M. B. Wang, and L. Huang. Microstructures and properties of an equimolar AlCoCrFeNi high entropy alloy printed by selective laser melting. *Intermetallics*, 104(July 2018):24–32, 2019.

[224] Dennis Karlsson, Amalraj Marshal, Filip Johansson, Mikael Schuisky, Martin Sahlberg, Jochen M. Schneider, and Ulf Jansson. Elemental segregation in an AlCoCrFeNi high-entropy alloy – A comparison between selective laser melting and induction melting. *Journal of Alloys and Compounds*, 784:195–203, 2019.

[225] P. F. Zhou, D. H. Xiao, Z. Wu, and X. Q. Ou. Al0.5FeCoCrNi high entropy alloy prepared by selective laser melting with gas-atomized pre-alloy powders. *Materials Science and Engineering A*, 739(July 2018):86–89, 2019.

[226] Shuncun Luo, Piao Gao, Hanchen Yu, Jingjing Yang, Zemin Wang, and Xiaoyan Zeng. Selective laser melting of an equiatomic AlCrCuFeNi high-entropy alloy: Processability, non-equilibrium microstructure and mechanical behavior. *Journal of Alloys and Compounds*, 771:387–397, 2019.

[227] Yin Wang, Ruidi Li, Pengda Niu, Zhijian Zhang, Tiechui Yuan, Jiwei Yuan, and Kun Li. Microstructures and properties of equimolar AlCoCrCuFeNi high-entropy alloy additively manufactured by selective laser melting. *Intermetallics*, 120(October 2019):106746, 2020.

[228] Mina Zhang, Xianglin Zhou, Dafeng Wang, Wuzhi Zhu, Jinghao Li, and Yaoyao Fiona Zhao. AlCoCuFeNi high-entropy alloy with tailored microstructure and outstanding compressive properties fabricated via selective laser melting with heat treatment. *Materials Science and Engineering A*, 743(November 2018):773–784, 2019.

[229] Hao Liu, Xiaojia Li, Jian Liu, Wenpeng Gao, Xiaotong Du, and Jingbin Hao. Microstructural evolution and properties of dual-layer CoCrFeMnTi0.2 high-entropy alloy coating fabricated by laser cladding. *Optics and Laser Technology*, 134(September 2020):106646, 2021.

[230] Tao Tsung Shun, Liang Yi Chang, and Ming Hua Shiu. Microstructures and mechanical properties of multiprincipal component CoCrFeNiTi x alloys. *Materials Science and Engineering A*, 556:170–174, 2012.

[231] Nokeun Park, Ikuto Watanabe, Daisuke Terada, Yoshihiko Yokoyama, Peter K. Liaw, and Nobuhiro Tsuji. Recrystallization Behavior of CoCrCuFeNi High-Entropy Alloy. *Metallurgical and Materials Transactions A: Physical Metallurgy and Materials Science*, 46(4):1481–1487, 2015.

[232] Ruirun Chen, Gang Qin, Huiting Zheng, Liang Wang, Yanqing Su, YuLung Chiu, Hongsheng Ding, Jingjie Guo, and Hengzhi Fu. Composition design of high entropy alloys using the valence electron concentration to balance strength and ductility. *Acta Materialia*, 144:129–137, 2 2018.

[233] Chung Jin Tong, Yu Liang Chen, Swe Kai Chen, Jien Wei Yeh, Tao Tsung Shun, Chun Huei Tsau, Su Jien Lin, and Shou Yi Chang. Microstructure characterization of AlxCoCrCuFeNi high-entropy alloy system with multiprincipal elements. *Metallurgical and Materials Transactions A: Physical Metallurgy and Materials Science*, 36(4):881–893, 2005.

[234] P. H. Wu, N. Liu, P. J. Zhou, Z. Peng, W. D. Du, X. J. Wang, and Y. Pan. Microstructures and liquid phase separation in multicomponent CoCrCuFeNi high entropy alloys. *Materials Science and Technology (United Kingdom)*, 32(6):576–580, 2016.

[235] Rogal. Semi-solid processing of the CoCrCuFeNi high entropy alloy. *Materials and Design*, 119:406–416, 2017.

[236] Caroline A. Schneider, Wayne S. Rasband, and Kevin W. Eliceiri. NIH Image to ImageJ: 25 years of image analysis, 7 2012.

[237] Seyed Amir Farzadfar, Martin J. Murtagh, and Navin Venugopal. Impact of IN718 bimodal powder size distribution on the performance and productivity of laser powder bed fusion additive manufacturing process. *Powder Technology*, 375:60–80, 2020.

[238] A. Verma, P. Tarate, A. C. Abhyankar, M. R. Mohape, D. S. Gowtam, V. P. Deshmukh, and T. Shanmugasundaram. High temperature wear in CoCrFeNiCux high entropy alloys: The role of Cu. *Scripta Materialia*, 161:28–31, 2019.

[239] W. H. Liu, Y. Wu, J. Y. He, Y. Zhang, C. T. Liu, and Z. P. Lu. The Phase Competition and Stability of High-Entropy Alloys. *Jom*, 66(10):1973–1983, 2014.

[240] Sheng Guo, Chun Ng, Jian Lu, and C. T. Liu. Effect of valence electron concentration on stability of fcc or bcc phase in high entropy alloys. *Journal of Applied Physics*, 109(10), 2011.

[241] Yong Dong, Yiping Lu, Li Jiang, Tongmin Wang, and Tingju Li. Effects of electro-negativity on the stability of topologically close-packed phase in high entropy alloys. *Intermetallics*, 52:105–109, 2014.

[242] Akira Takeuchi, Kenji Amiya, Takeshi Wada, Kunio Yubuta, Wei Zhang, and Akihiro Makino. Entropies in alloy design for high-entropy and bulk glassy alloys. *Entropy*, 15(9):3810–3821, 2013.

[243] Y. F. Ye, Q. Wang, J. Lu, C. T. Liu, and Y. Yang. The generalized thermodynamic rule for phase selection in multicomponent alloys. *Intermetallics*, 59:75–80, 2015.

[244] Y. F. Ye, Q. Wang, J. Lu, C. T. Liu, and Y. Yang. High-entropy alloy: challenges and prospects. *Materials Today*, 19(6):349–362, 2016.

[245] Y. F. Ye, Q. Wang, J. Lu, C. T. Liu, and Y. Yang. Design of high entropy alloys: A single-parameter thermodynamic rule. *Scripta Materialia*, 104:53–55, 2015.

[246] Zhijun Wang, Yunhao Huang, Yong Yang, Jincheng Wang, and C. T. Liu. Atomic-size effect and solid solubility of multicomponent alloys. *Scripta Materialia*, 94:28–31, 2015.

[247] Zhijun Wang, Weifeng Qiu, Yong Yang, and C. T. Liu. Atomic-size and lattice-distortion effects in newly developed high-entropy alloys with multiple principal elements. *Intermetallics*, 64:63–69, 2015.

[248] Lucy Farquhar, George Maddison, Liam Hardwick, Frances Livera, Iain Todd, and Russell Goodall. In-Situ Alloying of CoCrFeNiX High Entropy Alloys by Selective Laser Melting. *Metals*, 12(3), 2022.

[249] D. D. Gu, W. Meiners, K. Wissenbach, and R. Poprawe. Laser additive manufacturing of metallic components: Materials, processes and mechanisms, 2012.

[250] T. DebRoy, H. L. Wei, J. S. Zuback, T. Mukherjee, J. W. Elmer, J. O. Milewski, A. M. Beese, A. Wilson-Heid, A. De, and W. Zhang. Additive manufacturing of metallic components – Process, structure and properties. *Progress in Materials Science*, 92:112–224, 2018.

[251] Moataz M. Attallah, Rachel Jennings, Xiqian Wang, and Luke N. Carter. Additive manufacturing of Ni-based superalloys: The outstanding issues, 10 2016.

[252] S. F. Pugh. Relations between the elastic moduli and the plastic properties of polycrystalline pure metals. *Philosophical Magazine Series 7*, 45:823–843, 1954.

[253] M. Jamal, N. Kamali Sarvestani, A. Yazdani, and A. H. Reshak. Mechanical and thermodynamical properties of hexagonal compounds at optimized lattice parameters from two-dimensional search of the equation of state. *RSC Advances*, 4(101):57903–57915, 2014.

[254] Hongzhi Lan and T. A. Venkatesh. On the relationships between hardness and the elastic and plastic properties of isotropic power-law hardening materials. *Philosophical Magazine*, 94(1):35–55, 1 2014.

[255] Krishan Kanhaiya, Seonghan Kim, Wonpil Im, and Hendrik Heinz. Accurate simulation of surfaces and interfaces of ten FCC metals and steel using Lennard–Jones potentials. *npj Computational Materials*, 7(1), 12 2021.

[256] Devarakonda Annapurna Padmavathi. Potential Energy Curves and Material Properties. *Materials Sciences and Applications*, 02(02):97–104, 2011.

[257] Charles Kittel. *Introduction to solid state physics*. John Wiley & sons, inc, 2005.

[258] W. King, A. T. Anderson, R. M. Ferencz, N. E. Hodge, C. Kamath, and S. A. Khairallah. Overview of modelling and simulation of metal powder bed fusion process at Lawrence Livermore National Laboratory, 6 2015.

[259] Christoph Meier, Sebastian L. Fuchs, Nils Much, Jonas Nitzler, Ryan W. Penny, Patrick M. Praegla, Sebastian D. Proell, Yushen Sun, Reimar Weissbach, Magdalena Schreter, Neil E. Hodge, A. John Hart, and Wolfgang A. Wall. Physics-based modeling and predictive simulation of powder bed fusion additive manufacturing across length scales. *GAMM Mitteilungen*, 44(3), 9 2021.

[260] M. M. Francois, A. Sun, W. E. King, N. J. Henson, D. Tourret, C. A. Bronkhorst, N. N. Carlson, C. K. Newman, T. Haut, J. Bakosi, J. W. Gibbs, V. Livescu, S. A. Vander Wiel, A. J. Clarke, M. W. Schraad, T. Blacker, H. Lim, T. Rodgers, S. Owen, F. Abdeljawad, J. Madison, A. T. Anderson, J. L. Fattebert, R. M. Ferencz, N. E. Hodge, S. A. Khairallah, and O. Walton. Modeling of additive manufacturing processes for metals: Challenges and opportunities, 8 2017.

[261] John Goldak, Aditya Chakravarti, and Malcolm Bibby. A new finite element model for welding heat sources. *Metallurgical Transactions B*, 15(2):299–305, 1984.

[262] Kubra Karayagiz, Alaa Elwany, Gustavo Tapia, Brian Franco, Luke Johnson, Ji Ma, Ibrahim Karaman, and Raymundo Arróyave. Numerical and experimental analysis of heat distribution in the laser powder bed fusion of Ti-6Al-4V. *IISE Transactions*, 51(2):136–152, 2019.

[263] J J S Dilip, Shanshan Zhang, Chong Teng, Kai Zeng, Chris Robinson, Deepankar Pal, and Brent Stucker. Influence of processing parameters on the evolution of melt pool, porosity, and microstructures in Ti-6Al-4V alloy parts fabricated by selective laser melting. *Progress in Additive Manufacturing*, 2(3):157–167, 2017.

[264] Xufei Lu, Xin Lin, Michele Chiumenti, Miguel Cervera, Yunlong Hu, Xianglin Ji, Liang Ma, Haiou Yang, and Weidong Huang. Residual stress and distortion of rectangular and S-shaped Ti-6Al-4V parts by Directed Energy Deposition: Modelling and experimental calibration. *Additive Manufacturing*, 26:166–179, 2019.

[265] BY D Rosenthal. The Theory of Moving Sources of Heat and Its Application to Metal Treatments. Technical report, University of Cambridge, 1946.

[266] M Gaumann, C Bezenç On, P Canalis, and W Kurz. Single-crystal laser deposition of superalloys: processing- microstructure maps. Technical report, Swiss Federal Institute of Technology Lausanne, 2001.

[267] Lova Chechik, Katerina A. Christofidou, Jonathon F.S. Markanday, Alexander D. Goodall, James R. Miller, Geoff West, Howard Stone, and Iain Todd. Hardness variation in inconel 718 produced by laser directed energy deposition. *Materialia*, 26, 12 2022.

[268] Abdallah Reza, Cody A. Dennett, Michael P. Short, John Waite, Yevhen Zayachuk, Christopher M. Magazzeni, Simon Hills, and Felix Hofmann. Non-contact, non-destructive mapping of thermal diffusivity and surface acoustic wave speed using transient grating spectroscopy. *The Review of scientific instruments*, 91(5):054902, 2020.

[269] K. Jin, B. C. Sales, G. M. Stocks, G. D. Samolyuk, M. Daene, W. J. Weber, Y. Zhang, and H. Bei. Tailoring the physical properties of Ni-based single-phase equiatomic alloys by modifying the chemical complexity. *Scientific Reports*, 6, 2 2016.

[270] K Jin, S Mu, K An, W D Porter, G D Samolyuk, G M Stocks, and H Bei. Thermophysical properties of Ni-containing single-phase concentrated solid solution alloys. *Materials & Design*, 117:185–192, 2017.

[271] M. Vaidya, S. Trubel, B. S. Murty, G. Wilde, and S. V. Divinski. Ni tracer diffusion in CoCrFeNi and CoCrFeMnNi high entropy alloys. *Journal of Alloys and Compounds*, 688:994–1001, 2016.

[272] A Sh Agazhanov, D A Samoshkin, and Yu M Kozlovskii. Thermophysical properties of Inconel 718 alloy. *Journal of Physics: Conference Series*, 1382(1):012175, 2019.

[273] Ragnhild E Aune, Livio Battezzati, Robert Brooks, Ivan Egry, Hans-Jörg Fecht, Jean-Paul Garandet, Miyuki Hayashi, Ken C Mills, Alberto Passerone, Peter N Quested, Enrica Ricci, Frank Schmidt-Hohagen, Seshadri Seetharaman, Bernard Vinet, and Rainer K Wunderlich. Thermophysical properties of IN738LC, MM247LC AND CMSX-4 in the liquid and high temperature solid phase. Technical report, KTH, 2005.

[274] Kyomin Kim and Woochul Kim. Thermophysical properties of nickel-based superalloy CM247LC. *Transactions of the Korean Society of Mechanical Engineers, B*, 44(10):619–625, 2020.

[275] Shih-Jeh Wu, Pei-chieh Chin, and Hawking Liu. Measurement of Elastic Properties of Brittle Materials by Ultrasonic and Indentation Methods. *Applied Sciences*, 9:2067, 5 2019.

[276] Mehdi Rahimian. PhD Thesis Physical simulation of investment casting of Mar-M247 Ni-based superalloy. Technical report, UC3M, 2015.

[277] Taishi Matsushita, H.-J Fecht, Rainer Wunderlich, Ivan Egry, and Seshadri Seetharaman. Studies of the Thermophysical Properties of Commercial CMSX-4 Alloy. *Journal Chemical Engineering Data*, 54:2584–2592, 9 2009.

[278] Markus Ramsperger, Robert F Singer, and Carolin Körner. Microstructure of the Nickel-Base Superalloy CMSX-4 Fabricated by Selective Electron Beam Melting. *Metallurgical and Materials Transactions A*, 47(3):1469–1480, 2016.

[279] M Fahrmann, W Hermann, E Fahrmann, A Boegli, T M Pollock, and H G Sockel. Determination of matrix and precipitate elastic constants in (k-k%) Ni-base model alloys, and their relevance to rafting. Technical report, 1999.

[280] M. S.A. Karunaratne, S. Kyaw, A. Jones, R. Morrell, and R. C. Thomson. Modelling the coefficient of thermal expansion in Ni-based superalloys and bond coatings. *Journal of Materials Science*, 51(9):4213–4226, 5 2016.

[281] Kenneth C. Mills. *Recommended values of thermophysical properties for selected commercial alloys.* Woodhead Publishing, 2002.

[282] S D Conzone, D P But, and A H Bartlett. Joining MoSi 2 to 316L stainless steel. Technical report, Los Alamos National Laboratory, 1997.

[283] Spiros Zinelis, Athena Tsetsekou, and Triantafillos Papadopoulos. Thermal expansion and microstructural analysis of experimental metal-ceramic titanium alloys. *The Journal of Prosthetic Dentistry*, 90(4):332–338, 2003.

[284] W Kurz and R Trivedi. Rapid solidification processing and microstructure formation. Technical report, Swiss Federal Institute of Technology Lausanne,, 1994.

[285] Peng Chen, Xiyu Yao, Moataz M. Attallah, and Ming Yan. In-situ alloyed CoCrFeMnNi high entropy alloy: Microstructural development in laser powder bed fusion. *Journal of Materials Science and Technology*, 123:123–135, 10 2022.

[286] Yanjin Lu, Songquan Wu, Yiliang Gan, Tingting Huang, Chuanguang Yang, Lin Junjie, and Jinxin Lin. Study on the microstructure, mechanical property and residual stress of SLM Inconel-718 alloy manufactured by differing island scanning strategy. *Optics and Laser Technology*, 75:197–206, 7 2015.

[287] Michele Calandri, Shuo Yin, Barry Aldwell, Flaviana Calignano, Rocco Lupoi, and Daniele Ugues. Texture and microstructural features at different length scales in Inconel 718 produced by selective laser melting. *Materials*, 12(8), 2019.

[288] V. D. Divya, R. Muñoz-Moreno, O. M.D.M. Messé, J. S. Barnard, S. Baker, T. Illston, and H. J. Stone. Microstructure of selective laser melted CM247LC nickel-based superalloy and its evolution through heat treatment. *Materials Characterization*, 114:62–74, 4 2016.

[289] Bikash Kumar, Shreehard Sahu, Dheepa Srinivasan, and Balila Nagamani Jaya. Influence of Heat Input on Solidification Cracking in Additively Manufactured CM247LC Ni-based Superalloy. *Metallurgical and Materials Transactions A*, 6 2023.

[290] Luke N. Carter, Christopher Martin, Philip J. Withers, and Moataz M. Attallah. The influence of the laser scan strategy on grain structure and cracking behaviour in SLM

powder-bed fabricated nickel superalloy. *Journal of Alloys and Compounds*, 615:338–347, 12 2014.

[291] Yuanbo T Tang, Joseph N Ghoussoub, Chinnapat Panwisawas, David M Collins, Sajjad Amirkhanlou, John W G Clark, André A N Németh, D Graham McCartney, and Roger C Reed. The Effect of Heat Treatment on Tensile Yielding Response of the New Superalloy ABD-900AM for Additive Manufacturing. In *Superalloys 2020*, pages 1055–1065. Springer International Publishing, 2020.

[292] K A Christofidou, H T Pang, W Li, Y Pardhi, C N Jones, N G Jones, and H J Stone. Microstructural control and optimization of Haynes 282 manufactured through laser powder bed fusion. In *Superalloys 2020: Proceedings of the 14th International Symposium on Superalloys*, pages 1014–1023. Springer, 2020.

[293] Abdul Shaafi Shaikh, Fiona Schulz, Kevin Minet-Lallemand, and Eduard Hryha. Microstructure and mechanical properties of Haynes 282 superalloy produced by laser powder bed fusion. *Materials Today Communications*, 26, 3 2021.

[294] Kamran Aamir Mumtaz, Poonjolai Erasenthiran, and Neil Hopkinson. High density selective laser melting of Waspaloy®. *Journal of Materials Processing Technology*, 195(1-3):77–87, 1 2008.

[295] Angelika Jedynak, Alexander Sviridov, Markus Bambach, Daniel Beckers, and Gregor Graf. On the potential of using selective laser melting for the fast development of forging alloys at the example of waspaloy. In *Procedia Manufacturing*, volume 47, pages 1149–1153. Elsevier B.V., 2020.

[296] Inmaculada Lopez-Galilea, Benjamin Ruttert, Junyang He, Thomas Hammerschmidt, Ralf Drautz, Baptiste Gault, and Werner Theisen. Additive manufacturing of CMSX-4 Ni-base superalloy by selective laser melting: Influence of processing parameters and heat treatment. *Additive Manufacturing*, 30, 12 2019.

[297] Chandrika Kamath, Bassem El-Dasher, Gilbert F. Gallegos, Wayne E. King, and Aaron Sisto. Density of additively-manufactured, 316L SS parts using laser powder-bed fusion at powers up to 400 W. *International Journal of Advanced Manufacturing Technology*, 74(1-4):65–78, 2014.

[298] K. Saeidi, X. Gao, Y. Zhong, and Z. J. Shen. Hardened austenite steel with columnar subgrain structure formed by laser melting. *Materials Science and Engineering A*, 625:221–229, 2 2015.

[299] Yu Sun, Rainer J. Hebert, and Mark Aindow. Effect of heat treatments on microstructural evolution of additively manufactured and wrought 17-4PH stainless steel. *Materials and Design*, 156:429–440, 10 2018.

[300] Jordan S. Weaver, Justin Whiting, Vipin Tondare, Carlos Beauchamp, Max Peltz, Jared Tarr, Thien Q. Phan, and M. Alkan Donmez. The effects of particle size distribution on the rheological properties of the powder and the mechanical properties of additively manufactured 17-4 PH stainless steel. *Additive Manufacturing*, 39, 3 2021.

[301] P. D. Nezhadfar, Kathryn Anderson-Wedge, S. R. Daniewicz, Nam Phan, Shuai Shao, and Nima Shamsaei. Improved high cycle fatigue performance of additively manufactured 17-4 PH stainless steel via in-process refining micro-/defect-structure. *Additive Manufacturing*, 36, 12 2020.

[302] Patcharapit Promoppatum, Recep Onler, and Shi Chune Yao. Numerical and experimental investigations of micro and macro characteristics of direct metal laser sintered Ti-6Al-4V products. *Journal of Materials Processing Technology*, 240:262–273, 2 2017.

[303] Galina Kasperovich, Jan Haubrich, Joachim Gussone, and Guillermo Requena. Correlation between porosity and processing parameters in TiAl6V4 produced by selective laser melting. *Materials and Design*, 105:160–170, 9 2016.

[304] H. Attar, M. Calin, L. C. Zhang, S. Scudino, and J. Eckert. Manufacture by selective laser melting and mechanical behavior of commercially pure titanium. *Materials Science and Engineering A*, 593:170–177, 1 2014.

[305] Amanda S. Wu, Donald W. Brown, Mukul Kumar, Gilbert F. Gallegos, and Wayne E. King. An Experimental Investigation into Additive Manufacturing-Induced Residual Stresses in 316L Stainless Steel. *Metallurgical and Materials Transactions A: Physical Metallurgy and Materials Science*, 45(13):6260–6270, 10 2014.

[306] Wenhui Yu, Swee Leong Sing, Chee Kai Chua, and Xuelei Tian. Influence of re-melting on surface roughness and porosity of AlSi10Mg parts fabricated by selective laser melting. *Journal of Alloys and Compounds*, 792:574–581, 7 2019.

[307] A. Katz-Demyanetz, I. I. Gorbachev, E. Eshed, V. V. Popov, and M. Bamberger. High entropy Al0.5CrMoNbTa0.5 alloy: Additive manufacturing vs. casting vs. CALPHAD approval calculations. *Materials Characterization*, 167, 9 2020.

[308] Vladimir V Popov, Alexander Katz-Demyanetz, Andrey Koptyug, and Menachem Bamberger. Selective electron beam melting of Al0.5CrMoNbTa0.5 high entropy alloys using elemental powder blend. *Heliyon*, 5:1188, 2019.

[309] Christian Haase, Florian Tang, Markus B. Wilms, Andreas Weisheit, and Bengt Hallstedt. Combining thermodynamic modeling and 3D printing of elemental powder blends for high-throughput investigation of high-entropy alloys – Towards rapid alloy screening and design. *Materials Science and Engineering A*, 688(January):180–189, 2017.

[310] T. Borkar, B. Gwalani, D. Choudhuri, C. V. Mikler, C. J. Yannetta, X. Chen, R. V. Ramanujan, M. J. Styles, M. A. Gibson, and R. Banerjee. A combinatorial assessment of AlxCrCuFeNi2 (x = 0 - 1.5) complex concentrated alloys: Microstructure, microhardness, and magnetic properties. *Acta Materialia*, 116:63–76, 9 2016.

[311] Rui Wang, Kai Zhang, Christopher Davies, and Xinhua Wu. Evolution of microstructure, mechanical and corrosion properties of AlCoCrFeNi high-entropy alloy prepared by direct laser fabrication. *Journal of Alloys and Compounds*, 694:971–981, 2017.

[312] Tushar Borkar, Varun Chaudhary, Bharat Gwalani, Deep Choudhuri, Calvin V Mikler, Vishal Soni, Talukder Alam, Raju V. Ramanujan, and Rajarshi Banerjee. A Combinatorial Approach for Assessing the Magnetic Properties of High Entropy Alloys: Role of Cr in AlCoxCr1-xFeNi. *Advanced Engineering Materials*, 19(8):1700048, 2017.

[313] Yaqing Hou, Hang Su, Hao Zhang, Xuandong Wang, and Changchang Wang. Fabricating homogeneous FeCoCrNi high-entropy alloys via SLM in situ alloying. *Metals*, 11(6), 6 2021.

[314] Jingbo Gao, Yuting Jin, Yongqiang Fan, Dake Xu, Lei Meng, Cong Wang, Yuanping Yu, Deliang Zhang, and Fuhui Wang. Fabricating antibacterial CoCrCuFeNi high-entropy alloy via selective laser melting and in-situ alloying. *Journal of Materials Science and Technology*, 102:159–165, 3 2022.

[315] Danyang Lin, Lianyong Xu, Xiaojie Li, Hongyang Jing, Gang Qin, Hongning Pang, and Fumiyoshi Minami. A Si-containing FeCoCrNi high-entropy alloy with high strength and ductility synthesized in situ via selective laser melting. *Additive Manufacturing*, 35, 10 2020.

[316] F. Bachmann, R. Hielscher, and H. Schaeben. Texture analysis with MTEX- Free and open source software toolbox. In *Solid State Phenomena*, volume 160, pages 63–68. Trans Tech Publications Ltd, 2010.

[317] Anatoliy Popovich and Vadim Sufiiarov. Metal Powder Additive Manufacturing. In *New Trends in 3D Printing*. InTech, 7 2016.

[318] Mozhdeh Mehrabi, Jabbar Gardy, Fatemeh A. Talebi, Amin Farshchi, Ali Hassanpour, and Andrew E. Bayly. An investigation of the effect of powder flowability on the powder spreading in additive manufacturing. *Powder Technology*, 413, 1 2023.

[319] Salah Eddine Brika, Morgan Letenneur, Christopher Alex Dion, and Vladimir Brailovski. Influence of particle morphology and size distribution on the powder flowability and laser powder bed fusion manufacturability of Ti-6Al-4V alloy. *Additive Manufacturing*, 31, 1 2020.

[320] Zackary Snow, Richard Martukanitz, and Sanjay Joshi. On the development of powder spreadability metrics and feedstock requirements for powder bed fusion additive manufacturing. *Additive Manufacturing*, 28:78–86, 8 2019.

[321] G. K.L. Ng, A. E.W. Jarfors, G. Bi, and H. Y. Zheng. Porosity formation and gas bubble retention in laser metal deposition. *Applied Physics A: Materials Science and Processing*, 97(3):641–649, 2009.

[322] Marvin A ; Spurek, Lukas ; Haferkamp, Christian ; Weiss, Adriaan B ; Spierings, Johannes H ; Schleifenbaum, and Konrad Wegener. Influence of the particle size distribution of monomodal 316L powder on its flowability and processability in powder bed fusion. 2021.

[323] Katrin I Schwendner, Rajarshi Banerjee, Peter C Collins, Craig A Brice, and Hamish L Fraser. Direct laser deposition of alloys from elemental powder blends. Technical report, 2001.

[324] Lianfeng Wang, Jiubin Jue, Mujian Xia, Lijie Guo, Biao Yan, and Dongdong Gu. Effect of the thermodynamic behavior of selective laser melting on the formation of in situ oxide dispersion-strengthened aluminum-based composites. *Metals*, 6(11), 11 2016.

[325] Sarah J. Wolff, Hao Wu, Niranjan Parab, Cang Zhao, Kornel F. Ehmann, Tao Sun, and Jian Cao. In-situ high-speed X-ray imaging of piezo-driven directed energy deposition additive manufacturing. *Scientific Reports*, 9(1), 12 2019.

[326] Prince Valentine Cobbinah, Sae Matsunaga, and Yoko Yamabe-Mitarai. Controlled Crystallographic Texture Orientation in Structural Materials Using the Laser Powder Bed Fusion Process—A Review, 12 2023.

[327] Kai Chi Lo, Yao Jen Chang, Hideyuki Murakami, Jien Wei Yeh, and An Chou Yeh. An oxidation resistant refractory high entropy alloy protected by CrTaO 4 -based oxide. *Scientific Reports*, 9(1), 12 2019.

[328] Mathilde Laurent-Brocq, Xavier Sauvage, Alfiya Akhatova, Loïc Perrière, Eric Leroy, and Yannick Champion. Precipitation and Hardness of Carbonitrides in a CrMnFeCoNi High Entropy Alloy. *Advanced Engineering Materials*, 19(5), 5 2017.

[329] Jingzhi He, Yating Qiao, Ruixin Wang, Yu Tang, Shun Li, Xiyue Liu, Yicong Ye, Li'an Zhu, Zhen Wang, and Shuxin Bai. State and effect of oxygen on high entropy alloys prepared by powder metallurgy. *Journal of Alloys and Compounds*, 891, 1 2022.

[330] M. G. Poletti, C. M. McCaughey, G. Fiore, R. Goodall, and L. Battezzati. Refractory high entropy alloys: CrMoNbTiVWZr and AlxCryNbMoTiVzZry (x=0,0.6; y=0.3, z=0,0.6). *International Journal of Refractory Metals and Hard Materials*, 76(May):128–133, 2018.

[331] L. Lilensten, J. P. Couzinié, L. Perrière, J. Bourgon, N. Emery, and I. Guillot. New structure in refractory high-entropy alloys. *Materials Letters*, 132:123–125, 10 2014.

[332] Kexuan Zhou, Zhijun Wang, Feng He, Shaofei Liu, Junjie Li, Ji jung Kai, and Jincheng Wang. A precipitation-strengthened high-entropy alloy for additive manufacturing. *Additive Manufacturing*, 35, 10 2020.

[333] Chu Lun Alex Leung, Sebastian Marussi, Michael Towrie, Robert C. Atwood, Philip J. Withers, and Peter D. Lee. The effect of powder oxidation on defect formation in laser additive manufacturing. *Acta Materialia*, 166:294–305, 3 2019.

[334] Xinliang Yang, Feng Gao, Fengzai Tang, Xinjiang Hao, and Zushu Li. Effect of Surface Oxides on the Melting and Solidification of 316L Stainless Steel Powder for Additive Manufacturing. *Metallurgical and Materials Transactions A: Physical Metallurgy and Materials Science*, 52(10):4518–4532, 10 2021.

[335] Dongdong Gu and Donghua Dai. Role of melt behavior in modifying oxidation distribution using an interface incorporated model in selective laser melting of aluminum-based material. *Journal of Applied Physics*, 120(8):083104, 8 2016.

[336] N. R. Philips, M. Carl, and N. J. Cunningham. New Opportunities in Refractory Alloys. *Metallurgical and Materials Transactions A: Physical Metallurgy and Materials Science*, 51(7):3299–3310, 7 2020.

[337] Xiqian Wang, Luke N. Carter, Bo Pang, Moataz M. Attallah, and Michael H. Loretto. Microstructure and yield strength of SLM-fabricated CM247LC Ni-Superalloy. *Acta Materialia*, 128:87–95, 4 2017.

[338] A. Després, C. Mayer, M. Veron, E. F. Rauch, M. Bugnet, J. J. Blandin, G. Renou, C. Tassin, P. Donnadieu, and G. Martin. On the variety and formation sequence of second-phase particles in nickel-based superalloys fabricated by laser powder bed fusion. *Materialia*, 15, 3 2021.

[339] Peter Mercelis and Jean Pierre Kruth. Residual stresses in selective laser sintering and selective laser melting. *Rapid Prototyping Journal*, 12(5):254–265, 2006.

[340] Zhaopeng Tong, Xudong Ren, Jiafei Jiao, Wangfan Zhou, Yunpeng Ren, Yunxia Ye, Enoch Asuako Larson, and Jiayang Gu. Laser additive manufacturing of FeCrCoMnNi high-entropy alloy: Effect of heat treatment on microstructure, residual stress and mechanical property. *Journal of Alloys and Compounds*, 785:1144–1159, 5 2019.

[341] Qi Chao, Sebastian Thomas, Nick Birbilis, Pavel Cizek, Peter D. Hodgson, and Daniel Fabijanic. The effect of post-processing heat treatment on the microstructure, residual stress and mechanical properties of selective laser melted 316L stainless steel. *Materials Science and Engineering: A*, 821, 7 2021.

[342] C. R. Weinberger, B. L. Boyce, and C. C. Battaile. Slip planes in bcc transition metals, 2013.

Appendices

Appendix A

Design of Experiment Parameters for In-Situ alloying of CoCrFeNi-based HEAs

Table 1: *Parameters used in the PBF-LB/M of CoCrFeNi-based HEAs, designed using a central composite structure on the design of experiment software Minitab. The laser spot size and layer thickness were kept constant at 70 µm and 30 µm respectively.*

Part	Power (W)	Velocity (mm/s)	Hatch (µm)	VED (J/mm^3)
1	166	1118	108	45.8
2	130	850	75	68.0
3	94	1118	42	66.7
4	166	582	42	226.4
5	166	582	108	88.0
6	130	850	75	68.0
7	130	1300	75	44.4
8	130	850	130	39.2
9	94	582	108	49.8
10	130	400	75	144.4
11	190	850	75	99.3
12	130	850	20	254.9
13	70	850	75	36.6
14	130	850	75	68.0
15	130	850	75	68.0
16	94	582	42	128.2
17	166	1118	42	117.8
18	94	1118	108	26.0
19	130	850	75	68.0
20	130	850	75	68.0

Appendix B

Derivation of the Relationship between Coefficient of Thermal Expansion and Bond Energy

The formation of this methodology is adapted from work by Kittel [257]. The interaction of electrically neutral atoms can be modeled using the Lennard-Jones potential [255]:

$$u(r) = u_0 \left[\left(\frac{r_0}{r} \right)^{12} - 2 \left(\frac{r_0}{r} \right)^{6} \right] \tag{1}$$

Where using a Taylor expansion, the potential energy of the atoms at a displacement $x = r - r_0$ from equilibrium separation at absolute zero for small oscillations is:

$$u(x) = u_0 + bx + cx^2 + gx^3 + \cdots \tag{2}$$

where:

$$u_0 = u(r_0) \tag{3}$$

$$b = \frac{du(r_0)}{dr} = 0 \tag{4}$$

$$c = \frac{1}{2} \frac{d^2u(r_0)}{dr^2} = \frac{36\, u_0}{r_0^2} \tag{5}$$

$$g = -\frac{1}{6} \frac{d^3u(r_0)}{dr^3} = \frac{252\, u_0}{r_0^3} \tag{6}$$

Using the Boltzmann distribution function, the average atomic displacement can be calculated, by evaluating the thermodynamic probability of possible values of x:

$$\langle x \rangle = \frac{\int_{-\infty}^{\infty} \exp[-\beta u(x)]\, x\, dx}{\int_{-\infty}^{\infty} \exp[-\beta u(x)]\, dx} \tag{7}$$

where $\beta = 1/k_B T$. For displacements such that the $k_B T$ is much larger than anharmonic terms, substitution of Equation 2 into Equation 7, where only the magnitude of c and g are considered (as motion is oscillatory), yields [257]:

$$\langle x \rangle = \frac{3g}{4c^2} k_B T \tag{8}$$

Substituting in for g and c gives:

$$\langle x \rangle = \frac{7r_0}{48u_0} k_B T \tag{9}$$

The general definition of the linear thermal expansion coefficient is given by:

$$\alpha_{CTE} = \frac{1}{r_0} \frac{d\langle x \rangle}{dT} \tag{10}$$

Therefore an approximation to the material CTE is given by:

$$\alpha_{CTE} = \frac{7k_B}{48u_0} \tag{11}$$

Appendix C

Compression Curves for $Mo_5Nb_{35}Ti_{30}V_{30}$

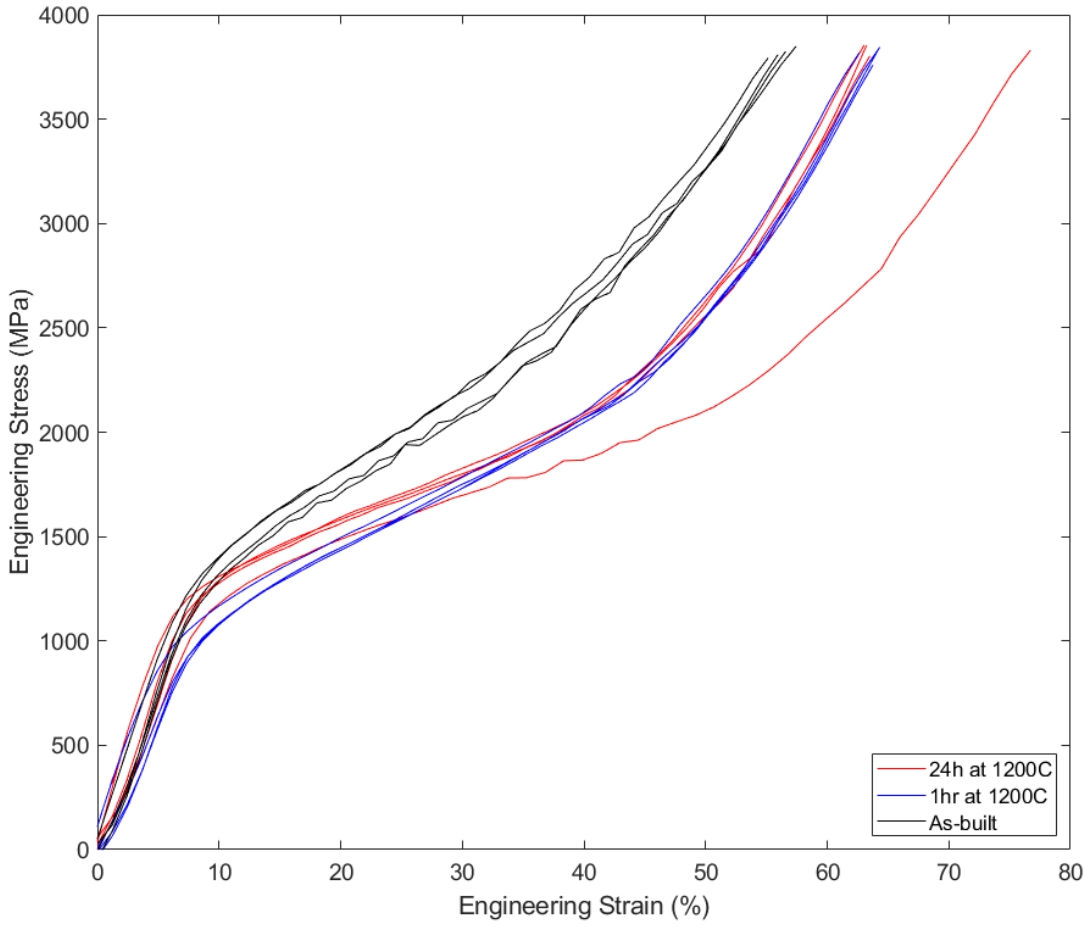

Figure 1: *Compressive engineering stress vs engineering strain curves for the $Mo_5Nb_{35}Ti_{30}V_{30}$ RHEA in the as-built, and after heat treatment for 1 hour and 24 hours at 1200°.*

Appendix D

Thermal Properties of $Mo_5Nb_{35}Ti_{30}V_{30}$

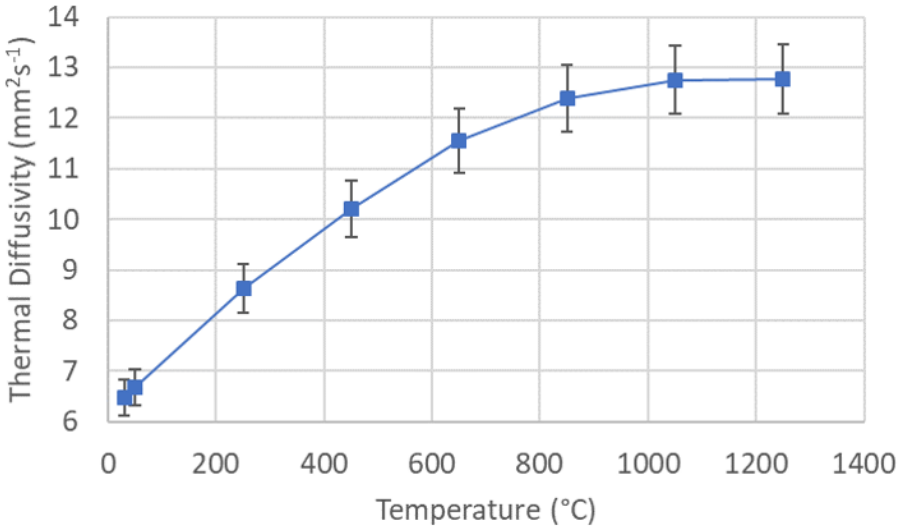

Figure 2: *Thermal diffusivity of as-built $Mo_5Nb_{35}Ti_{30}V_{30}$ for temperatures ranging from room temperature (25°C) to 1250 °C, measured by laser flash (NETZSCH LFA467).*

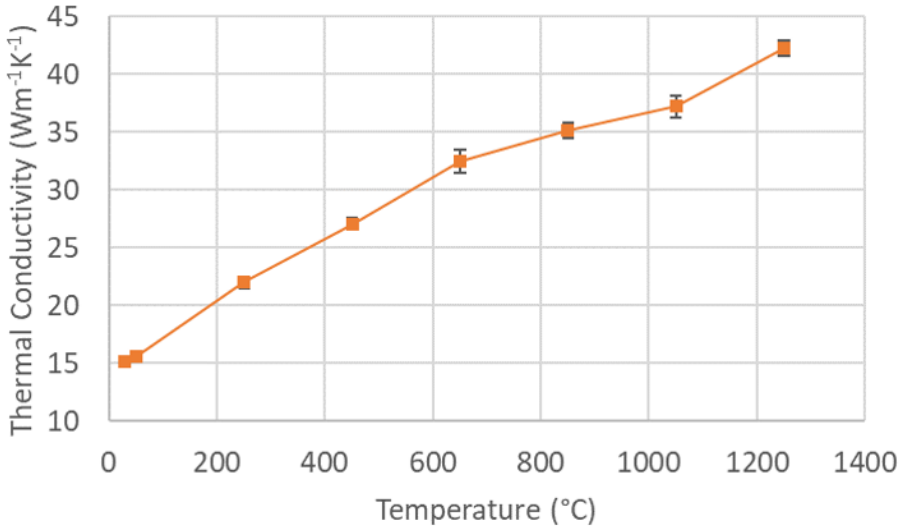

Figure 3: *Thermal conductivity of as-built $Mo_5Nb_{35}Ti_{30}V_{30}$ for temperatures ranging from room temperature (25°C) to 1250 °C, measured by laser flash (NETZSCH LFA467).*

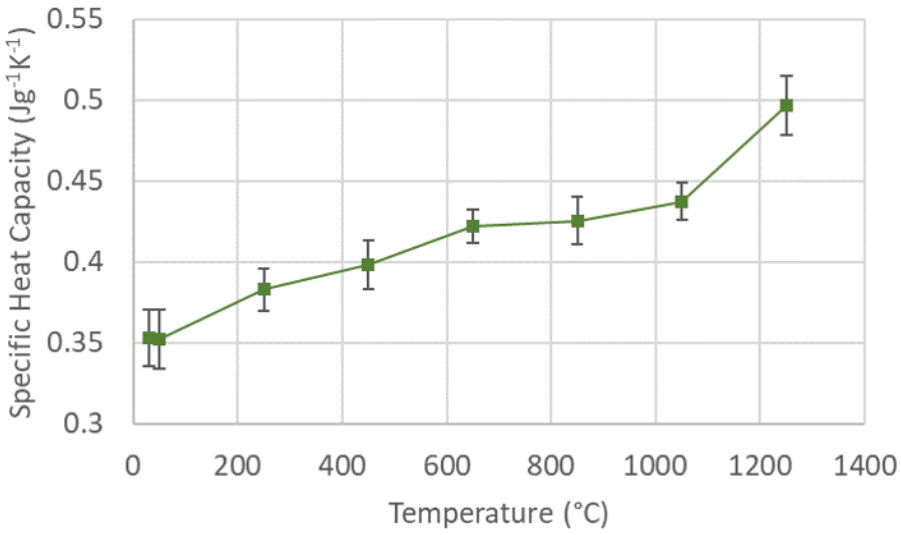

Figure 4: *Specific heat capacity of as-built $Mo_5Nb_{35}Ti_{30}V_{30}$ for temperatures ranging from room temperature (25°C) to 1250 °C, measured by laser flash (NETZSCH LFA467).*

Oxidation of $Mo_5Nb_{35}Ti_{30}V_{30}$

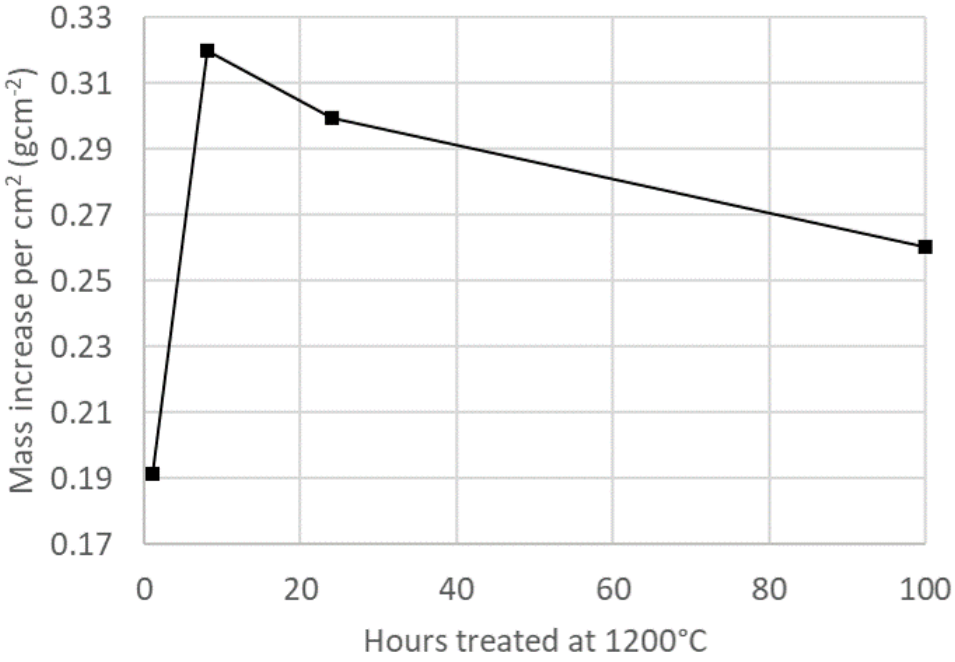

Figure 5: *Mass gain normalised by surface area of $Mo_5Nb_{35}Ti_{30}V_{30}$ after exposure to atmospheric conditions at 1200 °C for 1, 8, 24 and 100 hours. Where samples were put into the furnace at 1200 °, held at that temperature for the designated time and then removed immediately before cooling.*

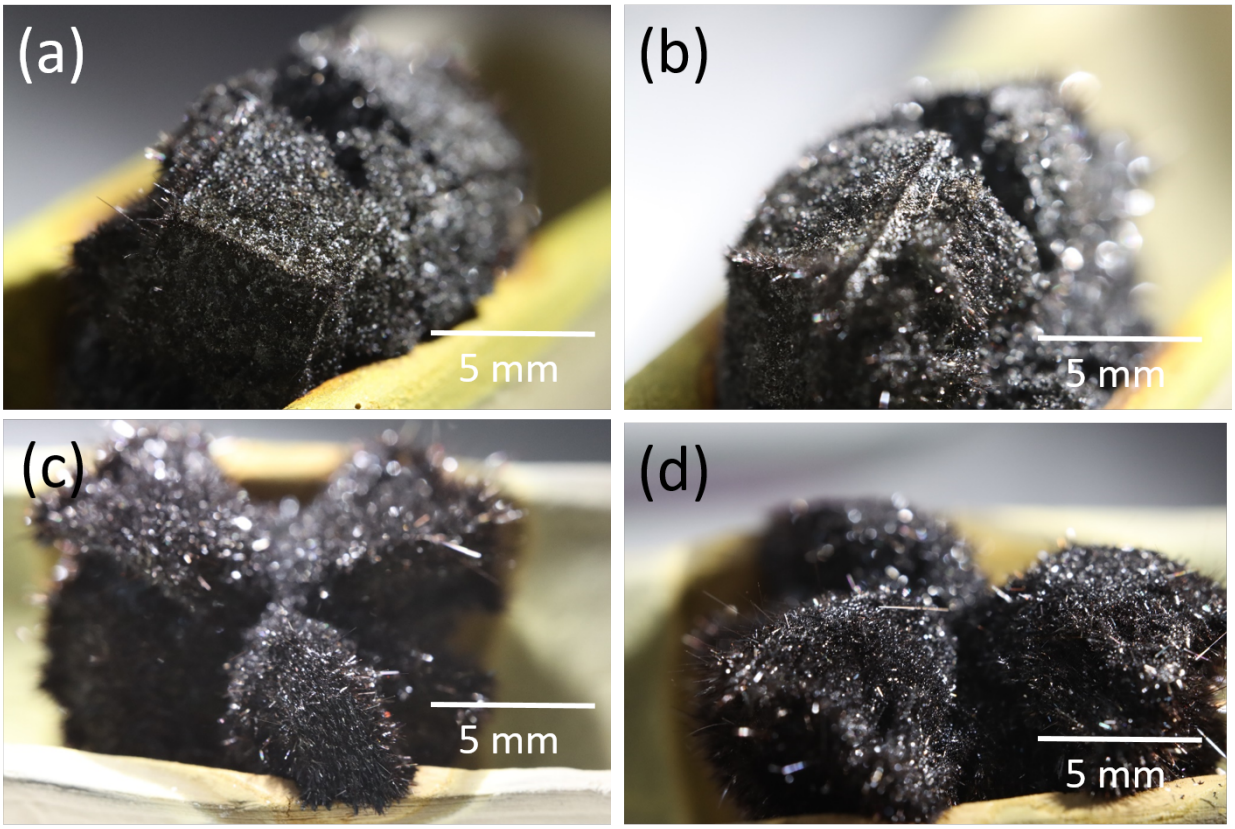

Figure 6: *Macro images of $Mo_5Nb_{35}Ti_{30}V_{30}$ after exposure to atmospheric conditions at 1200 °C for (a) 1, (b) 8, (c) 24 and (d) 100 hours. All scale bars are approximate.*